Electrically Detected Magnetic Resonance in Semiconductor and Carbon Nanodevices

Volker Lang
Trinity College Oxford

A Thesis submitted for the Degree of Doctor of Philosophy
at the University of Oxford
Hilary Term 2012

To my parents and grandparents.

"Für den Gläubigen steht Gott am Anfang,
für den Wissenschaftler am Ende
aller Überlegungen."

Max Planck, 1858 – 1947

Electrically Detected Magnetic Resonance in Semiconductor and Carbon Nanodevices

Volker Lang
Trinity College
Hilary Term 2012

Abstract of a Thesis
submitted for the Degree of Doctor of Philosophy

Electrically detected magnetic resonance (EDMR) is a sensitive spectroscopic technique, which can be used to readout few to single electron spins in semiconductor and carbon nanodevices for applications in solid state quantum information processing (QIP). Since only electrically active defects contribute to the EDMR signal, this technique can be used further to investigate defects and impurities in photovoltaic devices, in which they limit the sunlight-to-energy conversion efficiency significantly. Here, I employ X-band EDMR for semiconductor defect analysis and identify the most important recombination centres in Czochralski silicon with oxide precipitates, which can be intentionally grown to confine detrimental metallic impurities to inactive regions of the wafer in order to serve as a defect-free substrate for modern silicon photovoltaic devices. Those experiments show that oxide precipitation is accompanied by the formation of silicon dangling bonds. Furthermore, I describe a very promising route towards the fabrication and readout of few to single electron spins in carbon nanotube devices, which can be characterised structurally via transmission electron microscopy in order to relate their electrical and spin properties with their structure. Finally, I employ EDMR to read out electron spin states in donor-doped silicon field-effect transistors as a prerequisite for their application in QIP. I report on a novel cryogenic probe head for EDMR experiments in resonant microwave cavities operating at 0.35 T (9.7 GHz, X-band) and 3.34 T (94 GHz, W-band). This approach overcomes the inherent limitations of conventional X-band EDMR and permits the investigation of paramagnetic states with a higher spectroscopic resolution and signal intensity. Both advantages are demonstrated and discussed. I further report on a novel mechanism giving rise to the EDMR effect in donor-doped silicon field-effect transistors, which is capable of explaining why the EDMR signal intensities of the conduction electrons are enhanced by a factor of ~ 100, while the donor resonance signals increase by a factor of ~ 20 from X- to W-band only. The spin-relaxation and dephasing times are extracted from a series of pulsed-EDMR measurements and confirm this model. The author gratefully acknowledges funding from Trinity College Oxford, Department of Materials, EPSRC DTA, and Konrad-Adenauer-Stiftung e.V. (Begabtenförderung).

Acknowledgements

The completion of this work would not have been possible without the contribution of my supervisors, colleagues, collaborators as well as the support from my friends and family. Firstly, I would like to thank my supervisors Andrew Briggs, Arzhang Ardavan, and John Morton for giving me the opportunity to work in this exciting area of research. I thank *Andrew Briggs* for his support, encouragement, and vision driving this research programme as well as for giving me the opportunity to visit Peking University in China as a visiting researcher. I also thank *Arzhang Ardavan* for his support and for giving me access to the Centre for Advanced Electron Spin Resonance (CÆSR) housed in the Inorganic Chemistry Research Laboratory. Special thanks go to *John Morton* for his unyielding support of my research, various very fruitful discussions, and for giving me the opportunity to work on the different very interesting collaborative projects.

This work would not have been possible without the help and support of my colleagues and collaborators, who have generously given me the opportunity to learn from their experience and work on their devices. In particular, I thank my colleague *Richard George* for sharing his deep physical and technical understanding and for helping me to setup and perform different experiments in 020 and the CÆSR laboratory. I thank *John Murphy* for giving me the opportunity to study spin-dependent recombination in modern photovoltaic materials and for sharing his deep insight into defects, impurities, and internal gettering in silicon during various very fruitful discussions. I thank *Christopher Allan* for sharing his device and EBL experience and continuing my work on carbon nanodevices. Furthermore, I thank our technicians for maintaining the different instruments as well as for their advice during the experiments. To this end, I thank *Radka Chakalova* in Begbroke Science Park for sharing her expertise about semiconductor device fabrication and for helping me to

Figure 0.1.: 'The College of the Holy and Undivided Trinity in the University of Oxford, of the foundation of Sir Thomas Pope (Knight)' in MT 2009. Thank you to Trinity staff and MCR for the great time at Oxford.

prepare different samples. I thank *Paul Pattinson* for giving me access to our departmental EBL system and for providing me with miniature printed-circuit boards for my experiments. Thanks also go to *Jeffrey Harmer* and *Christiane Timmel* for introducing me to our EPR spectrometers in CÆSR and for their technical advise during my experiments. I thank the mechanical workshop in Clarendon Laboratory, namely *Simon Moulder*, *Robert Harris*, and *Mark Witney* for machining different mechanical components for my experimental setups. A real masterpiece of mechanical engineering is certainly the brass collet, which enabled me to perform EDMR experiments at W-band.

Away from Oxford, I would like to thank our collaborators at Walter Schottky Institute, University of California Berkley, Lawrence National Berkley Laboratory, Princeton University, and Peking University. In Munich, Germany, I thank *Martin Brandt*, *Konrad Klein*, and *Hans Hübl* for the always very fruitful exchange of ideas and for providing us with an amorphous hydrogenated silicon device structure. Special thanks go to my supervisor and mentor at Siemens AG, *Hans Cerva*, for arranging my first research visit to Oxford in 2006 as well as for his invaluable advice and support throughout my whole academic career.

In Berkley, USA, I thank *Jeffrey Bokor* and *Thomas Schenkel* for giving me the opportunity to perform EDMR experiments on silicon field-effect transistors, as well as *Stephen Lyon* and *Alexei Tyryshkin* in Princeton for supporting those experiments through numerous very fruitful discussions. I also thank *Cheuk Chi Lo* and *Christoph Weiss* for giving me the opportunity to work on bismuth doped silicon and for helping me to refine my transferable skills by developing a highly efficient way of

communication in the lab. Special thanks go to Cheuk, who designed and fabricated various silicon field-effect transistors for our EDMR experiments at low- and high magnetic fields. His deep insight into device physics as well as his determination and endurance throughout all experiments is always very inspiring. It was indeed always a pleasure doing experiments with Cheuk, having our daily lunch (and latte macchiato) in Maison Blanc, and dinner in Wagamama.

In Beijing, China, I thank *Liàn-Máo Péng* (彭練矛), *Jǐn Zhāng* (張錦), and *Yàn Lǐ* (李彥) for giving me access to their laboratories and sharing their expertise about fabricating and measuring carbon nanotube devices. I thank especially *Pàn Lǐ* (李盼), *Hǎitāo Xǔ* (海涛許), and *Jùn Luó* (羅俊) for helping me to grow carbon nanotubes on my device structures and for introducing me to the fascinating chinese culture – I really enjoyed my time in Beijing.

I thank my colleagues and friends in Oxford and London, namely my officemates *Marcus Schaffry* and *Yīmín Wú* (吴一民) as well as *Vasileia Filidou* (*Κάρλα*), *Edgar Pogna*, *Alessandra Sollberger*, *Marko Jung*, and *Alexander Dilthey*, who made my time in the UK very enjoyable and unforgettable. I also like to size this opportunity to thank my friends I met during my time as a visiting student at Oxford in 2006, namely *Martin Cooles*, *Jérôme Clarisse*, as well as *Kathryn and Mathijs Zandbergen* for introducing me to the university and college life, and for making my first stay at Oxford so pleasant and joyful. Moreover, I thank my best friends in Germany, namely *Tobias Gottschalk*, *Kerstin Mitternacht*, *Patrick Dipsche*, and *Maximilian Griebl* for their deep friendship, invaluable support and encouragement throughout the years, and the always very joyful time in Frankfurt am Main and Munich. Furthermore, I thank *Bettina Wörmann* for her love, enduring care and support, and the wonderful time we have been spending together.

Last but not least I would like to express my profound gratitude to my family, namely mom, dad, my sister, and grandmother for their love and unwavering support throughout my whole life and academic career in Frankfurt am Main, Munich, and Oxford.

Vielen Dank!

Contents

CHAPTER 1

Introduction

Contents

The detection, control, and manipulation of few to single electron spins have attracted considerable interest in the past few years as *quantum information processing* (QIP) [Nie00] and the related fields of spintronics[1] [Wol01, Žut04], molecular electronics [San06], and solotronics[2] [Koe11] have become realistic prospects. As a novel

[1] Abbreviation for spin transport electronics or spin-based electronics.
[2] From solitary dopant optoelectronics.

approach to information processing, QIP employs the discrete nature of quantum mechanics to encode, process, and transmit quantum information. It holds promise for device applications as diverse as quantum computers [Lad10], non-classical light sources for quantum key distribution [Fun02, Chi05b], and quantum sensing [Gio04], which demonstrate its great technological potential. Experimental challenges arise due to interactions with the local environment comprising nuclear spins as well as paramagnetic defects and impurities, which can lead to various unfavourable effects, such as the decay of quantum information.

The control over paramagnetic defects and impurities has also become technologically important owing to the enduring miniaturisation of modern semiconductor technology and recent advances in silicon photovoltaics, where they can lead to detrimental leakage currents and act as recombination centres limiting the power conversion efficiency, respectively.

A detailed understanding and exquisite control over electron spins as well as paramagnetic defects and impurities through their microscopic and spectroscopic characterisation on the nanoscale is therefore vital for refining and optimising both, QIP nanodevices and modern silicon photovoltaic materials.

1.1. Spin-based quantum information processing

QIP is a novel approach to information processing and utilises quantum effects, like quantisation, superposition, and entanglement of different spin states, each representing one unit of quantum information, a so-called quantum bit or *qubit* [Sch95]. Non-classical information can principally be encoded in spin [Kan98, Vri00] or charge qubits [Hol04]. Depending on the particular qubit architecture one differentiates

(i) *single spin qubits* formed by single conduction electron, hole, or donor electron spins [Los98],

(ii) *exchange-only qubits* formed by two electron spins exchange coupled to a third electron spin with the actual qubit being encoded in a spin doublet [DiV00b],

(iii) *singlet-triplet qubits*, where the ground and excited states of exchange coupled electrons are used to encode quantum information [Lev02], and

(iv) *hybrid qubits*, which are a combination of (ii) and (iii) [Shi12].

The suitability of a particular approach for applications in QIP is conventionally evaluated in terms of five major criteria [DiV00a]. Apart from the scalability, the most important criterion is the stability of the qubit against *decoherence*, which summarises all processes that contribute to the decay of quantum information encoded in the electron spin. These processes are quantitatively described by three time constants, namely the (i) *relaxation time* T_1 describing all energy relaxation

processes into energetically more favourable spin states, the (ii) *dephasing time* T_2 describing all energy conserving processes of a single electron spin, and the (iii) *ensemble dephasing time* T_2^*. The relaxation times of the most important semi-

Material	$\mathbf{T_1}$ **(ms)**		$\mathbf{T_2}$ **(ms)**		$\mathbf{T_2^*}$ **(µs)**	
GaAs	$\sim 10^{-5}$ C	[Cla76]			0.100 C	[Kik98]
	0.20 Q	[Fuj02]	0.001 Q	[Pet05]	0.010 Q	[Joh05a]
	0.85 Q	[Elz04]	200 Q	[Blu11]	0.025 Q	[Kop05]
	1,000 Q	[Ama08]			0.037 Q	[Kop08]
Silicon	$\sim 10^{-3}$ C	[Hon56]	0.240 C	[Gor58]		
n-Si	6,000 Td	[Pla11]	0.2 Td	[Pla11]	0.055 Td	[Pla11]
	10 Ti	[Xia10]			$0.22^{\dagger}$ Q	[Ass11]
^{28}Si	0.8 Q	[Sha10]	600 C	[Tyr11]	0.30 Q	[Sha10]
Si/SiGe	2,800 Q	[Sim11]	0.5 C	[Yab03]	0.36 Q	[Mau12]
Carbon	$\sim 10^5$ C	[Har06]	2.4 C	[Nay11]	30 C	[Miz07]
	0.003 Q	[Chu09b]			0.003 Q	[Chu09b]
	$> 10^{7\,\dagger}$ Q	[Bul08]				

Table 1.1.: Electron spin coherence times in electrostatically defined semiconductor quantum dots (subscript 'Q') and transistors ('T'). Electron spins bound to donors are subscripted with 'd', spins associated with defects and impurities with 'i'. Exemplary values obtained from crystals without any gate structure are subscripted with 'C' and given for comparison or if no other values obtained from device structures are available. The superscript '†' denotes extrapolations of experimental data and theoretical predictions, respectively.

conductor nanodevices fabricated on gallium arsenide/aluminum gallium arsenide (GaAs/AlGaAs), natural-silicon (n-Si), isotopically purified ^{28}Si, silicon germanium (SiGe), and carbon are compiled in Table 1.1. These time constants will form the basis for a comparison of the most important semiconductor nanostructures for applications in QIP in the following. They broadly fall into two categories: (i) semiconductor quantum dots and (ii) nanoscale field-effect transistors.

1.1.1. Semiconductor quantum dots

Quantum dots (QDs) are quasi zero-dimensional systems confining charge carriers in all spatial dimensions. The spatial confinement in QDs leads to energy quantisation similar to atoms, which gave rise to their nickname 'artificial atoms' [Kas93, Ash96, Kou98]. Among the various kinds of QDs, the best understood and technologically most advanced systems are electrostatically defined QDs, in which Schottky top-gates facilitate the electrostatic depletion of a *two-dimensional electron gas* (2DEG) embedded in a heterostructure [And82]. Electrostatically defined QDs have been reaslied in different material systems, such as Si [Mor11], epitaxially grown Si/SiGe [Sim07, Liu08], and GaAs/AlGaAs heterostructures [Han07], as well as in carbon nanotubes [Mas04] and nanostructured graphene [Sta08a, Sta08b, Mol09].

Quantum dots in traditional semiconductors

Owing to the tremendous experimental success, modulation-doped GaAs/AlGaAs heterostructures [Din78] have become the model system for the investigation of QDs and the underlying device physics. First time-resolved experiments on QDs in this heterosystem were carried out by T. Fujisawa *et al.* in 2001, who made use of fast voltage pulses on gate electrodes to measure the timescale over which electron spin qubits in GaAs/AlGaAs decohere [Fuj02]. The measured electron spin relaxation time $T_{1e} = 200\ \mu s$ (see Table 1.1) was interpreted in terms of the emission of phonons and 'forbidden transitions', which are mediated by spin-flip processes

revealing much longer decay times than allowed transitions, which typically have $T_{1e} \sim 10$ ns. In a second experiment, they also demonstrated coherent oscillations of a single electron spin between the orbitals in two coupled QDs, a so-called *double quantum dot* (DQD) by applying coherent voltage pulses to the different gate electrodes [Hay03]. Three years later and inspired by the experiments of M. Field *et al.* [Fie93], L. M. Vandersypen *et al.* combined this pulse scheme with a *quantum point contact* (QPC) [vWe88], which was used as a fast charge sensor to determine when an electron was entering and leaving the QD [Van04]. By pulsing the QD potential and employing the Pauli exclusion principle to make the tunnelling rate of the electron from the QD into the leads dependent on its spin state, they could readout the spin state of the target qubit by measuring the charge on the QD as a function of time. Two variations of this *spin-to-charge conversion* were later demonstrated to work in the single-shot readout mode, too [Elz04, Han05]. The spin dephasing time T_{2e} can be studied with a variety of techniques. The most common approach is *electron paramagnetic resonance* (EPR), whereby a static magnetic field $\mathbf{B_0}$ is used to split the spin states energetically through the Zeeman effect [Zee87] into spin-up $|\uparrow\rangle$ parallel and spin-down $|\downarrow\rangle$ anti-parallel to $\mathbf{B_0}$, and microwaves to excite resonant transitions between them [Poo83]. Early attempts to study the dephasing time for electron spins in QDs failed due to heating of the leads and photon-assisted tunnelling [Pla04], where electrons absorb one or more photons from the microwave field and tunnel out of the QD before the end of the applied microwave pulse. The first EPR experiment on QDs was performed by F. H. L. Koppens *et al.* in 2006 with a weakly-coupled DQD [Kop06], where the magnetic microwave field was applied with

a coplanar stripline, a technique, which is referred to as *local-EPR* in the following. Their readout scheme is based on the idea of H. A. Engel and D. Loss to tune a single QD to *Coloumb blockade*[1] with the electrochemical potential aligned such that this blockade is lifted when the electron spin is repeatedly flipped by EPR [Eng01]. The time-ensemble-averaged dephasing time T_{2e}^{*} was extracted from the exponential damping of the Rabi oscillations between the two spin states, and found to be about five orders of magnitude shorter than T_{1e}, i.e. $T_{2e}^{*} \sim 25$ ns (see Table 1.1). This observation was attributed to the hyperfine coupling between the electron spin in the QD and the nuclear spin carrying GaAs host nuclei in accord with the results of J. R. Petta *et al.* [Pet05]. The scalability of this approach was investigated in a series of *slanting Zeeman field EPR* experiments on triple QDs [Lai07, Pio08], in which a spatially dependent Zeeman field was applied through an on-chip micromagnet in order to address each spin selectively. Those and other experiments contributed to a detailed understanding of the main decoherence mechanisms of electron spins in GaAs/AlGaAs QDs, namely the

(i) *hyperfine interaction* with host nuclei, which has two effects on the electron spin: First, the nuclear spin bath exerts an effective magnetic field, the so-called *Overhauser field*, which fluctuates in time, and causes the electron spins to dephase [Pet05]. The second effect is referred to as *dynamical nuclear polarisation*, and involves electron and nuclear spin flip-flop processes,

[1] Coulomb blockade refers to the transport regime, in which Coulomb repulsion between the electrons on the QD and in the reservoirs leads to an energy cost for adding an extra electron to the QD [vHo92]. Electron tunnelling to or from the reservoirs is thus suppressed at low temperatures.

(ii) *spectral diffusion* at high magnetic fields due to the intrinsic dynamics of the nuclear spin bath caused by dipolar flip-flops [Cyw09b],

(iii) *co-tunnelling* of a charge carrier with a spin from the QD to the reservoir, where it is replaced by a charge carrier with the opposite spin [Ave90], and

(iv) *charge noise* due to fluctuations in the electrostatic environment of the QD, which leads to changes in the barrier height and level alignment [Hu06].

Owing to the detrimental effect of nuclear spins, current experiments in the GaAs/AlGaAs heterosystem focus on the suppression of the fluctuating Overhauser field as the predominant decoherence mechanism to protect the coherence of electron spins [Gre07, Rei08, Xu09]. These approaches do, however, require a very high polarisation of the nuclear spin bath [Cyw09a]. Hence, very complex laser or electric pulse sequences have to be applied additionally, which are experimentally challenging to implement and difficult to control.

The detrimental effect of the nuclear spin bath in GaAs/AlGaAs has spurred research into other material systems, such as Si/SiGe, where the natural abundance of isotopes with a non-zero nuclear spin amounts to 5 %, in contrast to 100 % in GaAs/AlGaAs. Typical dephasing times in Si/SiGe amount to $T_{2e} = 0.5$ ms, and can be enhanced further by using nuclear spin-free ^{28}Si/^{28}Si^{70}Ge, which reveals dephasing times of up to $T_{2e} = 600$ ms (see Table 1.1) – the first 2DEG in an isotopically engineered ^{28}Si/^{28}Si^{70}Ge heterostructure has been realised by J. Sailer *et al.* [Lan08a, Sai09]. In the presence of donors isotopic purification has, however,

an intrinsic limit as background donors of the same species limit the spin coherence time of a single target donor electron spin above a certain level of isotopic purification. For a single ^{31}P donor spin in ^{28}Si:P with a residual ^{29}Si concentration of $[^{29}\text{Si}] < 50$ ppm and $[^{31}\text{P}] = 1.2 \cdot 10^{14}$ cm^{-3}, for instance, the spin dephasing time was found to be limited to $T_{2e} = 600$ ms [Wit10, Tyr11]. Nevertheless, Si/SiGe and ^{28}Si/^{28}Si^{70}Ge, in particular, are very promising material systems for the implementation of QDs [Sim07, Sha08a]. The measurement of the spin coherence times and a detailed understanding of the main decoherence channels in this heterosystem is less understood than for GaAs/AlGaAs and requires further time-resolved experiments with EPR and related techniques.

Quantum dots in carbon nanomaterials

Another material, which has attracted considerable attention recently, is carbon (C) as the natural abundance of ^{13}C, the only carbon isotope with a non-zero nuclear spin, is even smaller than in isotopically purified ^{28}Si/^{28}Si^{70}Ge and amounts to $\sim$ 1 %. This leads to a very weak hyperfine interaction (see Table 1.2) and together with the comparatively weak spin-orbit coupling to extremely long spin coherence times as shown in Table 1.1. The most basic structural modification of carbon is *graphene*, which refers to a flat monolayer of carbon atoms, tightly packed into a two-dimensional honeycomb lattice with two atoms per unit cell, which give rise to two equivalent sublattices [Slo58]. Quantum mechanical hopping between the two sublattices leads to the formation of two energy bands, which intersect near

the edges of the (first) Brillouin zone and yield a conical energy spectrum with no bandgap. As a consequence, electrons in graphene remarkably exhibit a linear dispersion relation $E = \hbar k \nu_F$, as if they were massless relativistic particles traveling

Material	Δ_{SO} (meV)		Δ_{HI} (μeV)	
GaAs	340	[Mad02]	92	[Ass11]
Si	45	[Mad02]	0.2	[Ass11]
C	0.37	[Kue08]	1.0	[Fis09]
			100	[Chu09a, Chu09b]

Table 1.2.: Spin-orbit Δ_{SO} and hyperfine Δ_{HI} coupling constants in different semiconductors, namely GaAs, Si, and C.

with the Fermi velocity ν_F and momentum $\hbar k$, where k denotes the wave vector, and $\hbar$ Planck's constant divided by 2π. The formation of a two-dimensional gas of Dirac fermions [Nov05a] gives rise to the Klein tunnelling phenomenon [Kle29], the unimpeded penetration of relativistic particles through high and wide potential barriers. Klein's transmission probability depends weakly on the barrier height, and approaches the perfect transparency for very high barriers, in contrast to conventional non-relativistic tunnelling, where the transmission probability decreases with an increasing barrier height exponentially. Whereas electron transport in graphene has been investigated intensively [Nov05a, Zha05], experiments on graphene QDs are still in their infancy [Bun05, Gei07]. The first graphene QD was realised by C. Stampfer *et al.* in 2007, and obtained by micromechanical cleavage of bulk graphite [Nov04, Nov05b] and subsequent nanostructuring via reactive ion-etching (RIE) [Sta08a, Sta08b]. Electron transport through graphene DQDs was investi-

gated by F. Molitor *et al.* [Mol09] one year later, who used in-plane side gates to tune the system to the Coulomb blockade regime. The electron spin coherence and dephasing times have, however, not been measured in those systems so far. Another very important carbon allotrope are *carbon nanotubes* (CNTs), which were discovered in 1991 by S. Iijima [Iij91], and are formed by rolling a single layer of graphene at a specific angle to form a seamless cylinder – the combination of the rolling angle and radius of the CNT determines whether its shell is metallic or semiconducting [Ebb96].[1] CNTs can be synthesised by electric arc-discharge between two graphite electrodes [Iij91], laser ablation of a graphite target [Guo95a, Guo95b], and chemical vapour deposition (CVD) [Jos93], which is known to produce the cleanest CNTs suffering from almost no defects. The first CNT DQD was realised by N. Mason *et al.* [Mas04] and demonstrated to show the well-known honeycomb charge stability diagram as a function of the two plunger gate voltages [Han07]. The device could be tuned from the weak to the strong tunnel-coupling regime, but not to the single electron regime like in the technologically leading GaAs/AlGaAs DQDs. This limited tunability was not overcome until 2009, when G. Steele *et al.* demonstrated the successful capture of a single electron in a CNT DQD [Ste09a]. The actual role of the spin-orbit and hyperfine interaction and its effects on the spin coherence times is still subject to intense research. The fragmentary understanding of those decoherence channels has recently caused some confusion, when

[1] The rolling angle (or *chirality*) is described by the two components $(n, m) \in \mathbb{N}^2$ of the chiral vector $\mathbf{C} = n\mathbf{a_1} + m\mathbf{a_2}$, where $\mathbf{a_1}$ and $\mathbf{a_2}$ are the unit vectors of the graphene honeycomb lattice. Depending on (n, m) one differentiates between an *armchair* (n, n), *zigzag* $(n, 0)$, and *chiral* (n, m) $(n \neq m)$ configuration. CNTs are metallic for $(n - m) = 3j$ $(j \in \mathbb{N})$ and semiconducting otherwise. A nice review about their physical properties is given in [Ter03], for instance.

F. Kuemmeth *et al.* found a much stronger spin-orbit coupling than originally expected – this was attributed to their curvature and cylindrical topology [Kue08]. The coupling strength was measured to $\Delta_{SO} = 0.37$ meV, which is still lower than 340 meV in GaAs and 45 meV in Si (see Table 1.2). The values for the hyperfine interaction in CNTs are controversial and differ between $\Delta_{HI} = 0.1 - 100$ μeV as shown in Table 1.2. The resulting spin coherence times have not been measured experimentally so far and the complex interplay of structural, electronic, and spin properties of electrons and holes in CNTs need to be investigated further [Fis09] for carbon-based QIP to become a realistic prospect.

1.1.2. Nanoscale field-effect transistors

A second approach to confine, manipulate, and readout electron spins for applications in QIP are *metal-oxide-semiconductor (MOS) field-effect transistors* (FETs), the most important and fundamental building blocks of silicon integrated circuits (ICs). FETs are planar three-terminal devices comprising a semiconducting channel formed between a source and drain electrode, and a Schottky top-gate, which is separated from the device channel by a thin oxide barrier. Their operation relies on the control of the channel conductivity by the gate voltage, which is applied between the gate and one of the electrodes. Applying a positive gate voltage at a finite bias between source and drain induces a 2DEG and the FET is operated in the so-called

enhancement or *accumulation-mode*.[1] The miniaturisation of those devices has been the main driving force for technical advances in the late 20$^{\text{th}}$ century and the origin for sustaining economic benefits and improvements in device performance. As a consequence of this downward scaling, the entire device performance nowadays relies on only a few donors in the channel anymore, and random fluctuations in the number of donors have become a major issue in microelectronics [Kuh08]. This has led to technical refinements of ion implantation techniques and to the development of single ion implantation in particular [Mat97, Sch02, Bue02]. But reducing the length of the device channel in order to increase both, the operation speed and packing density, causes the electrostatic field of the gate to no longer resemble that of a planar capacitor. This gives rise to the emergence of unfavourable *short-channel effects*, such as increased leakage currents and the lowering of the punch-through breakdown voltage. Historically, short channel effects have motivated the development of novel FET architectures, such as finFETs [His98, Hua99, His00] and nanowire FETs [Xia06, Sel06, Coh07, The08]. Unlike a conventional FET, a *finFET* is a nonplanar, double-gate transistor, in which the conducting channel is wrapped by a thin silicon 'fin' forming the gate of the device. Owing to the experimental advances in single ion implantation techniques [Mit05, Shi05] and the increasing control over few to single electron spins, those devices have been proposed for applications in QIP [Cal06, Sar08, Ste11] as they offer the unique opportunity to control and manipulate single donors implanted into the device channel, where they can interact

[1] The device channel of depletion-mode FETs is highly doped and controlled with a negative gate voltage instead. The combination of n- and p-doped devices in modern silicon ICs is referred to as *complementary metal-oxide-semiconductor* (CMOS) technology.

with a 2DEG directly. In contrast to conventional electrostatically defined QDs, individual donors at low temperatures provide much sharper and more homogeneous three-dimensional confinement potentials, which makes them ideal for applications in QIP. The first observation of the effect of a single donor atom on electron transport was through random telegraph noise in MOSFETs [Ral84], QPC structures [Dek91], and later in bipolar transistors [Neu95]. Control over the wavefunction of a single donor embedded in the corner of a commercial finFET was demonstrated by G. P. Lansbergen *et al.* in 2008 for the first time [Lan08b], who controlled resonant tunnelling transitions of the neutral (D^0) and charged state (D^-) of a ^{31}P donor through the Stark effect.[1] More recently, single electron transport through single donor atoms has also been observed in dopant-rich environments [Tab10].

A similar device design, in which the donor atom is not directly implanted into the device channel, has been used by K. Y. Tan *et al.* to study charge (D^0, D^-) and spin states of individual phosphorus atoms in silicon [Tan10]. This design was adapted from S. J. Angus *et al.* [Ang07, Ang08] and comprises a single-electron *nanoscale-FET* (nanoFET), which is tunnel-coupled to a phosphorus [Mor09] or arsenic donor nearby [Gon12]. This hybrid DQD can be tuned such, that the shift of the electrochemical potential arising from the tunnelling of a single electron from a donor (or impurity) site (QD_1) into the single-electron transistor (QD_2) is large enough to switch the current through the device on and off. In the presence of an external

[1] Discovered in 1913, the *Stark effect* refers to the shift and splitting of the energy levels due to the presence of an electric field. Depending on whether the effect is linear or quadratic in the electric field, one distinguishes the first- and second-order Stark effect [Sta14].

magnetic field, this tunnelling transition becomes spin-dependent, and the spin state of a single donor can be detected by pulsing the electrochemical potentials in both QDs [Mor10]. Very recently, A. Morello *et al.* also demonstrated the coherent control of a single ^{31}P donor electron and nucleus in a series of electrically detected local-EPR experiments on n-Si nanoFETs for the first time, in which a coplanar stripline was used to apply both, the microwave and radio-frequency excitation. The associated spin relaxation and dephasing times were found to be significantly longer than in comparable GaAs/AlGaAs nanodevices as shown in Table 1.1.

The particular interaction between conduction electrons and donors has been subject of various past studies. R. Maxwell and A. Honig, for instance, performed an experiment, in which they measured the spin-dependent conductivity of phosphorus-doped silicon (Si:P) [Max66]. Their results were initially explained in terms of spin-dependent neutral impurity scattering, but later shown to be due to electron trapping and recombination instead [Tho73, Ste83]. The first direct observation of spin-dependent scattering is reported by R. N. Ghosh and R. H. Silsbee for a Si:P MOSFET [Gho92]. The particular nature of this interaction has been controversially discussed in literature [Mor74, Gra99, Mat06] and its potential applications for QIP and feasibility for an electron spin readout, in particular, are largely unexplored. A detailed understanding of the interaction between conduction electrons and donors as well as the associated decoherence channels are, however, vital for finding an ideal parameter regime with minimal decoherence and maximum qubit control for the implementation of QIP.

1.2. Defect engineering in silicon photovoltaics

The vast majority of silicon ICs as well as $\sim 40\,\%$ of silicon solar cells are fabricated on *Czochralski silicon* (Cz-Si), which is known to contain various defects and impurities incorporated into the crystal during its growth and subsequent device processing. They are particularly harmful for photovoltaic applications as they can act as *recombination centres* providing paramagnetic traps in the silicon bandgap, through which photoexcited charge carriers can recombine prior to their separation and extraction through the leads. This causes the power conversion efficiency in such solar cells to decrease owing to the drop in minority carrier diffusion length and lifetime, two key parameters for describing the performance of any photovoltaic device. The most important recombination centres in Cz-Si are introduced below.

1.2.1. Metallic impurities

The first group is formed by *metallic impurities*, which broadly fall into two categories, namely (i) *interstitial* diffusing metals, such as the transition metals iron, copper, chromium, and nickel [Web83], and (ii) *substitutional* diffusing metals like zinc, arsenic, antimony, and tin. Among those impurities, transition metals are known to provide particularly deep levels in the silicon bandgap $E_g = 1.11$ eV [Kit96] and act as very strong recombination centres [Dav80, Piz86, Ist00]. The energy levels of the most important dopants and impurities in silicon are depicted in Figure 1.1. The Fermi energy of undoped silicon lies in the middle of the bandgap and can be shifted

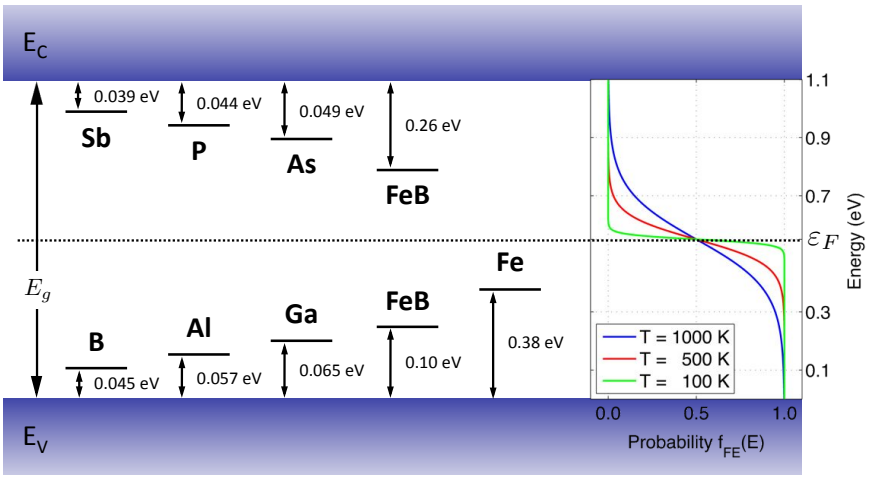

Figure 1.1.: Energy levels of the most important dopants and impurities relative to the conduction (E_C) and valence band (E_V). Relative positions are not to scale for clarity. The occupation probability of the different states is described by a Fermi-Dirac distribution, which depends on the Fermi energy ε_F (dotted line) and temperature as shown on the right hand side for undoped silicon at three different temperatures exemplarily. The ionisation energies of the different dopants and impurities are taken from [Mul86, Ist99, Rei05].

upwards and downwards by introducing donor and acceptor states, respectively. The ionisation level of phosphorus in silicon, for instance, amounts to $E_P = E_C - 0.044$ eV [Mul86] and the Fermi level of Si:P is given by $\varepsilon_F \sim E_V + (E_g - \frac{1}{2}E_P) = E_V + 1.078$ eV at low temperatures in a first order approximation.

Metallic impurities like iron, for instance, introduce particularly deep levels in the silicon bandgap, namely at $E_{Fe} = E_V + 0.38$ eV [Ist99]. Interstitial iron is paired with substitutional boron at room temperature to form the well-known metastable *iron-boron pair* (FeB). This complex dissociates into its constituents upon illumination with white light and introduces a donor and acceptor state into the silicon bandgap at $E_V + 0.10$ eV and $E_C - 0.26$ eV [Ist99], respectively, and dominates recombination at room temperature.

1.2.2. Oxygen and its related defects

Oxygen and its related defects form the second very important group of recombination centres in Cz-Si. One of the best studied oxygen related defects are *silicon dangling bonds* (DBs) formed by trivalent silicon atoms at the interface between silicon and (native) silicon-dioxide (Si/SiO_2) [Stu00].[1] Depending on their particular atomic configuration and orientation relative to the interface, one differentiates between P_b centres forming at the (111) Si/SiO_2 interface, as well as P_{b0} and P_{b1} centres forming at the (100) Si/SiO_2 interface [Poi81].

Particularly high densities of silicon DBs of up to 10^{19} cm^{-3} are found in amorphous silicon (a-Si) as a consequence of the very high disorder in this material caused by variations in bond lengths and angles [Bra92]. Beside Cz-Si, a-Si is another very interesting source material for photovoltaic devices as it can be deposited as thin-films with plasma-deposition techniques, which allow us to reduce the material consumption and fabrication costs – two very important arguments for terrestrial power applications – significantly and to fabricate more efficient multi-junction solar cells with multiple absorber layers with different bandgaps. Historically, a-Si has been a particularly important model system for defect engineering as its structural characterisation by EPR and related techniques has led to the development of hydrogen

[1] The first EPR signal attributed to silicon DBs is reported by M. H. Brodsky and R. S. Title for amorphous silicon and reveals a Landé g-factor of $g = 2.0055$ [Bro69]. There are various arguments for associating this resonance with silicon DBs. The most convincing is probably the investigation of the hyperfine interaction between a paramagnetic spin and ^{29}Si nuclei in an isotopically enriched ^{29}Si sample. The wavefunction deduced for this resonance reveals an sp^3 symmetry [Bie86] as one would expect for silicon DBs [Wat64].

passivation techniques, whereby hydrogen is incorporated during thin-film growth in order to saturate the DBs [Chi69]. This passivation process is nowadays used in photovoltaic thin-film technology [Sha04] to reduce the concentration of DBs from [DB] $\sim 10^{19}$ cm^{-3} in a-Si to $\sim 10^{15}$ cm^{-3} in hydrogenated amorphous silicon (a-Si:H) [Der83].[1] Furthermore, the incorporation of hydrogen enables doping of a-Si by boron and phosphorus as the Fermi level is not pinned by the huge defect density in the middle of the bandgap anymore [Spe75].[2]

A second very common oxygen related defect in silicon is *interstitial oxygen* (O), which is found in Cz-Si at concentrations of up to [O] $\sim 10^{18}$ cm^{-3}. Slightly smaller but still significant concentrations of [O] $\sim 10^{17}$ cm^{-3} are found in microcrystalline silicon (µc-Si) [Stu00], which has a smaller bandgap than a-Si:H and is employed as an absorber layer for low-energy photons in state-of-the-art a-Si:H/µc-Si:H two-junction (tandem) solar cells [Sch07], for instance. Interstitial oxygen has various guises, such as thermal donor defects [Ful57], boron-oxygen complexes [Fis73, Bot06], and (unstrained and strained) oxide precipitates (OPs) [Van95, Mur11a].

[1] The downside of this passivation process arises from the *Staebler-Wronski effect* (SWE) [Sta77, Sta80], the light-induced degradation of undoped a-Si:H, which has been the main limiting factor for the performance of a-Si:H based photovoltaic devices ever since. Current understanding of this effect is based on the work of H. Dersch *et al.*, who reaslised that the observed degradation is caused by a reversible increase of [DB] upon the absorption of light [Der81]. Other degradation mechanisms associated with the SWE are (i) Si−H bond dissociation involving the collision of two mobile hydrogen atoms [Bra99] and (ii) weak Si−Si bond breaking after trapping and bimolecular recombination of excess charge carriers at the same bond site [Stu85]. In contrast to the hydrogen collision model, the weak Si−Si bond breaking model predicts the presence of spatially correlated DB−H pairs, which were investigated in a series of studies involving multifrequency EPR and related techniques [Iso93, Bra98, Feh10, Feh11]. There is, however, still no consensus on the role of hydrogen and the particular mechanisms involved in the SWE [Stu86, dWa95, Bra99, Pow02].
[2] Boron doping shifts the Fermi energy ε_F towards the mobility edge of the valence band, whereas phosphorus doping allows us to shift ε_F in the opposite direction as a prerequisite for a detailed investigation of the density of states in a-Si:H [Stu83].

1.2.3. Impurity gettering in Czochralski silicon

The detrimental effects of those defects and impurities motivated the development of *internal gettering*, whereby impurities are confined to inactive regions of the wafer. Although OPs can act as recombination centres [Che11], they play a crucial role in internal gettering as they can be grown intentionally to act as sinks for detrimental metallic impurities [Tan77, Gil90, Mye00]. OPs undergo a morphological transformation during growth [Ber89], which is known to have implications for both, internal gettering [Fal04] and recombination of minority carriers [Mur11a]. The precipitates initially exist in an unstrained state, but after a certain threshold growth time – dependent on the density of nucleation sites – they change morphology into a strained state, which coincides with the transition from ineffective to totally effective impurity gettering [Fal04].

J. D. Murphy *et al.* have recently shown that the recombination rate at OPs depends (i) upon their strain state, and (ii) interestingly upon the precipitate density rather than size [Mur11a]. As the number of corners of the strained platelets is invariant with size, these discontinuities have been suggested to play a central role in the recombination process. The question about their particular microscopic and spectroscopic nature does, however, remain to be answered as the photoconductance methods [Sin96] used in this study do not easily allow their structure to be determined.

1.3. Aim and outline of this thesis

Our previous discussion has shown that there has been tremendous progress over the past several years towards the characterisation and control of electron spins for applications in QIP as well as defects and impurities for applications in silicon photovoltaics. Open questions regard

(i) the microscopic nature of defects associated with (strained) OPs in Cz-Si,

(ii) the interplay between structural, spin, and electronic properties of CNTs, and

(iii) the interaction between conduction and donor electrons in Si-FETs.

The aim of this thesis is to address those questions by using a comparatively new and very sensitive spectroscopic technique called *electrically detected magnetic resonance* (EDMR), which is introduced in Chapter 2.

In Chapter 3 we employ this EPR related technique to identify and characterise the most important recombination centres in Cz-Si with strained OPs. We study strained OPs with a wide range of densities and relate them to the electronic recombination times measured via EDMR. A refinement of our spectrometer enabling time-resolved EDMR measurements at X-band is discussed in the last section of Chapter 3 for an a-Si:H test structure.

Chapter 4 is about the fabrication and electrical characterisation of a novel CNT device architecture. Its design principally allows us to investigate the interplay of

spin, structural, and electronic properties of CNTs through its compatibility with EDMR and conventional materials characterisation techniques, such as transmission electron microscopy (TEM) and low-temperature transport measurements.

In Chapter 5 we employ EDMR to investigate the interaction between conduction electrons and channel implanted donors in Si-FETs. This involves the demonstration of high-field EDMR in a resonant microwave cavity with a higher sensitivity and spectral resolution, and a comparison to conventional low-field experiments. Chapter 5 concludes with the measurement of the relevant spin coherence and dephasing times via high-field pulsed-EDMR experiments. A final conclusion of the results presented in this work is given in Chapter 6.

CHAPTER 2

Principles of electrically detected magnetic resonance

Contents

EDMR builds on EPR and is a very powerful and sensitive experimental technique used throughout this work to control, manipulate, and characterise electron spins in semiconductor and carbon nanodevices. This technique has been particularly successful in the characterisation of low dimensional systems as (i) the EDMR signal

does not scale with the size of the device[1] and (ii) only electrically active defects contribute to the formation of the signal if bolometric effects are avoided. This chapter introduces the underlying principles of EPR and EDMR and develops the theoretical framework to understand the EDMR effect in semiconductor nanodevices.

2.1. Electron paramagnetic resonance

Discovered by Y. Zavoisky in 1945 [Zav45, Zav46], EPR is primarily a spectroscopic technique used to study chemical species with unpaired electrons and based on the manipulation of the net magnetisation $\mathbf{M}$ associated with their spin degree of freedom. For an ensemble of $N \in \mathbb{N}$ electron spins, $\mathbf{M}$ is given by

$$\mathbf{M} = \sum_{n=1}^{N} \boldsymbol{\mu}_\mathbf{n} = -\sum_{n=1}^{N} g\mu_B \mathbf{S}_\mathbf{n} \tag{2.1}$$

where $\boldsymbol{\mu}_\mathbf{n}$ and $\mathbf{S}_\mathbf{n}$ denote the magnetic moment and spin angular momentum of the n^{th} electron, respectively, g the Landé g-factor, and μ_B the Bohr magneton. In the presence of an external magnetic field $\mathbf{B_0} = B_0\hat{\mathbf{z}}$, the spin angular momentum $\mathbf{S}$ as described by its eigenvalue, the spin orientation quantum number m_s, aligns itself either parallel ($m_s = +1/2$) or antiparallel ($m_s = -1/2$) to $\mathbf{B_0}$, which causes the associated energy levels to split due to the *Zeeman effect* [Zee87]. The parallel alignment of the spin relative to $\mathbf{B_0}$ corresponds to the lower energy state $|\downarrow\rangle$, the

[1] Due to *Ohm's law*, the absolute value of the sample resistivity ρ_0 in thermal equilibrium depends on the size of the device. Hence, the relative resonant change of the sample resistivity $\frac{\Delta\rho}{\rho_0} := \frac{\rho-\rho_0}{\rho_0}$ is size independent, which is why the EDMR effect does not scale with the device size.

antiparallel configuration to the higher energy state $|\uparrow\rangle$, and the separation energy is $\Delta E = g\mu_B B_0$. Transitions between $|\downarrow\rangle$ and $|\uparrow\rangle$ with $\Delta m_s = \pm 1$ are excited by illumination with microwaves whenever their angular frequency ω_{mw} matches the *spin resonance condition* $\hbar\omega_{mw} = g\mu_B B_0$. Due to the limited lifetime of the excited spin state, the electron spins relax after a certain time to the ground state, which causes the magnetisation $\mathbf{M}$ in Equation (2.1) to decay towards the equilibrium $\mathbf{M}_0 = M_0\hat{\mathbf{z}}$. The dynamics of this process are described by the *Bloch equations*

$$\frac{\partial \mathbf{M}}{\partial t} = \gamma(\mathbf{M} \times \mathbf{B}) - \mathbf{r} \qquad \text{with} \qquad \mathbf{r} = \left(\frac{M_x}{T_2}, \frac{M_y}{T_2}, \frac{M_z - M_0}{T_1}\right) \tag{2.2}$$

where $\mathbf{r}$ describes the relaxation and $\gamma := g\mu_B/\hbar$ denotes the gyromagnetic ratio [Blo46]. T_1 and T_2 are the relaxation and dephasing time, respectively, and describe the exponential decay of the longitudinal and transversal component of $\mathbf{M}$. The Bloch equations can be solved for an ensemble of paramagnetic spins in an oscillating magnetic field $\mathbf{B} = B_0\hat{\mathbf{z}} + \mathbf{B_1}(t) = B_0(0,0,1) + B_1(\cos\omega_{mw}t, \sin\omega_{mw}t, 0)$ with the *Larmor frequency* $\omega_0 = \gamma B_0$ [Lev01]. For their solution it is convenient to transform Equation (2.2) into a coordinate system, which rotates about the z-axis at the angular frequency ω_{mw}. In this so-called *rotating frame*, the Bloch equations read

$$\frac{\partial \mathbf{M}^R}{\partial t} = \left(-\Omega M_y + \frac{M_x}{T_2}, -\Omega M_z - \omega_1 M_z + \frac{M_y}{T_2}, \omega_1 M_y + \frac{M_0 - M_z}{T_1}\right) \tag{2.3}$$

where $\Omega := \omega_0 - \omega_{mw}$ and $\omega_1 = \gamma B_1$ denotes the *Rabi frequency* describing the precession of $\mathbf{M}$ about $\mathbf{B_1}$ in the rotating frame. In the case of *slow-adiabatic passage*

[Weg60], i.e. a fast spin relaxation and low oscillation frequency of the applied microwave field, Equation (2.3) is solved by the magnetisation $\mathbf{M}^R = (M_x^R, M_y^R, M_z^R)$ with the components

$$\begin{aligned} M_x^R &= \frac{\omega_1(\omega_0 - \omega_{mw})T_2^2}{1 + (\omega_0 - \omega_{mw})^2 T_2^2 + \omega_1^2 (T_1 T_2)} M_0 \\ M_y^R &= \frac{-\omega_1 T_2}{1 + (\omega_0 - \omega_{mw})^2 T_2^2 + \omega_1^2 (T_1 T_2)} M_0 \\ M_z^R &= \frac{1 + (\omega_0 - \omega_{mw})T_2^2}{1 + (\omega_0 - \omega_{mw})^2 T_2^2 + \omega_1^2 (T_1 T_2)} M_0 \quad . \end{aligned} \tag{2.4}$$

In conventional EPR, the experimentally measured quantity is the magnetic susceptibility χ, which is defined through $\mathbf{M} = \chi \mathbf{B}/\mu_0$ and given by

$$\chi = \chi' + i\chi'' = \frac{1}{2}\mu_0 \left(\frac{M_x^R}{B_1} - i\frac{M_y^R}{B_1} \right) \tag{2.5}$$

where μ_m denotes the magnetic permeability of the sample, μ_0 the vacuum permeability, and χ' and χ'' the real and imaginary part of the magnetic susceptibility, respectively. If B_1 is small, i.e. $\gamma^2 B_1^2 (T_1 T_2) \ll 1$, Equation (2.5) simplifies to

$$\begin{aligned} \chi' &= (\omega_0 - \omega_{mw}) T_2 \chi'' \\ \chi'' &= \frac{1}{2}\mu_0 \frac{\gamma T_2}{1 + (\omega_0 - \omega_{mw})^2 T_2^2} M_0 \quad . \end{aligned} \tag{2.6}$$

The real part of the magnetic susceptibility χ' causes a shift of the resonance frequency of the microwave resonator, whereas the imaginary part χ'' causes the *quality factor* Q of the microwave cavity to change. Q is defined as the ratio between the energy stored in the resonator and the energy loss due to microwave absorption by the

sample, or equivalently, the ratio of the cavity bandwidth and resonance frequency. This energy loss is described by the absorbed microwave power [Pak73]

$$P_{mw} = -\frac{\partial}{\partial t}(\mathbf{M} \times \mathbf{B}) = \omega_{mw}\chi'' B_1^2 \tag{2.7}$$

and directly detected in a conventional EPR experiment. The imaginary part of the magnetic susceptibility, χ'', is a *Lorentzian* line arising from a homogeneous spin ensemble. Inhomogeneous broadening of a resonance line arises due to a set of overlapping lines of different spin ensembles and leads to a *Gaussian* lineshape. Since a standard EPR (and EDMR) experiment conventionally measures the derivative of the absorption line with respect to magnetic field, a more practical expression for a Lorentzian absorption line is given by

$$f_{\mathrm{L}}(B) = \frac{2a'(\Delta B_{pp})^3}{3(\Delta B_{pp})^2 + 4(B - B_0)^2} \tag{2.8}$$

and a Gaussian absorption line is described by

$$f_{\mathrm{G}}(B) = \frac{1}{4}a'\Delta B_{pp} \exp\left[\frac{1}{2} - \frac{2(B - B_0)^2}{(\Delta B_{pp})^2}\right] \tag{2.9}$$

where B_0 denotes the resonance field, a' the amplitude, and ΔB_{pp} the peak-to-peak linewidth of the Lorentzian and Gaussian derivative line, respectively. The relation between the absorption and its derivative line is depicted in Figure 2.1. A numerical integration of the derivative line is not very practical and accurate as it requires the correction of the baseline of the recorded signal. This is why the signal amplitudes a_{L}

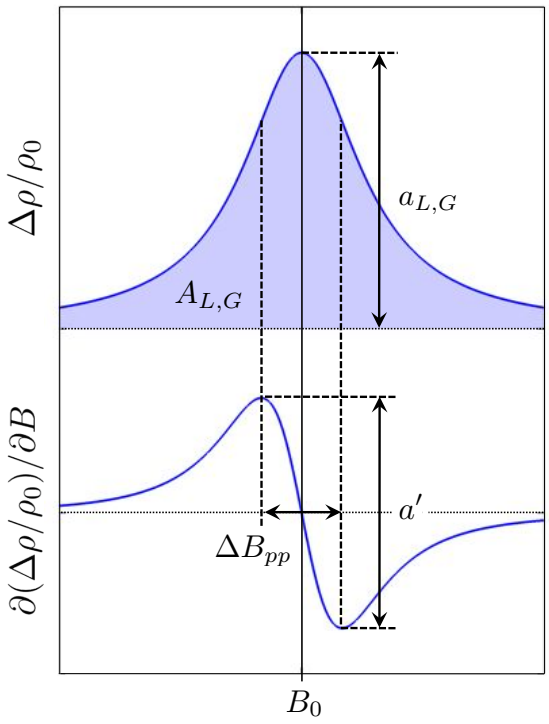

Figure 2.1.: Typical absorption line (top) and its first derivative (bottom) centred around the resonance field B_0. a' denotes the amplitude and ΔB_{pp} the peak-to-peak linewidth of the first derivative line. The amplitude of the absorption line is $a_{L,G}$ and $A_{L,G}$ its area (shaded). Please refer to the text for further details.

and a_G of a Lorentzian and Gaussian absorption line, respectively, are conventionally defined through a' and ΔB_{pp} of the respective derivative line and calculated via

$$\begin{aligned} a_\mathrm{L} &= f_\mathrm{L}(B_0) = \frac{2}{3} a' \Delta B_{pp} \\ a_\mathrm{G} &= f_\mathrm{G}(B_0) = \frac{1}{4} a' \Delta B_{pp} \quad . \end{aligned} \tag{2.10}$$

Integration of Equations (2.8) and (2.9) with respect to B results in

$$\begin{aligned} A_\mathrm{L} &= \int_{-\infty}^{\infty} \mathrm{dB}\ f_\mathrm{L}(B) = \frac{\pi}{\sqrt{3}} a' (\Delta B_{pp})^2 \\ A_\mathrm{G} &= \int_{-\infty}^{\infty} \mathrm{dB}\ f_\mathrm{G}(B) = \sqrt{\frac{\pi e}{2^5}} a' (\Delta B_{pp})^2 \end{aligned} \tag{2.11}$$

for the area A_L and A_G under a Lorentzian and Gaussian absorption line, respectively. This analysis will be important when comparing EDMR signal intensities at different magnetic fields in subsequent chapters.

Another very important quantity of an EPR spectrometer is its sensitivity, i.e. the minimum number of detectable spins per Gauss linewidth per square root of seconds measuring time. The sensitivity of conventional X-band EPR is limited to $\sim 8 \cdot 10^9$ spins/G$\sqrt{\text{Hz}}$ [Sch99] owing to the small Zeeman splitting of about $\varepsilon_Z \sim 40$ μeV at typical magnetic fields $B_0 \sim 0.35$ T [Bra04]. In order to achieve higher sensitivities, EPR has been combined with different measurement techniques, such as magnetic resonance force microscopy [Rug04] as well as optical [Bro59, Ges59, Wra93, Jel04] and electrical detection techniques [Elz04, Xia04, Ste06]. Among those methods, EDMR has been reported to provide the highest sensitivity, which is more than 10^6 times higher than for conventional EPR [Boe06b], and currently approaches the few to single electron regime [McC06].

2.2. Electrically detected magnetic resonance

Originally proposed by J. Schmidt and I. Solomon in 1966 [Sch66] and demonstrated for the first time by D. J. Lepine six years later [Lep72], EDMR refers to a spectroscopic technique, in which the sample is placed in an external static magnetic field $\mathbf{B_0}$, while the sample conductivity is measured under the irradiation with resonant microwaves. The EPR induced change in the population of the two

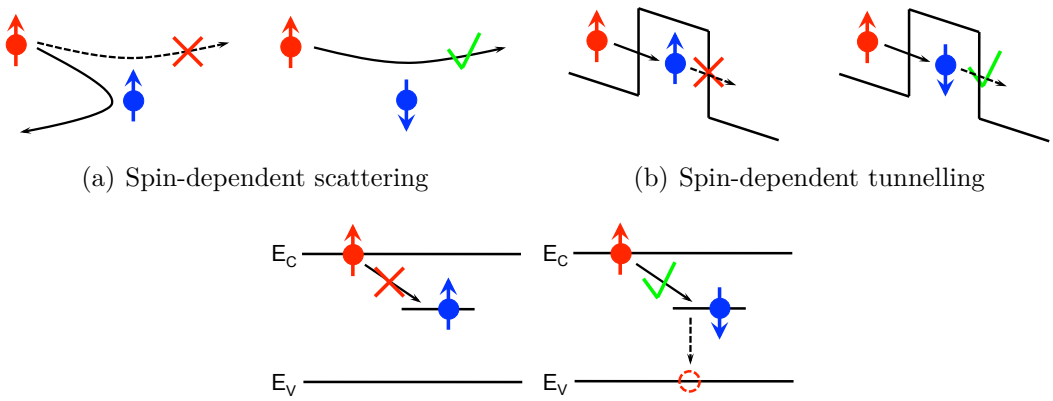

(a) Spin-dependent scattering

(b) Spin-dependent tunnelling

(c) Spin-dependent recombination

Figure 2.2.: Schematic representation of the main spin-to-charge conversion mechanisms. The spin dynamics depend on the mutual spin orientation of the free conduction electron (red) and the localised defect or impurity (blue), and give rise to spin-dependent scattering (a), spin-dependent tunnelling (b) and spin-dependent recombination (c). Please refer to the text for further details.

Zeeman states causes the electrical resistivity to vary due to so-called *spin-to-charge conversion* mechanisms, which involve the formation of a spin-pair. Depending on the mutual orientation of the two spins, the spin-pair can either be in a *singlet state* described by the vector $|\chi_s\rangle = \alpha\,|\uparrow\downarrow\rangle - \beta\,|\downarrow\uparrow\rangle$, where both spins are aligned antiparallel to each other, or a *triplet state* $|\chi_t\rangle = \alpha\,|\uparrow\uparrow\rangle + \beta\,|\downarrow\downarrow\rangle$ referring to the parallel configuration of the two spins ($\alpha, \beta \in \mathbb{C}$ with $|\alpha|^2 + |\beta|^2 = 1$). Owing to the Pauli exclusion principle, a particular transport channel is blocked if the spin-pair is in a triplet state. This *Pauli blockade* can be lifted by illumination with microwaves, which repeatedly flip either of the two electron spins on resonance and thus alter the total resistivity of the sample. The most important spin-to-charge conversion mechanisms are shown in Figure 2.2 schematically and discussed in the following three sections in more detail.

2.2.1. Spin-dependent scattering

If the spin-pair is formed by a free electron with coordinates $\mathbf{r_1}$ and a paramagnetic donor or defect with coordinates $\mathbf{r_2}$, the Pauli exclusion principle forces the spatial component of the overall wavefunction $\psi(\mathbf{r_1}, \mathbf{r_2}, \chi_{s,t}) : (\mathbb{R}^3 \times \mathbb{R}^3) \otimes \mathbb{C}^2 \rightarrow \mathbb{C} \otimes \mathbb{C}^2$ to be symmetric for spin singlets and antisymmetric for spin triplets, i.e

$$\psi_{s,t}(\mathbf{r_1}, \mathbf{r_2}) = \frac{1}{\sqrt{2}} \left[\psi_1(\mathbf{r_1})\psi_2(\mathbf{r_2}) \pm \psi_1(\mathbf{r_2})\psi_2(\mathbf{r_1})\right] \otimes |\chi_{s,t}\rangle \tag{2.12}$$

where the upper sign is for the singlet $|\chi_s\rangle$ and the lower sign for the triplet spin state $|\chi_t\rangle$, and $\psi_{1,2} : \mathbb{R}^3 \rightarrow \mathbb{C}$ denote the wavefunctions of the two scattering partners. The scattering matrix $\langle\psi_{s,t}| \hat{\mathscr{H}} |\psi_{s,t}\rangle \in \mathbb{C}^{2\times 2}$ describes the interaction between the two scattering partners with the interaction Hamiltonian $\hat{\mathscr{H}}$ and depends strongly on the spatial overlap of $\langle\psi_{s,t}|$ and $|\psi_{s,t}\rangle$, which is larger for singlet than triplet pairs from symmetry considerations of Equation (2.12). One therefore expects the scattering cross-section for singlet pairs Σ_s to be larger than for triplet pairs, i.e. $\Sigma_s > \Sigma_t$. This difference leads to a spin-dependent contribution to neutral impurity scattering (see Figure 2.2 (a)), which has been described within the effective mass approximation as the scattering of an electron off a hydrogen atom by G. L. Pearson and J. Bardeen in 1949 for the first time [Pea49]. A. Honig proposed a direct demonstration of neutral impurity scattering by exploiting the difference in singlet and triplet cross sections for the scattering of conduction electrons off neutral impurities [Hon66]. Early measurements of a spin-dependent photoconductivity signal in sili-

con were interpreted as spin-dependent scattering [Max66], but later shown [Tho73] to be due to the polarisation dependence of electron trapping and recombination instead [Ste83]. The first direct measurement of spin-dependent scattering of conduction electrons off neutral impurities was observed in a 2DEG and reported by R. N. Ghosh and R. H. Silsbee [Gho92], who measured the EDMR effect in Si:P MOSFETs at $T = 4$ K and a magnetic field of $B_0 = 0.32$ T. By treating the impurity electrons as a classical gas obeying Boltzmann statistics and the 2DEG electrons as a two-dimensional degenerate Fermi gas, they describe the relative change of the device resistivity $\Delta\rho/\rho_0$ in a first-order approximation by

$$\frac{\Delta\rho}{\rho_0} \propto \alpha p_{i0} p_{c0} \frac{\tau_t}{\tau_n} \qquad \text{where} \qquad \alpha := \frac{\langle \Sigma_s - \Sigma_t \rangle}{\langle \Sigma_s + 3\Sigma_t \rangle} \tag{2.13}$$

denotes the difference in scattering cross sections Σ_s and Σ_t when the 2DEG and donor electrons form singlet and triplet pairs, $\Delta\rho := \rho - \rho_0$ the difference between the device resistivity on and off resonance, p_{i0} and p_{c0} the impurity and conduction electron spin polarisations in thermal equilibrium, and τ_t and τ_n the total and neutral impurity scattering rate, respectively. Their results were, however, complicated by the overlap between the donor and 2DEG resonance signals due to the use of a highly doped substrate. More recently, similar measurements have been carried out to investigate charge carrier scattering in 2DEGs embedded in Si/SiO_2 [Gho92, Xia04], Si/SiGe [Gra99], and GaAs/AlGaAs heterostructures [Dob88, Jia01]. Furthermore, C. C. Lo *et al.* report on the electrical detection of the nuclear spin states of ^{121}Sb antimony donors, which have been implanted into the device channel of ^{28}Si-FETs

[Lo07, dSo09]. Their resonance spectra show well resolved signals from the conduction electrons in the 2DEG ($\Delta\rho/\rho_0 \sim 10^{-6}$) as well as hyperfine-split resonances from bound ^{121}Sb donor electrons ($\Delta\rho/\rho_0 \sim 10^{-7}$). Although those results were attributed to spin-dependent-scattering, the subsequent experiments described in Chapter 5 show that the EDMR effect in Si-FETs arises due to the polarisation dependent resistivity of the 2DEG instead.

2.2.2. Spin-dependent tunnelling

Tunnelling through a potential barrier as shown in Figure 2.2 (b) becomes spin-dependent if the tunnelling transition of an electron through a singly occupied into an unoccupied state depends on the mutual spin orientation of the two participating spins. It was first mentioned by N. Kishimoto *et al.* in their investigation of variable range hopping in amorphous silicon-gold alloys ($\Delta\rho/\rho_0 \sim 10^{-3}$ [Kis81]) and also observed as a consequence of the Pauli blockade in GaAs/AlGaAs [Ono02, Joh05b], Si/SiGe [Sha08a], Si-MOS [Liu08], and CNT DQDs [Bui08]. This mechanism is also the central idea behind B. E. Kane's original spin readout proposal [Kan98], where a spin-dependent tunnelling transition between a control donor and a nearby target qubit is employed to readout the spin state of the latter. Similar readout schemes involve spin-dependent tunnelling from paramagnetic trap states [Xia04] or donors to adjacent QDs [Mor09].

A conceptual extension of spin-dependent tunnelling is reaction-yield detected magnetic resonance (RYDMR) [Ani79, Tri80], where the spin-dependence of chemical reactions involving paramagnetic radicals is used to investigate the kinetics and rate-limiting educts. A similar method has been used to study charge pumping of gate oxides in Si-MOSFETs [Mas99].

2.2.3. Spin-dependent recombination

Charge carrier recombination in semiconductors with an indirect band gap is generally described in terms of the *Shockley-Read-Hall* model, where deep levels in the band gap capture pairs of electrons and holes from the conduction and valence band, respectively, and subsequently recombine prior to their re-emission [Sho52, Hal52].

In an external magnetic field, this process can become spin-dependent and charge carriers recombine through paramagnetic centres in the band gap. This process is commonly referred to as spin-dependent recombination and has been observed in crystalline silicon (c-Si) by D. J. Lepine for the first time [Lep72]. In his model, any electron in the conduction band can recombine with a hole in the valence band through a paramagnetic centre in the band gap. The associated recombination rate is determined by the mutual orientation of the two spins, which can only recombine if they form a spin singlet owing to the Pauli exclusion principle. Hence, the singlet recombination rate r_s is much larger than the recombination rate r_t associated with the triplet states. In the absence of an external magnetic field, the observed

recombination rate is therefore given by

$$r = \frac{1}{4}r_s + \frac{3}{4}r_t \approx \frac{1}{4}r_s \tag{2.14}$$

since the probability of the two spins forming a singlet and triplet state is $\frac{1}{4}$ and $\frac{3}{4}$, respectively. In the presence of a finite magnetic field the spin ensembles are polarised, i.e. the population of singlet states is decreased and the population of spin triplets increased. The recombination rate is then described by

$$r_0 = \left(\frac{1}{4} - p_{r0}p_{c0}\right) r_s \qquad \text{with} \qquad p_{r0} \approx p_{c0} = 1 - e^{-\frac{g\mu_B B_0}{k_B T}} \approx \frac{g\mu_B B_0}{k_B T} \tag{2.15}$$

where p_{r0} and p_{c0} denote the thermal polarisations of the recombination centres and conduction electrons, respectively, k_B the Boltzmann constant, and T the temperature. As transitions between the Zeeman levels of either of the two spin ensembles are excited through the application of microwaves, the respective thermal polarisation is altered and $r = \frac{1}{4}r_s$ on resonance. The relative change of the sample resistivity is therefore given by

$$\frac{\Delta\rho}{\rho_0} = \frac{\Delta r}{r_0} \approx p_{r0}p_{c0} \leq \left(\frac{g\mu_B B_0}{k_B T}\right)^2 \tag{2.16}$$

where $\Delta r := r - r_0$ denotes the difference between the recombination rates on and off resonance. This very strong temperature dependence was contradicted by various experiments on different materials [Bra91b, Sti95, Kaw97, Bra98, Eic98, Hir99, Stu00] including c-Si ($\Delta\rho/\rho_0 \sim 10^{-5}$ [Lep72]), a-Si:H ($\Delta\rho/\rho_0 \sim 10^{-3}$ [Der83]),

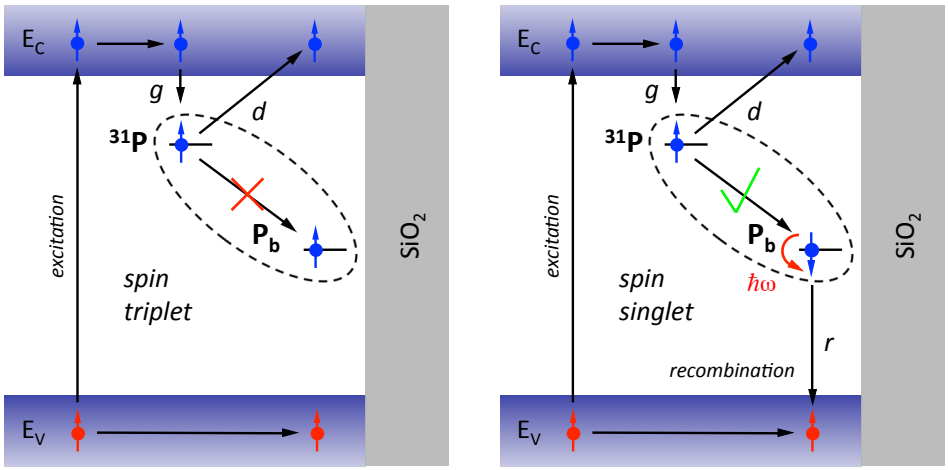

(a) Dissociation (b) Recombination

Figure 2.3.: Spin-dependent recombination in Si:P through P_b DBs formed at the Si/SiO_2 interface. Recombination through the P_b centre is only allowed if the ^{31}P-P_b pair (dashed line) is in a singlet state. The spin-pair is generated at the rate g, dissociates at the rate d, and recombines at the rate r.

and C_{60} fullerene thin-films ($\Delta\rho/\rho_0 \sim 10^{-2}$ [Bra92]). A model which can account for those results and the nearly constant temperature dependence of $\Delta\rho/\rho_0$, in particular, was proposed by D. Kaplan, I. Solomon, and N. F. Mott in 1978 [Kap78]. In contrast to Lepine's model, this so-called Kaplan-Solomon-Mott or *KSM model* assumes that electrons and holes are captured by two recombination centres independently of their mutual spin orientation. The spin-dependence of the recombination rate rather arises due to the formation of an intermediate spin-pair, which is formed prior to the actual recombination process. A typical example is provided by Si:P, in which the respective spin-pair formed by a paramagnetic ^{31}P donor and a P_b DB [Ste06] as depicted in Figure 2.3. The dynamics of this process can be described by the rate equation $\partial_t n = g - r - nd$, where n denotes the total number of electron spins in the conduction band, g the generation, r the

recombination, and d the dissociation rate of the spin-pair. Thermal polarisations of the spin system play a minor role in this model since the recombination is governed by the spin state of the pair alone and not by the ensemble of spins. The change of the resistivity is therefore given by the relative rates r and d and does not explicitly depend on the temperature or the magnetic field. While the KSM model assumes that triplet states cannot recombine, B. Movaghar *et al.* developed a similar model including a finite triplet recombination rate [Mov80].

The different spin-to-charge conversion mechanisms discussed above can principally be investigated with *continuous-wave* (cwEDMR) and *pulsed-EDMR* (pEDMR) [Boe03]. CwEDMR is mainly used to access the spectroscopic information, whereas pEDMR is used to access the dynamics of a particular spin-to-charge conversion mechanism. The principles of both techniques are described below.

2.3. Continuous-wave EDMR

CwEDMR is a well established spectroscopic technique, which has been employed for semiconductor defect analysis in various materials. It has been applied successfully to study e.g. ^{31}P donors in silicon [Sch66] at high [Hon78] and low magnetic fields [Sti95] and contributed to the understanding of the effect of phosphorus doping in a-Si [Stu00, Bra91b] and µc-Si [Kan00] for photovoltaic applications as introduced in the previous chapter.

2.3.1. Signal formation

CwEDMR is conventionally performed as an adiabatic field-sweep experiment, where the sample is exposed to a continuous microwave field and the resonant change of the electrical resistivity of the sample detected as a function of magnetic field. On resonance this leads to a change in the steady-state spin configuration, which translates into a change of the sample resistivity through the spin-to-charge conversion mechanisms discussed above. The resulting signal allows us to access the spectroscopic information through the spin-resonance condition. In contrast to pEDMR, where the transient change of the electrical resistivity is recorded as a function of the time after a coherent microwave excitation or pulse length, the signal amplitude observed in a cwEDMR experiment is proportional to the spin-flip rate of the excited spin-pair, which is – according to the Bloch Equations (2.2) – itself proportional to the magnetisation and the strength of the exciting microwave field. For cwEDMR, the microwave resonator is therefore tuned to a high quality factor of typically $Q \sim 5,000$ to obtain a high magnetic microwave field B_1, which induces high spin-flip rates and increases the signal intensity. Conductive parts of the sample, which are indispensable in any EDMR sample, are generally detrimental for achieving high quality factors due to surface currents induced by the microwave field. Lithographically defined contacts with a length exceeding the geometrical size of the resonator, however, do allow to overcome this limitation by contacting the active area of the device with thin metallic layers below the skin depth of microwaves of typically $\delta \sim 1$ µm at $\omega_{mw} = 10$ GHz [Poo83].

2.3.2. Phase-sensitive detection

CwEDMR is conventionally carried out by using a *lock-in detection* technique, where the magnetic field B_0 is modulated at a certain frequency and the resulting cwEDMR signal demodulated prior to its detection. In this case, the modulation frequency needs to be slow compared to T_1 and T_2 of the excited electron spin in order to comply with the slow-adiabatic passage condition [Weg60]. Furthermore, it is desirable to set the modulation frequency to a fractional multiple of the mains frequency $\omega \sim 50$ Hz in order to minimise any mains noise. The lock-in technique enables a phase-sensitive detection, reduces the detection bandwidth and noise level, and causes the signal to become the first derivative of the absorption line with respect to the magnetic field. The Landé g-factor can thus be measured more accurately as the zero-crossing of the first derivative is easier to determine than the position of the maximum of the absorption line. E. A. Schiff demonstrated that field modulation can be used further to separate different contributions to the cwEDMR signal by varying the lock-in phase between the excited and detected photocurrent in a-Si:H [Sch81]. In his model, the photocurrent is determined by the density of photo-excited electrons $n(t)$, which can be described by the rate equation

$$\frac{\mathrm{d}n}{\mathrm{d}t} = g - nr = g - nr_0(1 + ae^{i\omega_{mod}t}) \tag{2.17}$$

where g is the excitation, and $r = r_0(1+ae^{i\omega_{mod}t})$ the recombination rate modulated around its average value r_0 with the amplitude $ae^{i\omega_{mod}t}$ and the angular modulation

frequency ω_{mod}. Equation (2.17) can be solved with the ansatz $n = n_0 + n_1 e^{i\omega_{mod}t}$ [Mov80]. Comparing the coefficients in the ansatz with Equation (2.17) and neglecting the second order term $\mathcal{O}(e^{2i\omega_{mod}t}) = an_1 e^{2i\omega_{mod}t}$ results in

$$\begin{aligned} n &= n_0 - n_0 \frac{ar_0}{r_0 + i\omega_{mod}} e^{i\omega_{mod}t} = n_0 \left(1 - \frac{a}{1 + i\omega_{mod}\tau} e^{i\omega_{mod}t}\right) \\ &= n_0 \left(1 - a\frac{1 - i\omega_{mod}\tau}{1 + \omega_{mod}^2\tau^2} e^{i\omega_{mod}t}\right) =: n_0(1 - Ae^{i\omega_{mod}t}) \end{aligned} \tag{2.18}$$

where $\tau := 1/r_0$ denotes the lifetime of the particular recombination process. In other words, field modulation induces a phase shift

$$\Delta\phi = -\arctan\frac{\mathrm{Im}(A)}{\mathrm{Re}(A)} = \arctan\left(\omega_{mod}\tau\right) \tag{2.19}$$

between the exciting and detected photocurrent, which depends on the lifetime τ of the particular recombination process. A superposition between different recombination processes can thus be decomposed by varying the phase of the lock-in amplifier. The lifetime τ can be determined by measuring the absolute value of the EDMR signal $|\Delta\rho|$ as a function of the modulation frequency ω_{mod} and fitting it to

$$|\Delta\rho| = \left|\frac{1 - i\omega_{mod}\tau}{1 + \omega_{mod}^2\tau^2}\Delta\rho_0\right| = \frac{|\Delta\rho_0|}{\sqrt{1 + \omega_{mod}^2\tau^2}} \tag{2.20}$$

with $|\Delta\rho_0|$ and τ being the fit parameters. This technique has been successfully applied previously to study spin-dependent recombination at the silicon surface [Lep72], P_{b0} DBs [Len84], spin-dependent recombination in a-Si and a-Si:H [Bra92] as well as spin-dependent trapping at trivalent silicon centres in silicon bicrystals

[Len90]. We note, however, that the measurement error of this technique has to be evaluated carefully as the EDMR spectrum is distorted when ω_{mod} approaches the reciprocal lifetime of the spin-pair involved in the particular recombination process. In this case, the spins do not have enough time to relax between two successive modulation cycles and passage effects have to be considered [Weg60]. Nevertheless, this analysis can provide valuable insights into the dynamics of a particular recombination process if applied within the limits described above.

2.4. Pulsed-EDMR

CwEDMR provides valuable insights into incoherent processes, such as electron spin relaxation and recombination times. Coherent spin dynamics on the other side can be studied with pEDMR on a nanoseconds timescale. In pEDMR, the transient change of the electrical resistivity of the sample is either recorded as a function of the time after a coherent microwave excitation (single pulse or pulse train), which is referred to as *free induction decay* (FID), or as a function of the pulse length t_p. Together with the absolute value of the microwave field B_1, t_p determines the so-called *tip angle* $\theta = \gamma B_1 t_p$, i.e. the angle by which the magnetisation is rotated around the x-, y- or z-axis of the *Bloch sphere*[1] [Sch01], which is conventionally used to visualise any coherent spin motion in the eigenspace $\{|\uparrow\rangle, |\downarrow\rangle\}$ of any two-

[1] The north and south pole of the Bloch sphere correspond to the parallel and anti-parallel alignment of the magnetisation relative to the applied magnetic field $|\downarrow\rangle$ and $|\uparrow\rangle$, respectively. The tip angle θ can then be viewed as the angle between the magnetisation and quantisation axis $\hat{\mathbf{z}}$. A microwave pulse with $\theta = \pi$ ($\pi/2$) is referred to as π- ($\pi/2$-) pulse in the following for convenience.

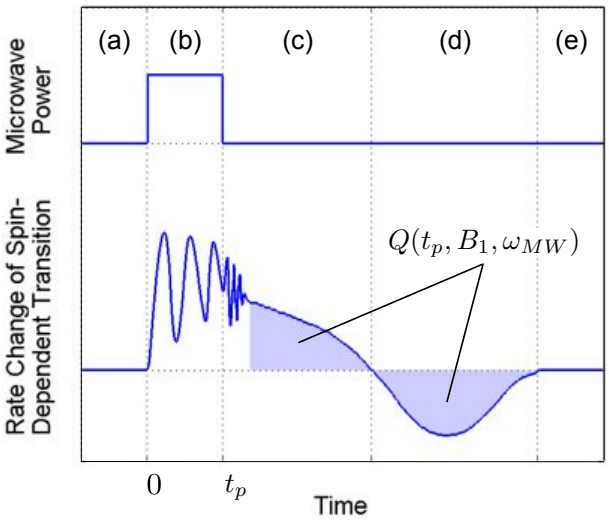

Figure 2.4.: Transition rate during and after a microwave pulse with length t_p. Please refer to the text for further details. Redrawn from [Boe06b].

level spin system. A conceptual sketch of a typical pEDMR experiment is shown in Figure 2.4. Before the application of a microwave pulse, the spin-pair ensemble remains in a steady state and precesses about the external magnetic field $\mathbf{B_0}$ with the Larmor frequency $\omega_0 = \gamma B_0$ (Figure 2.4 (a)). During the pulse (Figure 2.4 (b)), the spins start to precess about the net magnetic field $\mathbf{B} = \mathbf{B_0} + \mathbf{B_1}$ with the effective Rabi frequency

$$\Omega_r = \sqrt{(\gamma B_1)^2 + (\Delta\omega)^2} \tag{2.21}$$

where $\Delta\omega := \omega_0 - \omega_{mw}$ denotes the detuning between the Larmor and microwave frequency ω_0 and ω_{mw}, respectively. This Rabi oscillation then stops at the end of the microwave pulse and the spin-pair carries out Larmor oscillations only. Slightly different Larmor frequencies of the spin-pairs in the ensemble give rise to Larmor-beat oscillations before the ensemble relaxes back into its steady state as depicted in Figure 2.4 (c). This relaxation typically follows a multi-exponential transient and

can even lead to temporary quenching of the transition rate (Figure 2.4 (d)), before the spin ensemble returns into its steady state as depicted in Figure 2.4 (e). The time integral over the transition rate $Q(t_p, B_1, \omega_{mw})$ is proportional to the singlet

Pulse sequence	Variable	Measured quantity	
	τ	T_1 Inversion recovery	
	τ	T_2 Hahn echo	[Hah50]
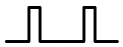	τ	T_2^* Ramsey fringe	[Ram50, Vio03]
	t_p	Rabi oscillations	[Rab37, Vio03]

Table 2.1.: Standard pEPR pulse sequences for measuring T_1, T_2, and T_2^* by varying the delay τ between the π- (⎍) and $\pi/2$-pulses (⎍), respectively. Rabi oscillations are induced by varying the pulse length t_p of the first microwave pulse.

content of the ensemble state at the end of the pulse [Boe03]. A direct detection of the relative resistivity change during the spin manipulation is generally not possible as the RC time constant of the sample and detection electronics is usually larger than typical pEDMR relaxation times. Hence, the minimisation of the absolute sample resistance, by using an interdigital contact geometry for instance, is quintessential for a fast current amplification in any pEDMR experiment. Due to the specific relaxation process back to the steady state configuration, the amplitude of the transient contains information about the transition rate at the end of the microwave pulse, and different pulse lengths lead to different transient amplitudes, which makes the detection of coherent spin motion experimentally accessible. The most important pulse sequences used to study coherent spin dynamics via conventional pEPR are compiled in Table 2.1. In order to employ those pulse sequences

for EDMR, an additional $\pi/2$-readout pulse needs to be added at the end of each sequence as EDMR only probes the longitudinal component of the magnetisation.[1] The reconstruction of coherent spin motion by measuring the signal in a fixed interval of time as a function of the pulse length was originally used to study spin nutation in radical pairs in transient RYDMR [Tad98, Ara00]. Later on, a similar concept was applied to study Rabi oscillations in Si:P with pEDMR [Ste06].

2.5. Conclusions

The EDMR effect has been shown to arise due to scattering, tunnelling, or recombination, which become spin-dependent in the presence of an external magnetic field due to the Pauli exclusion principle. EDMR has been used to study electron spins in various materials and can be performed as a continuous-wave or pulsed experiment. CwEDMR establishes a new steady state of the spin system, which alters the sample resistivity on resonance and allows us to access the spectroscopic information of the excited transition. PEDMR can be used to perform coherent spectroscopy through the measurement of the spin relaxation after the application of a coherent microwave pulse. The detection bandwidth and noise level of both techniques can be reduced by the application of a lock-in detection technique provided the RC time constant of the experimental setup is small enough.

[1] Please note that an EDMR-detected Ramsey experiment can be carried out without adding an additional $\pi/2$-pulse at the end of the sequence shown in Table 2.1 as the second $\pi/2$-pulse projects the nutating spins on either the singlet or triplet state already.

CHAPTER 3

Spin-dependent recombination in Czochralski silicon

Contents

The electrical performance of modern photovoltaic devices is determined by various material properties. The crystal quality of the intrinsic and doped layers, for instance, plays a particularly important role as it directly affects current-limiting

processes through the generation of space charges, internal electric fields, Schottky barriers at the contacts, and recombination centres. The complex interplay between those defect structures makes it difficult to study individual aspects of the material properties so that highly selective and very sensitive measurement techniques are required for device optimisation and quality control. The most common technique used to gain information about these defect structures and their complex interactions are standard IV- and photoconductance measurements [Sin96] under different illumination conditions.

Those conventional characterisation techniques do, however, not allow a simple and straightforward interpretation of the data as the current through the device does not tell us directly where and how charge carriers recombine in the device – a discrimination between signals from the contact layers, background from the substrate, and cell structure is therefore often very difficult. This is why EDMR has become a very useful and important characterisation technique in silicon photovoltaics [Beh09] as it probes individual recombination centres selectively and under ambient solar cell operating conditions.

The dynamics of a particular recombination process can either be studied by changing the modulation frequency in cwEDMR (see Section 2.3) or by employing coherent microwave pulses in pEDMR experiments (see Section 2.4). An analysis of the time evolution obtained from a two-dimensional pEDMR experiment ($\Delta\rho/\rho_0$ as a function of B_0 and time) allows us to deconvolute spectrally overlapping signals [Beh09]. Such experiments do allow us further to identify pairs of recombination centres con-

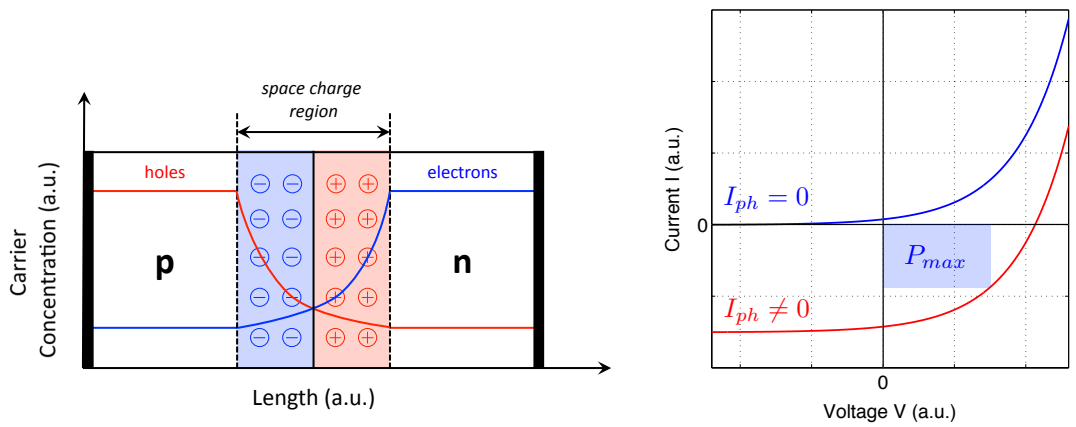

(a) pn-junction (b) IV-characteristics

Figure 3.1.: Schematic drawing (a) and IV-characteristic of a semiconductor pn-junction without ($I_{ph} = 0$) and with illumination ($I_{ph} \neq 0$) (b). The concentration of electrons and holes in the space charge region decays exponentially. The maximum power P_{max} delivered by such a device is the absolute value of the area of the largest rectangle under the IV-curve as indicated by the shaded region (blue). Please refer to the text for further details.

tributing to the same spin-dependent process, such as the ^{31}P-P$_b$ pair in Si:P [Ste06], as they reveal the same dynamic behaviour. EDMR is also sensitive enough to deal with the low defect and dopant concentrations in modern photovoltaic devices, which is another advantage of EDMR over conventional characterisation techniques.

The elementary building block of most electronic semiconductor devices, such as solar cells, light-emitting diodes, and bipolar transistors is the so-called *pn-junction* formed at the boundary between a p- and n-doped semiconductor of the same material. A schematic drawing of such a device is shown in Figure 3.1 (a). If a p- and n-doped semiconductor are brought together, electrons from the n-doped region will diffuse across the boundary into the p-doped region, where they recombine with holes. This leads to the formation of the so-called *depletion layer* or space charge

region, the active area of any pn-junction solar cell. Uncompensated charges on both sides create an internal electric field opposite to the diffusion current, which suppresses the continued exchange of charge carriers – the depletion layer has reached its thermal equilibrium. Impeding photons will now excite electron-hole pairs, which can be separated by applying an external voltage $V = \phi_p - \phi_n > 0$ (forward bias), where ϕ_p and ϕ_n denote the electric potential of the p- and n-doped region outside the depletion layer, respectively. The diode current I is then described by the *Shockley equation* [Mul86]

$$I(V) = I_0 \left(e^{\frac{V}{nV_{th}}} - 1 \right) - I_{ph} \qquad \text{with} \qquad V_{th} := \frac{k_B T}{e} \tag{3.1}$$

where I_0 denotes the reverse bias saturation current, n the quality factor, I_{ph} the photocurrent, and V_{th} the thermal voltage depending on the Boltzmann constant k_B, temperature T, and elementary charge e. The IV-characteristic of an ideal solar cell is schematically shown in Figure 3.1 (b). The maximum voltage supplied by a pn-junction solar cell is the *open circuit voltage* V_{OC}, which is defined by the condition $I(V_{OC}) = 0$ and according to Equation (3.1) given by

$$V_{OC} = \frac{n k_B T}{e} \ln \left(\frac{I_{ph}}{I_0} + 1 \right) \quad . \tag{3.2}$$

In other words, V_{OC} and thus the maximum power delivered by such a photovoltaic device increases with increasing quality factor, as expected. One of the most important parameters limiting the quality factor is the charge carrier extraction efficiency,

i.e. the efficiency with which electrons and holes can be extracted from the device prior to their recombination in order to drive a current through an external load. This efficiency is quantitatively described by the *recombination time* of photoexcited electron hole pairs, which can be captured by trapping and recombination centres in the bandgap of the respective material formed by crystal defects and impurities.

Cz-Si is the most common type of silicon and used for the vast majority of silicon ICs and ~ 40 % solar cells. Beside metallic impurities, one of the most important impurities in Cz-Si with concentrations of up to [O] $\sim 10^{18}$ cm^{-3} is interstitial oxygen (see Section 1.2). Oxygen has substantial beneficial as well as detrimental effects on silicon's material properties. It namely provides recombination centres through the formation of e.g. thermal donor defects [Ful57], boron-oxygen complexes [Fis73, Bot06], and unstrained OPs [Van95, Mur11a].

Strained OPs on the other side are very beneficial and play a particularly important role in modern defect engineering of Cz-Si as they can be intentionally created in inactive regions of the wafer by high temperature treatments to act as sinks for detrimental metallic impurities in a process known as *internal gettering* (see Section 1.2.2). Bright-field TEM micrographs of typical strained OPs are shown in Figure 3.2. They are shaped like square platelets (Figure 3.2 (a)) and can be surrounded by complex dislocation structures and stacking faults [Fal04] as shown in Figure 3.2 (b), (c), and (d). As the number of corners of the strained platelets is invariant in size and the rate of recombination associated with them dependent upon the precipitate density (rather than size), J. D. Murphy *et al.* speculated

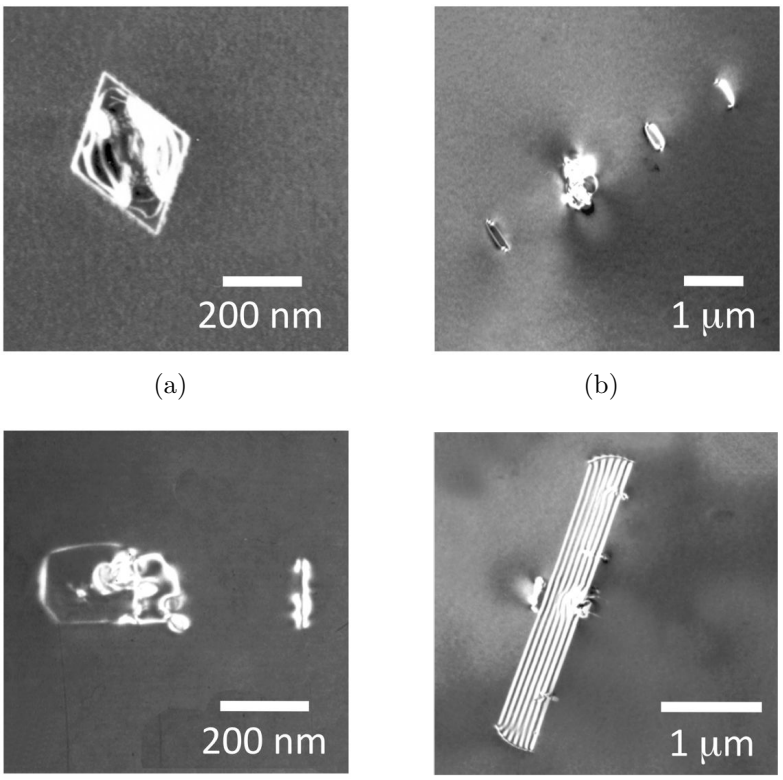

Figure 3.2.: Bright-field TEM micrographs of typical OPs. The strain contrast in (a) reveals their square platelet-like shape. (b) and (c) show a platelet surrounded by dislocation loops, the platelet shown in (d) is surrounded by stacking faults.

recently that the discontinuities associated with the corners play a crucial role in the recombination process [Mur11a]. Owing to the inherent limitations of the photoconductance methods [Sin96] used in this study, the spectroscopic nature of these defects has not been identified so far.

A detailed understanding and characterisation of the recombination centres associated with strained OPs is, however, technologically very important and vital for the optimisation of the gettering process, which is frequently employed for the fabrication of modern photovoltaic devices on Cz-Si wafers. This is why we employ

cwEDMR in this work to study defects and impurities in Cz-Si with strained OPs. We study a wide range of strained precipitate densities and relate these to spin-dependent recombination times extracted from our measurements.

Furthermore, we investigate intentionally iron-contaminated samples to improve understanding of the role of interstitial iron in the recombination process, which is one of the most detrimental metallic impurities in Cz-Si as it provides particularly deep levels in the silicon bandgap. Our results allow us to identify the most important recombination centres in Cz-Si as an important prerequisite for device optimisation in this expanding industry. In the second part of this chapter we present an extension of our cwEDMR spectrometer and present room temperature pEDMR spectra obtained from an a-Si:H test structure.

Selected results of this chapter are published in

[Lan12] V. Lang, J. D. Murphy, R. J. Falster, and J. J. L. Morton, *Spin-dependent recombination in Czochralski silicon containing oxide precipitates*, J. Appl. Phys. **111**, 013710 (2012). doi:10.1063/1.3675449.

3.1. Sample preparation and experimental setup

All samples were prepared from 150 mm diameter (100)-oriented high-purity p-type Cz-Si wafers doped with boron (B). The carbon content of all wafers was below the detection limit of $\sim 5 \cdot 10^{15}$ cm^{-3} of the Fourier transform infrared (FTIR) spec-

Initial [O]	**Nucleation time (h)**	**Growth time (h)**	**[OP] (10^{10} cm^{-3})**
low	6	8	0.08 ± 0.002
low	8	8	0.15 ± 0.031
low	6	8	0.22 ± 0.017
low	8	16	0.28 ± 0.033
low	16	8	0.64 ± 0.033
low	16	8	1.29 ± 0.217
low	16	16	2.27 ± 0.359
low	32	8	4.55 ± 0.768
low	32	16	6.98 ± 0.133
high	8	16	7.04 ± 0.789

Table 3.1.: Conditions for the growth of strained OPs with different concentrations. Please refer to the text for further details.

trometer used.[1] The oxygen and boron concentrations of 'low' oxygen concentration wafers amounted to [O] $= 7.8 \cdot 10^{17}$ cm^{-3} and [B] $= (1.3 \pm 0.2) \cdot 10^{15}$ cm^{-3}, respectively, whereas 'high' oxygen concentration wafers had [O] $= 9.3 \cdot 10^{17}$ cm^{-3} and [B] $= (1.1 \pm 0.1) \cdot 10^{15}$ cm^{-3}. All oxygen concentrations were measured by FTIR and are stated to the DIN50438/I (1995) standard. OPs were created by carefully controlled heat treatments, which are described in detail elsewhere [Kel99, Mur11a].

[1] In FTIR spectroscopy, the sample is irradiated with infrared (IR) light, which is partly absorbed by and transmitted through the sample. The resulting absorption and transmission spectra represent a molecular fingerprint and can be used to determine the boron, carbon, and oxygen content in the sample. More details can be found in [Gri07], for instance.

In summary, the precipitation treatment used has four stages comprising a homogenisation (15 min at 1,000 °C), nucleation ($8-32$ h at 650 °C), drift (4 h at 800 °C), and growth anneal ($8-16$ h at 1,000 °C). The concentration of OPs was varied in the investigated samples by changing the duration of the nucleation and growth anneal. Precipitate densities were measured by using a standard Schimmel etch on cross-sections of pieces from the wafer from which the samples were taken. The measured OP densities are compiled in Table 3.1. A precipitate-free sample of Cz-Si with a boron concentration of $[\mathrm{B}] = 8.0 \cdot 10^{14}\ \mathrm{cm}^{-3}$ was used for control purposes. Bulk iron concentrations were measured in wafers subjected to identical annealing conditions with quasi-steady-state photoconductance methods [Sin96], which measure the change in lifetime that occurs due to photodissociation of FeB pairs [Mur11a, Mur11b]. The iron concentration amounted to $[\mathrm{Fe}] < 3 \cdot 10^{11}\ \mathrm{cm}^{-3}$ in each sample.

A sample with a strained precipitate density of $[\mathrm{OP}] = 0.15 \cdot 10^{10}\ \mathrm{cm}^{-3}$ was intentionally contaminated with iron by rubbing the backside of the sample with a piece of iron (99.9 % purity) followed by subsequent annealing at 775 °C for 23 h. The bulk iron concentration was then measured in an identically-processed sample from the same precipitate-containing wafer to be $[\mathrm{Fe}] = 1.2 \cdot 10^{12}\ \mathrm{cm}^{-3}$. The iron concentration in an identically-processed precipitate-free sample amounted to $[\mathrm{Fe}] = 2.5 \cdot 10^{12}\ \mathrm{cm}^{-3}$. The difference between the two concentrations indicates that $\Delta[\mathrm{Fe}] = 1.3 \cdot 10^{12}\ \mathrm{cm}^{-3}$ of the bulk iron is gettered by the OPs in this specimen, as expected. Interdigitated chromium/gold (10/30 nm) thin-films were defined by

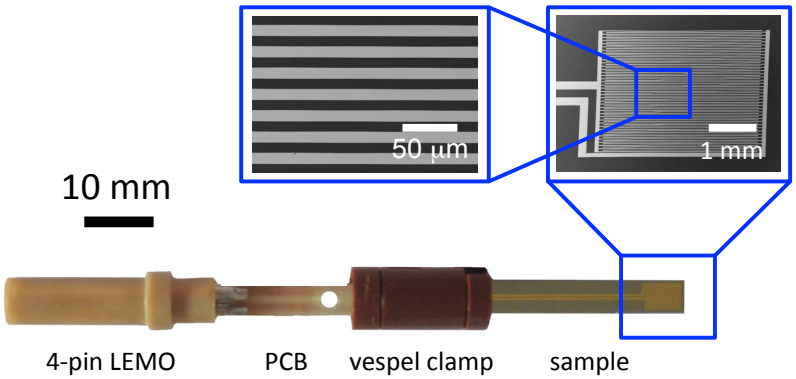

Figure 3.3.: OM and SEM micrographs of the overall sample arrangement. The sample is connected to a PCB through a miniature vespel clamp (bottom), which facilitates the electrical connection between the sample and the probe head through a 4-pin LEMO 00-series connector. SEM micrographs (top) show the interdigitated contact geometry at two different magnifications.

electron-beam lithography (EBL) on a JEOL JBX-5500-FS system. For this purpose an A8 polymethyl-methacrylate (PMMA, $(C_5O_2H_8)_n$) polymer[1] was spun onto the substrate with a Cee^{TM} 200CB Coat-Bake System and baked for 90 s at 180 °C prior to the exposure in the EBL system with a beam current of 10 nA and a dose of 800 µC/cm^2. A solution of 4-methyl-2-pentanone (MIBK, $C_6H_{12}O$) and isopropyl alcohol (IPA, C_3H_8O) with [MIBK]/[IPA] = 1/3 (volume percent) was used to develop the resist for 10 s at 25 °C prior to cleaning in IPA and metal deposition. The subsequent lift-off was carried out in acetone (C_3H_6O) at 90 °C. The resulting interdigitated thin-film was used to electrically contact the active area of the device with a minimised resistivity and without perturbing the microwave field in the cavity. The samples were diced into small chips of 2×20 mm^2 in size with a Loadpoint MicroAce Series 3 wafer saw and connected to a printed circuit board

[1] A8 refers to a solution of eight weight percent PMMA in anisole (C_7H_8O).

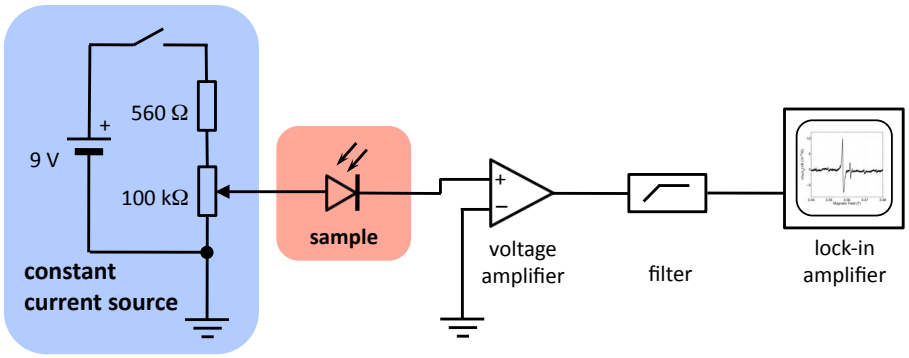

Figure 3.4.: Electrical detection unit used for cwEDMR on Cz-Si. A battery powered variable resistor network (blue) is used to drive a constant current through the sample (red). The modulated voltage drop across the device is preamplified with a differential voltage amplifier, filtered, and detected with a lock-in amplifier.

(PCB) with the miniature vespel clamp as shown in the optical microscopy (OM) images in Figure 3.3. The maximum diameter of the overall arrangement was chosen such that it can be inserted into a glass tube with an outer diameter of $\varnothing \sim 5$ mm to protect the sample against mechanical damage during its insertion into the cavity and against vibration during the measurement.

All experiments were carried out on a modified Bruker E380 X-band EPR spectrometer and an Oxford Instruments CF-935 helium-gas flow cryostat controlled by an Oxford Instruments ITC-503S temperature controller. The microwave excitation was generated with an Agilent Technologies E8267D PSG vector signal generator and applied with a Bruker Flexline ER4118X-MD5-W1 X-band dielectric ring resonator operating at a DC magnetic field $B_0 \sim 0.35$ T, which was aligned perpendicular to the growth direction of the sample, i.e. $\mathbf{B_0} \parallel [100]$, unless otherwise indicated. Magnetic field modulation (see Section 2.3.2) was applied with a Hewlett-Packard 33120A function generator and used to enhance the signal-to-noise ratio,

which results in the EDMR signal appearing as the first derivative of the relative change of the sample resistivity with respect to magnetic field $\partial(\Delta\rho/\rho_0)/\partial B$. The modulation amplitude was calibrated with a Bruker 2,2-diphenyl-1-picrylhydrazyl (DPPH, $C_{18}H_{12}N_5O_6$) reference sample and set to 0.1 mT with a modulation frequency $\omega_{mod} = 5.02$ kHz unless otherwise indicated. A battery powered variable resistor network was used to apply a constant current to the sample of typically $I = 20 - 100$ µA as shown in Figure 3.4.

The resonant change of the voltage drop across the sample was detected under constant illumination with a Schott KL1500 150 W halogen cold light source via a FEMTO DLPVA-100-FD variable gain low-noise voltage amplifier and a software controlled Stanford Research Systems SR830 lock-in amplifier.

3.2. Recombination centres in Czochralski silicon

The IV-characteristics were measured for each sample prior to the respective EDMR experiment in order to identify the optimal bias conditions. Figure 3.5 (a) shows the IV-characteristics of a typical Cz-Si sample with strained OPs, which can be separated into a linear and a saturation regime for $V < 0.15$ V and $V > 0.15$ V, respectively. The photocurrent in Figure 3.5 (a) reveals a similar saturation behaviour than the bias dependence of the EDMR signal intensity in Figure 3.5 (b). The signal-to-noise ratio was observed to decrease with increasing bias voltage in most of the investigated samples. EDMR was therefore carried out in the linear (ohmic) bias

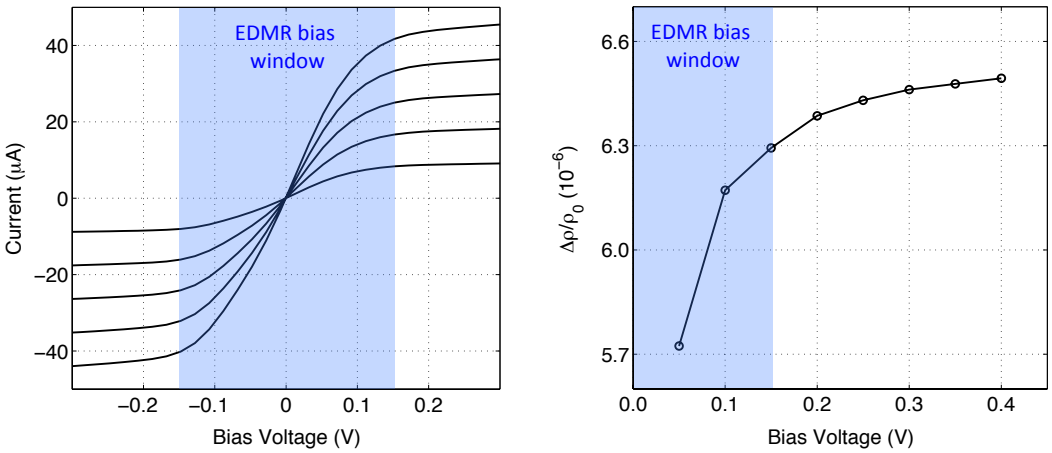

(a) IV-characterisation (b) Bias dependence of EDMR signal

Figure 3.5.: (a) IV-characteristics of a typical Cz-Si sample with OPs for five different illumination conditions at $T = 60$ K. (b) shows the dependence of the EDMR signal intensity on the bias voltage. The line is a guide for the eye only and the bias window used for EDMR is highlighted by a shading in both figures.

regime $V = [0.1\text{ V}, 0.2\text{ V}]$ close to saturation. The power dependence of the main EDMR signal is shown in Figure 3.6 (a) for three representative Cz-Si samples. Each sample reveals the typical saturation behaviour expected for the EDMR signal amplitude. Microwave power saturation typically occurred at ~ 50 mW, when the incident microwave power is high enough to populate the excited spin state faster than it can relax to its equilibrium population through intrinsic spin-lattice relaxation processes. All EDMR measurements discussed below were carried out under this condition before the onset of power broadening of the resonance line in order to maximise the EDMR signal intensity and detect the real width of the resonance line. If not otherwise indicated, the temperature was set to $T = 60$ K in all measurements, which was found to be the optimum in the signal-to-noise ratio as shown in Figure 3.6 (b). Typical EDMR spectra obtained from a (i) precipitate-free, a (ii) not

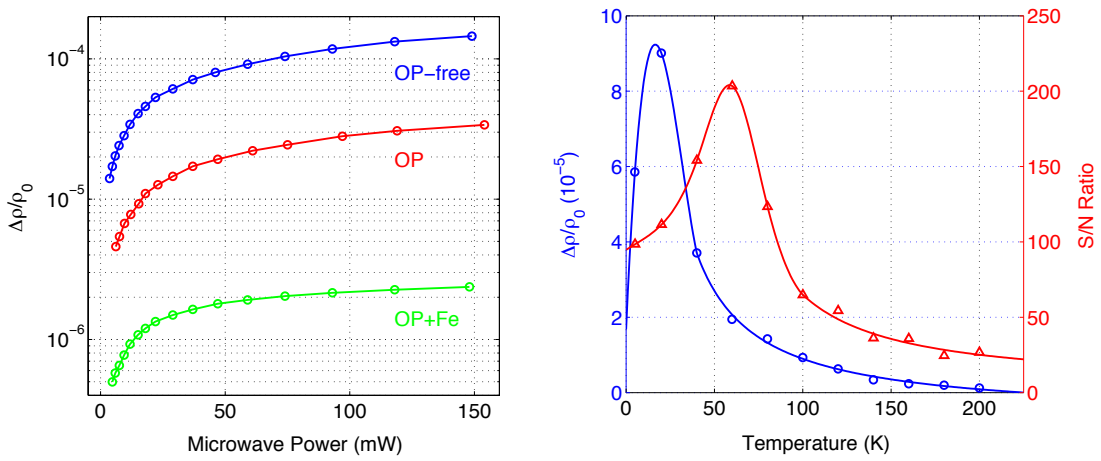

(a) (b)

Figure 3.6.: (a) Microwave power dependence of the EDMR signal intensity obtained from a precipitate-free sample (top, blue), a not intentionally contaminated (middle, red), and iron-contaminated sample (bottom, green) revealing the same concentration of strained OPs at $T = 60$ K on a semilogarithmic scale. (b) shows the temperature dependence of the EDMR signal amplitude (○, blue) and the respective S/N ratio (△, red). Solid lines in (a) and (b) are guides for the eye only.

intentionally contaminated sample with OPs, and a (iii) iron-contaminated sample with OPs ($[\mathrm{OP}] = 0.15 \cdot 10^{10}$ cm^{-3}) are shown in Figure 3.7 (a). In each case, the main resonance is a superposition of multiple resonance lines. The Landé g-factor of each resonance is indicated and numbered from the left to the right according to the order, in which the different lines are discussed in the following.

3.2.1. Interstitial iron and the iron-boron pair

A comparison of the lower-field features is shown in Figure 3.7 (b). Each spectrum reveals a resonance at $g_1 = 2.1350 \pm 0.0006$ with the signal intensity being weakest in the precipitate-free and strongest in the iron-contaminated sample. Interstitial

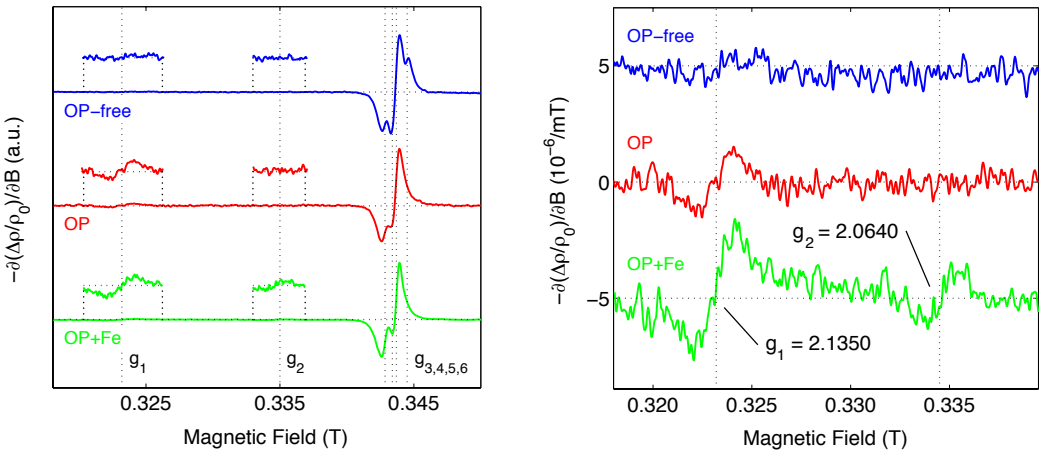

Figure 3.7.: (a) Comparison of normalised EDMR spectra obtained from the same selection of samples as in Figure 3.6 (a). Zooms are shown and vertical lines indicate the magnetic field values of the Landé g-factors $g_{1,2,\ldots,6}$. (b) shows a comparison of the low-field resonances g_1 and g_2. All spectra are offset for clarity.

Fe is well known to bind to substitutional B to form FeB pairs, so we assign g_1 to the FeB pair in accordance with the respective Landé g-factor reported in the literature [Ist99]. Another weak signal is observed in the iron-contaminated sample at $g_2 = 2.0640 \pm 0.0008$ only. It is interpreted in terms of interstitial Fe in good agreement with previous EPR and EDMR experiments [Geh83, Geh95].

The co-existence of the FeB and Fe defects is to be expected as the FeB pair dissociates under illumination with white light [Zot90, Mur11b] and the intensity of the illumination used in our experiments is unlikely to be sufficient for a complete dissociation into interstitial Fe and substitutional B.

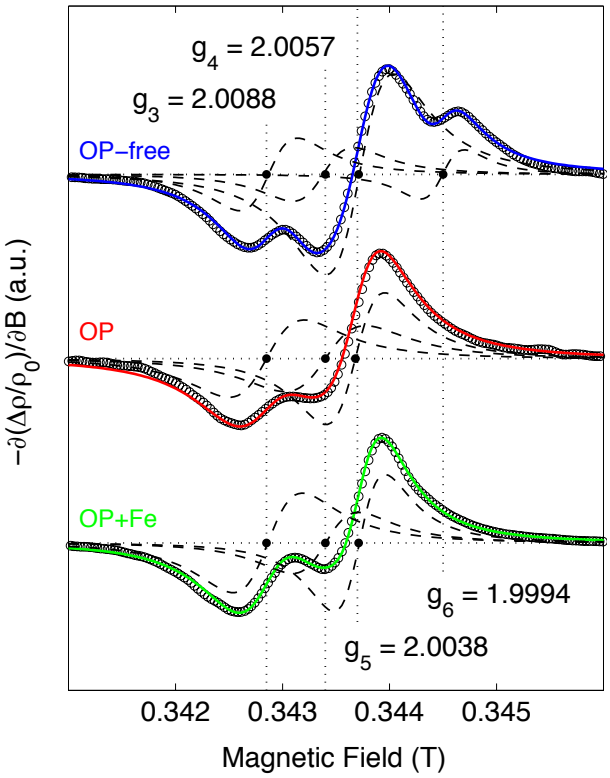

Figure 3.8.: Comparison of the main resonances for the same samples as in Figure 3.6 (a). Solid lines represent numerical best fits of the data (○) to a superposition of four and three Lorentzian derivative lines (dashed, black), respectively. All traces are offset for clarity and solid points (•) indicate the magnetic field values of the Landé g-factors $g_{3,4,5,6}$.

3.2.2. Oxide precipitates

A detailed comparison of the higher-field features of the spectra (close to $g = 2.0$) is shown in Figure 3.8. The spectra of the samples containing OPs are fit best by a superposition of three Lorentzian derivative lines with the Landé g-factors $g_{3,4,5}$, whereas the spectrum obtained from the precipitate-free sample is fit best by a superposition of four Lorentzian derivative lines with $g_{3,4,5,6}$. In other words, $g_{3,4,5}$ were observed in all samples with and without OPs, whereas g_6 was only observed

in the precipitate-free sample. It is therefore possible that the paramagnetic centre associated with $g_6 = 1.9994$ is annealed out during the high temperature growth of the OPs. $g_3 = 2.0088$ and $g_5 = 2.0038$ correspond to the two crystallographic

Our experiment	**Literature**	**Nature of defect**
$g_1 = 2.1350$	2.1345 [Ist99]	FeB pair
$g_2 = 2.0640$	2.0690 [Woo60, Lee77, Poi81, Geh83, Geh95]	interstitial Fe
$g_3 = 2.0088$	2.0086 [Car87, Bro87, Ste98b, Koi00]	P_{b0} DB
$g_4 = 2.0057$	2.0056 [Ste98b, Koi00]	P_{b1} DB
$g_5 = 2.0038$	2.0037 [Car87, Bro87, Ste98b, Koi00]	P_{b0} DB

Table 3.2.: Comparison between the main Landé g-factors observed in our experiments with their corresponding values reported in literature. The microscopic nature of each resonance is indicated in the last column.

orientations of P_{b0} DBs at the (100) Si/SiO_2 interface between the strained OPs and the surrounding silicon matrix. Both Landé g-factors are in good agreement with literature [Car87, Bro87, Ste98b, Koi00] (see Table 3.2). $g_4 = 2.0057$ is interpreted in terms of P_{b1} DBs [Ste98b].

In order to verify this interpretation we investigate the angular dependence of $g_{3,4,5}$, which allows us to identify the nature of these defects unambiguously owing to their inherent crystallographic symmetry. The crystallographic nature of both defects is shown schematically in Figure 3.9. The P_{b0} centre $\bullet Si \equiv Si_3$ is formed by a trivalent

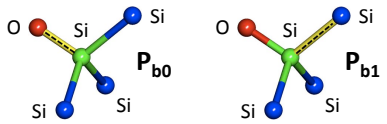

(a) Chemical nature of P_{b0} and P_{b1} centres

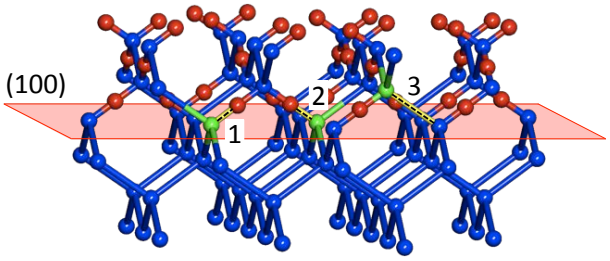

(b) Crystallographic nature of P_{b0} and P_{b1} centres

Figure 3.9.: (a) Chemical nature of P_{b0} and P_{b1} DBs. Each DB defect consists of three components: a central Si atom (green) with a dangling orbital (yellow, dashed line) and an O atom (red). The Si atom of the P_{b0} (P_{b1}) DB is back-bonded to three (two) other Si atoms of the surrounding matrix (blue). (b) shows the crystallographic nature of P_{b0} (1,2) and P_{b1} DBs (3) in an exemplary section of the (100) Si/SiO_2 interface. The P_{b0} centre has two different crystallographic orientations (1,2) relative to the (100) interface plane (red, shaded), which gives rise to two different Landé g-factors.

silicon atom back-bonded to three other silicon atoms, whereas the P_{b1} centre is associated with $\bullet\,Si \equiv Si_2O$, i.e. a partially oxidised silicon atom with a dangling orbital ($\bullet$). Figure 3.10 shows the EDMR spectrum of the iron-contaminated sample with strained OPs for three different orientations of the sample surface with respect to the external magnetic field $\mathbf{B_0}$. The different spectra are numerically best fit to a superposition of three, four, and two Lorentzian derivative lines for $\mathbf{B_0} \parallel [011], [111]$, and [100], respectively. The Landé g-factors extracted from those decompositions are compiled in Table 3.3.

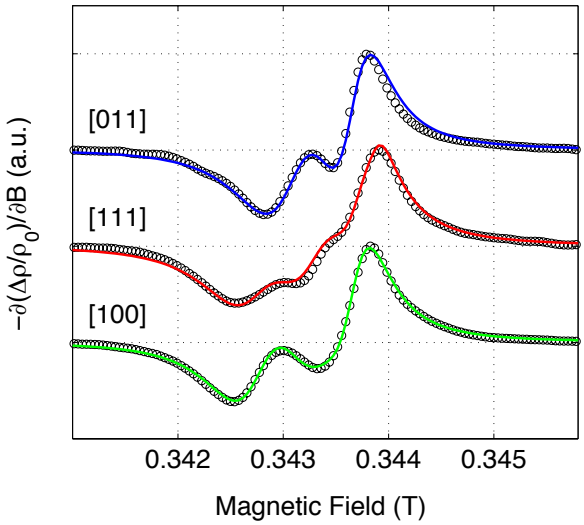

Figure 3.10.: Angular dependence of the main resonances observed in the iron-contaminated sample with strained OPs for $\mathbf{B_0} \parallel [011]$ (top, blue), [111] (middle, red), and [100] (bottom, green). Solid lines represent numerical best fits of the data (○) to a superposition of three, four, and two Lorentzian derivative lines, respectively. All spectra are normalised and offset for clarity.

For an axial (trigonal) symmetry, the shift as well as the disappearance and reappearance of the different resonances as a function of the rotation angle θ between $\mathbf{B_0}$ and the [100] sample normal is described by

$$g(\theta) = \sqrt{(g_{||}\cos\theta)^2 + (g_{\perp}\sin\theta)^2} \tag{3.3}$$

where $g_{||}$ and $g_{\perp}$ denote the principal g-values of the P_{b0} and P_{b1} DBs, respectively. A comparison between the experimentally observed and theoretically predicted values is shown in Table 3.3. The good agreement of the experimental and theoretical values obtained from Equation (3.3) supports our interpretation of $g_{3,5}$ in terms of P_{b0}, and g_4 in terms of P_{b1} DBs. Both defects have been associated with oxygen precipitation in a series of EPR experiments by M. Koizuka *et al.* before [Koi00] with-

out ruling out the possibility of recombination through DBs at the sample surface. T. Mchedlidze *et al.* carried out a similar study but did not observe any EDMR signal in Cz-Si with OPs [Mch98]. This led them to propose that only iron-decorated

Direction of B_0	**g-value of P_{b0}**		**g-value of P_{b1}**	
[011]	2.0088	(2.0086)	2.0054	(2.0056)
	2.0034	(2.0037)		
[111]	2.0078	(2.0078)	2.0046	(2.0045)
	2.0013	(2.0013)	2.0022	(2.0021)
[100]	2.0063	(2.0063)	2.0031	(2.0031)

Table 3.3.: Angular dependence of the Landé g-factors associated with P_{b0} and P_{b1} DBs. Theoretical values obtained from Equation (3.3) with the principal values from [Ste98b] are parenthesised.

OPs can act as recombination centres, which is in contrast to the experiments of M. Koizuka *et al.* as well as our observations.

3.2.3. Influence of OP density on recombination time

In order to identify and better understand the underlying process giving rise to the EDMR effect in Cz-Si with strained OPs, the electronic recombination times associated with recombination through P_{b0} and P_{b1} DBs have been measured in a series of samples with different concentrations of OPs [OP]$= (0.15 - 7.04) \cdot 10^{10}$ cm^{-3} (see Table 3.1 for growth conditions) by measuring the EDMR signal amplitude as a function of modulation frequency and fitting it to Equation (2.20) as described in Section 2.3.2. For this purpose we define the EDMR signal amplitude $|\Delta\rho|$ as the

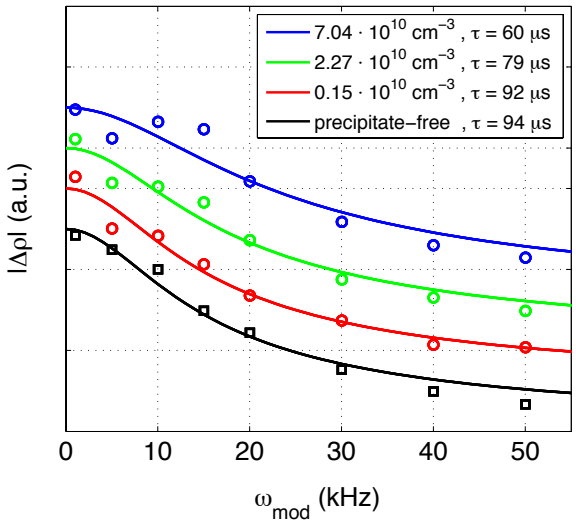

Figure 3.11.: Absolute EDMR signal amplitude $|\Delta\rho|$ as a function of modulation frequency ω_{mod} for the precipitate-free sample (□, black) and three exemplary samples with a low (○, red), medium (○, green), and high concentration of OPs (○, blue). Numerical best fits of the data to Equation (2.20) are shown (solid lines). The recombination times are indicated and decrease with an increasing concentration of OPs. All traces are offset for clarity.

difference between the absolute maximum and minimum of the DB resonance. The electronic recombination time τ thus corresponds to the total recombination time of charge carriers through P_{b0} and P_{b1} DBs.[1] The results are shown in Figure 3.11 for a set of four exemplary samples and were recorded with a modulation frequency $\omega_{mod} \leq 50$ kHz, well below the expected cutoff frequency of our experimental setup $\omega_{RC} \sim 350$ kHz. The extracted electronic recombination times decrease with an increasing concentration of OPs and approach the maximum value $\tau = (94 \pm 6)$ µs in the precipitate-free sample. Similar values have been observed for P_{b0} centres at

[1] The recombination times of the P_{b0} and P_{b1} centres were also measured separately by fitting the DB resonance to a superposition of three Lorentzian derivative lines with the Landé g-factors $g_{3,4,5}$ and the resulting signal amplitudes to Equation (2.20). This analysis did, however, reveal the same recombination time for both, P_{b0} and P_{b1} DBs, which is why we do not differentiate between P_{b0} and P_{b1} DBs in our recombination time measurements in the following.

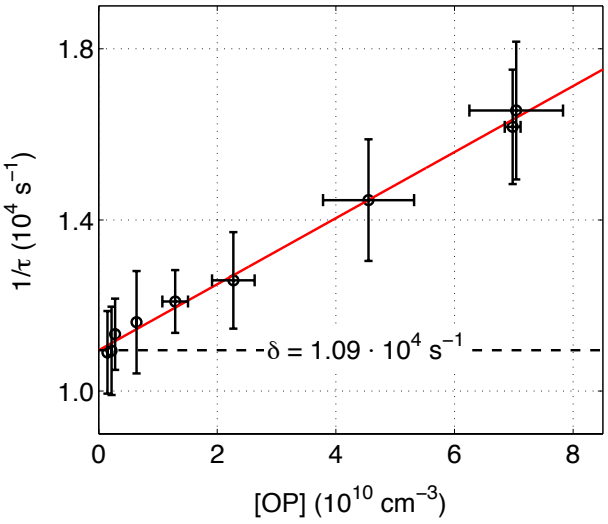

Figure 3.12.: Reciprocal carrier recombination time $1/\tau$ as a function of strained OP concentration [OP]. The linear fit (solid line, red) to the data (○) reveals a slope of $\gamma = 7.72 \cdot 10^{-8}$ cm^{3}s^{-1} and a y-axis intercept of $\delta = 1.09 \cdot 10^4$ s^{-1} (dashed line).

the (100) Si/SiO_2 surface with this technique before [Len90]. Previous photoconductance measurements on surface passivated Cz-Si samples with strained OPs have shown that the reciprocal of the recombination time $1/\tau$ increases with increasing OP concentration [OP] linearly according to [Mur11a]

$$\frac{1}{\tau} = \gamma[\mathrm{OP}] \qquad \text{with} \qquad \gamma := \sigma v_{th} = \sigma\sqrt{\frac{8k_BT}{\pi m^*}} \tag{3.4}$$

where γ and $\sigma > 0$ denote the capture coefficient and cross-section of OPs, respectively, v_{th} the average thermal velocity of the charge carrier distribution within the effective mass approximation [Kit96], k_B the Boltzmann constant, and $m^* = 0.19m_0$ the effective mass of an electron in Si [And82]. Our measurements reveal a similar relationship but with a non-zero y-axis intercept as shown in Figure 3.12. The data are best fit to $1/\tau = \gamma[\mathrm{OP}]+\delta$ with $\gamma = 7.72 \cdot 10^{-8}$ cm^{3}s^{-1} and $\delta = 1.09 \cdot 10^4$ s^{-1},

which corresponds to a lifetime $\tau_\delta := 1/\delta = 92$ µs. The electronic recombination time of the DBs in the iron-contaminated sample was $\tau(\mathrm{P_{b0}}) = \tau(\mathrm{P_{b1}}) = 92$ µs and the lifetime of the FeB pair $\tau(\mathrm{FeB}) = 64$ µs, which is significantly shorter than most of the recombination times observed in our samples.

3.2.4. Discussion

The sign of each EDMR signal discussed above was determined by measuring the DC change in sample resistivity on and off resonance. Those measurements confirm that the sample resistivity increases upon resonance, i.e. $\Delta\rho/\rho_0 > 0$, which corresponds to a resonant decrease of the photocurrent. At the same time, the sample resistivity has been observed to decrease with increasing temperature for all samples in the relevant temperature range, i.e. $\partial\rho_0/\partial T < 0$ as shown in Figure 3.13 for two representative samples exemplarily. Hence, bolometric heating can be ruled out as the predominant EDMR mechanism as that would produce an EDMR signal, which follows the sign of $\partial\rho_0/\partial T$. Furthermore, a resonance line associated with conduction band electrons has not been observed in our experiments. We therefore interpret our results in terms of spin-dependent recombination [Lep72] of photo-excited electron-hole pairs from the Urbach tails of the conduction band [Urb53] through the recombination centres compiled in Table 3.2.

The two lower-field features of the EDMR spectra $g_{1,2}$ shown in Figure 3.7 (b) have been explained in terms of the FeB pair and interstitial Fe, respectively. The obser-

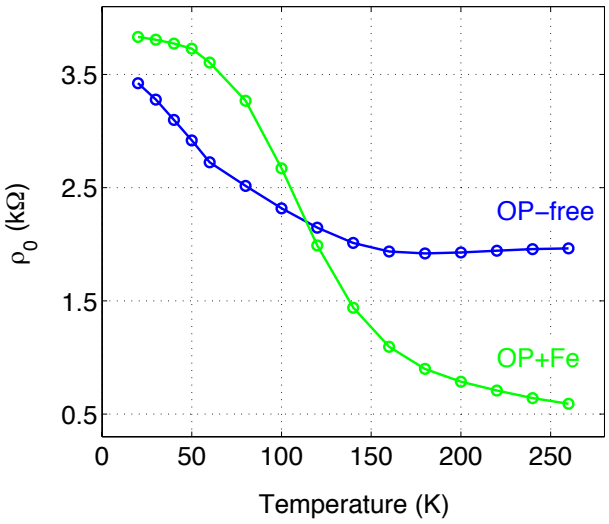

Figure 3.13.: Temperature dependence of the sample resistivity ρ_0 for a precipitate-free sample (blue) and an iron-contaminated sample with strained OPs (green, $[\mathrm{OP}] = 0.15 \cdot 10^{10}\ \mathrm{cm}^{-3}$). Solid lines are guides for the eye only.

vation of the FeB pair is particularly interesting as this impurity has – to our best knowledge – not been observed in EDMR before. Owing to its comparatively short electronic recombination time $\tau = 64\ \mu\mathrm{s}$, our results demonstrate that the FeB pair is a very active recombination centre and contributes to spin-dependent recombination in Cz-Si with strained OPs. The resonance line associated with interstitial Fe was only observed in the iron-contaminated sample and seems to be detectable in our experimental setup only if the concentration of dissolved iron exceeds a certain threshold. Neither of the interstitial Fe nor FeB pair were observed in any sample in standard EPR measurements carried out prior to each EDMR experiment. This is consistent with the fact that the maximum bulk iron concentration in our samples ($[\mathrm{Fe}] = 1.2 \cdot 10^{12}\ \mathrm{cm}^{-3}$, measured by photodissociation of FeB pairs) is an order of magnitude lower than the sensitivity of our EPR spectrometer. The

higher-field features of the EMDR spectra $g_{3,4,5} \sim 2.0$ have been explained in terms of P_{b0} and P_{b1} DBs. While P_{b0} DBs have been observed in EDMR before, there is no consensus in the literature over whether or not the P_{b1} defect is electrically active [Ger86, Ste98a, Mis00]. Our results shown in Figure 3.8 demonstrate, however, that P_{b1} is an electrically active defect and contributes to spin-dependent recombination. The recombination time associated with P_{b0} and P_{b1} DBs is $\tau = 94$ µs in the precipitate-free sample (see Figure 3.11), which coincides well with the lifetime $\tau_\delta = 1/\delta = 92$ µs extracted from the y-axis intercept δ of the measurement in Figure 3.12. This concurrence suggests that photo-excited electron-hole pairs recombine through DBs at the surface as well as through DBs at the strained OPs. The first recombination channel gives rise to the finite y-axis intercept, the latter to the finite capture coefficient $\gamma = 7.72 \cdot 10^{-8}$ cm^{3}s^{-1} in Figure 3.12.

The capture coefficient associated with strained OPs was measured by photoconductance measurements for a similar set of samples in a previous study [Mur11a] and found to amount to $\gamma \sim 1 \cdot 10^{-6}$ cm^{3}s^{-1} at room temperature, which is about two orders of magnitude higher than the results obtained in our EDMR experiments carried out at $T = 60$ K. The smaller γ derived from the latter cannot be explained in terms of the lower measurement temperature as the capture cross-section σ in Equation (3.4) is weakly dependent on T [Gog91] and the average thermal velocity v_{th} at $T = 60$ K only by a factor of ~ 2 smaller than at room temperature.

The different capture coefficients rather arise from the inherent differences between photoconductance and EDMR measurements. EDMR probes an individual recombi-

nation channel and measures the electronic recombination time for a specific recombination centre, whereas the recombination time obtained from photoconductance measurements is an effective recombination time

$$\frac{1}{\tau_{eff}} = \frac{1}{\tau_1} + \frac{1}{\tau_2} + ... + \frac{1}{\tau_N} \tag{3.5}$$

where τ_i ($i \leq N \in \mathbb{N}$) denote the recombination times of the different recombination channels in the sample, such as DBs, interstitial Fe, and the FeB pair. The higher capture coefficient obtained from photoconductance measurements may therefore be explained in terms of additional recombination channels, which do not contribute to charge transport in Cz-Si with strained OPs and are therefore not observed in EDMR. τ_{eff} can generally be derived from the continuity equation for the excess density of charge carriers (also called *injection level*) Δn and is given by [Nag99]

$$\frac{1}{\tau_{eff}} = \frac{1}{\Delta n}\left(g - \frac{\mathrm{d}}{\mathrm{dt}}\Delta n\right) \tag{3.6}$$

where g denotes the generation rate. As a direct consequence of Equation (3.6), τ_{eff} critically depends on the particular injection level, which can be controlled through the light intensity in a photoconductance measurement very accurately. The light intensity in our cwEDMR experiments on the other side is, however, unknown as the halogen light could only be directed onto the sample unfocused and through a window in the cryostat and grid at the microwave resonator. A measurement of the recombination time for different (calibrated) light intensities may therefore enable a

more quantitative comparison between photoconductance and EDMR experiments. Both techniques do, however, reveal $1/\tau \propto [\mathrm{OP}]$ and are therefore consistent with each other. Further to the linear correlation between $1/\tau$ and [OP], J. D. Murphy *et al.* observed that the y-axis intercept of the plot analogous to Figure 3.12 was very close to the origin in their photoconductance experiments [Mur11a]. The difference can be explained by the high quality surface passivation, which substantially reduces recombination at surface-related P_{b0} and P_{b1} centres. It is interesting to note that the size of the precipitate, as governed mainly by the growth time, does not seem to make a substantial contribution to the rate of recombination. This is why the previous study tentatively suggested that the size independence could be explained by recombination at the precipitate corners [Mur11a]. The EDMR experiments presented above show a linear dependence of the recombination rate associated with P_{b0} and P_{b1} DBs on [OP], similarly to [Mur11a]. This is why we speculate that P_{b0} and P_{b1} DBs form at the corners of the strained OPs.

3.3. Pulsed-EDMR in a-Si:H

In the previous section we have characterised Cz-Si with strained OPs by cwEDMR and identified the most important recombination centres in this material. The most common technique to access the dynamics of a particular recombination process as described by the spin relaxation and dephasing times T_1 and T_2 is, however, pEDMR, which was introduced in Section 2.4. In order to test and optimise our experimental

setup for the coherent characterisation of recombination centres in photovoltaic and other materials, we set up a pEDMR experiment on an a-Si:H test structure, which is known to reveal a very strong EDMR effect due to its large disorder.

3.3.1. Spin-dependent recombination in a-Si:H

Owing to its great technological importance, a-Si:H has become a model system for disordered materials, in which charge carrier transport and recombination is dominated by localised states in the bandgap. A-Si:H has been subject to intense research since the fabrication of the first a-Si solar cell in 1976 [Car76] and the pioneering work of D. L. Staebler and C. R. Wronski [Sta77], who demonstrated that silicon DBs are the most important trapping and recombination centres in this material at room temperature. Further mechanisms and recombination centres have been identified since then and contribute to the current understanding of the EDMR effect in a-Si:H, which is reviewed in [Stu00], for instance.

The most important recombination centres in a-Si:H are compiled in Table 3.4. DBs are the most efficient and predominant recombination centres in a-Si:H at room temperature (see Section 1.2.2) and associated with the Landé g-factor $g = 2.0055$. The DBs in a-Si:H are similar to P_b DBs at the (111) Si/SiO_2 interface but less localised compared to the latter [Bro83]. The sp hybridisation of the DB in a-Si:H has ~ 10 % s- and ~ 90 % p-character and its unpaired electron is localised on the threefold coordinated silicon atom with more than 50 % [Lip11]. Details of the spin-dependent

recombination mechanism through DBs in a-Si:H are depicted in Figure 3.14. Photoexcitation creates excess electrons in the conduction band, which can be trapped by so-called *band-tail states*, shallow localised states close to the conduction band

g-Value	**Interpretation**
2.0055	e-DB transition (undoped) [Sol77, Sch81, Str82, Der83, Bra91a, Bra91b, Lip92]
2.0050	[Der83, Bra91a, Bra91b, Lip92]
2.0090 – 2.0100	hopping of h in VB tail (doped) [Sch81, Der84, Bra91a, Bra91b, Lip92]
2.0040 – 2.0044	hopping of e in CB tail (undoped, doped) [Bra91a, Bra91b, Lip92]
2.0070 – 2.0080	e-h transition (undoped, doped) [Bra91a, Bra91b, Lip92]

Table 3.4.: Spin-dependent transitions in undoped and doped a-Si:H. The abbreviation 'e' denotes an electron in the conduction band (CB) and 'h' a hole in the valence band (VB).

edge originating from strained (weak) bonding and antibonding Si−Si bonds [Stu85]. Those electrons can either dissociate back into the conduction band with the rate d (Figure 3.14 (a)) or recombine via DBs at the rate r (Figure 3.14 (b)) as described by the KSM model, which was introduced in Section 2.2.3. Dissociation causes the photocurrent to rise, recombination of excitons causes the photocurrent to drop.

A second mechanism related to spin-dependent recombination is *spin-dependent hopping* [Boe06a] of electrons in the conduction band tail, which gives rise to the Landé g-factor $g = 2.0044$. This resonance is, however, lifetime-broadened at room temperature due to the thermal excitation of delocalised conduction band states and

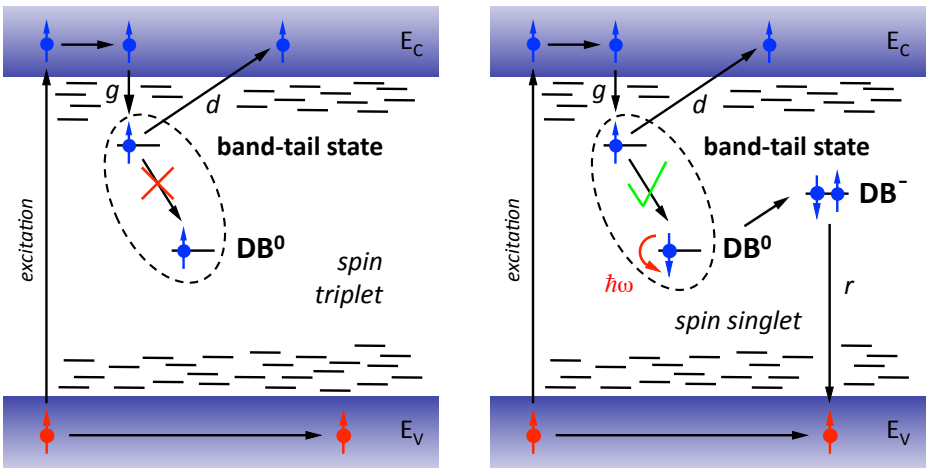

(a) Dissociation (b) Recombination

Figure 3.14.: Spin-dependent recombination through DBs in a-Si:H. Recombination through the intermediate (doubly-occupied) spin state DB^- is only allowed if the spin-pair formed by two electrons trapped in a band-tail and DB^0 state (dashed line) is a spin singlet.

reveals a linewidth of typically $\Delta B_{pp} \sim 200$ G, compared to and $\Delta B_{pp} \sim 7$ G at low temperatures. A more detailed review about spin-dependent recombination and hopping in undoped and doped a-Si:H is given in [Stu00].

3.3.2. Device geometry and experimental setup

The a-Si:H test structure used in this work comprises a 500 nm thick undoped a-Si:H thin-film deposited on a corning glass substrate via very high frequency (VHF) glow discharge at 90 MHz in a siliane-hydrogen (SiH_4 + H_2) atmosphere [Cur87]. An interdigitated gold thin-film was used to contact the active area of the device in order to avoid the disturbance of the microwave field in the cavity. Due to the small amount of material available, the sample was attached to a quartz substrate

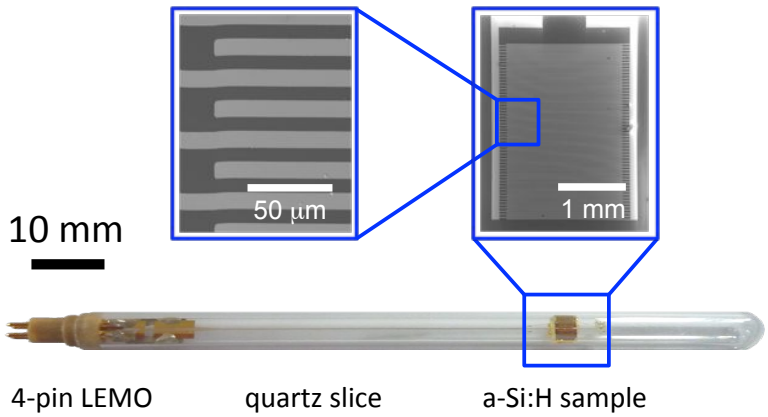

Figure 3.15.: Sample arrangement used for X-band EDMR on a-Si:H. The a-Si:H sample is attached and wire-bonded to a quartz slice equipped with a 4-pin LEMO connector (bottom) facilitating the electrical connection between the sample and the probe head. SEM micrographs show the interdigitated Cr/Au contacts at two different magnifications at 100× (right) and 1850× (left).

equipped with lithographically defined Cr/Au (10/50 nm) contacts. Gold wirebonds facilitated the electrical connection between the sample and a 4-pin LEMO 00-series connector at the top end of the quartz slice as shown in Figure 3.15. A standard $\varnothing = 4$ mm EPR quartz tube was used to encapsulate the device and to protect it against mechanical damage during its insertion into the microwave cavity similar to the contacts used for Cz-Si with strained OPs. In order to test the experimental setup and to identify optimal measurement conditions for our pEDMR experiments, the sample was first tested in the cwEDMR mode.

All experiments were carried out with a modified Bruker E380 X-band EPR spectrometer similar to the one described in Section 3.1. Since the resistivity of the a-Si:H structure amounted to $R_s \sim 18$ kΩ and was much larger than in Cz-Si, EDMR was carried out (under constant illumination) with a constant voltage rather than a

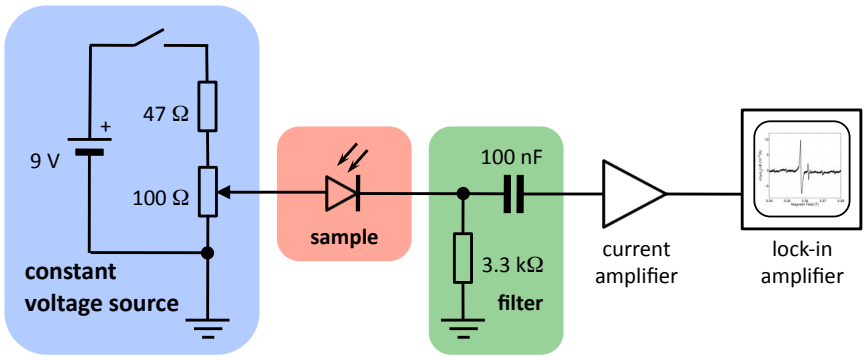

Figure 3.16.: Electrical detection setup used for cwEDMR on a-Si:H. A battery powered variable resistor network (blue) is used to bias the sample (red) with a constant voltage. The modulated photocurrent through the device is filtered (green), preamplified with a current amplifier, and detected with a lock-in amplifier.

constant current as depicted in Figure 3.16. A battery powered variable resistor network was used to bias the device with a constant voltage of typically $U_0 = 500$ mV. The resonant change of the photocurrent through the device was detected via an RC high-pass filter with the time constant $\tau = 330$ µs and a FEMTO DLPCA-200 low-noise current amplifier with a Stanford Research Systems SR830 lock-in amplifier. The modulation amplitude was calibrated and amounted to 0.2 mT with a modulation frequency of $\omega_{mod} = 1.02$ kHz. The experimental setup used for pEDMR differs only slightly from the setup used for conventional cwEDMR. Instead of being directly connected to the microwave resonator, the output of the microwave bridge containing the pulse shaping unit is connected to a traveling wave tube (TWT) amplifier (Applied Systems Engineering, model 117) with a maximum output of 2 kW in order to generate a microwave field B_1 of several Gauss at the sample. The output of the TWT amplifier was fed into a Bruker ER4118X-MD5-W1 X-band dielectric ring resonator. As pEDMR was carried out without using a lock-in technique, the

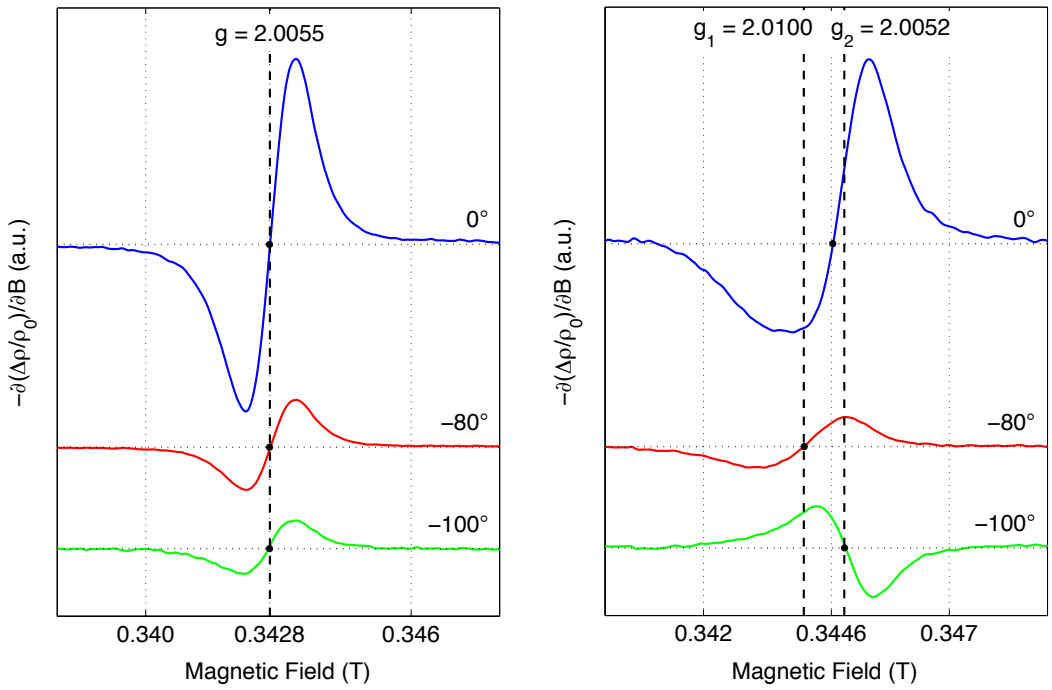

(a) Room temperature (b) $T = 125$ K

Figure 3.17.: EDMR spectra obtained from an a-Si:H sample at room temperature (a) and $T = 125$ K (b) for different lock-in phases $\phi = 0°$ (blue, top), $-80°$ (red, middle), and $-100°$ (green, centre). The observed Landé g-factors are indicated by dashed lines and solid points (•). All traces are offset for clarity.

lock-in amplifier shown in Figure 3.16 was substituted by a digital LeCroy WaveRunner 6100A oscilloscope to integrate and average the transient current change associated with the spin echo.

3.3.3. Phase-sensitive detection of EDMR

Typical cwEDMR spectra obtained from the a-Si:H sample are shown in Figure 3.17 for two measurement temperatures $T = 300$ K and 125 K. The lock-in phase ϕ between the applied magnetic field modulation and the detected photocurrent was

varied by changing the phase of the lock-in amplifier in order to separate different contributions to the EDMR effect with respect to their electronic recombination time based on Equation (2.19). The room temperature spectrum reveals a symmetric resonance line centred around $g = 2.0055$ independently of the lock-in phase, which coincides well with the Landé g-factor reported for spin-dependent recombination through DBs in a-Si:H (see Table 3.4).

The low temperature spectrum in Figure 3.17 (b) reveals an asymmetric line for $\phi = 0°$ centred around the same Landé g-factor. This asymmetry indicates a superposition of two resonance lines, which can be decomposed by varying the lock-in phase provided the two resonances reveal different recombination times as described in Section 2.3.2. For $\phi = -80°$ and $-100°$ we indeed observe two symmetric resonance lines centred around $g_1 = 2.0100$ and $g_2 = 2.0052$, respectively, which add up to the asymmetric line observed for $\phi = 0°$. The Landé g-factor g_1 is interpreted in terms of spin-dependent hopping of holes in the valence band tail in good agreement with the literature (see Table 3.4). The resonance line centred around $g_2 = 2.0052$ arises due to a combination of two processes with very similar recombination times, namely spin-dependent hopping of electrons in the conduction band tail ($g = 2.0044$) and spin-dependent recombination through DBs ($g = 2.0055$) resulting in a resonance line at $g = 2.0052$. Our observations are consistent with literature [Sch81, Der83, Bra92] and demonstrate that the lock-in technique can be used to resolve different contributions to the EDMR effect in a-Si:H.

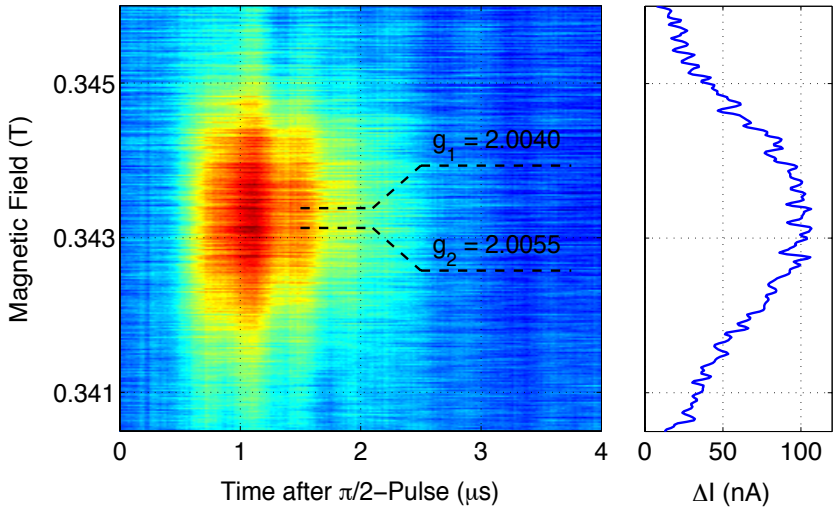

Figure 3.18.: Colour plot of an FID-detected field sweep on a-Si:H at room temperature (left). Red regions correspond to a low, blue regions to a high photoconductivity. The positions of the main Landé g-factors g_1 and g_2 are highlighted by dashed lines. Every time slice has the shape of a cwEDMR absorption spectrum as shown for 1.1 μs after the microwave excitation exemplarily (right).

3.3.4. Coherent spectroscopy of a-Si:H at room temperature

In order to test and optimise our EPR spectrometer for coherent spectroscopy we conducted a series of pEDMR experiments on the a-Si:H test structure described above. In a first experiment we recorded an FID-detected magnetic field sweep (see Section 2.4), in which a coherent $\pi/2$-pulse of length $t_{\pi/2} = 12$ ns is applied to the sample and the integrated transient change of the photocurrent detected as a function of magnetic field. In order to remove any microwave artefact transients we subtracted the off-resonant current transient from each measurement.[1] The results are shown in Figure 3.18 and reveal a broad quenching contribution centred around

[1] Please note that this procedure can only be applied if the sample conductivity is sufficiently independent of the magnetic field. This contribution would otherwise interfere with the resonant spin contribution, which is strongly dependent on the magnetic field.

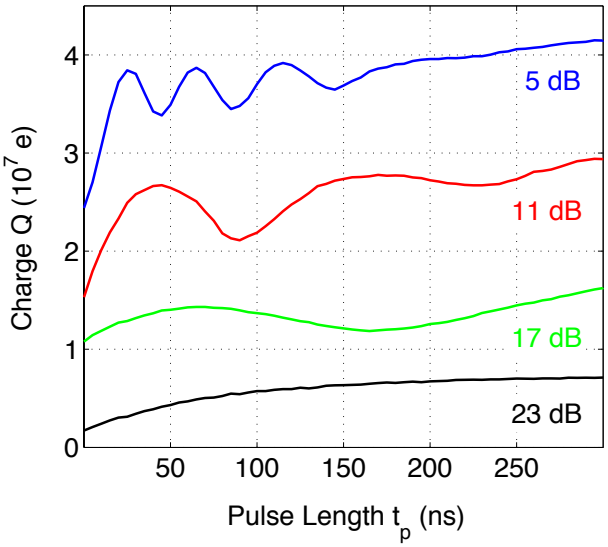

Figure 3.19.: Rabi oscillations of DBs in a-Si:H at room temperature. The oscillation frequency increases with decreasing attenuation $5 - 23$ dB.

$B_0 \sim 0.3434$ T, which corresponds to the Landé g-factor $g_1 = 2.0040$. This value coincides well with the g-factor associated with spin-dependent hopping of electrons in the conduction band tail (see Table 3.4). This resonance is known to reveal a characteristic lifetime broadening ($\Delta B_{pp} \sim 200$ G at $T = 300$ K) from previous experiments due to thermal excitation of delocalised conduction band states, which may also explain the large width of the overall resonance feature. $g_2 = 2.0055$ is the most prominent resonance and interpreted in terms of spin-dependent recombination through DBs in good agreement with our cwEDMR experiments and literature (see Table 3.4). In order to demonstrate a coherent spin manipulation with our spectrometer we induced Rabi oscillations of the DB resonance at $B_0 = 0.3431$ T in a second pEDMR experiment. For this purpose the length of the microwave pulse was varied between $t_p = 0 - 300$ ns. Figure 3.19 shows the integrated charge Q as a function of pulse length t_p for different attenuation levels and reveals pronounced

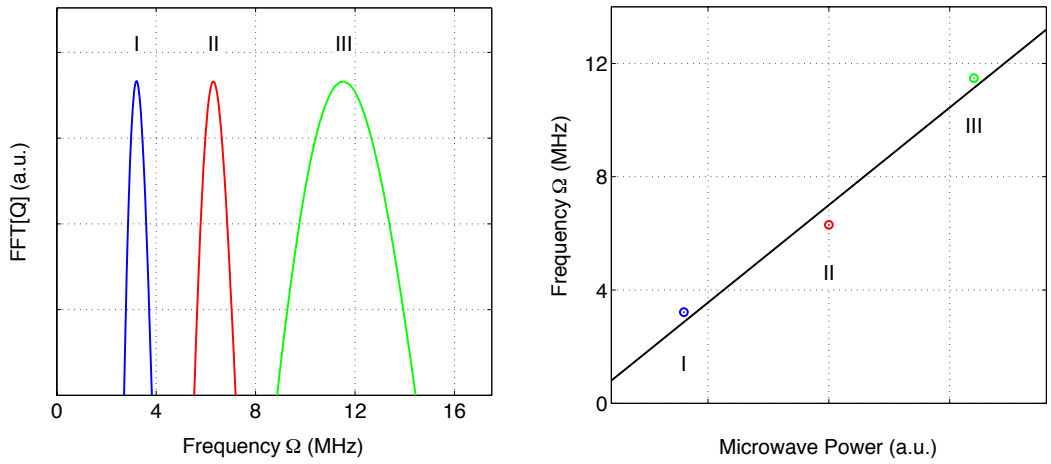

(a) (b)

Figure 3.20.: Fast Fourier transform of the integrated charge FFT[Q] (a) and plot of the observed Rabi frequency (○) versus microwave power (b). The linear fit (solid line) confirms the observation of Rabi oscillations.

oscillations.[1] To identify the observed oscillations as Rabi oscillations, it is vital to demonstrate that their oscillation frequency is proportional to the microwave power $P \propto B_1$ according to Equation (2.21). The fast Fourier transform (FFT) of the integrated charge FFT[Q] is shown in Figure 3.20 (a).

In order to enhance the frequency resolution of FFT[Q], Q was extended by a period of zero amplitude, which is known as zero-filling and can be disregarded in the practical evaluation of the FFT [Bar73]. FFT[Q] reveals three main frequency components $\Omega = \{3.2, 6.3, 11.5\}$ MHz. Ω increases linearly with increasing microwave power in accord with Equation (2.21) as shown in Figure 3.20 (b). Hence, our FFT analysis confirms the observation of Rabi oscillations.

[1] The attenuation level A (dB) determines the applied microwave power $P_{mw} = 10^{-A/20}$ and thus the microwave field B_1 in the cavity. The calibration factor $\kappa := P_{mw}/B_1$ for a particular experiment can be measured by measuring the power broadening of the resonance line [Kaw97], for instance. This calibration has, however, not been performed for the purpose of this experiment.

3.4. Conclusions

The most important recombination centres in Cz-Si with strained OPs have been identified via cwEDMR in the first half of this chapter. The recombination rate $1/\tau$ associated with P_{b0} and P_{b1} DBs was extracted from our cwEDMR spectra and found to increase linearly with an increasing concentration of strained OPs. The finite y-axis intercept of this linear relation has been interpreted in terms of P_{b0} and P_{b1} DBs forming at the sample surface, while the slope has been attributed to P_{b0} and P_{b1} DBs at the corners of the OPs. Furthermore, interstitial Fe and the FeB pair were observed in cwEDMR and demonstrated to reveal very short recombination times, which indicates that both impurities are very active recombination centres. In the second half of this chapter we modified our EPR spectrometer to perform pEDMR experiments. The setup was tested with an a-Si:H test structure revealing a particularly strong EDMR signal. The good agreement between our results and the literature demonstrates that our experimental setup is suitable for both, the investigation of photovoltaic materials by cwEDMR and pEDMR. Future experiments may involve pEDMR measurements of Cz-Si with OPs and focus on the comparison between electronic recombination times measured via cwEDMR and spin relaxation and coherence times measured via pEDMR. Such experiments are particularly interesting as they will allow us to identify any pairs of iron- and oxygen-related recombination centres that give rise to the same recombination channel. Our experiments provide an important step towards this goal and are a prerequisite for the optimisation of internal gettering in Cz-Si with strained OPs.

CHAPTER 4

A TEM compatible carbon nanotube device for QIP

Contents

Owing to their exceptional mechanical, electrical, and spin properties, CNTs have attracted considerable interest over the past few years (see Section 1.1) and tremendous progress has been made towards their integration into carbon nanodevices,

such as QDs and DQDs, for applications in QIP. Beside their long spin coherence times (see Table 1.1), their main advantage upon conventional semiconductor QDs is due to their one-dimensional structure. Spatial confinement of charge carriers, for instance, is principally easier to achieve in one-dimensional CNT QDs than in QDs defined electrostatically in two-dimensional electron gases. Furthermore CNTs can be filled with molecules, such as fullerenes, to form so-called *peapod structures*, which have been proposed for applications in QIP [Ben06] as they interface single molecule properties with nanodevices.

In this chapter we design and fabricate a CNT-based nanostructure on a semiconductor-on-insulator (SOI) substrate, which principally allows us to (i) manipulate and readout individual electron spins with EDMR through spin-dependent tunnelling, and to (ii) access the microscopic structure of the CNT with TEM in order to investigate the complex interplay between electrical and spin properties. Furthermore, we develop an experimental setup, which enables a high-throughput electrical characterisation of such nanodevices as well as EDMR experiments at room and low temperatures.

In the following few sections, I only describe the different fabrication steps and technical challenges involved in making TEM-compatible CNT devices on SOI substrates and discuss initial electron transport experiments at room temperature. Those preliminary results will serve as a basis for other researchers studying few to single electron spins and their dynamics in TEM-compatible and suspended CNT QDs.

4.1. Proposed device architecture

CNTs have been studied by material scientists since 1952 [Rad52] and became a worldwide research focus after the discovery of single-walled CNTs by S. Iijima *et al.* in 1993 [Iij93] and the fabrication of the first CNT FET [Tan98, Mar98]. Their technological importance for molecular electronics [Avo02] and QIP [Ben06] has triggered research towards the understanding of their electronic and structural properties. The latter has been investigated mainly with Raman spectroscopy [Dre04] and TEM, both providing valuable insights into structural parameters, such as diameter, chirality, and curvature of the CNT. TEM microscopy can be used further to support process development and device optimisation including the structural characterisation of electrodes, parasitic layers in the device structure (as a potential source for high leakage currents), interface defects and impurities, as well as adatoms on the CNT shell or molecules inside the CNT, each of which are known to critically affect its electrical and mechanical properties. This is why the correlation of electronic, spin, and structural properties is of great importance for both, fundamental materials research and applied physics.

Different FET architectures have been explored previously in order to combine TEM compatibility with electron transport measurements on individual CNTs [Mey04, Kim05] and peapod structures [Chi05a]. Owing to their architecture and fabrication, each approach requires lithographical steps after the growth of the CNT, which can degrade its electrical properties significantly owing to organic residues. Furthermore,

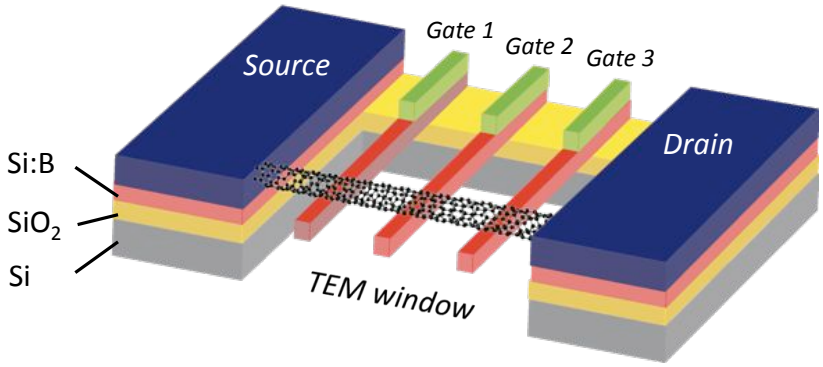

Figure 4.1.: TEM compatible CNT device for applications in QIP. Buried gate electrodes (red) are used to control electron transport through a CNT (black) grown between a source and drain electrode (blue). The silicon substrate (grey) and the silicon dioxide layer (yellow) can be etched away to suspend the gate electrodes and allow the structural characterisation of the CNT with TEM.

these approaches utilise large global gates to control electron transport through the CNT rather than local gate structures. Additional gates for the realisation of multi-gate devices, such as QDs and DQDs, are therefore difficult to add, which makes them incompatible with current device designs for applications in QIP and leaves the correlations between the electronic, spin, and structural properties of carbon nanotubes widely unexplored.

An alternative approach to a CNT nanodevice enabling the characterisation of the CNT in terms of its (i) electrical properties through electron and magneto-transport measurements, (ii) spin properties through EDMR, and (iii) structural properties through TEM is shown in Figure 4.1. It consists of a suspended single-walled CNT on an SOI substrate, which is grown in the very last step of the overall device fabrication process. This device architecture minimises the disorder and defects induced by organic residues and the exposure to an electron beam during EBL

[Smi01], which has been reported to lead to the formation of multiple unintentional QDs at low carrier densities [McE99]. Buried gate electrodes etched into boron-doped silicon (Si:B) facilitate the electrostatic control of electron transport from the source to the drain electrode of the device. By shorting all gates together or controlling them individually, the device can either be operated as a simple FET or as a QD, which allows us to characterise the electrical properties of the CNT via electron transport in a first step and to access its spin properties through spin-dependent tunnelling via EDMR thereafter. Furthermore, the SOI substrate can be chemically etched beneath the gate structure (and prior to the CNT growth) to expose a window for TEM microscopy.

4.1.1. Merits of suspension

The suspension of the CNT and its CVD growth in the very last step of the overall device fabrication process adds further advantages to the device architecture proposed above: Beside circumventing disorder from the substrate and organic residues from device fabrication, suspension enables transport studies on ultra-clean CNTs. Initial attempts to remove the disorder induced by the substrate involved wet-chemical etching of the device structure after its fabrication and CNT growth [Min04, Jar04]. The yield of these devices was very low and could be increased significantly with a new fabrication method, in which all chemical processing is performed prior to the CNT growth [Cao05, Ste09a] similar to the fabrication process developed and employed in this work.

Electron transport measurements on non-suspended CNTs have revealed the four-fold shell structure of CNTs [Cob02, Kue08, Mor05] arising from the two doubly-degenerated electronic subbands associated with the spin and orbital degrees of freedom, which give rise to the eigenspaces $\{|\uparrow\rangle, |\downarrow\rangle\}$ and $\{|\circlearrowright\rangle, |\circlearrowleft\rangle\}$, respectively, where $|\circlearrowright\rangle$ denotes the clockwise and $|\circlearrowleft\rangle$ the anti-clockwise orbital motion of an electron within the CNT [Nyg08]. The four-fold spin and valley degeneracy gives rise to an enhanced SU(4) Kondo effect in CNT QDs[1], where the spin and orbital degrees of freedom are fully entangled [Nyg00].

Other very interesting and more exotic transport phenomena, such as the electron-hole symmetry[2] [Jar04], Mott insulation[3] [Des09, Des10], and Wigner crystallisation of electrons at low density[4] [Des08], have, however, only been observed in ultra-clean and suspended CNT devices. Furthermore, suspension of the CNT allows us to employ its exceptional mechanical properties [Tra96] for nanoscale radio-frequency signal processing, ultra-sensitive mass detection [Las08], as well as for high-Q [Hue09b] non-linear [Ste09b] resonators [Saz04].

[1] The *Kondo effect* describes the spin-flip scattering of conduction electrons at magnetic impurities [And61, Kon64]. The most basic Kondo system is realised by an unpaired electron on a QD, which is exchange-coupled to delocalised electrons in the leads (Fermi sea). In an external magnetic field, co-tunnelling between the spin states leads to two additional resonances in the transport spectrum, which is called SU(2) Kondo effect. The coherent superposition of co-tunnelling processes between the spin and orbital states in a CNT QD results in a $\mathrm{SU}(2)\otimes\mathrm{SU}(2) = \mathrm{SU}(4)$ Kondo effect revealing the four-fold spin and valley degeneracy.

[2] *Electron-hole symmetry* refers to the observation of the same confinement energy for electrons and holes in semiconducting CNT QDs.

[3] A *Mott insulator* is an insulating material, which should be conductive from conventional band theory. This theory, however, breaks down in metals with half-filled energy bands as the very strong Coulomb repulsion makes the localisation of electrons at an atomic site energetically more favourable, which in turn leads to Mott insulation.

[4] *Wigner crystallisation* refers to a solid phase of electrons in an uniform, inert, and neutralising background. In a CNT, the conduction electrons were observed to form an evenly spaced lattice to minimise their potential energy. Wigner crystallisation in three dimensions is associated with a body-centred cubic lattice, whereas it reveals a triangular lattice in two-dimensional systems.

4.1.2. Merits of accessibility via TEM

Although being a very powerful analytical tool and having provided valuable insights into structural, electronic, and phonon properties of CNTs [Dre04], Raman spectroscopy is not a direct imaging technique. Its spectra arise from photo-excitation with laser spots with a diameter of $\varnothing = 300 - 500\,\mathrm{nm}$, which complicates their interpretation [Dre10]. This is why low-voltage high-resolution transmission electron microscopy (HRTEM) has become the foremost characterisation technique for directly imaging CNTs, and measuring their diameter, number of sidewalls, and chirality [Iij91, Iij93]. Owing to the recent advances in low-voltage aberration-corrected HRTEM [Bör11], the structure of CNTs can nowadays be studied with atomic resolution revealing atomic scale defects [Has04, Has05, Zhu05, Sat08, War09] and their dynamic behaviour [War10, War11]. A TEM compatible single-walled, and CVD-grown CNT QD device can thus be expected to provide very valuable insights into the correlations between electrical, mechanical, spin, and structural properties.

4.2. Device fabrication

The overall fabrication process of our proposed CNT device architecture is sketched in Figure 4.2. It involves five main steps, namely (i) patterning and RIE of source, drain, and gate electrodes, (ii) metallic thin-film deposition of source and drain contacts, (iii) metallisation of gate electrodes, (iv) wet-chemical etching of the TEM

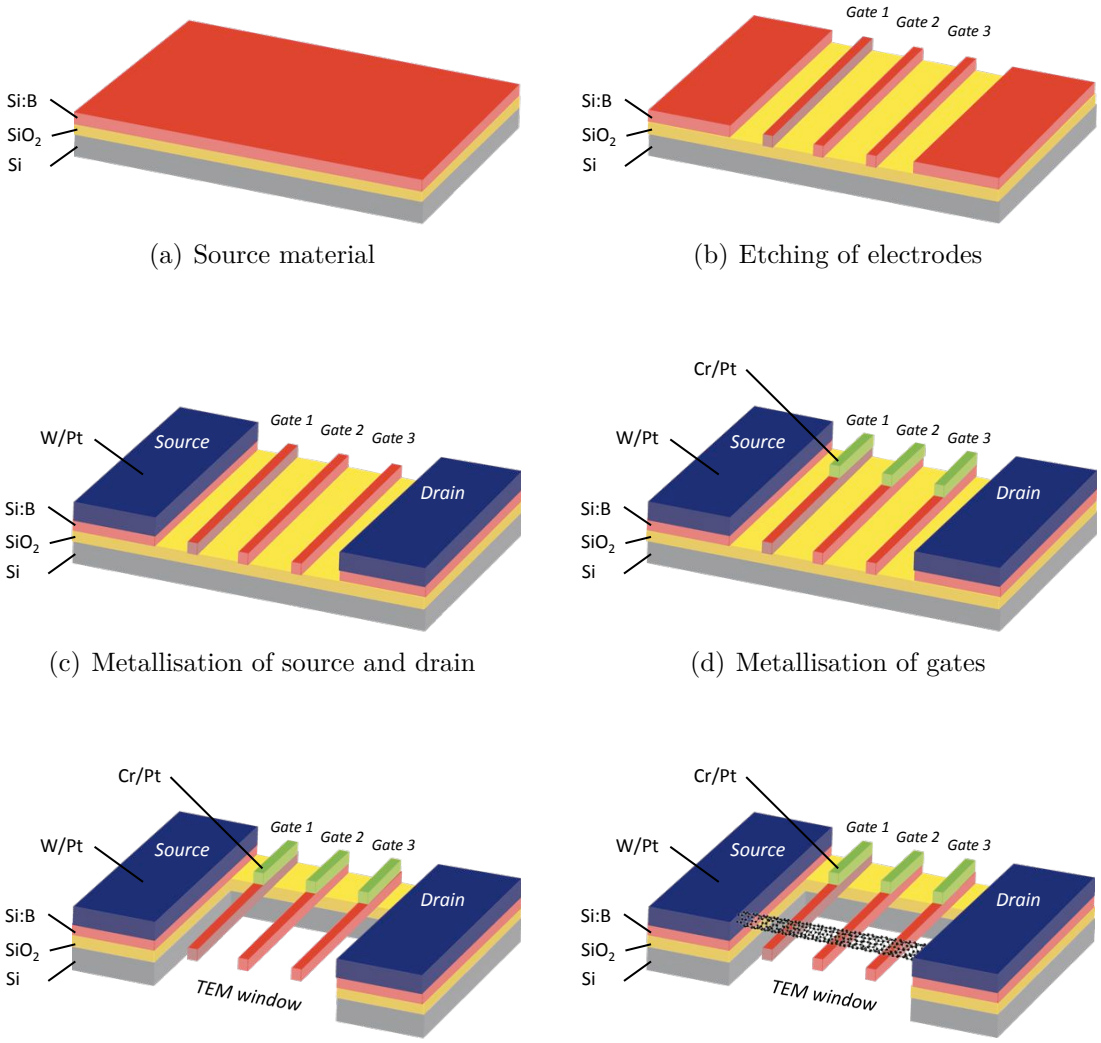

(a) Source material

(b) Etching of electrodes

(c) Metallisation of source and drain

(d) Metallisation of gates

(e) Etching of TEM window

(f) CVD growth of CNT

Figure 4.2.: Sample preparation of a TEM compatible multi-gate CNT device. Starting with the SOI source material (a), the process is organised into five main steps: Patterning and RIE of source, drain, and gate electrodes (b, red), metallisation of source and drain (c, blue), metallisation of gate electrodes (d, green), wet-chemical etching of a TEM window (e), and CNT growth via CVD (f).

(a) EBL system (b) FIB-SEM system

Figure 4.3.: Photographs of the JEOL JBX-5500FS EBL (a) and the ZEISS NVision40 FIB-SEM system (b) used to prepare and image CNT devices, respectively.

window, and (v) the CVD growth of a single CNT across the buried gate structure. The device is fabricated on an (100) $Si/SiO_2/Si$:B ($5,000/145/70$ nm) substrate with the top-layer being implanted with boron at 10 keV and the dose $5 \cdot 10^{14}$ cm^{-2}. The SOI substrate was diced into chips of 10×10 mm^2 with a Loadpoint MicroAce Series 3 wafer saw for convenient device handling. The most important process parameters are discussed in the following.

4.2.1. Electron beam lithography

All electrodes were defined by EBL, in which an electron beam is used to pattern a PMMA polymer spun onto the semiconductor surface. EBL was carried out on the JEOL JBX-5500FS EBL system shown in Figure 4.3 (a) with an acceleration

voltage of 25 kV, field size of 500 × 500 μm^2, and minimum step size of 1.0 nm – the minimum resolution of our EBL system is specified to 9.79 nm. The critical step during the exposure of the resist with the electron beam is the adjustment of the area dose, which determines the aspect ratio of the patterned structures through the *proximity effect*. The dose was optimised for each EBL step in a series of dose tests and subsequent imaging in the ZEISS NVision40 focused ion-beam (FIB) scanning electron microscope (SEM) shown in Figure 4.3 (b).

The different electrodes were either defined in A8 PMMA for structures larger than 10 µm with a dose of 600 $\mu C/cm^2$ and a beam current of 20 nA, or A5 PMMA for smaller structures with a dose of 500 $\mu C/cm^2$ and a beam current of 1 nA.[1] Both resists were spun onto the substrate with a Cee^{TM} 200CB Coat-Bake System and baked for 90 s at 180 °C prior to the exposure in the EBL. A solution of MIBK and IPA with [MIBK]/[IPA] = 1/3 volume percent was used to develop the resist for 10 s at 25 °C in ultrasound. The lift off was performed after the deposition of the metallic thin-film in 1-methyl-2-pyrrolidinone (NMP, C_5H_9NO) at a temperature $T = 130$ °C for 30 min.

4.2.2. Etching of silicon nanostructures

The first fabrication step (see Figure 4.2 (a)) involves patterning of the Si:B layer. To this purpose, all nanostructures were patterned in PMMA with EBL first and

[1] A5 and A8 refer to a solution of five and eight weight percent PMMA in anisole, respectively.

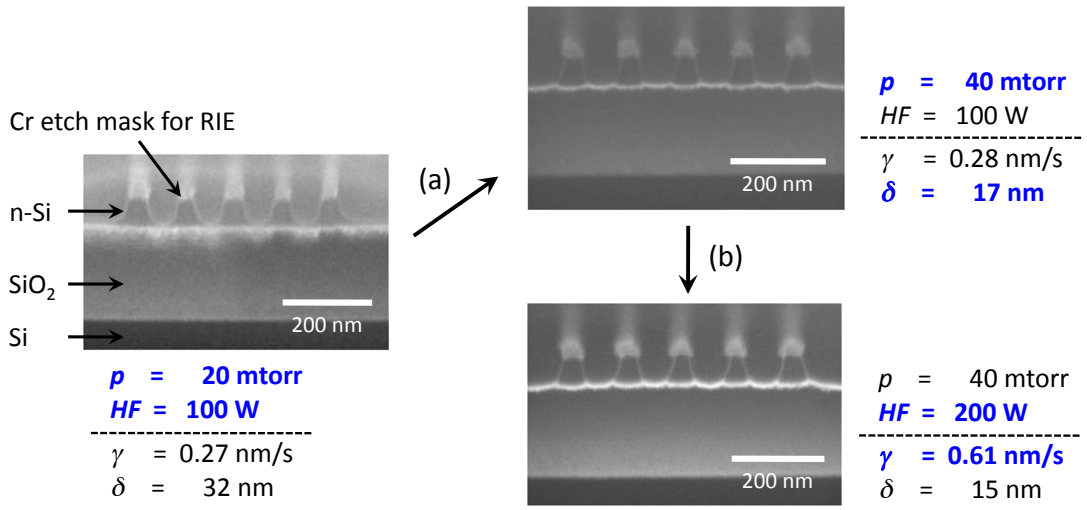

Figure 4.4.: Cross-sectional SEM micrographs of gate electrodes etched into Si:B by using chromium etch masks and RIE. (a) shows the influence of increasing plasma pressure p, (b) the influence of increasing HF-power on the etching rate γ and anisotropy δ, respectively. The latter is mainly determined by the pressure, whereas the etching rate γ predominantly depends on the HF-power.

subsequently etched in a plasma of carbon tetrafluoride (CF_4) and oxygen (O_2) (50 sccm and 10 sccm, respectively) formed in an Oxford PlasmaLab 80Plus RIE system by using a 30 nm thick chromium (Cr) etch mask [Lee83]. The etch parameters, such as pressure p and high frequency power HF, have been checked carefully and the etching rate γ and anisotropy δ optimised in a series of samples etched under different conditions and imaged in cross-section via FIB-SEM as shown in Figure 4.4. δ measures the deviation of the resulting trapezoidal from an ideal rectangular cross-section of the etched gate structure and is defined as the difference between the width of the Cr etch mask and the width of the etched nanostructure. The cross-sectional SEM micrographs in Figure 4.4 reveal the effect of increasing pressure and HF-power on the etch parameters γ and δ. The HF-power is found to mainly affect the etching rate γ, whereas the anisotropy δ is mainly determined by

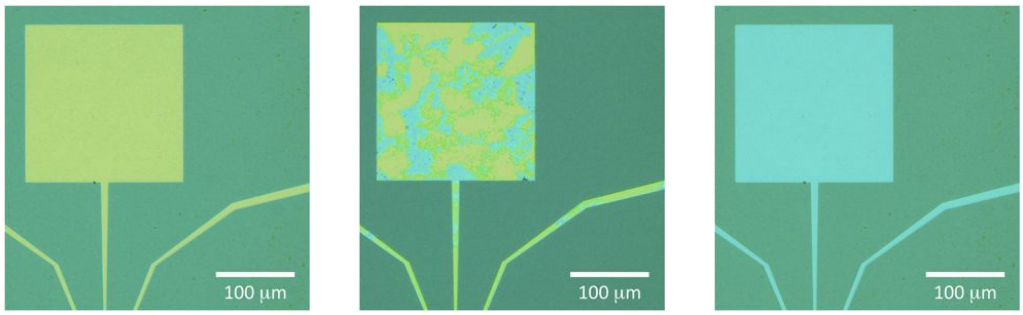

(a) 0 min (b) 2 min (c) 5 min

Figure 4.5.: Series of OM images showing the removal of the Cr etch mask (a) after 2 min (b) and 5 min (c) in the etchant.

the plasma pressure p. For the SOI substrate used in this work, optimal parameters are $p = 40$ mtorr and $HF = 200$ W. The chromium etch mask was removed after the RIE etch in a bath of ceric ammonium nitrate ($H_8N_8CeO_{18}$) and perchloric acid ($HClO_4$) for ~ 5 min at 80 °C as shown in Figure 4.5 for two different etching times. The Cr etching rate amounted to ~ 6 nm/min at this temperature.

4.2.3. Metallisation of source and drain

The second fabrication step (see Figure 4.2 (b)) involves the metallisation of the source and drain electrode. Its main technical challenge arises from the particular choice of the metal or alloy, which has to persist the high temperature during CNT growth, while maintaining a low contact resistance and good surface quality to act as a smooth and continuous substrate for CNT growth. Metals like chromium and cobalt, for instance, indeed have very high melting points above $T = 1,000$ °C, but very thin-films of those metals can partially melt and form disconnected islands.

The best results are reported for sputtered tungsten/platinum (W/Pt) contacts [Ste09a, Göt10]. A 5/30 nm thin-film of those elements was therefore employed for our devices and deposited in an Edwards Auto 306 magnetron sputtering system after the respective EBL step.

4.2.4. Metallisation of gate electrodes

The choice of the metallic thin-film used for the bond pads of the gate electrodes (see Figure 4.2 (c)) is equally important. It has to survive the high temperature during CNT growth while providing a good ohmic contact to the Si:B layer in order to enable the application of high frequency pulses for coherent spin manipulation via pEDMR. Its surface quality is less important as long as it permits conventional gold or aluminum wire-bonding.

Owing to the very high melting point and good adhesion to silicon, we have deposited a Cr/Pt (30/30 nm) bilayer to serve as an ohmic contact to Si:B. Its suitability was evaluated in terms of the resulting contact and Si:B sheet resistance measured in a series of *transmission lines* (TLs), which were annealed at different temperatures $T = 800 - 1,000\,^{\circ}\mathrm{C}$ to simulate the CNT growth. TLs allow us to measure the contact and sheet resistance separately and were successfully employed previously to optimise ohmic gold/antimony contacts to n-type Si [Wer94] as well as to Si/SiGe and isotopically engineered ^{28}Si/^{28}Si^{70}Ge heterostructures [Lan08a], for instance.

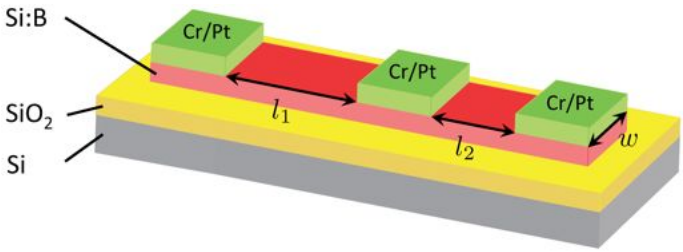

(a) TL geometry

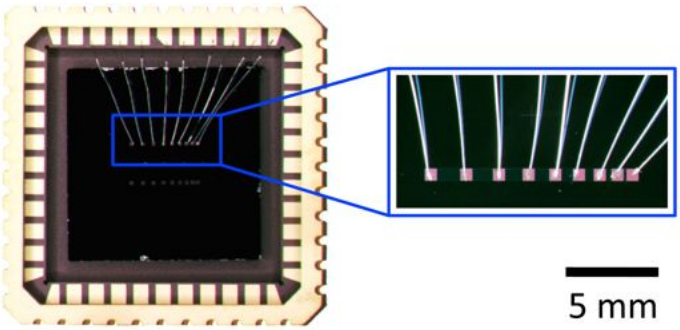

(b) Typical TL device

Figure 4.6.: Device geometry for a TL measurement. (a) shows a sketch of a typical TL used for the optimisation of ohmic Cr/Pt contacts (green) to Si:B (red) on an SOI substrate. (b) shows OM images of an SOI chip with two TLs mounted and connected to an LCC (left) with Al wirebonds (right).

Their basic geometry is sketched in Figure 4.6 (a). A typical TL comprises an etched Si:B mesa and a series of square-shaped Cr/Pt contacts with different separations l. The total resistance R_t of a TL is therefore given by [Ber72]

$$R_t = \frac{l}{w}\frac{\rho}{t} + 2R_c = \frac{l}{w}R_s + 2R_c \tag{4.1}$$

where w denotes the contact width, ρ the specific resistivity of the mesa material, $t = 70\,\text{nm}$ the thickness of the Si:B sheet, R_c the contact and R_s the sheet resistance. An OM micrograph of a typical TL mounted and wire-bonded into a commercial 44-pin leadless chip carrier (LCC) is shown in Figure 4.6 (b). The LCC

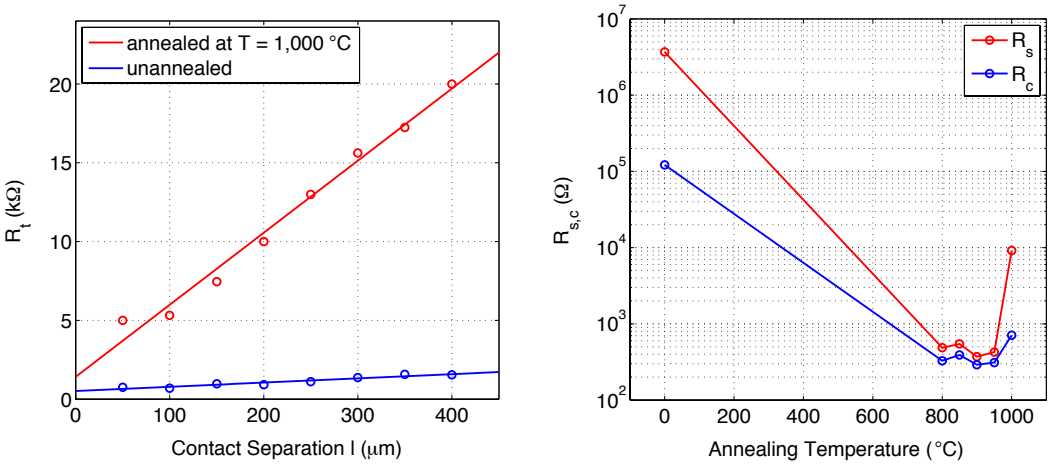

(a) (b)

Figure 4.7.: Results of a typical TL measurement. (a) shows the total resistance R_t as a function of the contact separation l for an unannealed (blue) and annealed sample (red). Solid lines represent numerical best fits of the data (○) to Equation (4.1). (b) shows the resulting contact and sheet resistance R_c and R_s, respectively, for different annealing temperatures. Solid lines are guides for the eye only.

facilitates the electrical connection between the device and our room-temperature measurement setup and can also be inserted into a cryogenic sample probe for low-temperature characterisation. The results of our TL measurements employed for the optimisation of Cr/Pt contacts are shown in Figure 4.7 (a). The total resistance R_t increases with an increasing separation length l between the contacts in accord with Equation (4.1). The temperature dependence of R_c and R_s is shown in Figure 4.7 (b), where $T = 0\,°\text{C}$ denotes an entirely unannealed contact. The contact resistance decreases from initially $R_c = 120\,\text{k}\Omega$ by three orders of magnitude down to $R_c = 328\,\Omega$ when annealed at $T = 800\,°\text{C}$. The steep decrease of the sheet resistance from $R_s = 3.68\,\text{M}\Omega/\square$ down to $R_s = 485\,\Omega/\square$ with increasing annealing temperature is associated with the activation of the boron implants. Similar values

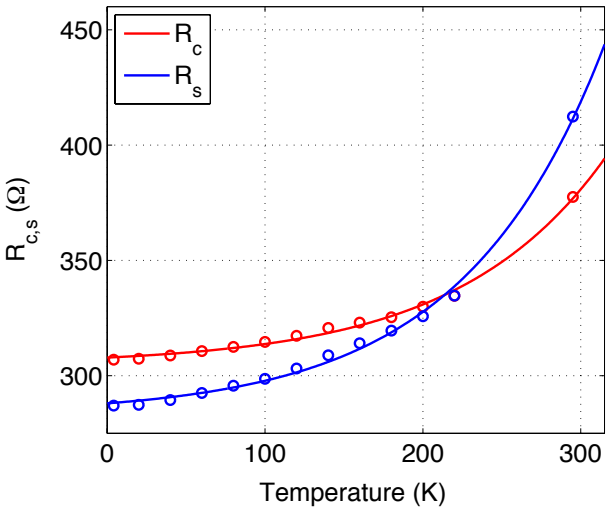

Figure 4.8.: Temperature dependence of the contact (red) and sheet resistance (blue) for a representative TL. Solid lines are guides for the eye only.

have been observed in boron activation anneals before [Col98]. For $T > 950\,°C$, R_c and R_s are observed to increase significantly. This temperature therefore sets the upper bound of the temperature window within which CNTs can be grown and Cr/Pt contacts employed for our suspended CNT devices.

The Cr/Pt contacts fabricated in this work reveal a weak temperature dependence only as shown in Figure 4.8 exemplarily for a TL, which was annealed at $T = 800\,°C$. R_c and R_s both decrease from room temperature down to $T = 1.4\,K$ by $\sim 25\,\%$, which demonstrates the compatibility of our recipe with the high-temperature CVD growth of suspended CNTs. The overall chip layout and an OM image of a typical CNT device processed until the fabrication step described in this section, i.e. prior to the etching of a TEM window and CNT growth, is shown in Figure 4.9.

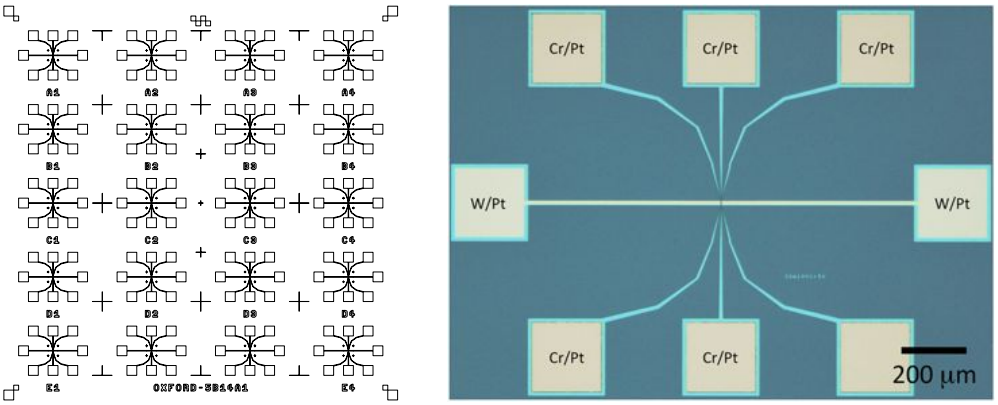

(a) Chip layout (b) Device structure

Figure 4.9.: AutoCAD drawing of the chip layout (a). Each chip accommodates 20 nanodevices. An OM micrograph of an individual device prior to the CNT growth is shown in (b). Please refer to the text for further details.

4.2.5. Etching of TEM window

The overall device architecture was designed such, that it allows us to optionally remove the substrate under the nanometer-sized gate structures prior to the CNT growth in a fifth fabrication step for TEM analyses (see Figure 4.2 (e)). The process proposed for the etching of a TEM window involves the EBL patterning of an array of alignment marks outside the device area on the polished backside of the chip and the subsequent removal of the bulk-Si in those areas by wet-chemical etching with tetramethylammonium hydroxide (TMAH, $C_4H_{13}NO$). The remaining SiO_2/Si:B (145/70 nm) membrane (outside the device area) can then either be punctured with a fine needle under a microscope or milled in a FIB system to generate a set of alignment marks, which can be used to align the back- to the frontside of the chip. A $\sim 5 \times 5$ µm^2 TEM window aligned to the gate structures on the frontside

can then be patterned on the polished backside of the chip in a second EBL step. The TEM window can be etched finally by a combination of TMAH and hydrofluoric acid (HF), which selectively etches bulk-Si and SiO_2, respectively. The Si:B gate structure is expected to remain intact during this procedure as HF does not etch any p-doped Si.

4.2.6. Carbon nanotube growth

CNTs were grown from the source across the buried gate structure to the drain electrode via CVD [Kon98] in the last step of the sample fabrication process (see Figure 4.2 (f)). For this purpose, a $2 \times 10\ mm^2$ window was defined on the source and drain contact in A5 PMMA via EBL first. We then developed the resist with our standard recipe and carefully deposited small droplets of iron(III) chloride ($FeCl_3$) catalyst nanoparticles diluted in 2.5 µmol/l ethanol (C_2H_5OH) onto the W/Pt electrodes with a 1 µl nanopipette. After baking the substrate at $T = 170\ °C$ for 5 min, the PMMA was lift-off in 1,2-dichloroethane ($C_2H_4Cl_2$) prior to cleaning the substrate with ethanol and nitrogen. The substrate was then transferred into a quartz tube inside a Thermo Scientific Lindberg/Blue M tube furnace.

The high temperature during CVD growth was found to critically determine various properties of the CNT devices, namely the (i) structural integrity of the SiO_2 and Si:B layers, (ii) structural integrity of the nanostructures etched into Si:B, (iii) yield of the CNT growth as well as the (iv) surface quality of the metallic Cr/Pt and

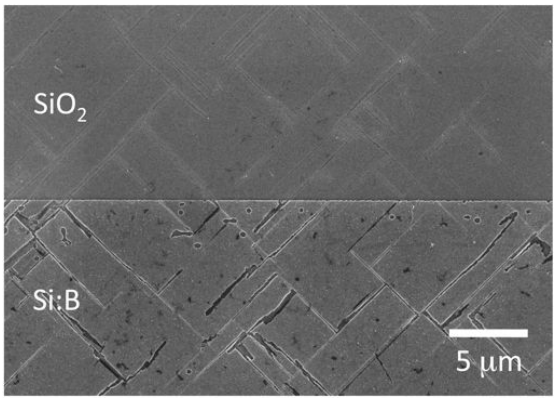

(a) $T_1 = 1,000$ °C

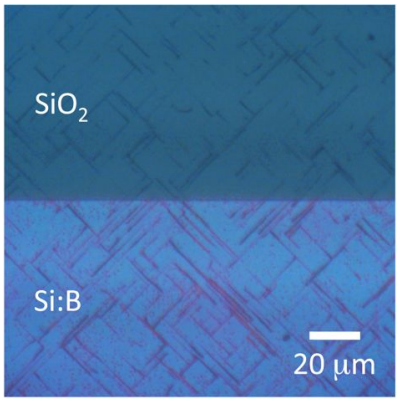

(b) $T_1 = 1,000$ °C

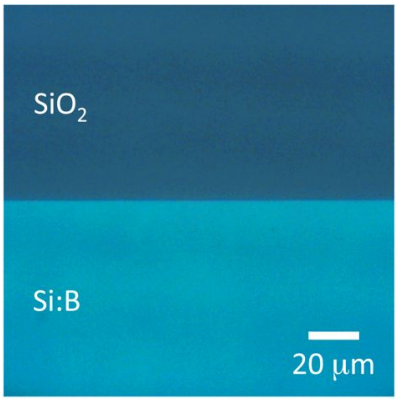

(c) $T_2 = 950$ °C

Figure 4.10.: Planar view SEM (a) and OM micrographs (b,c) of the Si:B and SiO_2 layer after annealing for ~ 10 min at $T_1 = 1,000$ °C (a,b) and $T_2 = 950$ °C (c), respectively. The comparison between the two temperatures reveals the formation of a distinct defect structure in both layers for annealing temperatures $T \gtrsim T_2$.

W/Pt thin-films. The effect of the growth temperature on the structural integrity of the SiO_2 and Si:B layers is shown in Figure 4.10 for two samples, which were annealed in an argon (Ar) atmosphere at $T_1 = 1,000$ °C and $T_2 = 950$ °C, respectively, to simulate the CVD growth. A comparison between the micrographs reveals the formation of severe cracks in the SiO_2 layer along two crystallographic orientations. The Si:B layer sustains the same defect structure as evidenced by the SEM micrograph in Figure 4.10 (a). The cracks in the SiO_2 layer form owing to the rapid cool

down of the sample after the heat treatment as a consequence of the difference in linear thermal expansion coefficients α_L between bulk-Si and SiO_2, which amounts to $\Delta\alpha_L := \alpha_L(\mathrm{Si}) - \alpha_L(\mathrm{SiO_2}) = 2.55\,^{\circ}\mathrm{C}^{-1}$ [Lin10]. For $T \gtrsim T_2$, the Si:B layer recrystallises along the same crystallographic orientations than the cracks in the SiO_2 during the heat treatment in order to minimise the inbuilt strain induced by the cracks in the SiO_2 layer. This temperature coincides well with the sharp increase of the sheet resistance observed for $T \gtrsim 950\,^{\circ}\mathrm{C}$ in our TL measurements (see Figure 4.7 (b)). Since the RIE etching rate is determined by, i.a., the crystallographic orientation of the material to be etched, we expect different RIE etching rates for the samples annealed at $T_1 = 1,000\,^{\circ}\mathrm{C}$ and $T_2 = 950\,^{\circ}\mathrm{C}$, respectively. This difference has indeed been observed in a series of RIE etch tests after the different heat treatments, which supports the interpretation of the Si:B defect structure as a consequence of a recrystallisation process.

A high temperature treatment does also have severe consequences on the nanostructures defined in the Si:B layer. The sample shown in Figure 4.11 (a,b), for instance, was annealed in an Ar atmosphere at $T_2 = 950\,^{\circ}\mathrm{C}$. It does not reveal any cracks, which indicates that their formation is suppressed for $T \lesssim T_2$. The Si:B nanostructures do, however, reveal structural holes, which presumably formed by blasting out small fragments of Si:B during the heat treatment or the subsequent cool down. Reducing the temperature of the CVD growth further to $T_3 = 900\,^{\circ}\mathrm{C}$ results in intact SiO_2 and Si:B layers as evidenced by Figure 4.11 (c,d). Those annealing studies demonstrate that the temperature during the CVD growth as well as the rate of the

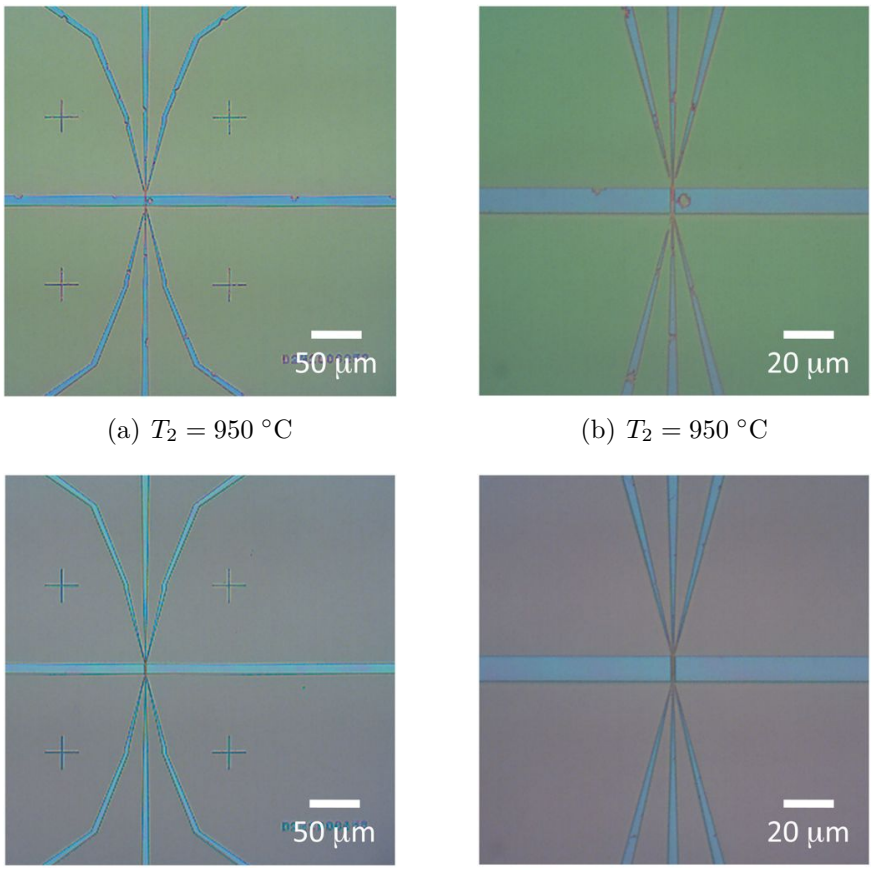

(a) $T_2 = 950\ °C$ (b) $T_2 = 950\ °C$

(c) $T_3 = 900\ °C$ (d) $T_3 = 900\ °C$

Figure 4.11.: OM micrographs showing the effect of two different annealing temperatures on the structural integrity of Si:B nanostructures at two different magnifications. High temperatures $T \gtrsim T_2 = 950\ °C$ lead to the formation of structural holes in the Si:B layer (a,b). A reduction of the annealing temperature to $T_3 = 900\ °C$ precludes the formation of any defect structure (c,d).

subsequent cool down have to be controlled carefully in order to avoid the formation of unfavourable cracks in the SiO_2 and the disintegration of buried Si:B gate structures. The yield of the CNT growth has been observed to be determined by the particular growth temperature as well as the gas mixture and pressure during the CVD growth. The best results were obtained for a growth temperature $T = 850\ °C$ and a continuous unidirectional flow of 170 sccm H_2 and 80 sccm Ar for 20 min,

which was used to vaporise the ethanol precursor gas. Heating up and cooling down was done under a continuous flow of Ar in order to protect the CNTs from oxidation. The cool down rate was set to ~ 8 °C/min. The yield was measured by low-voltage SEM microscopy after the CVD growth and typically amounted to ~ 40 % under those conditions, i.e. 8 out of 20 devices on one chip comprised a single CNT across the buried gate structure.

SEM micrographs of a representative CNT device fabricated with the optimised parameters described above are shown in Figure 4.12 at two different magnifications. Both images show a triple-gate device with a single CVD-grown CNT from the source to the drain electrode. Both micrographs were recorded with a beam current of 1.0 kV to minimise any damage induced by the incident electron beam. The metallic thin-films of the source and drain electrode are partially molten as a consequence of the high-temperature CVD growth. The electrical properties of those devices are discussed below after the introduction of our measurement setup in the following.

4.3. Experimental setup for transport measurements

Since the cool down of a device to cryogenic temperatures is very time consuming, we have developed a special 31-pin sample probe for the high-throughput low-temperature characterisation of semiconductor nanodevices at cryogenic temperatures. Our sample probe fits into a custom made 1.4 K cryostat inside an Oxford Instruments superconducting split-coil magnet with a maximum magnetic field

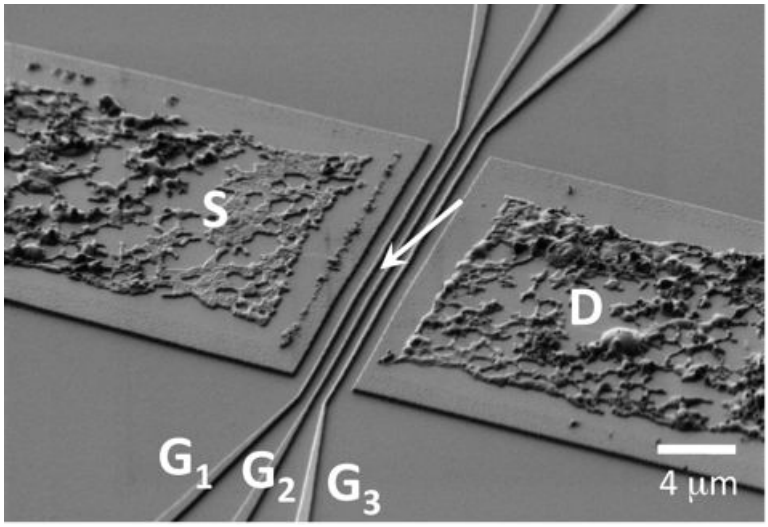

(a) $35,000\times$ magnification

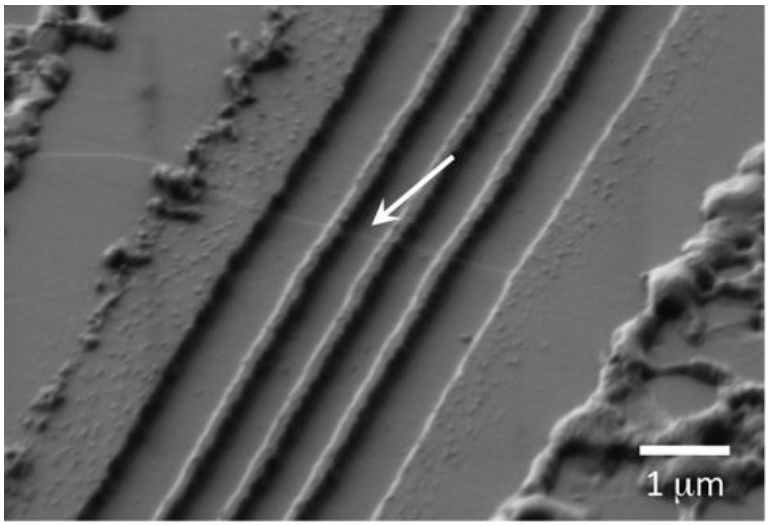

(b) $150,000\times$ magnification

Figure 4.12.: SEM micrographs of a representative nanodevice comprising a single CNT (white arrow) grown from the source (S) to the drain electrode (D) across three buried Si:B gates (G_1, G_2, and G_3) at two different magnifications (a,b).

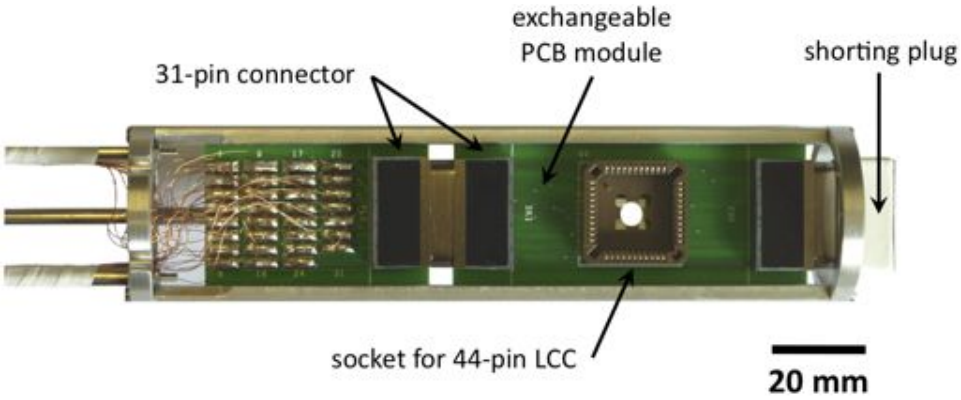

Figure 4.13.: Sample probe used for the characterisation of CNT devices at low temperatures. The device is mounted and wire-bonded into an LCC, which can be plugged into an LCC socket on a PCB module. A shorting plug protects devices against electrostatic discharge during wire-bonding and assembly, and 31-pin connectors facilitate the electrical connection between the module and probe head.

$B_0 = 6$ T and an inner diameter of $\varnothing = 36$ mm. The lower end of this probe is shown in Figure 4.13. The 10×10 mm^2 silicon sample can be mounted and wire-bonded into a commercial 44-pin LCC. This assembly can then be connected to an LCC socket, which facilitates the electrical connection between the sample and a double-sided PCB equipped with two modified Glenair Micro-D 31-pin MWDM-31PCBR connectors at each end. The first connector facilitates the connection between the PCB and the sample probe, whereas the second connector can be used to short all pins together with a shorting plug in order to protect the device against electrostatic discharge during wire-bonding and probe assembly. Since most of the electron transport and spin resonance experiments on CNT QDs and DQDs are performed in the limit where the Zeeman energy $\varepsilon_Z = g\mu_B B_0$ is much larger than the thermal energy $\varepsilon_T = k_B T$, i.e. $g\mu_B B_0 \gg k_B T$, we have designed a special X-band dielectric ring resonator operating in this regime in collaboration with Bruker BioSpin GmbH.

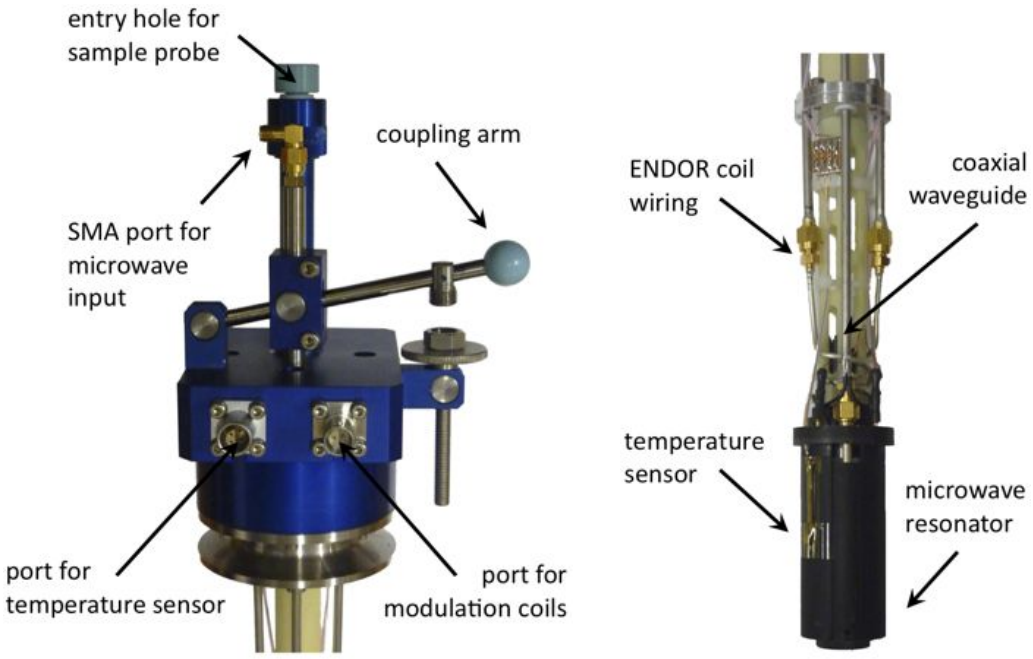

(a) Probe head (b) Probe tip

Figure 4.14.: Optical images of the probe head (a) and tip (b) of the microwave resonator designed for X-band EPR and EDMR at $T \leq 1.4$ K. Please refer to the text for further details.

This sample probe is compatible with our 6 T superconducting magnet and shown in Figure 4.14. The probe head and tip have been adapted from a Bruker ER4118 X-MD-4-W1 electron-nuclear double resonance (ENDOR) cavity. A Lakeshore CX-1030 cernox resistor connected to a LEMO EBC-1S-304-CLL connector can be used to measure the temperature close to the sample. The modulation coils are connected through Huber+Suhner 23-BNO-0-0-2/133-NE, the ENDOR coils through two Elspec JS50141 R20-M coaxial stainless steel cables attached to Huber+Suhner 25-N-50-2-14/133-NE jacks on the backside of the probe head. Its frequency spectrum is shown in Figure 4.15 for two different temperatures. The quality factor Q is given by $Q = f_{mw}/FWHM$ [Poo83], where f_{mw} denotes the eigenfrequency of

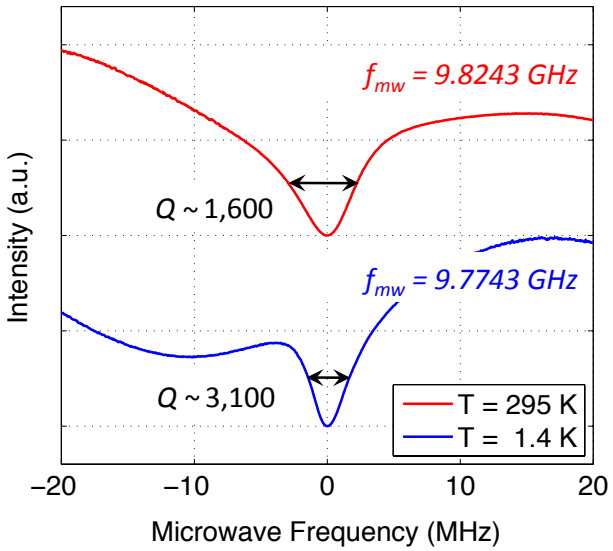

Figure 4.15.: Eigenmode spectra of our X-band microwave cavity at room temperature (red, top) and $T = 1.4$ K (blue, bottom). The resonance frequency f_{mw} and FWHM (black arrows) of each trace are indicated and correspond to a Q-factor of $Q \sim 1,600$ and $\sim 3,100$, respectively. Both traces were normalised and their x-axes offset by f_{mw} for a better comparison.

the cavity and $FWHM$ the full-width-at-half-maximum of the resonance dip. For an empty microwave cavity, it typically amounts to $Q \sim 1,600$ at room temperature and increases to $Q \sim 3,100$ at $T = 1.4$ K, which demonstrates its suitability for low-temperature X-band EPR and EDMR experiments in our superconducting split-coil magnet.

4.4. Room temperature characterisation

Since not every device is suited for low-temperature measurements and wire-bonding into LCCs and both procedures are comparatively time consuming, it is desirable to characterise the devices on a probe station at room temperature for preselection

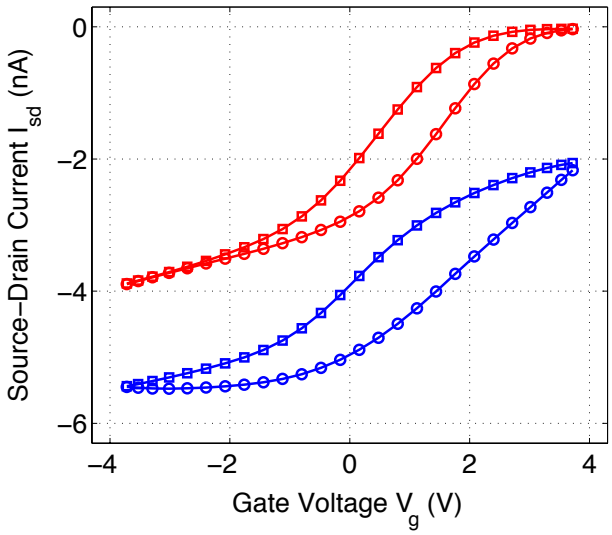

Figure 4.16.: Gate transfer characteristics of a representative CNT device showing the hysteresis of two different gate electrodes (red, blue) for an up- (□) and down-sweep (○). Only every second data point is shown and the two traces at the bottom (blue) offset by $\Delta I_{sd} = -2$ nA for clarity.

first. Measuring the source-drain current I_{sd} through the sample as a function of gate voltage V_g allows us to determine, which device is worth cooling down and whether the respective CNT is semiconducting or metallic. The gate transfer characteristics of a representative device at room temperature biased under ambient conditions with $V_{sd} = 1.0$ V are shown in Figure 4.16 for two different gate electrodes and two sweep directions. Both measurements reveal a field-effect and a pinch off of the source-drain current I_{sd} for $V_g > 3.5$ V. The leakage current of both gate electrodes amounted to less than 30 pA and was below the noise level.

Both gate electrodes reveal a hysteresis between the up- and down-sweep, which has been observed by other groups before and attributed to charge trapping by water molecules around the CNT and SiO_2 surface-bound water proximal to the device

structure [Nyg01, Kim03, Lee07]. The hysteresis-free operation of a suspended CNT FET under ambient conditions in a cleanroom has been demonstrated recently and achieved by a tapered, suspended contact geometry, which avoids the occurrence of hysteresis-inducing oxides [Muo10]. An important measure for the performance of an FET device is its carrier mobility μ, which measures how fast the charge carriers respond to an external electric field. It is generally defined as $\mu = v_d/E$, where v_d denotes the drift velocity of the charge carriers, and E the applied electric field.

The mobility of a semiconductor can generally be measured by two methods: The first one utilises the Hall effect and is called *Hall mobility*, whereas the second method is based on the analysis of the transfer characteristics and referred to as *field-effect mobility*. A Hall measurement is only applicable to two-dimensional systems and is conventionally performed in *van der Pauw geometry*, where four contacts are placed at the circumference of an arbitrarily shaped sample [vdP58]. The mobility of an one-dimensional CNT FETs is accessed through its transfer characteristics and referred to as *field-effect mobility*, which is given by

$$\mu_{FE} = \frac{L}{C_g}\left|\frac{\partial G}{\partial V_g}\right| = \frac{L}{C_g}\frac{1}{V_{sd}}\left|\frac{\partial I_{sd}}{\partial V_g}\right| \qquad \text{with} \qquad C_g = \frac{2\pi\varepsilon_0}{\ln(4t/d)} \tag{4.2}$$

where G denotes the conductance, C_g the gate capacitance per unit length, ε_0 the vacuum permittivity, $t \sim 10$ nm the distance between the gate electrode and CNT, $L = 2$ µm the length and $d \sim 2$ nm the diameter of the CNT – the gate capacitance per unit length amounts to $C_g = 18$ aF/µm under those conditions, which is com-

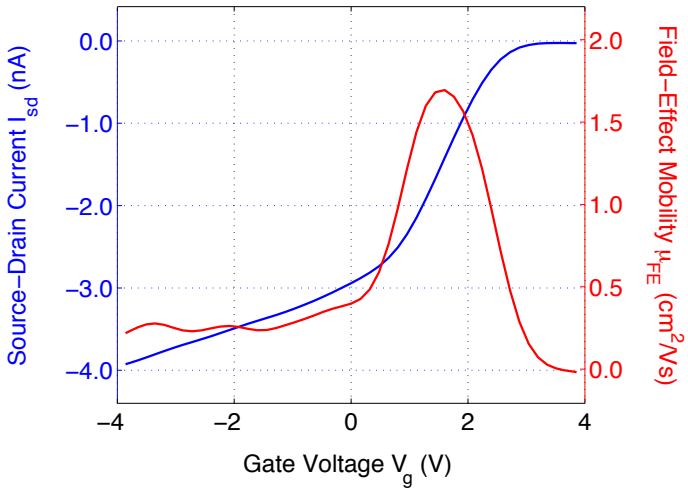

Figure 4.17.: Transfer characteristic (blue) and field-effect mobility μ_{FE} (red) for a representative CNT device. Please refer to the text for further details.

parable to other CNT devices [Bie08]. The transconductance can be derived from Figure 4.16 through differentiation of I_{sd} with respect to V_g and is shown in Figure 4.17 as a function of gate voltage. For $C_g = 18$ aF/µm, the field-effect mobility amounts to $\mu_{FE}^{max} \sim 1.69\,\mathrm{cm}^2/\mathrm{Vs}$, which is much lower than the highest field-effect mobility $\mu_{FE} \sim 79,000\,\mathrm{cm}^2/\mathrm{Vs}$ reported for a back-gated CVD-grown CNT FET on an SOI substrate at room temperature [Dür04]. This may indicate the formation of amorphous carbon along the circumference of the CNT.

Future experiments may therefore involve the optimisation of the CVD growth conditions through changing the growth temperature and H_2 flow, for instance, as well as the low-temperature characterisation of such devices with the cryogenic sample probe developed within this work.

4.5. Conclusions

Our previous discussion has shown that the correlation of electronic, spin, and structural properties is an important prerequisite for CNT-based QIP to become a realistic prospect. The device design proposed in this chapter allows us to control few to single electrons in TEM-compatible and suspended CNT QDs via local gates and to manipulate and detect their spin state via EDMR. The resulting spin relaxation and coherence times can then be correlated to the structural properties of the CNT obtained from TEM analyses.

The transport measurements discussed above demonstrate the practicability of our approach and provide a very promising pathway towards the correlation of electronic, spin, and structural properties as a prerequisite for CNT-based QIP.

CHAPTER 5

Electron spin readout in silicon field-effect transistors

Contents

Chapter 3 has shown that EDMR is a spectroscopic technique, which can be employed as a materials characterisation technique to study defects and impurities in

the solid state. Owing to its high sensitivity, EDMR can also be employed to readout few to single electron spins in semiconductor nanodevices for applications in QIP. In this chapter we employ cwEDMR and pEDMR for the spin readout in ^{28}Si-FETs, in which channel implanted donor electrons can interact with conduction electrons directly. We further demonstrate that EDMR serves as a quantum non-demolition readout of nuclear spins in such devices.

In order to enhance the sensitivity and spectral resolution of this readout scheme, a novel cryogenic sample probe has been developed, which allows us to perform EDMR experiments at high magnetic fields $B_0 \sim 3.36$ T in a resonant microwave cavity with a microwave frequency of $\omega_{mw} \sim 94$ GHz (W-band). Spin resonance signals from the conduction electrons of the 2DEG interacting with neutral donors embedded into the device channel are observed. High-field EDMR is shown to have several experimental advantages over conventional low-field approaches and demonstrated to result in an enhanced EDMR signal intensity, spectral resolution, and signal-to-noise ratio.

A comparison of low- and high-field EDMR experiments on the same device allows us further to identify the underlying mechanism giving rise to the EDMR effect in donor-doped ^{28}Si-FETs. Our observations are in conflict with the models proposed in literature and interpreted in terms of a new EDMR mechanism originating from the polarisation dependent resistivity of the 2DEG.

Selected results of this chapter are published in

[Lan11] V. Lang, C. C. Lo, R. E. George, S. A. Lyon, T. Schenkel, J. Bokor, A. Ardavan, and J. J. L. Morton, *Electrically detected magnetic resonance in a W-band microwave cavity*, Rev. Sci. Instrum. **82**, 034704 (2011). doi:10.1063/1.3557395, and

[Lo11b] C. C. Lo, V. Lang, R. E. George, J. J. L. Morton, A. M. Tyryshkin, S. A. Lyon, J. Bokor, and T. Schenkel, *Electrically detected magnetic resonance of neutral donors interacting with a two-dimensional electron gas*, Phys. Rev. Lett. **106**, 207601 (2011). doi:10.1103/PhysRevLett.106.207601.

5.1. Experimental setup

EDMR and EPR are conventionally carried out at low magnetic fields $B_0 \sim 0.35$ T and low microwave frequencies $\omega_{mw} \sim 9.7$ GHz, which is historically referred to as X-band. For a material system with a gyroscopic ratio of $g \sim 2$, this corresponds to a Zeeman splitting of $\varepsilon_Z \sim 40$ µeV. Hence, the sensitivity of conventional X-band EPR is limited and typically requires at least 10^{10} paramagnetic sites in the sample [Mai97]. Higher sensitivities and spectral resolutions can be achieved by using higher magnetic fields and higher microwave frequencies, as the EPR signal intensity scales with the spin polarisation, and the g-factor resolution with the microwave frequency, linearly. M. W. Bayerl *et al.*, for instance, could resolve two resonance lines in gallium-nitride/manganese (GaN:Mg) films at 34 GHz (Q-band), which could not be separated with conventional X-band EPR spectroscopy [Bay98]. The gain in sensitivity has been demonstrated by D. Schmalbein *et al.*, for instance, who report on the detection of EPR at W-band with a sensitivity of $2 \cdot 10^7$ spins/G$\sqrt{\text{Hz}}$,

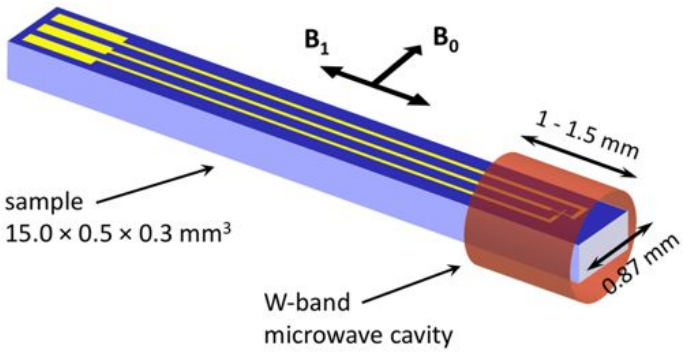

Figure 5.1.: Schematic drawing showing the sample placement inside a W-band EPR microwave cavity. Black arrows indicate the orientations of the static magnetic Zeeman and microwave fields $\mathbf{B_0}$ and $\mathbf{B_1}$, respectively.

which is about 400 times higher than for conventional X-band EPR spectroscopy [Sch99]. High sensitivities and high spectral resolutions are also very desirable for EDMR experiments as they offer the opportunity to selectively address and readout single electron spins electrically in the emerging fields of spintronics and QIP.

5.1.1. High-field EDMR (W-band)

So far, high-field EDMR has been carried out at 7.2 T [Hon78] and 8.5 T on Si:P [Mor08a, Mor08b, McC08] with multi-mode (Fabry-Pérot) cavities only, which require comparatively long pulse duration times of the order of a few hundred nanoseconds for a π-pulse [Mor08b, McC08, McC10]. The sensitivity in those experiments was limited to $\sim 5 \cdot 10^7$ spins in the sample [Mor08b]. The implementation of fast microwave pulses with large excitation bandwidths for the coherent control of electron spins by pEDMR [Boe03] thus remains technologically challenging and has not been achieved at high magnetic fields so far. Single-mode cavities allow us to over-

come those instrumental limitations as they offer fast microwave pulses ($\pi \sim 32$ ns in our system) to achieve large excitation bandwidths. In addition, the distribution of the microwave field in a single-mode cavity is well defined. Hence, the sample can be placed at the position where the magnetic field component is maximal and the electrical field component minimal, which is much more difficult to achieve in multi-mode resonators but essential for the minimisation of microwave-induced rectification noise. Since the half-wavelength of free space microwaves at 94 GHz amounts to $\lambda_{mw} \sim 1.6$ mm, the size of a W-band microwave resonator typically lies within the range of a millimetre as shown in Figure 5.1 schematically. Hence, W-band EDMR experiments require (i) a small sample size, (ii) an optimised geometry and metallisation for reduced microwave absorption, and (iii) an accurate sample placement inside the resonator. The sample probe wiring has to enable the detection of small voltages and currents with a low noise level.

The cryogenic sample probe developed within this work meets those requirements and was designed for use in a commercial Bruker Teraflex EN 600-1021H TE_{011} mode pulsed-ENDOR resonator, which has an inner diameter of $\varnothing = 0.87$ mm and a length of $\ell = 1 - 1.5$ mm depending on the particular tuning condition (see Figure 5.1). Our sample probe facilitates a safe and accurate sample placement inside the microwave cavity and is shown in Figure 5.2. A micrometre screw equipped with a vacuum seal at the probe head (Figure 5.2 (a)) is used to withdraw the fragile sample within the collet (Figure 5.2 (b)) in order to protect it while the probe is inserted into the cryostat. Once the sample probe is aligned against the resonator

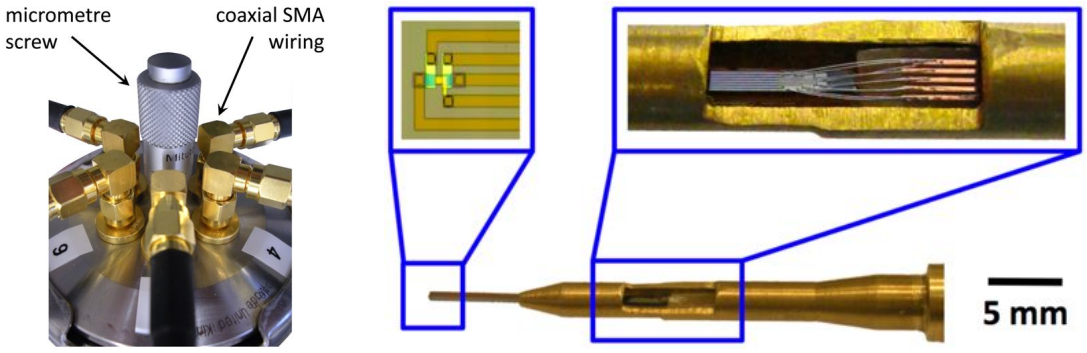

(a) Probe head (b) Probe tip

Figure 5.2.: Optical images of the probe head (a) and tip (b) of the sample probe developed for W-band EDMR. (a) A micrometre screw is used to withdraw, insert, and position the sample inside the cavity accurately, and coaxial SMA wiring inside and outside the sample probe provides isolation against electronic noise. (b) shows a series of optical images of an FET (top-left) being inserted into the brass collet (bottom) used to guide the device into the cylindrical microwave cavity. Aluminum wirebonds connect the device with a PCB and are visible through the window in the sample collet (top-right).

window, the micromanipulator can be used to push the sample out of the collet and to position it inside the resonator with $\sim$ 100 µm precision. The eigenfrequency of the microwave cavity shifts during the sample insertion by typically $\sim$ 200 MHz non-linearly as shown in Figure 5.3 (a). The non-linearity of the frequency shift as a function of insertion length reveals the particular device geometry, such as metallised and doped regions. After the complete insertion of the device into the microwave cavity – typical insertion lengths amount to $\sim$ 1.4 mm – the tuning was optimised by changing the eigenfrequency and coupling arm with two respective micrometre screws at the probe head of the microwave resonator. An optimum tuning condition for cwEDMR is achieved when almost no microwaves are reflected but the energy completely stored in the cavity. The quality factor typically amounts to

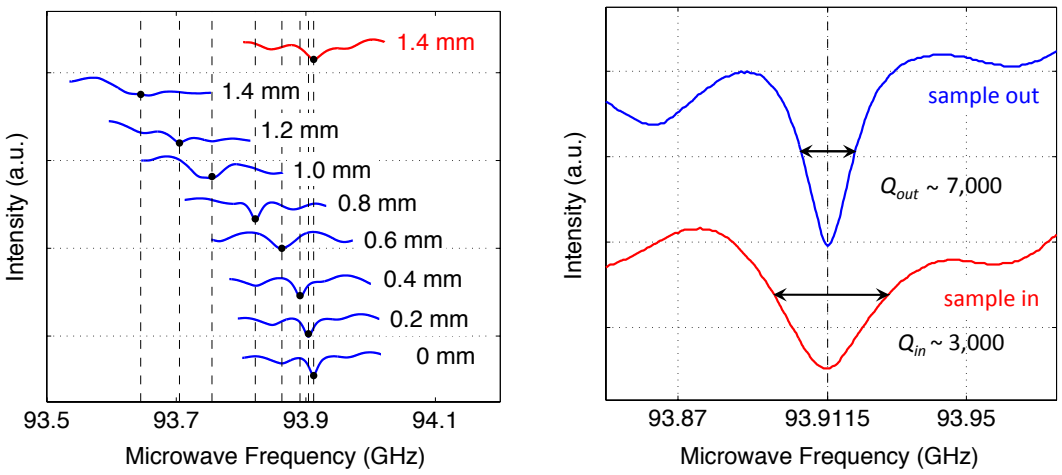

(a) (b)

Figure 5.3.: Tuning conditions of the W-band microwave cavity during sample insertion. (a) shows the shift of the resonator dip (• and dashed vertical lines) for different insertions lengths $0 - 1.4$ mm of a typical FET device inside the microwave cavity (blue). The intensity of the dip is optimised by changing the microwave frequency and coupling upon the complete insertion of the sample (red). (b) compares the cavity dips without (blue) and with the sample (red) after adjusting the cavity volume and coupling. Black arrows indicate the FWHM as a measure for the cavity Q-factor, which decreases upon sample insertion from typically $Q_{out} \sim 7,000$ to $Q_{in} \sim 3,000$ at $T = 5$ K.

$Q_{out} = 7,000$ for an empty cavity and decreases to $Q_{in} = 3,000$ after the insertion of an FET as shown in Figure 5.3 (b). Once the experiment is finished, the sample was withdrawn from the cavity back into the collet, to protect the device from mechanical damage during the extraction of the sample probe from the cryostat. An alternative sample collet machined out of G1040 glass epoxy was used to measure the same sample in a commercial X-band cavity without changing the sample probe and disturbing the microwave field. The dimensions of those two collets are shown in Appendix A. All samples were diced into small chips of $15.0 \times 0.5 \times 0.3$ mm^3 in size, and connected to a double-sided PCB via aluminum wirebonds, which are visible

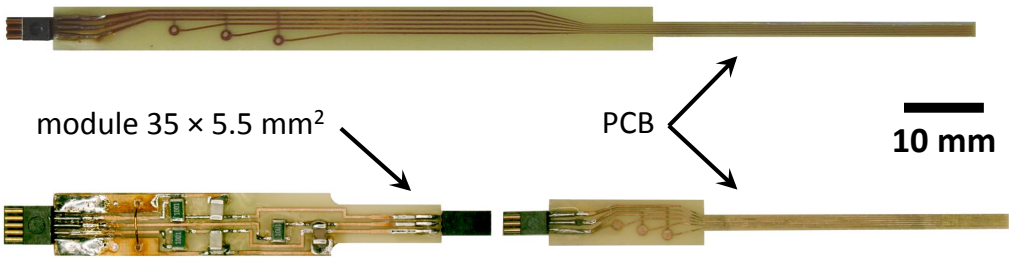

Figure 5.4.: OM images of the PCB used to contact our devices (top). An additional (e.g. filter) module built with surface mount components can be attached to the device if necessary (bottom).

through the window in the brass tip shown in the top-right image of Figure 5.2 (b). This arrangement allows us to contact the active area of the device by metallic layers with a thickness of ~ 0.1 µm below the skin depth of microwaves at $\omega_{mw} = 94$ GHz [Poo83] and to minimise the disturbance of the microwave field in the resonator. The PCB is equipped with a 6-pin Omnetics PZN-06-DD miniature connector at its top end, and its overall length was chosen such that an additional module built with surface mount components can be attached to the device if necessary as shown in Figure 5.4. A thin layer of gold was deposited electrochemically onto the copper tracks at the lower end of the PCBs in order to support wire-bonding. The 6-pin connector facilitates the connection between the PCB and stainless steel coaxial cables (LakeShore CC-SS). The coaxial lines terminate in female vacuum-tight SMA connectors at the probe head. From the capacitance of the coaxial cables used in the probe stick ($C_p \sim 200$ pF), a measurement bandwidth of 10 kHz is expected to be possible with the current set-up for a sample resistance of $R_s \sim 100$ kΩ. All W-band cwEDMR experiments discussed below were performed with a Bruker ElexSys E680 W-band EPR spectrometer and an Oxford Instruments CF-1200 helium-gas

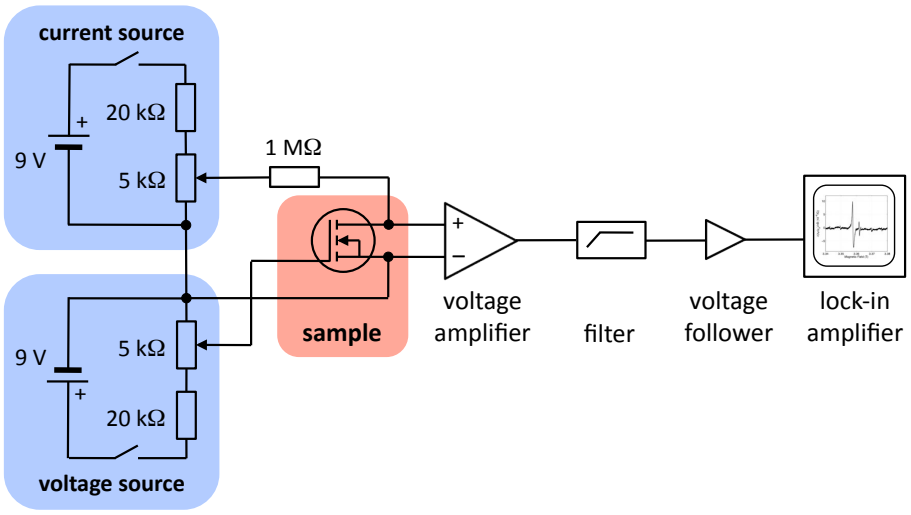

Figure 5.5.: Circuit diagram of the electrical measurement setup used to detect cwEDMR on ^{28}Si-FETs. The device (red) is biased with variable resistor networks (blue) and the modulated voltage drop across the device detected with a voltage amplifier. This signal is fed into a voltage follower through a filter and detected with a lock-in amplifier.

flow cryostat in combination with an Oxford Instruments ITC-503S temperature controller. The DC magnetic field $B_0 \sim 3.36$ T was generated with a Bruker EPR 6T SC superconducting magnet. The measurement temperature was set to $T = 5.0$ K, and the Zeeman field aligned in the plane of the 2DEG, perpendicular to the direction of current flow, i.e. $\mathbf{B_0} \parallel$ 2DEG, unless otherwise indicated. Magnetic field modulation was employed at X- and W-band to enhance the signal-to-noise ratio (see Section 2.3.2). The field modulation amplitude was calibrated with a manganese reference sample and amounted 0.2 mT throughout.

The circuitry used to provide isolation from mains noise and to detect the resonant change of the sample resistivity is shown in Figure 5.5. Battery powered variable resistor networks were used to apply a constant current to the device and to bias

it with a constant gate voltage, typically $V_g = 0.3$ V. The resonant change of the source-drain voltage across the device was detected via a battery powered variable-gain and low-noise voltage amplifier (Femto DLPVA-100-F-D) and a bandpass filter (Princeton Applied Research 5210 lock-in amplifier) tuned to the modulation frequency of $\omega_{mod} = 5.02$ kHz. A voltage follower (OPA TL074CN) facilitated the impedance matching between the circuitry and the lock-in amplifier of the Bruker ElexSys E680 unit, which was used to demodulate and record the cwEDMR signal.

5.1.2. Low-field EDMR (X-band)

X-band EDMR was performed under the same conditions and with the same circuitry with a Bruker ElexSys E680 X-band EPR spectrometer and an Oxford Instruments CF-935 helium-gas flow cryostat. The microwave excitation was applied using a Bruker Flexline ER4118X-MD5-W1 X-band dielectric ring resonator operating at a DC magnetic field $B_0 \sim 0.35$ T and a microwave frequency of $\omega_{mw} \sim 9.7$ GHz.

5.1.3. Device design and basic FET operation

A basic FET consists of a gate, a channel region connecting source and drain electrodes, and an oxide barrier separating the gate from the channel. The FETs investigated in this work were fabricated on 1 µm thick 99.99 % isotopically purified ^{28}Si, grown epitaxially on a high resistivity n-Si substrate. The epitaxial layer was background doped with $3 \cdot 10^{16}$ cm^{-3} phosphorus (^{31}P) donors. The channel was

typically $L = 160$ µm long with a width of $W = 40$ µm, and $t_{ox} = 20$ nm gate oxide thickness throughout. The centre region received an additional implantation of arsenic (^{75}As) donors – the implantation energy amounted to 50 keV with a dose of $4 \cdot 10^{11}$ cm^{-2}. The peak concentration is $\delta = 15 - 30$ nm away from the oxide interface of the device channel, where they can directly interact with the 2DEG electrons. The degenerately doped source and drain regions are formed by phosphorus diffusion, and aluminum was used for forming ohmic contacts. Finally, a silicon dioxide/aluminum stack (1,000/130 nm), acting as a microwave shunt [Lo12], was deposited over the sample in order to minimise any microwave-induced rectification noise, which turned out to be crucial for our EDMR experiments.

Previous studies on similar devices at X-band have shown that the cwEDMR signal intensity decreases with a decreasing channel length of the FET [Lo11a]. This observation has been attributed to spin drift and spin diffusion of electrons from the highly n-doped source-drain regions with a low electron spin polarisation into the device channel with a higher spin polarisation. If the device channel is too short, the injected electrons do not have enough time to thermalise and can therefore not contribute to the EDMR effect, which causes the cwEDMR signal amplitude to decrease. This is why most of the devices studied have a triple-gate geometry for enhancing the spin polarisation of the injected conduction electrons by applying suitable gate voltages to the two additional top-gates. This bias lowers their Fermi energy ε_F and increases their polarisation p_{n+} due to $p_{n+} = g\mu_B B_0 / 2\varepsilon_F$ [Bur90, Kit96]. A schematic of such a triple-gate FET is shown in Figure 5.6 and details

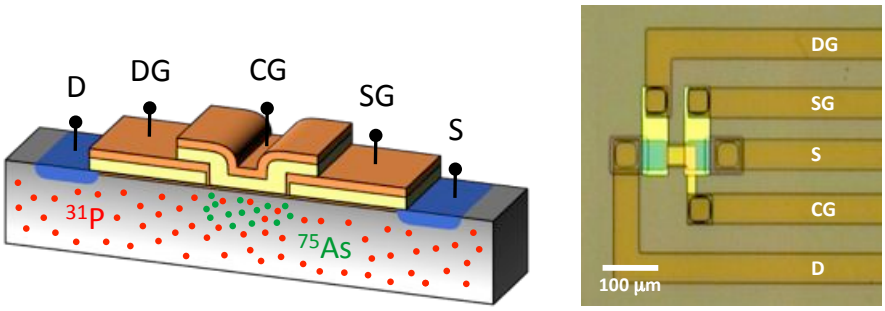

(a) Schematic drawing (b) OM micrograph

Figure 5.6.: Schematic drawing of a triple-gate FET (a). The electron density in the device channel between the source (S) and drain (D) electrodes (blue) can be tuned with three Schottky top-gates DG, CG, and SG (orange). ^{31}P (red) and ^{75}As donors (green) reside in the device channel. (b) shows a respective OM micrograph, in which the different aluminum electrodes are labelled accordingly.

about their fabrication can be found in References [Lo09] and [Lo11a]. For the purpose of this work, all three gates were biased together and the whole device is considered as a simple three-terminal FET. The operation of the device relies on the control of the channel conductivity by the gate voltage V_g, which is applied between the gate and the source. Increasing the gate voltage at a finite source-drain bias V_{sd} induces a 2DEG. This is why one also refers to such devices as *accumulation-mode* FETs (aFETs). As a consequence, the channel becomes conductive above a certain *threshold voltage* V_{th}, which is defined as the gate voltage where a continuous inversion layer forms at the interface between the insulating oxide and the substrate, the so-called *body*. An FET can generally be operated in three different regimes:

(i) *Subthreshold regime*, where $V_g < V_{th}$. In this regime, the device is not turned on and only thermally excited charge carriers contribute to transport.

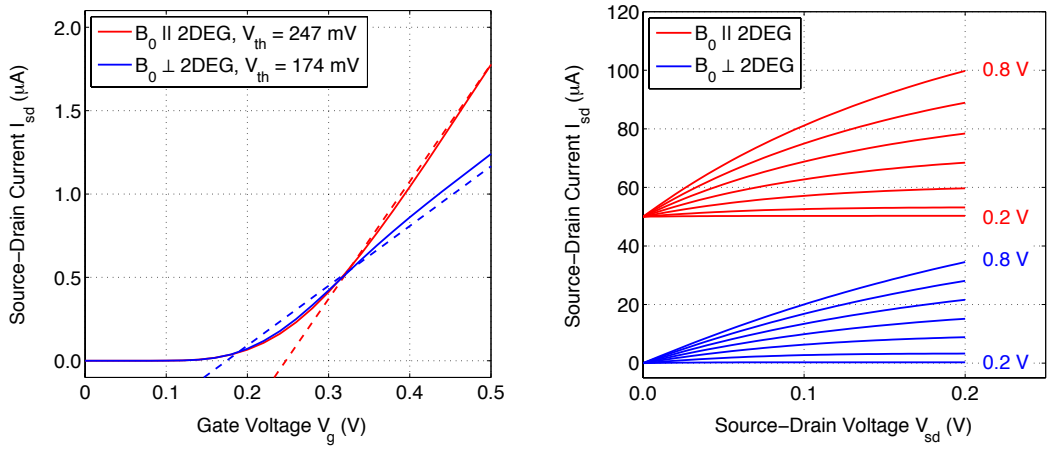

(a) (b)

Figure 5.7.: Transfer characteristics of a representative aFET for two different orientations of the external magnetic field $\mathbf{B_0}$ with respect to the plane of the 2DEG, $\mathbf{B_0} \parallel$ 2DEG (red) and $\mathbf{B_0} \perp$ 2DEG (blue), respectively. (a) shows $I_{sd}(V_g)$ and was used to extract the threshold voltage V_{th} through a linear extrapolation (dashed line) of the asymptotic behaviour of the data (solid line). (b) shows $I_{sd}(V_{sd})$ for different gate voltages $V_g = 0.2, 0.3, ..., 0.8$ V. All traces for $\mathbf{B_0} \parallel$ 2DEG (red) are offset by $\Delta I_{sd} = 50$ μA for clarity.

(ii) *Linear (Ohmic) regime* (or triode mode), where $V_g > V_{th}$ and $V_{sd} < V_g - V_{th}$, and the FET operates like a resistor, controlled by the gate voltage.

(iii) *Saturation regime*, where $V_g > V_{th}$ and $V_{sd} > V_g - V_{th}$. Here, the drain voltage is higher than the gate voltage and the 2DEG spreads out, which causes its density to vary over the 2DEG area.

In order to avoid spatial fluctuations of the electron density, EDMR was always carried out in the linear regime close to saturation. The different regimes are reflected in the transfer characteristics of a typical aFET in Figure 5.7 (a), which shows the source-drain current I_{sd} as a function of gate voltage V_g for two different orientations

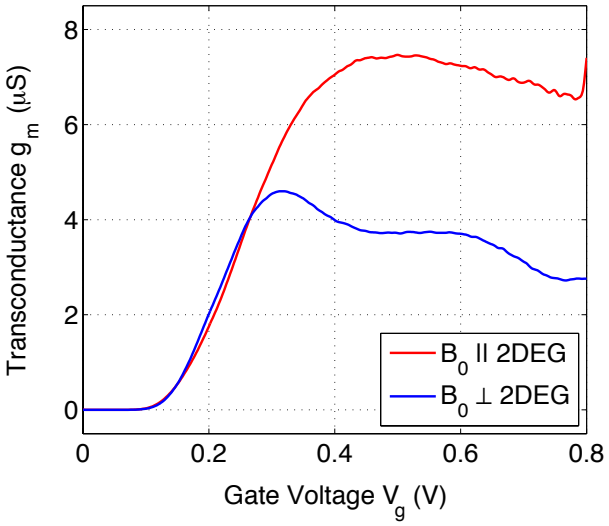

Figure 5.8.: Transconductance of a typical device for two different orientations of the external magnetic field $\mathbf{B_0}$ with respect to the plane of the 2DEG, namely $\mathbf{B_0} \parallel$ 2DEG (red) and $\mathbf{B_0} \perp$ 2DEG (blue). Please refer to the text for further details.

of $\mathbf{B_0}$ with respect to the 2DEG plane. The threshold voltage can be derived from the x-axis intercept of a linear extrapolation of the asymptotic behaviour of $I_{sd}(V_g)$. It amounts to $V_{th} = 247$ mV and $V_{th} = 174$ mV for $\mathbf{B_0} \parallel$ 2DEG and $\mathbf{B_0} \perp$ 2DEG, respectively. For $V_g < V_{th}$, $I_{sd} \sim 0$ and the device operates in the subthreshold regime, while I_{sd} increases for $V_g > V_{th}$ and the device operates in the linear and saturation regime, respectively, as shown in Figure 5.7 (b). The threshold voltage V_{th} allows us to determine the electron density n in the device channel through

$$n = \frac{C_g}{e}\,(V_g - V_{th}) \qquad \text{for} \qquad V_g > V_{th} \tag{5.1}$$

where $C_g = \varepsilon\varepsilon_0/t_{ox}$ denotes the gate insulator capacitance per unit area, $\varepsilon = 3.9$ the relative permittivity of the oxide, and e the elementary charge. Under standard EDMR operating conditions, typical values range from $n = 1 \cdot 10^{11}\,\mathrm{cm}^{-2}$

to $6 \cdot 10^{11}$ cm^{-2}. The field-effect mobility is determined by the transconductance $g_m := \partial I_{sd}/\partial V_g$ of the device shown in Figure 5.8 for $\mathbf{B_0} \parallel$ 2DEG and $\mathbf{B_0} \perp$ 2DEG. For the first orientation, the transconductance $g_m(V_g)$ increases for $V_g > V_{th}$ and reaches its maximum value at $V_g \sim 0.5$ V before it starts to decrease again.[1] The respective measurement for $\mathbf{B_0} \perp$ 2DEG resembles this overall trend, but interestingly reveals an additional oscillatory behaviour for $V_g > 0.3$ V. Since the gate voltage effectively sets the Fermi level of the 2DEG, we interpret these oscillations in terms of degenerated Landau levels[2], which are sequentially populated and depopulated as the gate voltage is increased. The field-effect mobility μ_{FE} is an important measure for the performance of an FET and can be derived from

$$\mu_{FE} = \frac{L}{WC_g}\frac{1}{V_{sd}}\left|\frac{\partial I_{sd}}{\partial V_g}\right| \tag{5.2}$$

similar to Equation (4.2). For $V_{sd} = 10$ mV, typical values amount to $\mu_{FE} = 17,000$ cm^2/Vs and $\mu_{FE} = 10,000$ cm^2/Vs for $\mathbf{B_0} \parallel$ 2DEG and $\mathbf{B_0} \perp$ 2DEG, respectively, under standard EDMR measurement conditions, which is much higher than in the CNT FETs discussed in Chapter 4.

[1] The maximum is due to the mobility dependence on the electric field, which shifts the electron confinement towards the (strained) surface of the aFET channel, where surface roughness scattering causes the field-effect mobility to decrease.

[2] *Landau levels* are quantised cyclotron orbits in a 2DEG $\perp \mathbf{B_0}$ with an energy $\varepsilon_n = \hbar\omega_c(n + 1/2)$, where $\omega_c = eB_0/m^*$ denotes the cyclotron frequency, e the elementary charge, m^* the electron's mass, and $n \in \mathbb{N}_0$ the quantum number of the Landau level. Scattering into these states causes localisation of electrons on cyclotron orbits and reduces the number of free carriers contributing to electron transport – the sample resistivity therefore increases. Increasing the gate voltage shifts the Fermi energy ε_F, and ε_F occasionally coincides with the energy of the n^{th} Landau level, i.e. $\varepsilon_F \simeq \varepsilon_n$. Owing to their thermal energy $\varepsilon_T = k_B T$, electrons can now scatter out of these localised states, which corresponds to a decrease of the sample resistivity. Hence the longitudinal resistivity of the sample oscillates as a function of gate voltage as the Fermi level sequentially passes through the different Landau levels. A more detailed and quantum mechanical description of this so-called *Quantum Hall effect* [vKl80] can be found in [Ilb03], for instance.

5.2. EDMR effect in ^{28}Si-FETs

The setup described in the previous section was used to readout donor nuclear spins in ^{28}Si-aFETs through their interaction with conduction electrons. The cwEDMR spectra obtained are the first derivative of the relative change of the device resistivity with respect to magnetic field, i.e. $\partial(\Delta\rho/\rho_0)/\partial B$, owing to the use of a lock-in detection technique (see Section 2.3.2). A comparison of typical X- and W-band EDMR spectra is shown in Figure 5.9. They reveal three groups of resonance lines: The intense centre line has a Landé g-factor of $g_{\mathrm{2DEG}} = 1.9999$ and is assigned to the 2DEG [Gra99, Sha08b]. The two adjacent lines, split by 4.2 mT and with a centre-of-gravity g-factor of $g_{\mathrm{P}} = 1.9987$ correspond to ^{31}P donors (spin-$^1/_2$) [Feh59a]. The low-field ^{31}P line coincides with the 2DEG resonance at W-band as the difference in g-factors $\Delta g = g_{\mathrm{2DEG}} - g_{\mathrm{P}}$ corresponds to a relative shift of the 2DEG resonance field by $\Delta B = -2.1$ mT at this microwave frequency. Four smaller satellite peaks farther out on both sides are split by 7.1 mT and correspond to the four different nuclear spin projections of ^{75}As donors (spin-$^3/_2$) [Dir90]. Exchange-coupled donor pairs and clusters give rise to a resonance signal at the centre of the hyperfine-split lines [New84], which overlaps with the 2DEG resonance at X-band, and is well separated from the 2DEG signal at W-band. With the spin transitions being saturated, the cwEDMR signal intensity $\Delta\rho/\rho_0$ as defined by Equation (2.10) increases from X- to W-band by a factor of ~ 100 and ~ 20 for the 2DEG and donor lines, respectively. The superior signal amplitudes at W- over X-band improve the signal-to-noise ratio S/N from $S/N = 4:1$ at X- to $8:1$ at W-band for a single scan. The number

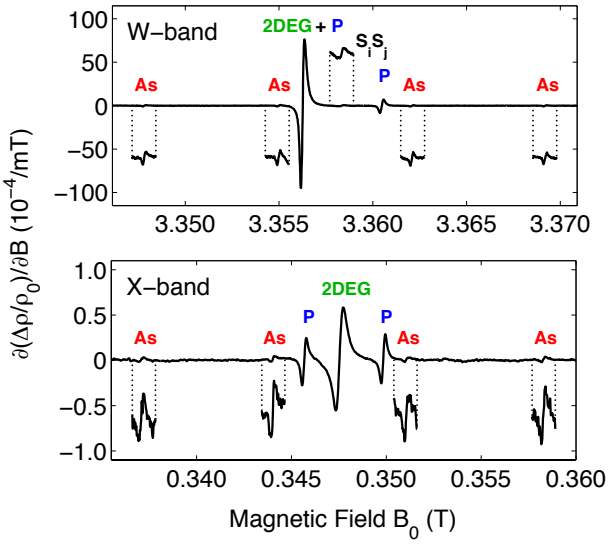

Figure 5.9.: Comparison between W- (top) and X-band EDMR spectra (bottom). The main resonance is due to the 2DEG, the weaker lines are due to ^{31}P and ^{75}As donors, respectively. The resonance line associated with exchange-coupled donor pairs and clusters S_iS_j is well separated from the 2DEG at W-band only. Tenfold zooms are shown for the S_iS_j and ^{75}As lines and offset for clarity.

of arsenic spins detected in this experiment is smaller than $\sim 10^6$, and from the S/N in our W-band measurements, a sensitivity of $2 \cdot 10^4$ spins per hyperfine line should be achievable in a single scan. This is very encouraging as high-field cwEDMR has not been demonstrated for fewer than $\sim 10^9$ spins and a sensitivity better than $5 \cdot 10^7$ so far [Mor08b]. The origin of the EDMR effect in Si-FETs is controversially discussed in literature. Our measurements were carried out in the spin drift and diffusion regime, in the absence of any photoexcited carriers. Hence, a contribution of spin-dependent tunnelling (see Section 2.2.2) and spin-dependent recombination (see Section 2.2.3) can be ruled out as possible spin-to-charge conversion mechanisms. We will therefore only discuss our results in terms of (i) bolometric heating, (ii) spin-dependent scattering, and (iii) a novel polarisation transfer model below.

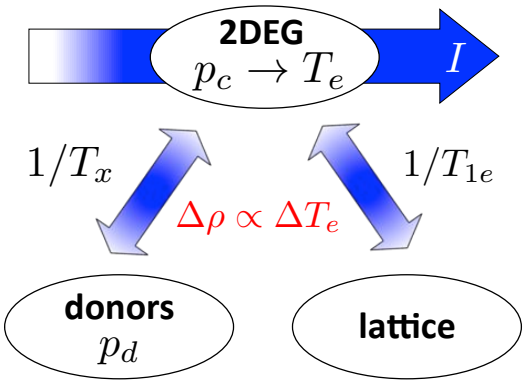

Figure 5.10.: Bolometric heating of a 2DEG occurs through energy transfer from the 2DEG to the donor spins and lattice, mediated by the spin-orbit interaction.

5.2.1. Bolometric heating

Bolometric heating refers to an incoherent response of the 2DEG resistivity due to resonant heating upon microwave absorption. It occurs when the 2DEG orbital electron temperature T_e rises as a result of an increase of the 2DEG spin temperature and thus a resonant decrease of the 2DEG spin density polarisation via spin-orbit coupling [Mor74]. The energy transfer from the 2DEG spins to the lattice occurs through T_{1e} relaxation processes, and from donor spins through T_x flip-flop processes via exchange scattering with the 2DEG as sketched in Figure 5.10. The expected resistivity change $\Delta\rho$ is proportional to the change of T_e, i.e. $\Delta\rho \propto \Delta T_e$. In order to access a possible contribution of bolometric heating to the EDMR effect in Si-FETs, the device resistivity was measured over the temperature range $T = 5 - 12$ K, where acoustic phonon scattering does not contribute to the overall carrier mobility significantly [Kaw82, And82]. Hence, any temperature dependence of the resistivity is a result of changes in T_e only and independent of the lattice

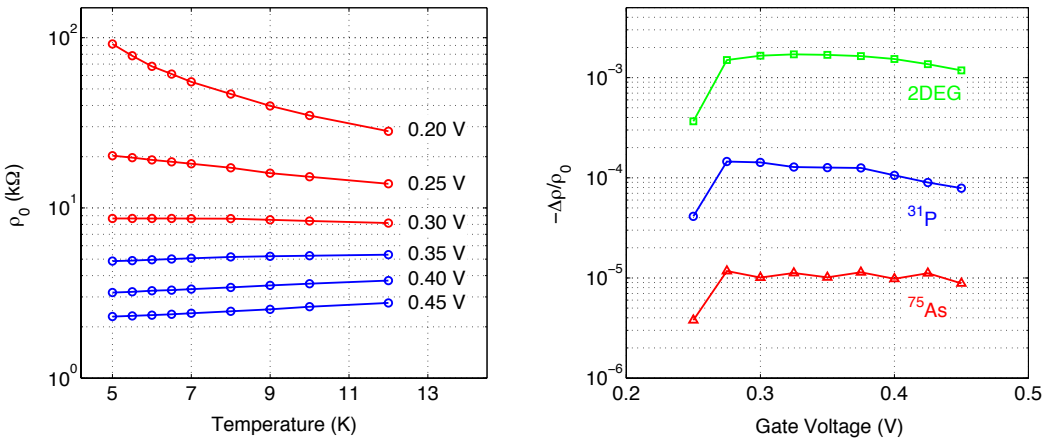

(a) (b)

Figure 5.11.: (a) Temperature dependence of device resistivity for different gate voltages $V_g = 0.20 - 0.45$ V on a semilogarithmic scale. The colouring indicates two transport regimes with different slopes $\partial\rho_0/\partial T < 0$ (red) and > 0 (blue), respectively. (b) shows the gate voltage dependence of the EDMR signal $\Delta\rho/\rho_0$ for the 2DEG (□, green), phosphorus (○, blue), and arsenic (△, red) resonance line on a semilogarithmic scale.

temperature. The results are shown in Figure 5.11 (a) for different gate voltages $V_g = 0.20 - 0.45$ V. They reveal two different transport regimes:

(i) $\partial\rho_0/\partial T < 0$ for $V_g \leq 0.3$ V, the activated transport regime, and

(ii) $\partial\rho_0/\partial T > 0$ for $V_g > 0.3$ V, the metallic regime.

For bolometric heating, one would expect the sign of $\Delta\rho = \rho - \rho_0$ to follow the sign of $\partial\rho_0/\partial T$. The sign of the EDMR signal $\Delta\rho/\rho_0$ should therefore change at around $V_g = 0.3$ V if bolometric heating predominantly contributes to the EDMR effect. This sign was carefully checked for different gate voltages by tracing through phase shifts in the measurements setup and by measuring the DC change in sample resistivity directly on and off resonance as shown in Figure 5.11 (b). The sign of the

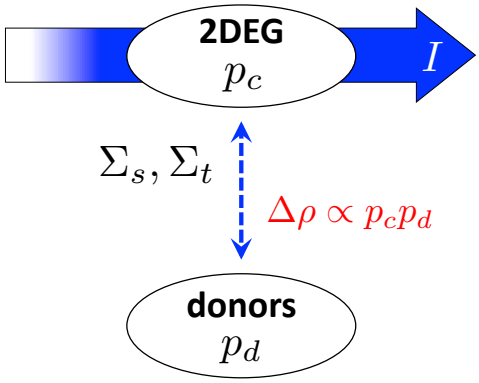

Figure 5.12.: Spin-dependent elastic scattering (dashed line) of conduction off donor electrons arises as a result of a difference in scattering cross sections Σ_s and Σ_t for spin singlets and triplets, respectively.

EDMR signal is negative upon resonance and independent of the gate voltage, i.e. $\Delta\rho/\rho_0 < 0 \; \forall \; V_g$. A predominant contribution of bolometric heating to the EDMR effect in Si-FETs can thus be ruled out.

5.2.2. Spin-dependent scattering

The second mechanism proposed in literature is spin-dependent scattering. This refers to the elastic scattering of conduction off donor electrons as depicted in Figure 5.12 and becomes spin-dependent owing to a difference in scattering cross sections for singlet and triplet pairs as described in Section 2.2.1. Our results cannot be explained in terms of this spin-to-charge conversion mechanism because of the following three reasons: First, according to Equation (2.13), the model proposed for spin-dependent scattering predicts a positive sign for the EDMR signal, i.e. $\Delta\rho/\rho_0 > 0$ as $\Sigma_s > \Sigma_t$ [dSo09], which is in contrast to our observations presented

above.[1] Second, the model requires the 2DEG signal intensity to be equal to the sum of the hyperfine-split donor signal intensities. This can only be the case if other paramagnetic centres, such as DBs (see Section 1.2), also contribute to the 2DEG signal. Such resonance signals were, however, not observed in our experiments. The third reason is given by the scaling of the cwEDMR signal intensity with magnetic field. From the increase in thermal equilibrium polarisations of the 2DEG and donors, $p_c \propto g\mu_B B_0$ and $p_d = \tanh(g\mu_B B_0/k_B T)$, respectively, the spin-dependent scattering signal $\Delta\rho/\rho_0 \propto p_c p_d$ is expected to be enhanced by a factor of ~ 80 at $T = 5$ K from X- to W-band. The comparison in Figure 5.9, however, reveals a stronger enhancement for the 2DEG line, while the enhancement of the donor signals is substantially smaller.

5.2.3. Polarisation transfer model

The contradictions between our experimental data and the two models discussed above motivated the proposal of a third EDMR mechanism, which originates from the polarisation dependent resistivity of the 2DEG [Abr01, Pud02, Oka04] as observed for high mobility 2DEGs in silicon [Gra99, Mat06], for instance. In this picture, donor electrons can transfer their polarisation to 2DEG electrons via exchange scattering as depicted in Figure 5.13. For a more quantitative description we assume that the 2DEG resistivity ρ can be approximated by $\rho = \rho_1 + \rho_2 p_c^2$ [Gra99],

[1] We note note, however, that a refined theoretical calculation taking the full anisotropy of the silicon band structure into account might indeed lead to cases where $\Delta\rho/\rho_0 < 0$ [Kwo91].

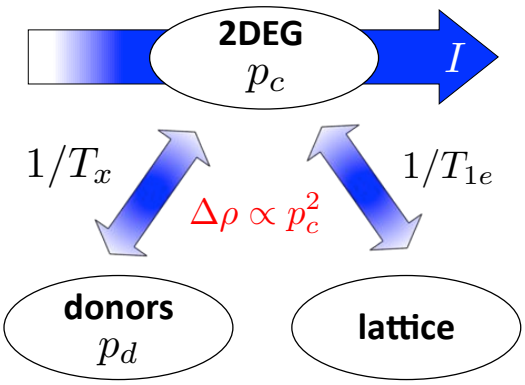

Figure 5.13.: Schematic of the polarisation transfer model proposed to explain the resonant change of the 2DEG resistivity. Please refer to the text for further details.

where $\rho_1 > 0$ and ρ_2 denote the polarisation independent and polarisation dependent components of the resistivity, respectively. With p_{c0} denoting the polarisation of the conduction electrons off resonance, the resonant change of the 2DEG resistivity is

$$\left.\frac{\Delta\rho}{\rho_0}\right|_{\text{2DEG}} = \frac{(\rho_1 + \rho_2 p_c^2) - (\rho_1 + \rho_2 p_{c0}^2)}{(\rho_1 + \rho_2 p_{c0}^2)} = \frac{p_c^2 - p_{c0}^2}{\rho_1/\rho_2 + p_{c0}^2} \quad . \tag{5.3}$$

Under full saturation, i.e. $p_c = 0$, this equation reads

$$\left.\frac{\Delta\rho}{\rho_0}\right|_{\text{2DEG}} = -\frac{p_{c0}^2}{\rho_1/\rho_2 + p_{c0}^2} \approx -p_{c0}^2 \frac{\rho_2}{\rho_1} \quad (\rho_1/\rho_2 \gg p_{c0}^2) \tag{5.4}$$

and the donor EDMR signal is by analogy to Equation (5.3) given by

$$\left.\frac{\Delta\rho}{\rho_0}\right|_{\text{donor}} = \frac{p_d^2 - p_{c0}^2}{\rho_1/\rho_2 + p_{c0}^2} \approx -(p_d^2 - p_{c0}^2)\frac{\rho_2}{\rho_1} \tag{5.5}$$

where p_d denotes the polarisation of the donor electrons on resonance. The in-plane magnetoresistance of a representative device is shown in Figure 5.14. Both traces

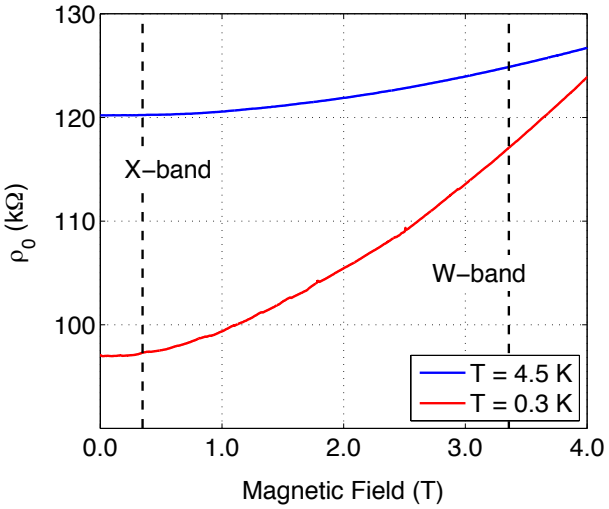

Figure 5.14.: In-plane magnetoresistance of a representative ^{28}Si-FET for two different temperatures $T = 4.5$ K (blue) and 0.3 K (red). Both traces reveal a positive magnetoresistance, i.e. $\partial\rho_0/\partial B > 0$. The magnetic field values of typical X- and W-band EDMR experiments are indicated by two dashed lines.

reveal a positive magnetoresistance $\partial\rho_0/\partial B > 0$, and therefore a positive correlation between the 2DEG resistivity and polarisation [Abr01, Pud02, Oka04], which implies $\rho_2 > 0$. From Equations (5.4) and (5.5) we thus expect the 2DEG and donor EDMR signal to be negative, i.e. $\Delta\rho/\rho_0 < 0$, which was indeed observed in our experiments. If we further estimate that $p_c = g\mu_B B_0 = 1\,\%$ at X-band, we have $\rho_1/\rho_2 = 10$ as $\Delta\rho/\rho_0 \approx -10^{-5}$ (see Figure 5.9, X-band). Since $p_c \propto B_0$, the 2DEG signal should increase by a factor of 100 from X- to W-band in accord with the spectra shown in Figure 5.9. The scaling of the donor signal intensities on the other side depends on the effectiveness of the polarisation transfer from the donor to the 2DEG spin system, which is determined by (i) the spin relaxation rate of the 2DEG T_{1e}^{-1} and (ii) the spin exchange scattering rate T_x^{-1}. The latter varies

from donor to donor depending on its distance to the oxide interface [dSo09].[1] If $T_x^{-1} \ll T_{1e}^{-1}$, the polarisation of the 2DEG electrons p_c returns to its thermal equilibrium rapidly, and the polarisation transfer from the donor to the 2DEG electrons has little effect on p_c and is not very effective. A donor resonance signal should consequently not be observed in this case. In the opposite limit where $T_x^{-1} \gg T_{1e}^{-1}$, p_c and p_d are strongly coupled and indistinguishable. One would therefore expect the 2DEG and donor signal intensities to be equal. Neither of those scaling behaviours were, however, observed in our experiments. Since T_x^{-1} does not change much with magnetic field in the temperature range of our experiments (see Equation (11) in [dSo09]), the different 2DEG and donor signal intensity ratios between W- and X-band can be explained if T_{1e}^{-1} becomes larger at higher magnetic fields as donors with $T_x^{-1} \gtrsim T_{1e}^{-1}$ at X-band will be less effective in changing p_c than at W-band, where $T_x^{-1} < T_{1e}^{-1}$. This implies that only a reduced number of donors can contribute to the donor resonance signal at W-band, which causes the respective signal intensity to drop and explains the observed increase in the 2DEG-to-donor signal intensity ratio. The microwave power dependence of the cwEDMR signals at X- and W-band is shown in Figure 5.15. The data reveals a typical saturation behaviour for all transitions. Power saturation only occurs if the incident microwave power is high enough to populate the excited spin state of the particular spin system faster than it can relax to its equilibrium population through intrinsic spin-lattice relaxation processes [Poo83]. Hence, Figure 5.15 demonstrates that the microwave field B_1

[1] The spin relaxation rate of the donors is assumed to be much smaller than that of the 2DEG, which is consistent with References [Tyr03, Sch06, Sha08b, Sha10].

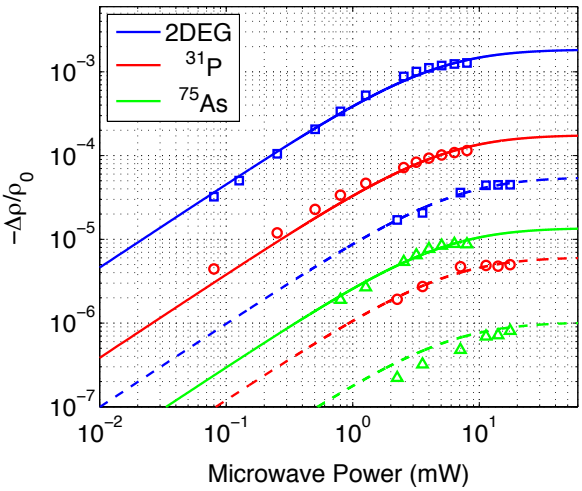

Figure 5.15.: Microwave power dependence of the 2DEG (□, blue), ^{31}P (○, red), and ^{75}As (△, green) signal intensities measured at X- (dashed line) and W-band (solid line). All lines represent numerical best fits to Equation (5.7).

in our X- and W-band cavity is high enough to induce power saturation of all transitions, which is difficult to achieve in non-resonant microwave cavities. From Equation (2.4) we expect

$$p_c = \frac{p_{c0}}{1 + \gamma^2 B_1^2 T_{1e} T_{2e}} =: \frac{p_{c0}}{1 + \beta P_{mw}} \tag{5.6}$$

where $P_{mw} \propto B_1^2$ denotes the absorbed microwave power. As a direct consequence of Equation (5.3) the power dependence of the cwEDMR signal is described by

$$\frac{\Delta\rho}{\rho_0} = \alpha \left[\left(\frac{1}{1 + \beta P_{mw}} \right)^2 - 1 \right] \tag{5.7}$$

with the fit parameters $\alpha, \beta \in \mathbb{R}$. The good agreement between the experimentally observed data and the numerical fits to Equation (5.7) (see Figure 5.15) support the polarisation transfer model.

5.3. Coherent spectroscopy of ^{28}Si-FETs at W-band

The magnetic field dependence of T_{1e}^{-1} has not been measured in the metallic limit of a disordered 2DEG so far. This provides motivation for pEDMR experiments at W-band to investigate the dynamics of the polarisation transfer model. These experiments allow us to verify the polarisation transfer model and to gain further insights into the spin relaxation mechanisms in donor-coupled 2DEGs.

5.3.1. Spin relaxation of 2DEG electrons

Spin relaxation in 2DEGs is due to the spin-orbit interaction and generally discussed in terms of two main mechanisms [Fab99, Žut04]. The first one is referred to as *Elliott-Yafet mechanism* and based on the observation that the momentum eigenstates (Bloch states) are not spin eigenstates in real crystals anymore [Ell54, Yaf63]. The spin degeneracy is lifted by the spin-orbit interaction, which originates from the local electric field induced by the lattice ions. As a consequence, spin relaxation occurs through momentum scattering of electrons and the spin-relaxation rate is directly proportional to the momentum scattering rate $1/\tau_m$, i.e.

$$\frac{1}{T_{1e}^{EY}} = \alpha_{EY} \frac{1}{\tau_m} \tag{5.8}$$

where the Elliott-Yafet coefficient α_{EY} is a measure for the strength of the spin-orbit coupling. The momentum scattering time is determined by the mobility of the

2DEG, which is – according to the *Drude model* [Dru00] – given by

$$\mu = \frac{e\tau_m}{m^*} \tag{5.9}$$

where e denotes the elementary charge and $m^* = 0.19\, m_0$ [And82] the effective mass of the electrons in the crystal. The Elliott-Yafet mechanism has been found to describe the spin relaxation of conduction electrons in bulk-Si for $T > 60$ K very well [Che10] but a complete theoretical description for an MOS 2DEG is, however, still lacking. The second mechanism arises from the lift of the spin degeneracy due to the presence of either an external or in-built electric field and is referred to as *D'yakonov-Perel' mechanism* [Dya71]. Depending on the physical origin of the electric field, one differentiates between the (i) crystal field arising from the lack of a bulk inversion symmetry and (ii) an external electric field, which induces a structural asymmetry. The first one is referred to as *Dresselhaus field* [Dre55] and gives rise to spin relaxation in the III-V heterosystem, for instance. The second one is called *Bychkov-Rashba field* [Byc84] and induced in the plane of a 2DEG by the electric field applied through the gate electrode. The D'yakonov-Perel' mechanism causes the spin-relaxation rate to be inversely proportional to $1/\tau_m$, i.e.

$$\frac{1}{T_{1e}^{DP}} = \alpha_{DP}\tau_m = \alpha_{DP}\frac{\mu m^*}{e} \tag{5.10}$$

with the D'yakonov-Perel' coefficient α_{DP}. In other words, a decrease of the carrier mobility leads to a longer T_{1e}^{DP}, which is opposite to the Elliott-Yafet mech-

anism (see Equation (5.8)) and allows us principally to discriminate the two. A more detailed description of spin relaxation in 2DEGs can be found in [Wu10], for instance. The effective fluctuating magnetic fields arising from the Elliott-Yafet and D'yakonov-Perel' mechanism do have interesting consequences for EPR and EDMR experiments with 2DEGs. If the Zeeman field $\mathbf{B_0}$ is applied along the $\hat{\mathbf{z}}$-direction perpendicular to the plane of the 2DEG, fluctuations of the magnetic field $\overline{\delta B_i^2}$ in $i = \hat{\mathbf{x}}$-, $\hat{\mathbf{y}}$-, and $\hat{\mathbf{z}}$-direction alter T_{1e} and T_{2e} according to [Tyr05]

$$\begin{aligned} \frac{1}{T_{1e}} &= \gamma^2 \left(\overline{\delta B_x^2} + \overline{\delta B_y^2} \right) \frac{\tau_c}{1 + \omega_0^2 \tau_c^2} \\ \frac{1}{T_{2e}} &= \gamma^2 \, \overline{\delta B_z^2} \, \tau_c + \frac{1}{2T_{1e}} \end{aligned} \tag{5.11}$$

where γ denotes the electron gyromagnetic ratio, $\tau_c \sim \tau_m$ the correlation time, and ω_0 the Larmor frequency.[1] Isotropic fluctuations $\overline{\delta B_x^2} = \overline{\delta B_y^2} = \overline{\delta B_z^2}$ therefore imply $T_{1e} \geq T_{2e}$. For a 2DEG confined in the $\hat{\mathbf{z}}$-direction, the in-plane fluctuating fields $\overline{\delta B_x^2}$ and $\overline{\delta B_y^2}$ are generally larger than the out-of plane component $\overline{\delta B_z^2}$ due to Bychkov-Rashba fields and $T_{2e} = 2T_{1e}$ for $\overline{\delta B_z^2} \approx 0$. Hence, a rotation of the Zeeman field into the plane of the 2DEG causes the Bychkov-Rashba field to contribute more to the T_{2e} relaxation process. As a consequence, T_{2e} decreases whereas T_{1e} increases upon the rotation of the Zeeman field from the $\hat{\mathbf{z}}$-direction into the $(\hat{\mathbf{x}}, \hat{\mathbf{y}})$-plane if the D'yakonov-Perel' mechanism dominates the spin relaxation in the system.

[1] Please note that Equation (5.11) only holds in the Redfield limit, where $\gamma \delta B \tau_c \ll 1$, and if the fluctuations along the different axes are uncorrelated.

5.3.2. Spin relaxation of donor electrons

Spin relaxation of isolated donor electrons in bulk crystals arises due to spin-orbit coupling modulated by the electron-phonon interaction [Feh59b, Orb61]. The first measurement of donor electron spin relaxation and dephasing times is reported by A. Honig and J. Combrisson for As donors in Si at $T = 4\,\mathrm{K}$ [Hon56]. Their results were first assigned to nuclear spin relaxation processes [Hon54] but later confirmed to be due to electron spin relaxation. Particularly long spin relaxation times $T_{1d} \sim 1\,\mathrm{h}$ were found for $T \sim 1\,\mathrm{K}$, and attributed to *single-phonon processes* for which $T_{1d}^{-1} \propto T$ [Feh59b]. At slightly higher temperatures, donor electron spins relax owing to *Raman processes*, where phonons scatter inelastically off donor electrons with $T_{1d}^{-1} \propto T^7$ [Cas63]. Higher energy *two-phonon Orbach processes* with $T_{1d}^{-1} \propto e^{-1/T}$ can be observed for $T \gtrsim 5\,\mathrm{K}$ and reduce T_{1d} by many orders of magnitude down to $T_{1d} \sim 1\,\mu\mathrm{s}$ [Cas62, Cas67]. The spin dephasing time of donor electrons T_{2d} in n-Si on the other side is limited by T_{1d} for temperatures $T \gtrsim 10\,\mathrm{K}$ and by spectral diffusion at lower temperatures [dSo03, Tyr03].

The situation for donor electrons interacting with a 2DEG is, however, very different as T_{1d} is now limited by electron scattering in the 2DEG instead. A theoretical model describing the effect of electron scattering in a 2DEG on the spin relaxation time T_{1d} of channel-implanted donors is still lacking. The pEDMR experiments carried out within this work in order to better understand spin-relaxation and dephasing in donor-coupled 2DEGs are discussed below.

5.3.3. Experimental setup and lock-in detection

The RC time constant of our experimental setup amounts to $\tau_{RC} \sim 100$ µs, which corresponds to a cutoff frequency of $\omega_{RC} = 10$ kHz. The timescales associated with the spin dynamics are, however, expected to be much shorter and of the order of 100 ns or 10 MHz $> \omega_{RC}$. Hence, a direct detection of the current transient after a single microwave pulse is not practical. This is why we employed a lock-in technique for our pEDMR experiments, which allows us to detect the fractional change of the current transient after a chain of microwave pulses below the above mentioned cutoff frequency. Very recently, a similar technique has been developed independently and employed to study spin-dependent recombination in Si:P epilayers with pEDMR at X-band [Hoe12]. The underlying principle of our approach is depicted in Figure 5.16. The pulse sequence comprises two half periods ① and ② formed by a chain of $+\pi$- and alternating $\pm\pi/2$-pulses, respectively.[1] Each inversion pulse in ① induces an FID and their sum forms the first half of the lock-in cycle with length $\tau/2$. The second half ② is formed by a series of alternating $\pm\pi/2$-pulses, which do not induce any FID but do keep the net amount of any microwave heating constant over the whole cycle. The sum of both periods ① and ② consequently oscillates with the angular frequency $\omega_{mod} = 2\pi/\tau$ and can be demodulated with a lock-in amplifier tuned to ω_{mod}. This modulation frequency was set to a value lower than the cutoff frequency ω_{RC} in order to overcome the above mentioned limitation of our experimental setup. The demodulated signal corresponds to the sum of current

[1] $\pm\pi$ ($\pm\pi/2$) denotes a π- ($\pi/2$-) pulse around the $\pm x$-axis, i.e. a pulse with $\mathbf{B_1} \parallel \pm\hat{\mathbf{x}}$.

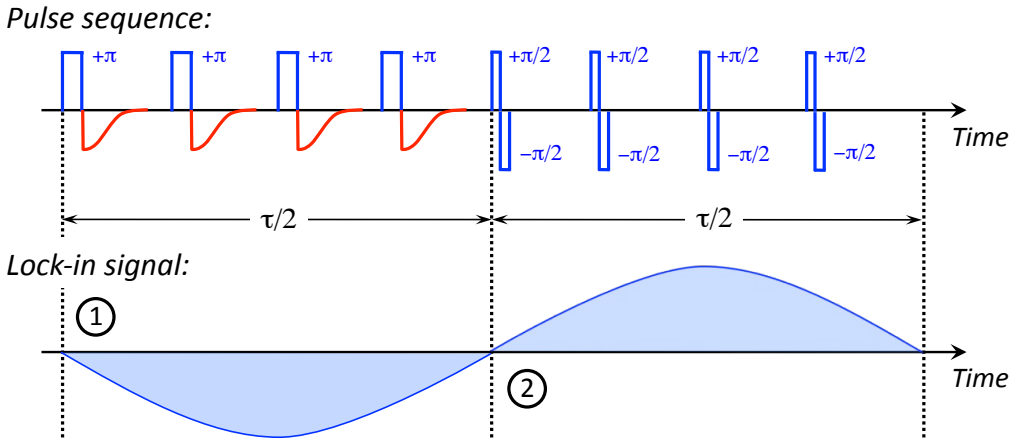

Figure 5.16.: Schematic drawing of the lock-in technique employed for our pEDMR experiments to overcome the limitation given by the RC time constant of our experimental setup. Please refer to the text for further details.

transients and contains the dynamic information about the coherent spin motion. All experiments were carried out on a modified Bruker ElexSys E680 spectrometer and in a Bruker TeraFlex EN 600-1021H pENDOR resonator at $T = 5$ K as described in Section 5.1.1. The square wave reference signal used for the lock-in detection was generated with a HP 33120A function generator ($\omega_{mod} = 5.02$ kHz, peak-to-peak voltage $V_{pp} = 100$ mV) and used to trigger the pulse shaping unit (Bruker PatternJet™) as well as a Princeton 5210 lock-in amplifier used to demodulate the signal. The demodulated output of this lock-in amplifier was fed into the DC input of the software-driven Bruker SpecJet2™, which was used to digitise and process the signal. The 2DEG plane was oriented parallel to the external magnetic field, i.e. 2DEG $\parallel \mathbf{B_0}$, in all experiments described below if not otherwise indicated. The sample was biased with a Keithley 4200 Semiconductor Characterization System at a constant source-drain voltage of typically $V_{sd} = 40$ mV and a gate voltage of $V_g = 300$ mV, which corresponds to a source-drain current of $I_{sd} = 1.5$ µA. The

pulse sequences used to induce coherent spin motion and measure the relevant spin relaxation and decoherence times are based on the pEPR sequences compiled in Table 2.1 and depicted in Figure 5.17. Phase cycling of the readout and preparation pulses generates the oscillating lock-in signal and removes any unwanted FIDs and avoids any microwave heating.

5.3.4. Rabi oscillations and echo formation

In order to measure the length t_π^0 of an ideal π-pulse, we induced Rabi oscillations of the 2DEG conduction electrons with the pulse sequence depicted in Figure 5.17 (a) first. This sequence comprises a preparation pulse of length t_ϑ followed by two phase cycled $\pi/2$-readout pulses with a length of $t_{\pi/2}^{exp} = 52$ ns each. The results are shown in Figure 5.18 for three different microwave powers $P_1 > P_2 > P_3$.[1] The asymmetric shape of the Rabi oscillations is a consequence of the EDMR detection technique, which only measures the z-component of the magnetisation. It was simulated by calculating the time evolution of the density matrix for an ensemble of non-interacting 2DEG electrons subject to the pulse train described above. Details of this simulation are given in Appendix B. The Rabi oscillations in Figure 5.18 show that the magnetisation is inverted after $t_\vartheta = 240$ ns, which corresponds to the length of an ideal π-pulse $t_\pi^0 := 240$ ns. The optimum length for a $\pi/2$- (preparation or readout) pulse is therefore $t_{\pi/2}^0 = t_\pi^0/2 = 120$ ns. This pulse length is by a

[1] A calibration of the respective microwave powers based on our measurements is not possible as the microwave power can only be set on an unknown highly non-linear scale on our spectrometer.

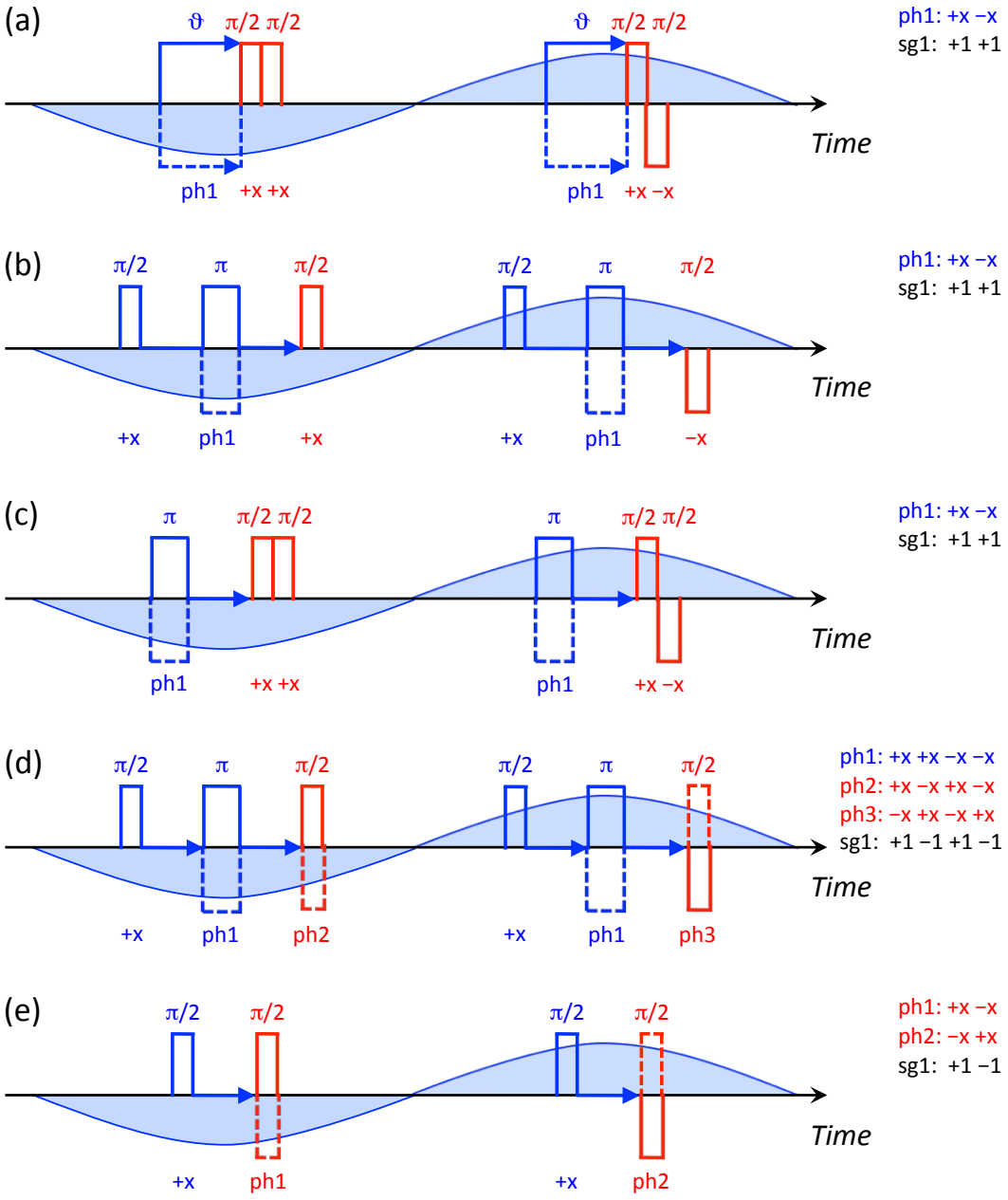

Figure 5.17.: Schematic drawings of the pulse sequences used to induce Rabi oscillations (a), recording the formation of the echo in the time domain (b) as well as for measuring T_1 (c), T_2 (d), and T_2^* (e). All readout pulses (red) were phase cycled (solid, dashed) in order to implement the lock-in detection as indicated by the shaded regions (blue). The preparation pulses (blue) were phase cycled additionally in order to remove any FIDs and unwanted echoes, and to avoid microwave heating. All phases are indicated and labelled '± x', 'ph1', 'ph2', and 'ph3'. The times varied during the experiment (pulse length or delay) are highlighted with blue arrows. The resulting echoes were multiplied with 'sg1' prior to their summation to correct for the alternating sign of the echo in each phase cycle.

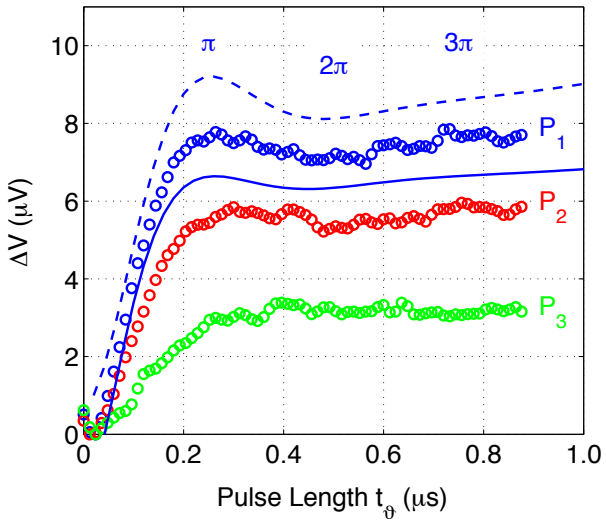

Figure 5.18.: Rabi oscillations of conduction electrons as function of the length of the preparation pulse t_ϑ for three different microwave powers $P_1 > P_2 > P_3$ (○, blue, red, and green). All traces were averaged over 10 scans and only one third of the data points is shown for clarity. The solid and dashed lines represent simulations of Rabi oscillations for the microwave power P_1 and with $t^{sim}_{\pi/2} = t^0_{\pi/2}$ (dashed, blue) and $t^{sim}_{\pi/2} = t^{exp}_{\pi/2}$ (solid, blue) long $\pi/2$ preparation pulses, respectively, and have been offset by $\pm$ 1 μV for clarity.

factor of about two longer than $t^{exp}_{\pi/2}$ used in our experiments, which explains the different amplitudes of the experimentally observed and simulated Rabi oscillations with $t^{sim}_{\pi/2} = t^0_{\pi/2}$. An unambiguous proof of their origin can generally be provided by plotting the oscillation frequency as a function of microwave power and fitting it to Equation (2.21). The very fast decay of the Rabi oscillations observed in our experiments indicates a comparatively short T^*_{2e} and does not allow us to reliably extract the respective Rabi frequencies. The simulation with a nominal $\pi/2$-pulse of length $t^{sim}_{\pi/2} = t^{exp}_{\pi/2} < t^0_{\pi/2}$ does, however, agree very well with our experimental data, which supports their interpretation in terms of Rabi oscillations. Furthermore, using a pulse length $t^{exp}_{\pi/2} < t^0_{\pi/2}$ for the subsequent experiments is very desirable owing to

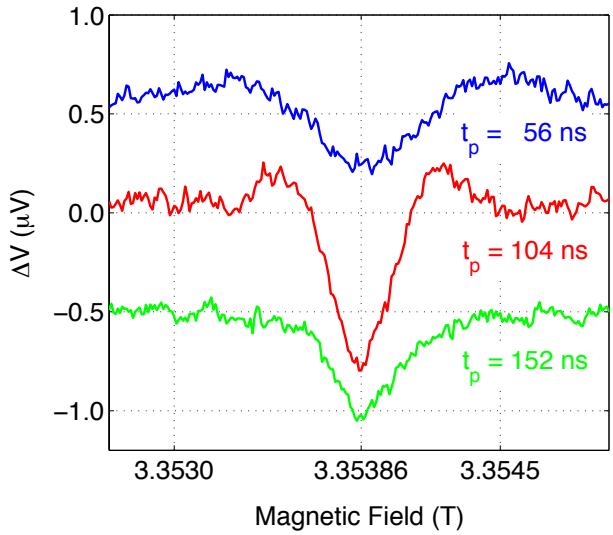

Figure 5.19.: Echo detected field sweep after a microwave pulse with different pulse lengths $t_p = 56, 104, 152$ ns. The maximum signal intensity is observed for $t_p = 104$ ns (red). The respective area under the signal is by a factor of $\sim \sqrt{2}$ larger than for the signal recorded with $t_p = 56$ ns. The top and bottom trace were offset by $\pm\, 0.5$ μV for clarity.

the limited duty cycle of our TWT amplifier, which is defined as the ratio between the average and maximum microwave power of a given pulse train and amounts to ~ 1 %. Figure 5.19, for example, shows echo detected field sweeps for different pulse lengths t_p. The maximum signal intensity is observed for a pulse length of $t_p = 104$ ns, which is consistent with the length $t^0_{\pi/2} = 120$ ns of an ideal $\pi/2$-pulse derived from the Rabi oscillations in Figure 5.18. Halving the pulse length results in a decrease of the signal intensity by a factor of $\sim \sqrt{2}$. On the other hand, the signal intensity is expected to increase linearly with the number of lock-in cycles, which can be doubled when halving the pulse length without changing the duty cycle of the respective pulse train. This is why we intentionally shortened the pulse length in the following experiments and employed $t^{exp}_{\pi/2} = 52$ ns instead of $t^0_{\pi/2} = 120$ ns

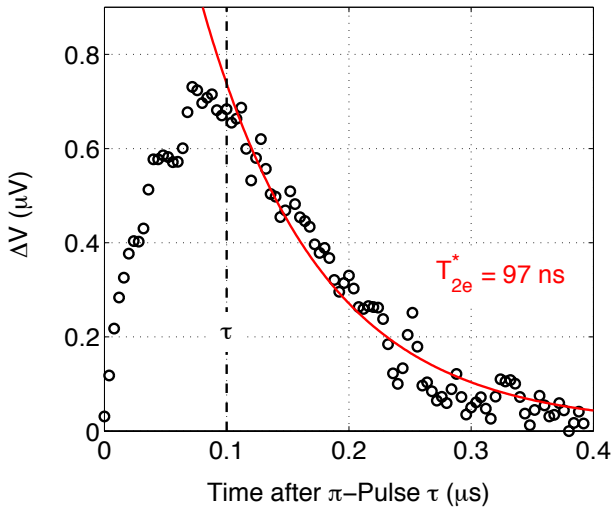

Figure 5.20.: Echo formation in the time domain averaged over 50 scans. The echo forms at $\tau = 100$ ns (dashed line, black) after the inversion pulse. Its decay is determined by the spin dephasing time $T_{2e}^{*} = 97$ ns as indicated by the fit of the data (○, black) to a simple mono-exponential (red).

long $\pi/2$-pulses. This choice is a reasonable tradeoff between the reduced signal intensity due to imperfect microwave pulses and the doubling of the total number of pulses in one duty cycle as the signal intensity is expected to increase by a factor of $\sim 2/\sqrt{2}$ under those conditions. The formation of the echo in the time domain was recorded with the pulse sequence depicted in Figure 5.17 (b) and is shown in Figure 5.20. As expected, the echo forms at $\tau = 100$ ns after the readout pulse, which corresponds to the delay between the two pulses at the end of the sequence. The shape of the echo is distorted by the FID induced by the first preparation pulse. An increase of the pulse length to $t_{\pi/2}^{exp} = t_{\pi/2}^{0}$ is therefore expected to result in an entirely symmetric echo. Its decay is well described by a mono-exponential decay with the decay constant $T_{2e}^{*} = 97$ ns.

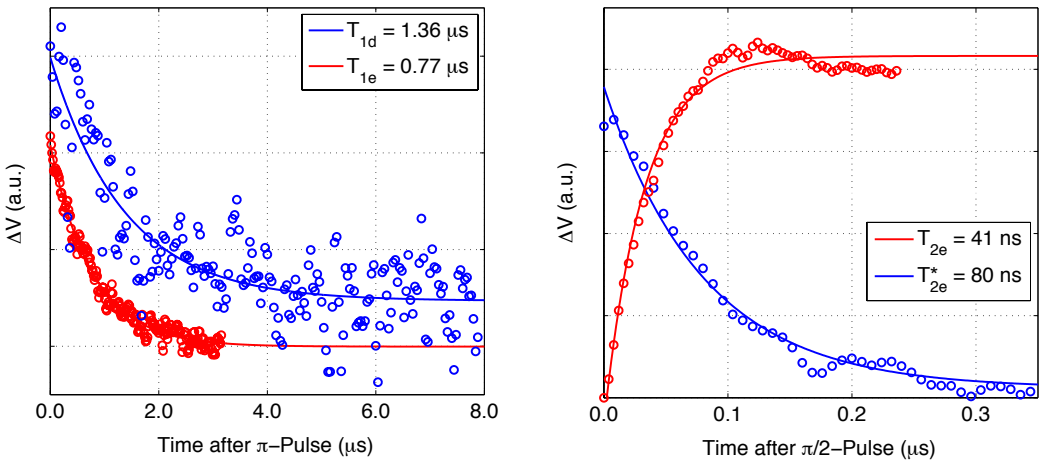

(a) Spin relaxation times

(b) Spin dephasing times

Figure 5.21.: Measurement of the spin relaxation (a) and dephasing times (b). T_{1e} (red) and T_{1d} (blue) were averaged over 5 and 20 scans, respectively, normalised, and offset for clarity. The T_{2e} and T_{2e}^{*} measurements shown in (b) were averaged over 5 scans. Solid lines represent numercial best fits to mono-exponentials.

5.3.5. Spin relaxation in donor-coupled 2DEGs

Further to the formation of the echo in the time domain we measured the spin relaxation time of the 2DEG and donor electrons with the pulse sequence depicted in Figure 5.17 (c) – the signal associated with the channel-implanted ^{75}As donors was too small to be measured with a reasonable amount of averages and has therefore not been investigated via pEDMR in this work. The resulting mono-exponential decays for the 2DEG and ^{31}P donor electrons are shown in Figure 5.21 (a). Both traces are well described by mono-exponential decays with the decay constants $T_{1e} = 0.77$ µs for the 2DEG and $T_{1d} = 1.36$ µs for the donor electron spin, respectively. T_{1d} is expected to increase with an increasing distance δ between the 2DEG and the interacting ^{31}P donors. The respective decay observed for ΔV in Figure 5.21 (a) is

therefore expected to be described by a weighted sum of mono-exponential decays with different time constants similar to the expression

$$\Delta V(t) \sim \int_0^\infty \mathrm{d}\delta \; \rho(\delta) e^{-t/T_{1d}(\delta)} \tag{5.12}$$

where $\rho(\delta)$ is a convolution of the donor distribution and an (exponential) function describing how effective implanted donors at different depths δ do contribute to the EDMR signal. We are, however, unaware of any theoretical model describing $\rho(\delta)$ and $T_{1d}(\delta)$, which is why we fit our experimental data to a simple mono-exponential decay with the decay constant $T_{1d} = 1.36$ µs.

$T_{1d} > T_{1e}$ is consistent with the polarisation transfer model as the polarisation of the donor electrons would otherwise decay away before being transferred to the 2DEG electrons – cwEDMR spectra should therefore not reveal any donor resonances if $T_{1d} < T_{1e}$, which is in contrast to our observations. The dephasing times $T_{2e,d}$ and $T^*_{2e,d}$ were measured with the pulse sequences depicted in Figure 5.17 (d) and (e), respectively. The results are shown in Figure 5.21 (b) for the 2DEG electrons exemplarily and reveal $T_{2e} = 41$ ns and $T^*_{2e} = 80$ ns, which is consistent with the decay constant extracted from Figure 5.20. Analogous experiments for the ^{31}P donor electrons reveal $T_{2d} = 80$ ns and $T^*_{2d} = 28$ ns. T_{1e} and T_{2e} were further observed to decrease upon the rotation of the plane of the 2DEG with respect to the external magnetic field $\mathbf{B_0}$ and amount to $T_{1e} = 0.39$ µs and $T_{2e} = 43$ ns, respectively, for 2DEG $\perp \mathbf{B_0}$, which is discussed in the following.

5.4. Conclusions

The spin relaxation and dephasing times observed for 2DEG and ^{31}P donor electrons in our pEDMR experiments are compiled in Table 5.1. For 2DEG $\parallel \mathbf{B_0}$, T_{1e} was found to amount to $T_{1e} = 0.77$ µs. The transconductance of this device is shown

	$\mathbf{T_1}$ (µs)	$\mathbf{T_2}$ (ns)	$\mathbf{T_2^*}$ (ns)
2DEG	0.77 (0.39)	41 (43)	80
^{31}P	1.36	80	28

Table 5.1.: Comparison of the spin relaxation and dephasing times of conduction and ^{31}P donor electrons in ^{28}Si-FETs measured via pEDMR with 2DEG $\parallel \mathbf{B_0}$. Parenthesised values were recorded with 2DEG $\perp \mathbf{B_0}$.

in Figure 5.8 and corresponds to a field-effect mobility of $\mu_{FE} = 17,000$ cm^2/Vs, which corresponds to a momentum scattering time of $\tau_m = 1.84$ ps according to Equation (5.9). Z. Wilamowski and W. Jantsch estimated the Elliott-Yafet coefficient for a 2DEG confined in a Si/SiGe heterostructure with a similar mobility to amount to $\alpha_{EY} \leq 2.4 \cdot 10^{-6}$ [Wil04]. From Equation (5.8) we therefore expect a spin relaxation time of $T_{1e}^{EY} = 0.76$ µs assuming that the spin-orbit coupling strength in Si/SiGe is of the same order of magnitude than in ^{28}Si-FETs. This value coincides very well with the spin relaxation time observed for the 2DEG electrons in our pEDMR experiments. Since the momentum scattering time is expected to be inversely proportional to the 2DEG density n – electrons will scatter less when their density is reduced – Equation (5.8) further implies $T_{1e}^{EY} \propto n^{-1}$, which has indeed been observed in the experiments shown in Figure 5.22. This analysis indicates

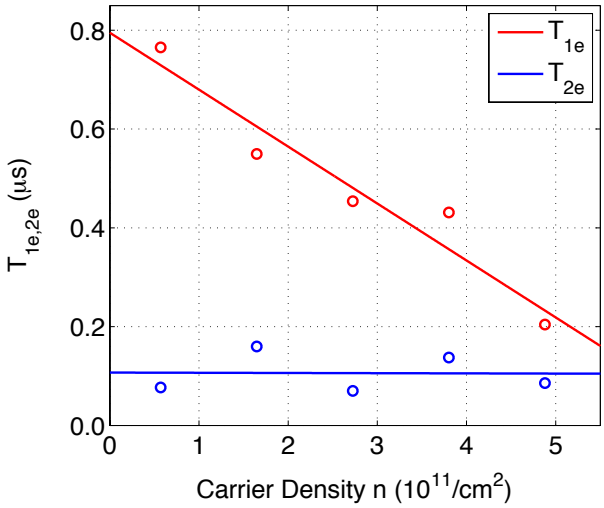

Figure 5.22.: Carrier density dependence of the electron spin relaxation (red) and dephasing time (blue). T_{1e} decreases with increasing carrier density n, whereas T_{2e} remains nearly constant. n was derived from Equation (5.1), solid lines represent linear fits to the data (○).

that the Elliott-Yafet mechanism is the predominant process giving rise to electron spin relaxation in 2DEGs $\| \mathbf{B_0}$. The angular dependence of T_{1e} and T_{2e} shown in Table 5.1 can, however, not be explained by this process. Based on the two data points recorded for 2DEG $\| \mathbf{B_0}$ and 2DEG $\perp \mathbf{B_0}$, an explanation in terms of the D'yakonov-Perel' mechanism is also unlikely to succeed as one would expect T_{1e} to increase and T_{2e} to decrease upon the rotation of the Zeeman field, which is in contradiction to our experimental observations.

A conclusive understanding of the electron and donor spin relaxation dynamics in donor-doped Si-FETs does therefore require further W-band pEDMR experiments based on the lock-in detection technique developed within this work. Those experiments may involve detailed studies of the gate and angular dependence of $T_{1e,d}$ and $T_{2e,d}$ as well as a comparison to analogous experiments at X-band.

CHAPTER 6

Conclusions

Chapter 1 has shown that there has been tremendous progress towards the control of few to single electron spins and the nanoscopic characterisation of paramagnetic centres in the solid state over the past few years. This has been rendered possible by (i) successive refinements of the experimental setups used for spin detection and the (ii) development of novel device architectures, such as QDs and FETs, which allow us to spatially confine individual electron spins. Particularly important in the context of instrumental advances has been the combination of conventional EPR with an electrical detection scheme. This technique became known as EDMR and utilises spin-to-charge conversion mechanisms governed by spin-selection rules rather than the direct detection of the sample's microwave absorption. Hence, the information about the spin state of an electron is no longer associated with the

Zeeman energy $\varepsilon_Z \sim 40$ μeV but rather with the Coulomb energy $\varepsilon_C \sim 1$ eV, which is much larger than ε_Z and leads to an up to 10^7 times higher sensitivity of EDMR than conventional EPR. The aim of this thesis was to utilise this gain in sensitivity and to employ EDMR to study recombination centres in photovoltaic materials and to readout electron spins in carbon and silicon nanodevices for applications in QIP.

After a brief introduction of EPR and EDMR in Chapter 2, I studied *spin-dependent recombination* in Cz-Si with and without strained OPs as well as in amorphous hydrogenated silicon in Chapter 3. Strained OPs are square-shaped platelets and were intentionally grown in inactive regions of Cz-Si wafers in a process called *internal gettering* to act as sinks for detrimental metallic impurities. The angular dependence of the EDMR spectra obtained from those materials in this work demonstrates that OPs are associated with P_{b0} and P_{b1} DBs. Our EDMR experiments further provide evidence that interstitial iron and iron-boron, two of the most common and detrimental metallic impurities in Cz-Si, do also contribute to spin-dependent recombination in this photovoltaic material. A detailed analysis of the electronic recombination time on a series of samples containing different concentrations of OPs revealed further that those recombination centres form at the Si/SiO_2 interfaces at the sample surface and at the corners of strained OPs. An analogous analysis of the electronic recombination time of the FeB pair demonstrates that this impurity is a particularly active recombination centre. In the second half of Chapter 3, I presented a technical extension of our EDMR spectrometer, which has allowed us to perform pEDMR experiments on different materials. Its performance was demonstrated with an a-Si:H

reference sample revealing a very large EDMR signal. The results were shown to be consistent with literature, which demonstrates the suitability of our instrumental refinement. Future experiments may involve pEDMR experiments on Cz-Si with strained OPs and aim to relate the electronic recombination with spin relaxation times associated with oxide- and iron-related defects and impurities. Our results are a prerequisite for the optimisation of internal gettering in Cz-Si wafers used for ICs and photovoltaic applications.

In Chapter 4, I proposed and fabricated a CNT device which was designed to permit the relation of structural properties obtained from TEM with electrical and spin properties obtained from electron transport and EDMR measurements. It comprises a CVD-grown CNT suspended over a buried gate structure on an SOI substrate, which facilitates the electrostatic definition of a QD and enables the readout of electron spin states through *spin-dependent tunnelling*. Initial transport measurements revealed a gate effect and very low leakage currents as a prerequisite for the exploration of the EDMR effect in suspended and TEM-compatible CNT QDs. I have further developed an experimental apparatus for the high-throughput characterisation of such (and other) nanodevices at low temperatures with and without any microwave excitation. Future experiments may therefore focus on electron transport measurements on such CNT devices in the few to single electron regime.

In Chapter 5, I investigated the *spin-dependent polarisation transfer* in donor-doped ^{28}Si-FETs with cw- and pEDMR at X- (0.35 T, 9.7 GHz) and W-band (3.34 T, 94 GHz) in resonant microwave cavities. A novel cryogenic sample probe was pre-

sented for low-noise EDMR measurements at both microwave frequencies. The sample probe allows us to centre and position the sample within the cavity accurately, which is increasingly important at high microwave frequencies owing to the decreasing cavity size. Based on the comparison of X- and W-band EDMR spectra obtained from a ^{28}Si-FETs with channel implanted ^{75}As and ^{31}P donors, I demonstrated that the EDMR effect in such devices arises from the polarisation dependent resistivity of the 2DEG, which is modulated by a polarisation transfer between the donor and conduction electrons. This novel spin-to-charge conversion mechanism is supported by a series of cw- and pEDMR experiments both employing a lock-in detection technique. Our pEDMR experiments indicated in particular, that the Elliott-Yafet mechanism is the predominant electron spin relaxation process in 2DEGs embedded in ^{28}Si-FETs if the plane of the 2DEG is oriented parallel to the external magnetic field. Future experiments may focus on the measurement of the gate and angular dependence of the electron and donor spin relaxation and dephasing times in order to better understand the polarisation transfer dynamics.

The results presented in this thesis demonstrate that EDMR is a very sensitive spectroscopic technique to manipulate and detect electron spins in the solid state. It can be used to characterise and optimise a large number of entirely different materials and devices ranging from photovoltaic materials to carbon and silicon nanostructures. EDMR therefore provides a promising pathway towards the realisation of highly efficient and low-cost solar cells as well as a high-fidelity single-spin readout for applications in solid-state based QIP.

Appendix

APPENDIX A

Sample collet for W-band EDMR

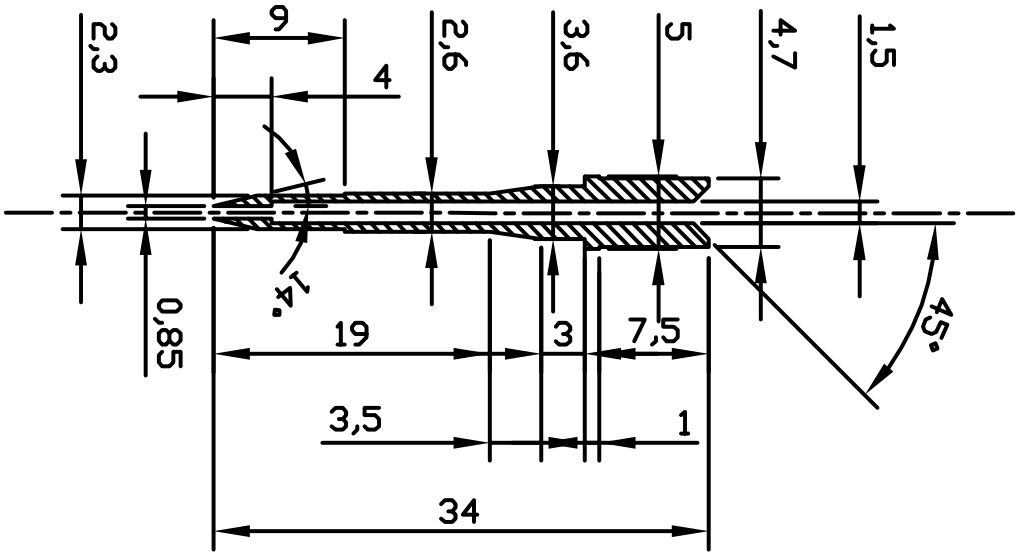

Figure A.1.: AutoCAD drawing of the brass collet designed for W-Band EDMR. The sample collet is compatible with a commercial Bruker Teraflex EN 600-1021H pulsed-ENDOR resonator. All dimensions are in milimetre if not otherwise indicated.

APPENDIX B

Simulation of coherent spin motion for pEDMR

PEDMR is conventionally carried out without any phase cycling and lock-in detection technique as the detection bandwidth of the experimental setup is usually much larger than the bandwidth of the current transient owing to an optimised tank detection circuitry [Hue09a] or sample geometry.

As outlined in Section 5.3.3 the detection bandwidth of our experimental setup used for pEDMR measurements on ^{28}Si-FETs at W-band is, however, limited to $\omega_{RC} \sim 10$ kHz, which is too low to detect signals in the 10 MHz regime. Employing a lock-in detection technique is therefore vital. In order to better understand the formation of a phase cycled and lock-in detected pEDMR signal and to simulate the signals arising from the pulse sequences depicted in Figure 5.17 in particular, we calculated the time evolution of the density matrix for an ensemble of non-interacting

2DEG electrons in an external magnetic field $\mathbf{B_0} = B_0\hat{\mathbf{z}}$ and under the influence of microwave pulses. The polarisation p of an ensemble of $n_\uparrow + n_\downarrow$ electrons with spin

$$|\uparrow\rangle := \begin{pmatrix} 1 \\ \\ 0 \end{pmatrix} \in \mathbb{C}^2 \quad \text{and} \quad |\downarrow\rangle := \begin{pmatrix} 0 \\ \\ 1 \end{pmatrix} \in \mathbb{C}^2 \tag{B.1}$$

parallel and anti-parallel to $\mathbf{B_0}$, respectively, is given by

$$p := p_c = \frac{n_\uparrow - n_\downarrow}{n_\uparrow + n_\downarrow} \quad . \tag{B.2}$$

For a 2DEG in thermal equilibrium, this polarisation is well described by [Gho92]

$$p_0 = \frac{g\mu_B B_0}{2(\varepsilon_F - \varepsilon_0)} = \frac{1}{2}\frac{D_{\text{2DEG}}}{n_c} g\mu_B B_0 \tag{B.3}$$

where g denotes the Landé g-factor, μ_B the Bohr magneton, ε_F the Fermi energy, ε_0 the bottom of the first subband, n_c the electron density, and D_{2DEG} the density of states. At $B_0 \sim 3.35$ T and $T = 5$ K, p_0 is typically in the range of $15 - 20$ % and is therefore set to $p_0 = 0.2$ in the following.

Hence, our ensemble of non-interacting 2DEG electrons can therefore be described with the density matrix

$$\hat{\rho}(t=0) := \hat{\rho}(0) = \begin{pmatrix} 1 + \frac{p_0}{2} & 0 \\ \\ 0 & 1 - \frac{p_0}{2} \end{pmatrix} = \begin{pmatrix} 1.1 & 0 \\ \\ 0 & 0.9 \end{pmatrix} \tag{B.4}$$

in thermal equilibrium. The expectation value of its magnetisation $\mathbf{M}$ in

$i = \pm x, \pm y, \pm z$ direction is given by

$$[M_i] = \mathrm{Tr}(\hat{\rho}\hat{\sigma}_i) \tag{B.5}$$

where $\hat{\sigma}_i$ denote the Pauli matrices

$$\hat{\sigma}_{\pm x} = \pm \begin{pmatrix} 0 & \frac{1}{2} \\ \frac{1}{2} & 0 \end{pmatrix}, \ \hat{\sigma}_{\pm y} = \pm \begin{pmatrix} 0 & -\frac{1}{2}i \\ \frac{1}{2}i & 0 \end{pmatrix}, \text{ and } \hat{\sigma}_{\pm z} = \pm \begin{pmatrix} \frac{1}{2} & 0 \\ 0 & -\frac{1}{2} \end{pmatrix}, \tag{B.6}$$

respectively. Under the influence of an external magnetic field $\mathbf{B_0} \parallel \hat{\mathbf{z}}$, $\mathbf{M}$ precesses about the z-axis of the system at the Larmor frequency ω_L and with the rotation angle θ_z given by

$$\theta_z(\delta t) = \omega_L \delta t = \frac{(g - g_0)\mu_B B_0}{\hbar}\ \delta t \tag{B.7}$$

for a time interval δt. Inhomogeneous broadening of the resonance lines is accounted for by a Gaussian distribution g_0 in the g-factor. The tip angle of a microwave pulse about the $\pm x$-axis with the microwave field $B_{1,j}$, microwave frequency ω_1, and pulse length δt is given by

$$\theta_{\pm x}(\delta t) = \omega_1 \delta t = \pm \frac{g\mu_B B_{1,j}}{\hbar}\ \delta t \quad . \tag{B.8}$$

Based on this description, each pulse sequence was divided into $N \in \mathbb{N}$ equidistant intervals with length $\delta t := t_{j+1} - t_j$ and microwave field $B_{1,j}$ $(j = 0, 1, ..., N-1)$ as depicted in Figure B.1 and a period δt of free evolution was associated with $B_{1,j} = 0$. In the rotating frame, the time evolution of the density matrix $\hat{\rho}(t)$ can therefore be

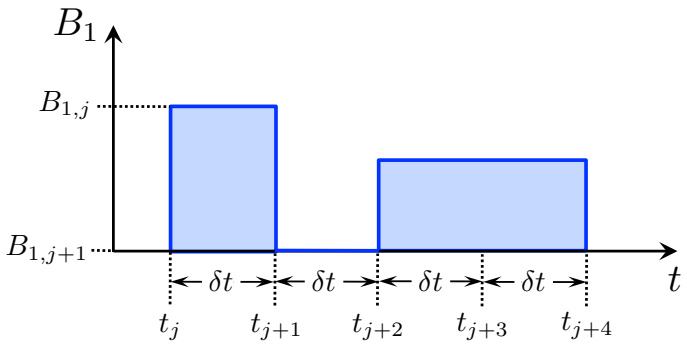

Figure B.1.: Iterative calculation of $\hat{\rho}(t)$. Each pulse sequence (blue, shaded) is divided into N time intervals of length δt. A microwave pulse is described by a finite microwave field $B_{1,j}$, while a period of free evolution is associated with the microwave field $B_{1,j} = 0$.

simulated with the iteration

$$\begin{cases} \hat{\rho}(t_0) & = \hat{\rho}(0) \\ \hat{\rho}(t_{j+1}) & = \exp\left[-i\theta_{z,j}\hat{\sigma}_z - i\theta_{\pm x,j}\hat{\sigma}_{\pm x}\right]\hat{\rho}(t_j)\exp\left[+i\theta_{\pm x,j}\hat{\sigma}_{\pm x} + i\theta_{z,j}\hat{\sigma}_z\right] \end{cases} \tag{B.9}$$

since all pulses were applied about the $\pm x$-axis in our experiments.[1] Spin relaxation during each time interval δt_j was also included into our model by considering the additional time evolution of the density matrix

$$\hat{\rho}(t_j) = \hat{\rho}(t_0) + \begin{pmatrix} \left[\rho_{11}(t_j) - \rho_{11}(t_0)\right] e^{-\delta t/T_1} & \rho_{12}(t_j)e^{-\delta t/T_2} \\ \rho_{21}(t_j)e^{-\delta t/T_2} & \left[\rho_{22}(t_j) - \rho_{22}(t_0)\right] e^{-\delta t/T_1} \end{pmatrix} \tag{B.10}$$

where T_1 and T_2 denote the longitudinal and transversal relaxation time, respectively. The pEDMR signal ΔV arising from the positive $(+\phi)$ and negative half

[1] The *rotating frame* is a very convenient non-inertial reference frame, which rotates relative to the laboratory frame and synchronously with one of the rotating components of the microwave field $\mathbf{B_1}$ at the microwave frequency ω_1. As a consequence, one of the components of B_1 as well as the magnetisation $\mathbf{M} \perp \mathbf{B_1}$ appear stationary, which simplifies the description of any coherent spin motion. Further details can be found in e.g. [Poo83].

period of the lock-in cycle $(-\phi)$ is proportional to the polarisation squared, i.e. $p^2 \propto [M_z]^2 = [\mathrm{Tr}(\hat{\rho}_N \hat{\sigma}_z)]^2$, and can be approximated by

$$\Delta V = \xi \left(\sum_{n=+\phi} p_n^2 - \sum_{m=-\phi} p_m^2 \right) \quad . \tag{B.11}$$

where $\xi \in \mathbb{R}$ describes the amplitude of the pEDMR spectra. ΔV contains the dynamic information of the pEDMR signal and is plotted in Figure 5.18.

List of Abbreviations

2DEG	Two-dimensional electron gas
µc-Si	Microcrystalline silicon
a-Si	Amorphous silicon
a-Si:H	Amorphous hydrogenated silicon
aFET	Accumulation-mode field-effect transistor
c-Si	Crystalline silicon
CMOS	Complementary metal-oxide semiconductor
CNT	Carbon nanotube
CVD	Chemical vapour deposition
cwEDMR	Continuous-wave electrically detected magnetic resonance
Cz-Si	Czochralski silicon
DB	Dangling bond

DQD	Double quantum dot
EBL	Electron beam lithography
EDMR	Electrically detected magnetic resonance
ENDOR	Electron-nuclear double resonance
EPR	Electron paramagnetic resonance
FET	Field-effect transistor
FFT	Fast Fourier transform
FIB	Focused ion beam
FID	Free induction decay
FTIR	Fourier transform infrared spectroscopy
HRTEM	High-resolution transmission electron microscopy
IC	Integrated circuit
IR	Infrared
KSM model	Kaplan-Solomon-Mott model
LCC	Leadless chip carrier
MOSFET	Metal-oxide-semiconductor field-effect transistor
n-Si	Natural silicon
nanoFET	Single-electron nanoscale field-effect transistor
OM	Optical microscopy
OP	Oxide precipitate

PCB	Printed-circuit board
pEDMR	Pulsed electrically detected magnetic resonance
QD	quantum dot
QIP	Quantum information processing
QPC	Quantum point contact
RIE	Reactive ion-etching
RYDMR	Reaction-yield detected magnetic resonance
SEM	Scanning electron microscopy
SOI	Silicon-on-insulator
SWE	Staebler-Wronski effect
TEM	Transmission electron microscopy
TL	Transmission line
TMAH	Tetramethylammonium hydroxide
TWT	Travelling wave tube

List of Figures

List of Publications

Publications released within this Dissertation

1. V. Lang, J. D. Murphy, R. J. Falster, J. J. L. Morton, *Spin-dependent recombination in Czochralski silicon containing oxide precipitates*, J. Appl. Phys. **111**, 013710 (2012). doi:10.1063/1.3675449.

2. C. C. Lo, V. Lang, R. E. George, J. J. L. Morton, A. M. Tyryshkin, S. A. Lyon, J. Bokor, and T. Schenkel, *Electrically detected magnetic resonance of neutral donors interacting with a two-dimensional electron gas*, Phys. Rev. Lett. **106**, 207601 (2011). doi:10.1103/PhysRevLett.106.207601.

3. V. Lang, C. C. Lo, R. E. George, S. A. Lyon, T. Schenkel, J. Bokor, A. Ardavan, and J. J. L. Morton, *Electrically detected magnetic resonance in a W-band microwave cavity*, Rev. Sci. Instrum. **82**, 034704 (2011). doi:10.1063/1.3557395.

Other Publications of the Author

1. C. D. Weis, C. C. Lo, V. Lang, A. M. Tyryshkin, R. E. George, K. M. Yu, J. Bokor, S. A. Lyon, J. J. L. Morton, T. Schenkel, *Electrical activation and electron spin resonance measurements of implanted bismuth in isotopically enriched silicon-28*, Appl. Phys. Lett. **100**, 172104 (2012). doi:10.1063/1.4704561.

2. H. Wang, J. Luo, A. Robertson, Y. Ito, W. Yan, V. Lang, M. Zaka, F. Schäffel, M. Rümmeli, G. A. D. Briggs, and J. Warner, *High performance field effect transistors from solution processed carbon nanotubes*, ACS Nano **4**, 6659 (2010). doi:10.1021/nn1020743.

3. J. Sailer, A. Wild, V. Lang, A. Siddiki, and D. Bougeard, *Quantum Hall resistance overshoot in two-dimensional electron gases: Theory and experiment*, New J. Phys. **12**, 113033 (2010). doi:10.1088/1367-2630/12/11/113033.

4. D. Bougeard, N. Sircar, S. Ahlers, V. Lang, G. Abstreiter, A. Trampert, J. M. LeBeau, S. Stemmer, D. W. Saxey, and A. Cerezo, *$Ge_{1-x}Mn_x$ clusters: Central structural and magnetic building blocks of nanoscale wire-like self-assembly in a magnetic semiconductor*, Nano Lett. **9**, 3743 (2009). doi:10.1021/nl901928f.

5. J. Sailer, V. Lang, G. Abstreiter, G. Tsuchiya, K. M. Itoh, J. W. Ager III, E. E. Haller, D. Kupidura, D. Harbusch, S. Ludwig, and D. Bougeard, *A Schottky top-gated two-dimensional electron system in a nuclear spin free Si/SiGe heterostructure*, Phys. Stat. Solidi RRL **3**, 61 (2009). doi:10.1002/pssr.200802275.

Bibliography

[Abr01] E. Abrahamas, S. V. Kravchenko, and M. P. Sarachik. *Metallic behavior and related phenomena in two dimensions*. Rev. Mod. Phys. **73**, 251 (2001). doi:10.1103/RevModPhys.73.251. (Cited on pages 133 and 135)

[Ama08] S. Amasha, K. MacLean, I. P. Radu, D. M. Zumbühl, M. A. Kastner, and M. P. Hanson. *Electrical control of spin relaxation in a quantum dot*. Phys. Rev. Lett. **100**, 046803 (2008). doi:10.1103/PhysRevLett.100.046803. (Cited on page 4)

[And61] P. W. Anderson. *Localized magnetic states in metals*. Phys. Rev. **124**, 41 (1961). doi:10.1103/PhysRev.124.41. (Cited on page 88)

[And82] T. Ando, A. B. Fowler, and F. Stern. *Electronic properties of two-dimensional systems*. Rev. Mod. Phys. **54**, 437 (1982). doi:10.1103/RevModPhys.54.437. (Cited on pages 5, 66, 130, and 139)

[Ang07] S. J. Angus, A. J. Ferguson, A. S. Dzurak, and R. G. Clark. *Gate-defined quantum dots in intrinsic silicon*. Nano Lett. **7**, 2051 (2007). doi:10.1021/nl070949k. (Cited on page 14)

[Ang08] S. J. Angus, A. J. Ferguson, A. S. Dzurak, and R. G. Clark. *A silicon radio-frequency single electron transistor*. Appl. Phys. Lett. **92**, 112103 (2008). doi:10.1063/1.2831664. (Cited on page 14)

[Ani79] O. A. Anisimov, V. M. Grigoryants, V. K. Molchanov, and Y. N. Molin. *Optical detection of ESR absorption of short-lived ion-radical pairs produced in solution by ionizing radiation*. Chem. Phys. Lett. **66**, 265 (1979). doi:10.1016/0009-2614(79)85013-7. (Cited on page 34)

[Ara00] Y. Araki, K. Maeda, and H. Murai. *Observation of two-spin controlling of a radical pair by pulsed irradiation of microwave monitored by absorption detected magnetic resonance.* Chem. Phys. Lett. **332**, 515 (2000). doi:10.1016/S0009-2614(00)01291-4. (Cited on page 44)

[Ash96] R. C. Ashoori. *Electrons in artificial atoms.* Nature **379**, 413 (1996). doi:10.1038/379413a0. (Cited on page 5)

[Ass11] L. V. C. Assali, H. M. Petrilli, R. B. Capaz, B. Koiller, X. Hu, and S. Das Sarma. *Hyperfine interactions in silicon quantum dots.* Phys. Rev. B **83**, 165301 (2011). doi:10.1103/PhysRevB.83.165301. (Cited on pages 4 and 10)

[Ave90] D. V. Averin and Y. V. Nazarov. *Virtual electron diffusion during quantum tunnelling of the electric charge.* Phys. Rev. Lett. **65**, 2446 (1990). doi:10.1103/PhysRevLett.65.2446. (Cited on page 8)

[Avo02] P. Avouris. *Molecular electronics with carbon nanotubes.* Acc. Chem. Res. **35**, 1026 (2002). doi:10.1021/ar010152e. (Cited on page 85)

[Bar73] E. Bartholdi and R. R. Ernst. *Fourier spectroscopy and the causality principle.* J. Magn. Reson. **11**, 9 (1973). doi:10.1016/0022-2364(73)90076-0. (Cited on page 81)

[Bay98] M. W. Bayerl, M. S. Brandt, H. Angerer, O. Ambacher, and M. Stutzmann. *Spin-dependent processes and Mg-acceptors in GaN single quantum well diodes and p-type GaN films.* Phys. Stat. Sol. (b) **210**, 389 (1998). doi:10.1002/(SICI)1521-3951(199812)210:2<389::AID-PSSB389>3.0.CO;2-Y. (Cited on page 115)

[Beh09] J. Behrends, A. Schnegg, M. Fehr, A. Lambertz, S. Haas, F. Finger, B. Rech, and K. Lips. *Electrical detection of electron spin resonance in microcrystalline silicon pin solar cells.* Philos. Mag. **89**, 2655 (2009). doi:10.1080/14786430903008472. (Cited on page 46)

[Ben06] S. C. Benjamin, A. Ardavan, G. A. D. Briggs, D. A. Britz, D. Gunlycke, J. Jefferson, M. A. G. Jones, D. F. Leigh, B. W. Lovett, A. N. Khlobystov, S. A. Lyon, J. J. L. Morton, K. Porfyrakis, M. Sambrook, and A. M. Tyryshkin. *Towards a fullerene-based quantum computer.* J. Phys.: Condens. Matt. **18**, S867 (2006). doi:10.1088/0953-8984/18/21/S12. (Cited on pages 84 and 85)

[Ber72] H. H. Berger. *Models for contacts to planar devices.* Solid State Electron. **15**, 145 (1972). doi:10.1016/0038-1101(72)90048-2. (Cited on page 96)

[Ber89] W. Bergholz, M. J. Binns, G. R. Booker, J. C. Hutchison, S. H. Kinder, S. Messoloras, R. C. Newman, R. J. Stewart, and J. G. Willkes. *A study of*

oxygen precipitation in silicon using high-resolution transmission electron microscopy, small-angle neutron scattering and infrared absorption. Philos. Mag. B **59**, 499 (1989). doi:10.1080/13642818908211173. (Cited on page 20)

[Bie86] D. K. Biegelsen and M. Stutzmann. *Hyperfine studies of dangling bonds in amorphous silicon*. Phys. Rev. B **33**, 3006 (1986). doi:10.1103/PhysRevB.33.3006. (Cited on page 18)

[Bie08] M. J. Biercuk, S. Ilani, C. M. Marcus, and P. L. McEuen. *Electrical transport in single-wall carbon nanotubes*. Top. Appl. Phys. **111**, 455 (2008). doi:10.1007/978-3-540-72865-8_15. (Cited on page 111)

[Blo46] F. Bloch. *Nuclear induction*. Phys. Rev. **70**, 460 (1946). doi:10.1103/PhysRev.70.460. (Cited on page 25)

[Blu11] H. Bluhm, S. Foletti, I. Neder, M. Rudner, D. Mahalu, V. Umansky, and A. Yacoby. *Dephasing time of GaAs electron-spin qubits coupled to a nuclear bath exceeding* $200\,\mu s$. Nature Phys. **7**, 109 (2011). doi:10.1038/nphys1856. (Cited on page 4)

[Boe03] C. Boehme and K. Lips. *Theory of time-domain measurement of spin-dependent recombination with pulsed electrically detected magnetic resonance*. Phys. Rev. B **68**, 245105 (2003). doi:10.1103/PhysRevB.68.245105. (Cited on pages 37, 43, and 116)

[Boe06a] C. Boehme and L. K. *The Investigation of Charge Carrier Recombination and Hopping Transport with Pulsed Electrically Detected Magnetic Resonance Techniques, in Charge Transport in Disordered Solids with Applications in Electronics (ed. S. Baranovski)*. Wiley, Chichester, England, Hoboken, NJ, 2006. doi:10.1002/0470095067.ch5. (Cited on page 73)

[Boe06b] C. Boehme and K. Lips. *The ultra-sensitive electrical detection of spin-Rabi oscillation at paramagnetic defects*. Physica B **376-377**, 930 (2006). doi:10.1016/j.physb.2005.12.231. (Cited on pages 29 and 42)

[Bör11] F. Börrnert, A. Bachmatiuk, B. Büchner, and M. H. Rümmeli. *Low-voltage aberration-corrected transmission electron microscopy: Progressing carbon nanostructures*. Microscopy: Science, Technology, Applications and Education **1-3**, 1846 (2011). http://www.formatex.info/microscopy4/1846-1852.pdf. (Cited on page 89)

[Bot06] K. Bothe and J. Schmidt. *Electronically activated boron-oxygen-related recombination centers in crystalline silicon*. J. App. Phys. **99**, 013701 (2006). doi:10.1063/1.2140584. (Cited on pages 19 and 49)

[Bra91a] M. S. Brandt and M. Stutzmann. *Excitons and light-induced degradation of amorphous hydrogenated silicon*. Appl. Phys. Lett. **58**, 1620 (1991). doi:10.1063/1.105144. (Cited on page 73)

[Bra91b] M. S. Brandt and M. Stutzmann. *Spin-dependent conductivity in amorphous hydrogenated silicon*. Phys. Rev. B **43**, 5184 (1991). doi:10.1103/PhysRevB.43.5184. (Cited on pages 35, 37, and 73)

[Bra92] M. S. Brandt. *Spinabhängiger Transport und Rekombination in Halbleitern*. PhD Thesis, Max-Planck-Institut für Festkörperphysik, Stuttgart, Germany, 1992. (Cited on pages 18, 36, 40, and 78)

[Bra98] M. S. Brandt, M. W. Bayerl, M. Stutzmann, and C. F. O. Graeff. *Electrically detected magnetic resonance of a-Si:H at low magnetic fields: The influence of hydrogen on the dangling bond resonance*. J. Non-Cryst. Solids **227-230**, 343 (1998). doi:10.1016/S0022-3093(98)00073-8. (Cited on pages 19 and 35)

[Bra99] H. M. Branz. *Hydrogen collision model: Quantitative description of metastability in amorphous silicon*. Phys. Rev. B **59**, 5498 (1999). doi:10.1103/PhysRevB.59.5498. (Cited on page 19)

[Bra04] M. S. Brandt, S. T. B. Goennenwein, T. Graf, H. Huebl, S. Lauterbach, and M. Stutzmann. *Spin-dependent transport in elemental and compound semiconductors and nanostructures*. Phys. Stat. Sol. (c) **1**, 2056 (2004). doi:10.1002/pssc.200404763. (Cited on page 29)

[Bro69] M. H. Brodsky and R. S. Title. *Electron spin resonance in amorphous silicon, germanium, and silicon carbide*. Phys. Rev. Lett. **23**, 581 (1969). doi:10.1103/PhysRevLett.23.581. (Cited on page 18)

[Bro59] J. Brossel, S. Geschwind, and A. L. Schawlow. *Optical detection of paramagnetic resonance in crystals at low temperatures*. Phys. Rev. Lett. **3**, 548 (1959). doi:10.1103/PhysRevLett.3.548. (Cited on page 29)

[Bro83] K. L. Brower. *^{29}Si hyperfine structure of unpaired spins at the Si/SiO_2 interface*. Appl. Phys. Lett. **43**, 1111 (1983). doi:10.1063/1.94244. (Cited on page 72)

[Bro87] K. L. Brower. *Structural features at the Si-SiO_2 interface*. Z. Phys. Chem. **151**, 177 (1987). http://www.oldenbourg-link.com/doi/abs/10.1524/zpch.1987.151.Part_1_2.177. (Cited on page 61)

[Bue02] T. M. Buehler, R. P. McKinnon, N. E. Lumpkin, R. Brenner, D. J. Reilly, L. D. Macks, A. R. Hamilton, A. S. Dzurak, and G. Clark. *A self-aligned fabrication process for silicon quantum computer devices*. Nanotechnology **13**, 686 (2002). doi:10.1088/0957-4484/13/5/330. (Cited on page 13)

[Bui08] M. R. Buitelaar, J. Fransson, A. L. Cantone, C. G. Smith, D. Anderson, G. A. C. Jones, A. Ardavan, A. N. Khlobystov, A. A. R. Watt, K. Porfyrakis, and G. A. D. Briggs. *Pauli spin blockade in carbon nanotube double quantum dots*. Phys. Rev. B **77**, 245439 (2008). doi:10.1103/PhysRevB.77.245439. (Cited on page 33)

[Bul08] D. V. Bulaev, B. Trauzettel, and D. Loss. *Spin-orbit interaction and anomalous spin relaxation in carbon nanotube quantum dots*. Phys. Rev. B **77**, 235301 (2008). doi:10.1103/PhysRevB.77.235301. (Cited on page 4)

[Bun05] J. S. Bunch, Y. Yaish, M. Brink, K. Bolotin, and P. L. McEuen. *Coulomb oscillations and Hall effect in quasi-2D graphite quantum dots*. Nano Lett. **5**, 287 (2005). doi:10.1021/nl048111+. (Cited on page 10)

[Bur90] G. Burns. *Solid State Physics*. Academic Press, San Diego, 1990. (Cited on page 123)

[Byc84] Y. A. Bychkov and E. I. Rashba. *Oscillatory effects and the magnetic susceptibility of carriers in inversion layers*. J. Phys. C **17**, 6039 (1984). doi:doi:10.1088/0022-3719/17/33/015. (Cited on page 139)

[Cal06] M. J. Calderón, B. Koiller, X. Hu, and S. Das Sarma. *Quantum control of donor electrons at the Si-SiO_2 interface*. Phys. Rev. Lett. **96**, 096802 (2006). doi:10.1103/PhysRevLett.96.096802. (Cited on page 13)

[Cao05] J. Cao, Q. Wang, and H. Dai. *Electron transport in very clean, as-grown suspended carbon nanotubes*. Nature Mat. **4**, 745 (2005). doi:10.1038/nmat1478. (Cited on page 87)

[Car76] D. E. Carlson and C. R. Wronski. *Amorphous silicon solar cell*. Appl. Phys. Lett. **28**, 671 (1976). doi:10.1063/1.88617. (Cited on page 72)

[Car87] W. E. Carlos. *Paramagnetic centers at Si-SiO_2 interfaces in silicon-on-insulator films*. Appl. Phys. Lett. **50**, 1450 (1987). doi:10.1063/1.97798. (Cited on page 61)

[Cas62] T. G. J. Castner. *Direct measurement of the valley-orbit splitting of shallow donors in silicon*. Phys. Rev. Lett. **8**, 13 (1962). doi:10.1103/PhysRevLett.8.13. (Cited on page 141)

[Cas63] T. G. Castner. *Raman spin-lattice relaxation of shallow donors in silicon*. Phys. Rev. **130**, 58 (1963). doi:10.1103/PhysRev.130.58. (Cited on page 141)

[Cas67] T. G. Castner. *Orbach spin-lattice relaxation of shallow donors in silicon*. Phys. Rev. **155**, 154 (1967). doi:10.1103/PhysRev.155.816. (Cited on page 141)

[Che10] J. L. Cheng, M. W. Wu, and J. Fabian. *Theory of the spin relaxation of conduction electrons in silicon*. Phys. Rev. Lett. **104**, 016601 (2010). doi:10.1103/PhysRevLett.104.016601. (Cited on page 139)

[Che11] L. Chen, X. Yu, P. Chem, P. Wang, X. Gu, J. Lu, and D. Yang. *Effect of oxygen precipitation on the performance of Czochralski silicon solar cells.* Sol. Energ. Mat. Sol. C. **95**, 3148 (2011). doi:10.1016/j.solmat.2011.06.044. (Cited on page 20)

[Chi69] R. C. Chittick, J. H. Alexander, and H. F. Sterling. *The preparation and properties of amorphous silicon.* J. Electrochem. Soc. **116**, 77 (1969). doi:10.1149/1.2411779. (Cited on page 19)

[Chi05a] S. B. Chikkannanavar, D. E. Luzzi, S. Paulson, and A. T. J. Johnson. *Synthesis of peapods using substrate-grown SWNTs and DWNTs: An enabling step toward peapod devices.* Nano Lett. **5**, 151 (2005). doi:10.1021/nl049854y. (Cited on page 85)

[Chi05b] L. Childress, J. M. Taylor, A. S. Sørensen, and M. D. Lukin. *Fault-tolerant quantum repeaters with minimal physical resources and implementations based on single-photon emitters.* Phys. Rev. A **72**, 052330 (2005). doi:10.1103/PhysRevA.72.052330. (Cited on page 2)

[Chu09a] H. O. H. Churchill, A. J. Bestwick, J. W. Harlow, F. Kuemmeth, D. Marcos, C. H. Stwertka, S. K. Watson, and C. M. Marcus. *Electron-nuclear interaction in ^{13}C nanotube double quantum dot.* Nature Phys. **5**, 321 (2009). doi:10.1038/nphys1247. (Cited on page 10)

[Chu09b] H. O. H. Churchill, F. Kuemmeth, J. W. Harlow, A. J. Bestwick, E. I. Rashba, K. Flensberg, C. H. Stwertka, T. Taychatanapat, S. K. Watson, and C. M. Marcus. *Relaxation and dephasing in a two-electron ^{13}C nanotube double quantum dot.* Phys. Rev. Lett. **102**, 166802 (2009). doi:10.1103/PhysRevLett.102.166802. (Cited on pages 4 and 10)

[Cla76] A. H. Clark, R. D. Burnham, D. J. Chadi, and R. M. White. *Spin relaxation of conduction electrons in GaAs.* Solid State Commun. **20**, 385 (1976). doi:10.1016/0038-1098(76)90531-7. (Cited on page 4)

[Cob02] D. H. Cobden and J. Nygård. *Shell filling in closed single-wall carbon nanotube quantum dots.* Phys. Rev. Lett. **89**, 046803 (2002). doi:10.1103/PhysRevLett.89.046803. (Cited on page 88)

[Coh07] G. M. Cohen, M. J. Rooks, J. O. Chu, S. E. Laux, P. M. Solomon, J. A. Ott, R. J. Miller, and W. Haensch. *Nanowire metal-oxide-semiconductor field effect transistor with doped epitaxial contacts for source and drain.* Appl. Phys. Lett. **90**, 233110 (2007). doi:10.1063/1.2746946. (Cited on page 13)

[Col98] E. J. H. Collart, K. Weemers, D. J. Gravesteijn, and J. G. M. van Berkum. *Characterization of low-energy ($100\,eV - 10\,keV$) boron ion implantation.* J. Vac. Sci. Technol. B **16**, 280 (1998). doi:10.1116/1.589795. (Cited on page 98)

[Cur87] H. Curtins, N. Wyrsch, M. Favre, and A. V. Shah. *Influence of plasma excitation frequency for a-Si:H thin film deposition*. Plasma Chem. Plasma Processing **7**, 267 (1987). doi:10.1007/BF01016517. (Cited on page 74)

[Cyw09a] Ł. Cywiński, W. M. Witzel, and S. Das Sarma. *Electron spin dephasing due to hyperfine interactions with a nuclear spin bath*. Phys. Rev. Lett. **102**, 057601 (2009). doi:10.1103/PhysRevLett.102.057601. (Cited on page 8)

[Cyw09b] Ł. Cywiński, W. M. Witzel, and S. Das Sarma. *Pure quantum dephasing of a solid-state electron spin qubit in a large nuclear spin bath coupled by long-range hyperfine-mediated interactions*. Phys. Rev. B **79**, 245314 (2009). doi:10.1103/PhysRevB.79.245314. (Cited on page 8)

[dSo03] R. de Sousa and S. Das Sarma. *Theory of nuclear-induced spectral diffusion: Spin coherence of phosphorus donors in Si and GaAs quantum dots*. Phys. Rev. B **68**, 115322 (2003). doi:10.1103/PhysRevB.68.115322. (Cited on page 141)

[dSo09] R. de Sousa, C. C. Lo, and J. Bokor. *Spin-dependent scattering in a silicon transistor*. Phys. Rev. B **80**, 045320 (2009). doi:10.1103/PhysRevB.80.045320. (Cited on pages 33, 132, and 136)

[dWa95] C. G. V. de Walle and R. A. Street. *Silicon-hydrogen bonding and hydrogen diffusion in amorphous silicon*. Phys. Rev. B **51**, 10615 (1995). doi:10.1103/PhysRevB.51.10615. (Cited on page 19)

[Dek91] C. Dekker, A. J. Scholten, F. Liefrink, R. Eppenga, H. van Houten, and C. T. Foxon. *Spontaneous resistance switching and low-frequency noise in quantum point contacts*. Phys. Rev. Lett. **66**, 2148 (1991). doi:10.1103/PhysRevLett.66.2148. (Cited on page 14)

[Der81] H. Dersch and J. Stuke, J. Beichler. *Light-induced dangling bonds in hydrogenated amorphous silicon*. Appl. Phys. Lett. **38**, 456 (1981). doi:10.1063/1.92402. (Cited on page 19)

[Der83] H. Dersch, L. Schweitzer, and J. Stuke. *Recombination processes in a-Si:H: Spin-dependent photoconductivity*. Phys. Rev. B **28**, 4678 (1983). doi:10.1103/PhysRevB.28.4678. (Cited on pages 19, 35, 73, and 78)

[Der84] H. Dersch and L. Schweitzer. *Spin-dependent hole diffusion in a-Si:H*. Philos. Mag. B **50**, 397 (1984). doi:10.1080/13642818408238864. (Cited on page 73)

[Des08] V. V. Deshpande and M. Bockrath. *The one-dimensional Wigner crystal in carbon nanotubes*. Nature Phys. **4**, 314 (2008). doi:10.1038/nphys895. (Cited on page 88)

[Des09] V. V. Deshpande, B. Chandra, R. Caldwell, D. S. Novikov, J. Hone, and M. Bockrath. *Mott insulating state in ultraclean carbon nanotubes*. Science **323**, 106 (2009). doi:10.1126/science.1165799. (Cited on page 88)

[Des10] V. V. Deshpande, M. Bockrath, L. I. Glazman, and A. Yacoby. *Electron liquids and solids in one dimension*. Nature **464**, 209 (2010). doi:10.1038/nature08918. (Cited on page 88)

[Din78] R. Dingle, H. L. Störmer, A. C. Gossard, and W. Wiegmann. *Electron mobilities in modulation-doped semiconductor heterojunction superlattices*. Appl. Phys. Lett. **33**, 665 (1978). doi:10.1063/1.90457. (Cited on page 5)

[Dir90] J. Dirksmeyer and O. F. Schirmer. *Characterization of shallow donor-doped silicon molecular beam epitaxial layers by electron spin resonance*. Thin Solid Films **184**, 55 (1990). doi:10.1016/0040-6090(90)90397-V. (Cited on page 128)

[DiV00a] D. P. DiVincenzo. *The physical implementation of quantum computation*. Fortschr. Phys. **48**, 771 (2000). doi:10.1002/3527603182.ch1. (Cited on page 3)

[DiV00b] D. P. DiVincenzo, D. Bacon, J. Kempe, G. Burkard, and K. B. Whaley. *Universal quantum computation with the exchange interaction*. Nature **408**, 339 (2000). doi:10.1038/35042541. (Cited on page 3)

[Dav80] J. R. Davis Jr., A. Rohatgi, R. H. Hopkins, P. D. Blais, P. Rai-Choudhury, J. R. McCormick, and H. C. Mollenkopf. *Impurities in silicon solar cells*. IEEE Trans. Electron Dev. **27**, 677 (1980). doi:10.1109/T-ED.1980.19922. (Cited on page 16)

[Dob88] M. Dobers, K. v. Klitzing, and G. Weimann. *Electron-spin resonance in the two-dimensional electron gas of $GaAs/Al_xGa_{1-x}As$ heterostructures*. Phys. Rev. B **38**, 5453 (1988). doi:10.1103/PhysRevB.38.5453. (Cited on page 32)

[Dre55] G. Dresselhaus. *Spin-orbit coupling effects in zinc blende structures*. Phys. Rev. **100**, 580 (1955). doi:10.1103/PhysRev.100.580. (Cited on page 139)

[Dre04] M. S. Dresselhaus, G. Dresselhaus, R. Saito, and A. Jorio. *Raman spectroscopy of carbon nanotubes*. Phys. Rep. **409**, 47 (2004). doi:10.1016/j.physrep.2004.10.006. (Cited on pages 85 and 89)

[Dre10] M. S. Dresselhaus, A. Jorio, M. Hofmann, G. Dresselhaus, and R. Saito. *Perspectives on carbon nanotubes and graphene Raman spectroscopy*. Nano Lett. **10**, 751 (2010). doi:10.1021/nl904286r. (Cited on page 89)

[Dru00] P. Drude. *Zur Elektronentheorie der Metalle*. Ann. Phys. **306**, 566 (1900). doi:10.1002/andp.19003060312. (Cited on page 139)

[Dür04] T. Dürkop, S. A. Getty, E. Cobas, and M. S. Fuhrer. *Extraordinary mobility in semiconducting carbon nanotubes*. Nano Lett. **4**, 35 (2004). doi:10.1021/nl034841q. (Cited on page 111)

[Dya71] M. I. D'yakonov and V. I. Perel'. *Spin relaxation of conduction electrons in noncentrosymmetric semiconductors*. Sov. Phys. Solid State **13**, 3023 (1971). (Cited on page 139)

[Ebb96] T. W. Ebbesen, H. J. Lezec, H. Hiura, J. W. Bennett, H. F. Ghaemi, and T. Thilo. *Electrical conductivity of individual carbon nanotubes*. Nature **382**, 54 (1996). doi:10.1038/382054a0. (Cited on page 11)

[Eic98] T. Eickelkamp, S. Roth, and M. Mehring. *Electrically detected magnetic resonance in photoexcited fullerenes*. Mol. Phys. **95**, 967–972 (1998). doi:10.1080/00268979809483230. (Cited on page 35)

[Ell54] R. J. Elliott. *Theory of the effect of spin-orbit coupling on magnetic resonance in some semiconductors*. Phys. Rev. **96**, 266 (1954). doi:10.1103/PhysRev.96.266. (Cited on page 138)

[Elz04] J. M. Elzerman, R. Hanson, L. H. W. van Beveren, B. Witkamp, L. M. K. Vandersypen, and L. P. Kouwenhoven. *Single-shot read-out of an individual electron spin in a quantum dot*. Nature **430**, 431 (2004). doi:10.1038/nature02693. (Cited on pages 4, 6, and 29)

[Eng01] H.-A. Engel and D. Loss. *Detection of single spin decoherence in a quantum dot via charge currents*. Phys. Rev. Lett. **86**, 4648 (2001). doi:10.1103/PhysRevLett.86.4648. (Cited on page 7)

[Fab99] J. Fabian and S. Das Sarma. *Spin relaxation of conduction electrons*. J. Vac. Sci. Technol. B **17**, 1708 (1999). doi:10.1116/1.590813. (Cited on page 138)

[Fal04] R. Falster, V. V. Voronkov, V. Y. Resnik, and M. G. Milvidskii. *Thresholds for effective internal gettering in silicon wafers*. Proc. Electrochem. Soc. **5**, 188 (2004). http://www.electrochem.org/dl/ma/206/pdfs/1066.pdf. (Cited on pages 20 and 49)

[Feh59a] G. Feher. *Electron spin resonance experiments on donors in silicon. I. Electronic structure of donors by the electron nuclear double resonance technique*. Phys. Rev. **114**, 1219 (1959). doi:10.1103/PhysRev.114.1219. (Cited on page 128)

[Feh59b] G. Feher and A. Gere. *Electron spin resonance experiments on donors in silicon. II. Electron spin relaxation effects*. Phys. Rev. **114**, 1245 (1959). doi:10.1103/PhysRev.114.1245. (Cited on page 141)

[Feh10] M. Fehr, A. Schnegg, C. Teutloff, R. Bittl, O. Astakhov, F. Finger, B. Rech, and K. Lips. *Hydrogen distribution in the vicinity of dangling bonds in hydrogenated amorphous silicon (a-Si:H).* Phys. Stat. Sol. (a) **207**, 552 (2010). doi:10.1002/pssa.200982876. (Cited on page 19)

[Feh11] M. Fehr, A. Schnegg, B. Rech, K. Lips, O. Astakhov, F. Finger, G. Pfanner, C. Freysoldt, J. Neugebauer, R. Bittl, and C. Teutloff. *Combined multifrequency EPR and DFT study of dangling bonds in a-Si:H.* Phys. Rev. B **84**, 245203 (2011). doi:10.1103/PhysRevB.84.245203. (Cited on page 19)

[Fie93] M. Field, C. G. Smith, D. A. Ritchie, J. E. F. Frost, G. A. C. Jones, and D. G. Hasko. *Measurements of Coulomb blockade with a noninvasive voltage probe.* Phys. Rev. Lett. **70**, 1311 (1993). doi:10.1103/PhysRevLett.70.1311. (Cited on page 6)

[Fis73] H. Fischer and W. Pschunder. *Investigation of photon and thermal induced changes in silicon solar cells.* Proc. 10th IEEE PVSC 404 (1973). (Cited on pages 19 and 49)

[Fis09] J. Fischer, B. Trauzettel, and D. Loss. *Hyperfine interaction and electron-spin decoherence in graphene and carbon nanotube quantum dots.* Phys. Rev. B **80**, 155401 (2009). doi:10.1103/PhysRevB.80.155401. (Cited on pages 10 and 12)

[Fuj02] T. Fujisawa, D. G. Austing, Y. Tokura, Y. Hirayama, and S. Tarucha. *Allowed and forbidden transitions in artificial hydrogen and helium atoms.* Nature **419**, 278 (2002). doi:10.1038/nature00976. (Cited on pages 4 and 5)

[Ful57] C. S. Fuller and R. A. Logan. *Effect of heat treatment upon the electrical properties of silicon crystals.* J. Appl. Phys. **28**, 1427 (1957). doi:10.1063/1.1722672. (Cited on pages 19 and 49)

[Fun02] A. C. Funk and M. G. Raymer. *Quantum key distribution using nonclassical photon-number correlations in macroscopic light pulses.* Phys. Rev. A **65**, 042307 (2002). doi:10.1103/PhysRevA.65.042307. (Cited on page 2)

[Geh83] W. Gehlhoff and K. H. Segsa. *EPR of iron-boron centres in silicon.* Phys. Stat. Sol. (b) **115**, 443 (1983). doi:10.1002/pssb.2221150214. (Cited on pages 59 and 61)

[Geh95] W. Gehlhoff, N. T. Bagraev, and L. E. Klyachkin. *Shallow and deep centers in heavily doped silicon quantum wells.* Mater. Sci. Forum **196**, 467 (1995). doi:10.4028/www.scientific.net/MSF.196-201.467. (Cited on pages 59 and 61)

[Gei07] A. K. Geim and K. S. Novoselov. *The rise of graphene*. Nature Mater. **6**, 183 (2007). doi:10.1038/nmat1849. (Cited on page 10)

[Ger86] G. J. Gerardi, E. H. Poindexter, P. J. Caplan, and N. M. Johnson. *Interface traps and P_b centers in oxidized (100) silicon wafers*. Appl. Phys. Lett. **49**, 348 (1986). doi:10.1063/1.97611. (Cited on page 69)

[Ges59] S. Geschwind, R. J. Collins, and A. L. Schawlow. *Optical detection of paramagnetic resonance in an excited state of Cr^{3+} in Al_2O_3*. Phys. Rev. Lett. **3**, 545 (1959). doi:10.1103/PhysRevLett.3.545. (Cited on page 29)

[Gho92] R. N. Ghosh and R. H. Silsbee. *Spin-spin scattering in a silicon two-dimensional electron gas*. Phys. Rev. B **46**, 12508 (1992). doi:10.1103/PhysRevB.46.12508. (Cited on pages 15, 32, and 160)

[Gil90] D. Gilles and E. R. Weber. *Mechanism of internal gettering of interstitial impurities in Czochralski-grown silicon*. Phys. Rev. Lett. **64**, 196 (1990). doi:10.1103/PhysRevLett.64.196. (Cited on page 20)

[Gio04] V. Giovannetti, S. Lloyd, and L. Maccone. *Quantum-enhanced measurements: Beating the standard quantum limit*. Science **306**, 1330 (2004). doi:10.1126/science.1104149. (Cited on page 2)

[Göt10] G. T. J. Götz. *Single Electron-ics with Carbon Nanotubes*. PhD Thesis, Delft University of Technology, The Netherlands, 2010. http://repository.tudelft.nl/view/ir/uuid:faf67a50-ab3e-4ad2-933d-f7686ab99739. (Cited on page 95)

[Gog91] D. Goguenheim and M. Lannoo. *Theoretical calculation of the electron-capture cross section due to a dangling bond at the Si(111)-SiO_2 interface*. Phys. Rev. B **44**, 1724 (1991). doi:10.1103/PhysRevB.44.1724. (Cited on page 69)

[Gon12] M. Gonzalez-Zalba, D. Heiss, and A. Ferguson. *A hybrid double-dot in silicon*. New J. Phys. **14**, 023050 (2012). doi:10.1088/1367-2630/14/2/023050. (Cited on page 14)

[Gor58] J. P. Gordon and K. D. Bowers. *Microwave spin echoes from donor electrons in silicon*. Phys. Rev. Lett. **1**, 368 (1958). doi:10.1103/PhysRevLett.1.368. (Cited on page 4)

[Gra99] C. F. O. Graeff, M. S. Brandt, M. Stutzmann, M. Holzmann, G. Abstreiter, and F. Schaeffler. *Electrically detected magnetic resonance of two-dimensional electron gases in Si/SiGe heterostructures*. Phys. Rev. B **59**, 13242 (1999). doi:10.1103/PhysRevB.59.13242. (Cited on pages 15, 32, 128, and 133)

[Gre07] A. Greilich, A. Shabaev, D. R. Yakovlev, A. L. Efros, I. A. Yugova, D. Reuter, A. D. Wieck, and M. Bayer. *Nuclei-induced frequency focusing of electron spin coherence*. Science **317**, 1896 (2007). doi:10.1126/science.1146850. (Cited on page 8)

[Gri07] P. R. Griffiths and J. A. De Haseth. *Fourier transform infrared spectrometry*. John Wiley & Sons, New York, USA, 2007. (Cited on page 52)

[Guo95a] T. Guo, P. Nikolaev, A. G. Rinzler, D. Tománek, D. T. Colbert, and R. E. Smalley. *Self-assembly of tubular fullerenes*. J. Phys. Chem. **99**, 10694 (1995). doi:10.1021/j100027a002. (Cited on page 11)

[Guo95b] T. Guo, P. Nikolaev, A. Thess, D. T. Colbert, and R. E. Smalley. *Catalytic growth of single-walled nanotubes by laser vaporization*. Chem. Phys. Lett. **243**, 49 (1995). doi:10.1016/0009-2614(95)00825-O. (Cited on page 11)

[Hah50] E. L. Hahn. *Spin echoes*. Phys. Rev. **80**, 580 (1950). doi:10.1103/PhysRev.80.580. (Cited on page 43)

[Hal52] R. N. Hall. *Electron-hole recombination in germanium*. Phys. Rev. **87**, 387 (1952). doi:10.1103/PhysRev.87.387. (Cited on page 34)

[Han05] R. Hanson, L. H. W. van Beveren, I. T. Vink, J. M. Elzerman, W. J. M. Naber, F. H. L. Koppens, L. P. Kouwenhoven, and L. M. K. Vandersypen. *Single-shot readout of electron spin states in a quantum dot using spin-dependent tunnel rates*. Phys. Rev. Lett. **94**, 196802 (2005). doi:10.1103/PhysRevLett.94.196802. (Cited on page 6)

[Han07] R. Hanson, L. P. Kouwenhoven, J. R. Petta, S. Tarucha, and L. M. K. Vandersypen. *Spins in few-electron quantum dots*. Rev. Mod. Phys. **79**, 1217 (2007). doi:10.1103/RevModPhys.79.1217. (Cited on pages 5 and 11)

[Har06] J. Harrison, M. J. Sellars, and N. B. Manson. *Centres in diamond*. Diamond Relat. Mater. **15**, 586 (2006). doi:10.1016/j.diamond.2005.12.027. (Cited on page 4)

[Has04] A. Hashimoto, K. Suenaga, A. Gloter, K. Urita, and S. Iijima. *Direct evidence for atomic defects in graphene layers*. Nature **430**, 870 (2004). doi:10.1038/nature02817. (Cited on page 89)

[Has05] A. Hashimoto, K. Suenaga, K. Urita, T. Shimada, T. Sugai, S. Bandow, H. Shinohara, and S. Iijima. *Atomic correlation between adjacent graphene layers in double-wall carbon nanotubes*. Phys. Rev. Lett. **94**, 045504 (2005). doi:10.1103/PhysRevLett.94.045504. (Cited on page 89)

[Hay03] T. Hayashi, T. Fujisawa, H. D. Cheong, Y. H. Jeong, and Y. Hirayama. *Coherent manipulation of electronic states in a double quantum dot*. Phys. Rev. Lett. **91**, 226804 (2003). doi:10.1103/PhysRevLett.91.226804. (Cited on page 6)

[Hir99] I. Hiromitsu, Y. Kaimori, M. Kitano, and T. Ito. *Spin-dependent recombination of photoinduced carriers in phthalocyanine/C_{60} heterojunctions*. Phys. Rev. B **59**, 2151 (1999). doi:10.1103/PhysRevB.59.2151. (Cited on page 35)

[His98] D. Hisamoto, W.-C. Lee, J. Kedzierski, H. Takeuchi, K. Asano, C. Kuo, T.-J. King, J. Bokor, and C. Hu. *A folded-channel MOSFET for deep-sub-tenth micron era*. IEDM Tech. Dig. 1032 (1998). doi:10.1109/IEDM.1998.746531. (Cited on page 13)

[His00] D. Hisamoto, W.-C. Lee, J. Kedzierski, H. Takeuchi, K. Asano, C. Kuo, T.-J. King, J. Bokor, and C. Hu. *FinFET – A self-aligned double-gate MOSFET scalable to 20 nm*. IEEE Trans. Electron Devices **47**, 2320 (2000). doi:10.1109/16.887014. (Cited on page 13)

[Hoe12] F. Hoehne, L. Dreher, J. Behrends, M. Fehr, H. Huebl, K. Lips, A. Schnegg, M. Suckert, M. Stutzmann, and M. S. Brandt. *Lock-in detection for pulsed electrically detected magnetic resonance*. Rev. Sci. Instrum. **83**, 043907 (2012). doi:10.1063/1.4704837. (Cited on page 142)

[Hol04] L. C. L. Hollenberg, A. S. Dzurak, C. Wellard, A. R. Hamilton, D. J. Reilly, G. J. Milburn, and R. G. Clark. *Charge-based quantum computing using single donors in semiconductors*. Phys. Rev. B **69**, 113301 (2004). doi:10.1103/PhysRevB.69.113301. (Cited on page 3)

[Hon54] A. Honig. *Polarization of arsenic nuclei in a silicon semiconductor*. Phys. Rev. **96**, 234 (1954). doi:10.1103/PhysRev.96.234. (Cited on page 141)

[Hon56] A. Honig and J. Combrisson. *Paramagnetic resonance in As-doped silicon*. Phys. Rev. **102**, 917 (1956). doi:10.1103/PhysRev.102.917.2. (Cited on pages 4 and 141)

[Hon66] A. Honig. *Neutral-impurity scattering and impurity Zeeman spectroscopy in semiconductors using highly spin-polarized carriers*. Phys. Rev. Lett. **17**, 186 (1966). doi:10.1103/PhysRevLett.17.186. (Cited on page 31)

[Hon78] A. Honig and M. Moroz. *Precision absolute measurements of strong and highly inhomogeneous magnetic fields*. Rev. Sci. Instrum. **49**, 183 (1978). doi:10.1063/1.1135379. (Cited on pages 37 and 116)

[Hu06] X. Hu and S. Das Sarma. *Charge-fluctuation-induced dephasing of exchange-coupled spin qubits*. Phys. Rev. Lett. **96**, 100501 (2006). doi:10.1103/PhysRevLett.96.100501. (Cited on page 8)

[Hua99] X. Huang, W.-C. Lee, C. Kuo, D. Hisamoto, L. Chang, J. Kedzierski, E. Anderson, H. Takeuchi, Y.-K. Choi, K. Asano, V. Subramanian, T.-J. King, J. Bokor, and C. Hu. *Sub 50-nm FinFET: PMOS*. IEDM Tech. Dig. 67 (1999). doi:10.1109/IEDM.1999.823848. (Cited on page 13)

[Hue09a] H. Huebl, R. P. Starrett, D. R. McCamey, A. J. Ferguson, and L. H. W. van Beveren. *Electrically detected magnetic resonance using radio-frequency reflectometry*. Rev. Sci. Instrum. **80**, 114705 (2009). doi:10.1063/1.3258206. (Cited on page 159)

[Hue09b] A. K. Huettel, G. A. Steele, B. Witkamp, M. Poot, L. P. Kouwenhoven, and H. S. J. van der Zant. *Carbon nanotubes as ultrahigh quality factor mechanical resonators*. Nano Lett. **9**, 2547 (2009). doi:10.1021/nl900612h. (Cited on page 88)

[Iij91] S. Iijima. *Helical microtubules of graphitic carbon*. Nature **354**, 56 (1991). doi:10.1038/354056a0. (Cited on pages 11 and 89)

[Iij93] S. Iijima and T. Ichihasi. *Single-shell carbon nanotubes of 1-nm diameter*. Nature **363**, 603 (1993). doi:10.1038/363603a0. (Cited on pages 85 and 89)

[Ilb03] H. Ilbach and H. Lüth. *Solid-State Physics: An Introduction to Principles of Materials Science*. Springer Berlin, 2003. (Cited on page 127)

[Iso93] J. Isoya, S. Yamasaki, H. Okushi, A. Matsuda, and K. Tanaka. *Electron-spin-echo envelope-modulation study of the distance between dangling bonds and hydrogen atoms in hydrogenated amorphous silicon*. Phys. Rev. B **47**, 7013 (1993). doi:10.1103/PhysRevB.47.7013. (Cited on page 19)

[Ist99] A. A. Istratov, H. Hieslmair, and E. R. Weber. *Iron and its complexes in silicon*. Appl. Phys. A **69**, 13 (1999). doi:10.1007/s003390050968. (Cited on pages 17, 59, and 61)

[Ist00] A. A. Istratov, H. Hieslmair, and E. R. Weber. *Iron contamination in silicon technology*. Appl. Phys. A **70**, 489 (2000). doi:10.1007/s003390051074. (Cited on page 16)

[Jel04] F. Jelezko, T. Gaebel, I. Popa, A. Gruber, and J. Wrachtrup. *Observation of coherent oscillations in a single electron spin*. Phys. Rev. Lett. **92**, 076401 (2004). doi:10.1103/PhysRevLett.92.076401. (Cited on page 29)

[Jar04] P. Jarillo-Herrero, S. Sapmaz, C. Dekker, L. P. Kouwenhoven, and H. S. J. van der Zant. *Electron-hole symmetry in a semiconducting carbon nanotube quantum dot*. Nature **429**, 389 (2004). doi:10.1038/nature02568. (Cited on pages 87 and 88)

[Jia01] H. W. Jiang and E. Yablonovitch. *Gate-controlled electron spin resonance in GaAs/$Al_xGa_{1-x}As$ heterostructures*. Phys. Rev. B **64**, 041301 (2001). doi:10.1103/PhysRevB.64.041307. (Cited on page 32)

[Joh05a] A. C. Johnson, J. M. Petta, J. R. Taylor, A. Yacoby, M. D. Lukin, C. M. Marcus, M. P. Hanson, and A. C. Gossard. *Triplet-singlet spin relaxation via nuclei in a double quantum dot*. Nature **435**, 925 (2005). doi:10.1038/nature03815. (Cited on page 4)

[Joh05b] A. C. Johnson, J. R. Petta, C. M. Marcus, M. P. Hanson, and A. C. Gossard. *Singlet-triplet spin blockade and charge sensing in a few-electron double quantum dot*. Phys. Rev. B **72**, 165308 (2005). doi:10.1103/PhysRevB.72.165308. (Cited on page 33)

[Jos93] M. José-Yacamàn, M. Miki-Yoshida, L. Rendón, and J. G. Santiesteban. *Catalytic growth of carbon microtubules with fullerene structure*. Appl. Phys. Lett. **62**, 657 (1993). doi:10.1063/1.109315. (Cited on page 11)

[Kan98] B. E. Kane. *A silicon-based nuclear spin quantum computer*. Nature **393**, 133 (1998). doi:10.1038/30156. (Cited on pages 3 and 33)

[Kan00] P. Kanschat, K. Lips, and W. Fuhs. *Identification of non-radiative recombination path in microcrystalline silicon (μc-Si:H)*. J. Non-Cryst. Solids **266**, 524 (2000). doi:10.1016/S0022-3093(99)00807-8. (Cited on page 37)

[Kap78] D. Kaplan, I. Solomon, and N. F. Mott. *Explanation of the large spin-dependent recombination effect in semiconductors*. J. Phys. **39**, L–51 (1978). doi:10.1051/jphyslet:0197800390405100. (Cited on page 36)

[Kas93] M. A. Kastner. *Artificial atoms*. Phys. Today **46**, 24 (1993). doi:10.1063/1.881393. (Cited on page 5)

[Kaw82] Y. Kawaguchi and S. Kawaji. *A study of electron mobility and electron-phonon interaction in Si MOSFETs by negative magnetoresistance experiments*. Jpn. J. Appl. Phys. **21**, L709 (1982). doi:10.1143/JJAP.21.L709. (Cited on page 130)

[Kaw97] G. Kawachi, C. F. O. Graeff, M. S. Brandt, and M. Stutzmann. *Saturation measurements of electrically detected magnetic resonance in hydrogenated amorphous silicon based thin-film transistors*. Jpn. J. Appl. Phys. **36**, 121 (1997). doi:10.1143/JJAP.36.121. (Cited on pages 35 and 81)

[Kel99] K. F. Kelton, R. Falster, D. Gambaro, M. Olmo, M. Cornara, and P. F. Wei. *Oxygen precipitation in silicon: Experimental studies and theoretical investigations within the classical theory of nucleation*. J. Appl. Phys. **85**, 8097 (1999). doi:10.1063/1.370648. (Cited on page 52)

[Kik98] J. M. Kikkawa and D. D. Awschalom. *Resonant spin amplification in n-type GaAs*. Phys. Rev. Lett. **80**, 4313 (1998). doi:10.1103/PhysRevLett.80.4313. (Cited on page 4)

[Kim03] W. Kim, A. Javey, O. Vermesh, Q. Wang, Y. Li, and H. Dai. *Hysteresis caused by water molecules in carbon nanotube field-effect transistors*. Nano Lett. **3**, 193 (2003). doi:10.1021/nl0259232. (Cited on page 110)

[Kim05] T. Kim, J.-M. Zuo, E. A. Olson, and I. Petrov. *Imaging suspended carbon nanotubes in field-effect transistors configured with microfabricated slits for transmission electron microscopy*. Appl. Phys. Lett. **87**, 173108 (2005). doi:10.1063/1.2115070. (Cited on page 85)

[Kis81] N. Kishimoto, K. Morigaki, and K. Murakami. *Conductivity change due to electron spin resonance in amorphous Si-Au system*. J. Phys. Soc. Jpn. **50**, 1970 (1981). doi:10.1143/JPSJ.50.1970. (Cited on page 33)

[Kit96] C. Kittel. *Introduction to Solid State Physics*. John Wiley & Sons, New York, USA, 1996. (Cited on pages 16, 66, and 123)

[Kle29] O. Klein. *Die Reflexion von Elektronen an einem Potentialsprung nach der Relativistischen Dynamik von Dirac*. Z. Phys. **53**, 157 (1929). doi:10.1007/BF01339716. (Cited on page 10)

[Koe11] P. M. Koenraad and E. Flatté. *Single dopants in semiconductors*. Nature Mat. **10**, 91 (2011). doi:10.1038/nmat2940. (Cited on page 1)

[Koi00] M. Koizuka and H. Yamada-Kaneta. *Electron spin resonance centers associated with oxygen precipitates in Czochralski silicon crystals*. J. Appl. Phys. **88**, 1784 (2000). doi:10.1063/1.1305325. (Cited on pages 61 and 63)

[Kon64] J. Kondo. *Resistance minimum in dilute magnetic alloys*. Prog. Theor. Phys. **32**, 37 (1964). doi:10.1143/PTP.32.37. (Cited on page 88)

[Kon98] J. Kong, H. T. Soh, A. M. Cassell, C. F. Quate, and H. Dai. *Synthesis of individual single-walled carbon nanotubes on patterned silicon wafers*. Nature **395**, 878 (1998). doi:10.1038/27632. (Cited on page 100)

[Kop05] F. H. L. Koppens, J. A. Folk, J. M. Elzerman, R. Hanson, L. H. W. van Beveren, I. T. Vink, H. P. Tranitz, W. Wegscheider, L. P. Kouwenhoven, and L. M. K. Vanderypen. *Control and detection of singlet-triplet mixing in a random nuclear field*. Science **309**, 1346 (2005). doi:10.1126/science.1113719. (Cited on page 4)

[Kop06] F. H. L. Koppens, C. Buizert, K. J. Tielrooij, I. T. Vink, K. C. Nowack, T. Meunier, L. P. Kouwenhoven, and L. M. K. Vandersypen. *Driven coherent oscillations of a single electron spin in a quantum dot*. Nature **442**, 766 (2006). doi:10.1038/nature05065. (Cited on page 6)

[Kop08] F. H. L. Koppens, K. C. Nowack, and L. M. K. Vandersypen. *Spin echo of a single electron spin in a quantum dot*. Phys. Rev. Lett. **100**, 236802 (2008). doi:10.1103/PhysRevLett.100.236802. (Cited on page 4)

[Kou98] L. P. Kouwenhoven and C. M. Marcus. *Quantum dots*. Phys. World **11**, 35 (1998). http://physicsworldarchive.iop.org/full/pwa-pdf/11/6/phwv11i6a26.pdf. (Cited on page 5)

[Kue08] F. Kuemmeth, S. Ilani, D. C. Ralph, and P. L. McEuen. *Coupling of spin and orbital motion of electrons in carbon nanotubes*. Nature **452**, 448 (2008). doi:10.1038/nature06822. (Cited on pages 10, 12, and 88)

[Kuh08] K. Kuhn, C. Kenyon, A. Kornfeld, M. Liu, A. Maheshwari, W. Shih, S. Sivakumar, G. Taylor, P. VanDerVoorn, and K. Zawadzki. *Managing process variation in Intel's* 45 *nm CMOS technology*. Intel Technol. J. **12**, 93 (2008). doi:10.1535/itj.1202.03. (Cited on page 13)

[Kwo91] K. C. Kwong, J. Callaway, N. Y. Du, and R. A. La Violette. *Elastic scattering of electrons by neutral donor impurities in silicon*. Phys. Rev. B **43**, 1576 (1991). doi:10.1103/PhysRevB.43.1576. (Cited on page 133)

[Lad10] T. D. Ladd, F. Jelezko, R. Laflamme, Y. Nakamura, C. Monroe, and J. L. O'Brian. *Quantum computers*. Nature **464**, 45 (2010). doi:10.1038/nature08812. (Cited on page 2)

[Lai07] E. A. Laird, C. Barthel, E. I. Rashba, C. M. Marcus, M. P. Hanson, and A. C. Gossard. *Hyperfine-mediated gate-driven electron spin resonance*. Phys. Rev. Lett. **99**, 246601 (2007). doi:10.1103/PhysRevLett.99.246601. (Cited on page 7)

[Lan08a] V. Lang. *Characterisation of two-dimensional Electron Systems in natural and isotopically pure Si/SiGe Heterostructures*. Diploma Thesis, Walter Schottky Institut, Munich, Germany, 2008. (Cited on pages 8 and 95)

[Lan08b] G. P. Lansbergen, R. Rahman, C. J. Wellard, I. Woo, J. Caro, N. Collaert, S. Biesemans, L. C. L. Klimeck, G. Hollenberg, and S. Rogge. *Gate-induced quantum-confinement transition of a single dopant atom in a silicon FinFET*. Nature Phys. **4**, 656 (2008). doi:10.1038/nphys994. (Cited on page 14)

[Lan11] V. Lang, C. C. Lo, R. E. George, S. A. Lyon, T. Schenkel, J. Bokor, A. Ardavan, and J. J. L. Morton. *Electrically detected magnetic resonance in a W-band microwave cavity*. Rev. Sci. Instrum. **82**, 034704 (2011). doi:10.1063/1.3557395. (Cited on page 115)

[Lan12] V. Lang, J. D. Murphy, R. J. Falster, and J. J. L. Morton. *Spin-dependent recombination in Czochralski silicon containing oxide precipitates*. J. Appl. Phys. **111**, 013710 (2012). doi:10.1063/1.3675449. (Cited on page 51)

[Las08] B. Lasangne, D. Garcia-Sanchez, A. Aguasca, and A. Bachtold. *Ultrasensitive mass sensing with a nanotube electromechanical resonator*. Nano Lett. **8**, 3735 (2008). doi:10.1021/nl801982v. (Cited on page 88)

[Lee77] Y. H. Lee, R. L. Kleinhenz, and J. W. Corbett. *EPR of a thermally induced defect in silicon*. Appl. Phys. Lett. **31**, 142 (1977). doi:10.1063/1.89630. (Cited on page 61)

[Lee83] Y. H. Lee and M.-M. Chen. *Silicon etching mechanism and anisotropy in CF_4+O_2 plasma*. J. Appl. Phys. **54**, 5966 (1983). doi:10.1063/1.331774. (Cited on page 93)

[Lee07] J. S. Lee, S. Ryu, K. Yoo, I. S. Choi, W. S. Yun, and J. Kim. *Origin of gate hysteresis in carbon nanotube field-effect transistors*. J. Phys. Chem. C **111**, 12504 (2007). doi:10.1021/jp074692q. (Cited on page 110)

[Len84] P. M. Lenahan and W. K. Schubert. *Effects of light and modulation frequency on spin-dependent trapping at silicon grain boundaries*. Phys. Rev. B **30**, 1544 (1984). doi:10.1103/PhysRevB.30.1544. (Cited on page 40)

[Len90] P. M. Lenahan and M. A. Jupina. *Spin dependent recombination at the silicon/silicon dioxide interface*. Colloids and Surfaces **45**, 191 (1990). doi:10.1016/0166-6622(90)80023-W. (Cited on pages 41 and 66)

[Lep72] D. J. Lepine. *Spin-dependent recombination on silicon surface*. Phys. Rev. B **6**, 436 (1972). doi:10.1103/PhysRevB.6.436. (Cited on pages 29, 34, 35, 40, and 67)

[Lev01] M. H. Levitt. *Spin dynamics: Basics of nuclear magnetic resonance*. John Wiley & Sons, New York, USA, 2001. (Cited on page 25)

[Lev02] J. Levy. *Universal quantum computation with spin-1/2 pairs and Heisenberg exchange*. Phys. Rev. Lett. **89**, 147902 (2002). doi:10.1103/PhysRevLett.89.147902. (Cited on page 3)

[Lin10] V. Lindroos, M. Tilli, A. Lehto, and T. Motooka. *Handbook of Silicon Based MEMS Materials and Technologies*. William Andrew, Norwich, New York, USA, 2010. http://www.sciencedirect.com/science/book/9780815515944. (Cited on page 102)

[Lip92] K. Lips, S. Schuette, and W. Fuhs. *Microwave-induced resonant changes in transport and recombination in hydrogenated amorphous silicon*. Philos. Mag. B **65**, 945 (1992). doi:10.1080/13642819208217912. (Cited on page 73)

[Lip11] K. Lips, M. Fehr, and J. Behrends. *Electron-Spin Resonance (ESR) in Hydrogenated Amorphous Silicon (a-Si:H), in Advanced Characterization Techniques for Thin Film Solar Cells (ed. D. Abou-Ras, T. Kirchartz,*

and U. Rau). Wiley, Chichester, England, Hoboken, NJ, 2011. doi:10.1002/9783527636280.ch10. (Cited on page 72)

[Liu08] H. W. Liu, T. Fujisawa, Y. Ono, H. Inokawa, A. Fujiwara, K. Takashina, and Y. Hirayama. *Pauli-spin-blockade transport through a silicon double quantum dot*. Phys. Rev. B **77**, 073310 (2008). doi:10.1103/PhysRevB.77.073310. (Cited on pages 5 and 33)

[Lo07] C. C. Lo, J. Boker, T. Schenkel, J. He, A. M. Tyryshkin, and S. A. Lyon. *Spin-dependent scattering off neutral antimony donors in ^{28}Si field-effect transistors*. Appl. Phys. Lett. **91**, 242106 (2007). doi:10.1063/1.2817966. (Cited on page 33)

[Lo09] C. C. Lo, A. Persaud, S. Dhuey, D. Olynick, F. Borondics, M. C. Martin, H. A. Bechtel, J. Bokor, and T. Schenkel. *Device fabrication and transport measurements of FinFETs built with ^{28}Si SOI wafers toward donor qubits in silicon*. Semicond. Sci. Technol. **24**, 105022 (2009). doi:10.1088/0268-1242/24/10/105022. (Cited on page 124)

[Lo11a] C. C. Lo. *Electrical Detection of Spin-Dependent Transport in Silicon*. PhD Thesis, Electrical Engineering and Computer Science, University of California at Berkeley, USA, 2011. http://www.eecs.berkeley.edu/Pubs/TechRpts/2011/EECS-2011-54.html. (Cited on pages 123 and 124)

[Lo11b] C. C. Lo, V. Lang, R. E. George, J. J. L. Morton, A. M. Tyryshkin, S. A. Lyon, J. Bokor, and T. Schenkel. *Electrically detected magnetic resonance of neutral donors interacting with a two-dimensional electron gas*. Phys. Rev. Lett. **106**, 207601 (2011). doi:10.1103/PhysRevLett.106.207601. (Cited on page 115)

[Lo12] C. C. Lo, F. R. Bradbury, A. M. Tyryshkin, C. D. Weis, J. Bokor, T. Schenkel, and S. A. Lyon. *Suppression of microwave rectification effects in electrically detected magnetic resonance measurements*. Appl. Phys. Lett. **100**, 063510 (2012). doi:10.1063/1.3684247. (Cited on page 123)

[Los98] D. Loss and D. P. DiVincenzo. *Quantum computation with quantum dots*. Phys. Rev. A **57**, 120 (1998). doi:10.1103/PhysRevA.57.120. (Cited on page 3)

[Mad02] O. Madelung, U. Rössler, and M. Schulz. *Landolt-Börnstein – Group III Condensed Matter 41A 1B, Numerical Data and Functional Relationships in Science and Technology*. Springer, New York, USA, 2002. doi:10.1007/b80447. (Cited on page 10)

[Mai97] D. C. Maier. *New frontiers in X-band cw-EPR sensitivity*. Bruker Rep. **144**, 13 (1997). (Cited on page 115)

[Mar98] R. Martel, T. Schmidt, H. R. Shea, T. Hertel, and P. Avouris. *Single- and multi-wall carbon nanotube field-effect transistors.* Appl. Phys. Lett. **73**, 2447 (1998). (Cited on page 85)

[Mas99] P. Masson, J.-L. Autran, and J. Brini. *On the tunneling component of charge pumping current in ultrathin gate oxide MOSFETs.* IEEE Electron Device Lett. **20**, 92 (1999). doi:10.1109/55.740662. (Cited on page 34)

[Mas04] N. Mason, M. J. Biercuk, and C. M. Marcus. *Local gate control of a carbon nanotube double quantum dot.* Science **303**, 655 (2004). doi:10.1126/science.1093605. (Cited on pages 5 and 11)

[Mat97] T. Matsukawa, T. Fukai, S. Suzuki, K. Hara, M. Koh, and I. Ohdomari. *Development of single-ion implantation – controllability of implanted ion number.* Appl. Surf. Sci. **117-118**, 677 (1997). doi:10.1016/S0169-4332(97)80163-8. (Cited on page 13)

[Mat06] J. Matsunami, M. Ooya, and T. Okamato. *Electrically detected electron spin resonance in a high-mobility silicon quantum well.* Phys. Rev. Lett. **97**, 066602 (2006). doi:10.1103/PhysRevLett.97.066602. (Cited on pages 15 and 133)

[Mau12] B. M. Maune, M. G. Borselli, B. Huang, T. D. Ladd, P. W. Deelman, K. S. Holabird, A. A. Kiselev, I. Alvarado-Rodriguez, R. S. Ross, A. E. Schmitz, M. Sokolich, C. A. Watson, M. F. Gyure, and A. T. Hunter. *Coherent singlet-triplet oscillations in a silicon-based double quantum dot.* Nature **481**, 344 (2012). doi:10.1038/nature10707. (Cited on page 4)

[Max66] R. Maxwell and A. Honig. *Neutral-impurity scattering experiments in silicon with highly spin-polarized electrons.* Phys. Rev. Lett. **17**, 188 (1966). doi:10.1103/PhysRevLett.17.188. (Cited on pages 15 and 32)

[McC06] D. R. McCamey, H. Huebl, M. S. Brandt, W. D. Hutchison, J. C. McCallum, R. G. Clark, and A. R. Hamilton. *Electrically detected magnetic resonance in ion-implanted Si:P nanostructures.* Appl. Phys. Lett. **89**, 182115 (2006). doi:10.1063/1.2358928. (Cited on page 29)

[McC08] D. R. McCamey, G. W. Morley, H. A. Seipel, L. C. Brunel, J. van Tol, and C. Boehme. *Spin-dependent processes at the crystalline Si/SiO_2 interface at high magnetic fields.* Phys. Rev. B **78**, 045303 (2008). doi:10.1103/PhysRevB.78.045303. (Cited on page 116)

[McC10] D. R. McCamey, J. van Tol, G. W. Morley, and C. Boehme. *Electronic spin storage in an electrically readable nuclear spin memory with a lifetime > 100 seconds.* Science **330**, 1652 (2010). doi:10.1126/science.1197931. (Cited on page 116)

[McE99] P. L. McEuen, M. Bockrath, D. H. Cobden, Y.-G. Yoon, and S. G. Louie. *Disorder, pseudospins, and backscattering in carbon nanotubes*. Phys. Rev. Lett. **83**, 5098 (1999). doi:10.1103/PhysRevLett.83.5098. (Cited on page 87)

[Mch98] T. Mchedlidze and K. Matsumoto. *Electrically detected magnetic resonance signal from iron contaminated Czochralski silicon crystal*. J. App. Phys. **83**, 4042 (1998). doi:10.1063/1.367160. (Cited on page 64)

[Mey04] J. C. Meyer, D. Obergfell, S. Roth, S. Yang, and S. Yang. *Transmission electron microscopy and transistor characteristics of the same carbon nanotube*. Appl. Phys. Lett. **85**, 2911 (2004). doi:10.1063/1.1805701. (Cited on page 85)

[Min04] E. D. Minot, Y. Yaish, V. Sazonova, and P. L. McEuen. *Determination of electron orbital magnetic moments in carbon nanotubes*. Nature **428**, 536 (2004). doi:10.1038/nature02425. (Cited on page 87)

[Mis00] T. D. Mishima, P. M. Lenahan, and W. Weber. *Do P_{b1} centers have levels in the Si band gap? Spin-dependent recombination study of the P_{b1} "hyperfine spectrum"*. Appl. Phys. Lett. **76**, 3771 (2000). doi:10.1063/1.126776. (Cited on page 69)

[Mit05] M. Mitic, S. E. Andresen, C. Yang, T. Hopf, V. Chan, E. Gauja, F. E. Hudson, T. M. Buehler, R. Brenner, A. J. Ferguson, C. I. Pakes, S. M. Haerne, G. Tamanyan, D. J. Reilly, A. R. Hamilton, D. N. Jamieson, A. S. Dzurak, and R. G. Clark. *Single atom Si nanoelectronics using controlled single-ion implantation*. Microelectron. Eng. **78-79**, 279 (2005). doi:10.1016/j.mee.2004.12.096. (Cited on page 13)

[Miz07] J. Mizubayashi, J. Haruyama, I. Takesue, T. Okazaki, H. Shinohara, Y. Harada, and Y. Awano. *Anomalous Coulomb diamonds and power-law behavior sensitive to back-gate voltages in carbon nanoscale peapod quantum dots*. Phys. Rev. B **75**, 205431 (2007). (Cited on page 4)

[Mol09] F. Molitor, S. Droescher, J. Guettinger, A. Jacobsen, C. Stampfer, T. Ihn, and K. Ensslin. *Transport through graphene double dots*. Appl. Phys. Lett. **94**, 222107 (2009). doi:10.1063/1.3148367. (Cited on pages 5 and 11)

[Mor74] K. Morigaki and M. Onda. *Spin-dependent conductivity of phosphorus-doped silicon in the intermediate concentration region*. J. of the Phys. Soc. of Jpn **36**, 1049 (1974). doi:10.1143/JPSJ.36.1049. (Cited on pages 15 and 130)

[Mor05] S. Moriyama, T. Fuse, M. Suzuki, Y. Aoyagi, and K. Ishibashi. *Four-electron shell structures and an interacting two-electron system in carbon-nanotube quantum dots*. Phys. Rev. Lett. **94**, 186806 (2005). doi:10.1103/PhysRevLett.94.186806. (Cited on page 88)

[Mor08a] G. W. Morley, L.-C. Brunel, and J. van Tol. *A multifrequency high-field pulsed electron paramagnetic resonance/electron-nuclear double resonance spectrometer*. Rev. Sci. Instrum. **79**, 064703 (2008). doi:10.1063/1.2937630. (Cited on page 116)

[Mor08b] G. W. Morley, D. R. McCamey, H. A. Seipel, L.-C. Brunel, J. vam Tol, and C. Boehme. *Long-lived spin coherence in silicon with an electrical spin trap readout*. Phys. Rev. Lett. **101**, 207602 (2008). doi:10.1103/PhysRevLett.101.207602. (Cited on pages 116 and 129)

[Mor09] A. Morello, C. C. Escott, H. Huebl, L. H. Willems van Beveren, L. C. L. Hollenberg, D. N. Jamieson, A. S. Dzurak, and R. G. Clark. *Architecture for high-sensitivity single-shot readout and control of the electron spin of individual donors in silicon*. Phys. Rev. B **80**, 081307 (2009). doi:10.1103/PhysRevB.80.081307. (Cited on pages 14 and 33)

[Mor10] A. Morello, J. J. Pla, F. A. Zwanenburg, K. W. Chan, K. Y. Tan, M. Huebl, H. Möttönen, D. Nugroho, C. Yang, J. A. Van Donkelaar, A. D. C. Alves, D. N. Jamieson, C. C. Escott, C. L. Hollernberg, R. G. Clark, and A. S. Dzurak. *Single-shot readout of an electron spin in silicon*. Nature **467**, 687 (2010). doi:10.1038/nature09392. (Cited on page 15)

[Mor11] J. J. L. Morton, D. R. McCamey, M. A. Eriksson, and S. A. Lyon. *Embracing the quantum limit in silicon computing*. Nature **479**, 345 (2011). doi:10.1038/nature10681. (Cited on page 5)

[Mov80] B. Movaghar, B. Ries, and L. Schweitzer. *Theory of the resonant and nom-resonant conductivity changes in amorphus silicon*. Philos. Mag. B **41**, 159 (1980). doi:10.1080/13642818008245377. (Cited on pages 37 and 40)

[Mul86] R. S. Muller and T. I. Kamins. *Device electronics for integrated circuits*. John Wiley & Sons, New York, USA, 1986. (Cited on pages 17 and 48)

[Muo10] M. Muoth, T. Helbling, L. Durrer, S.-W. Lee, C. Roman, and C. Hierold. *Hysteresis-free operation of suspended carbon nanotube transistors*. Nature Nanotechnol. **5**, 589 (2010). doi:10.1038/nnano.2010.129. (Cited on page 110)

[Mur11a] J. D. Murphy, K. Bothe, M. Olmo, V. V. Voronkov, and R. J. Falster. *The effect of oxide precipitates on minority carrier lifetime in p-type silicon*. J. Appl. Phys. **110**, 053713 (2011). doi:10.1063/1.3632067. (Cited on pages 19, 20, 49, 50, 52, 53, 66, 69, and 71)

[Mur11b] J. D. Murphy and R. J. Falster. *Contamination of silicon by iron at temperatures below* 800 °*c*. Phys. Stat. Sol. RRL **5**, 370 (2011). doi:10.1002/pssr.201105388. (Cited on pages 53 and 59)

[Mye00] S. M. Myers, M. Seibt, and W. Schröter. *Mechanisms of transition-metal gettering in silicon*. J. Appl. Phys. **88**, 3795 (2000). doi:10.1063/1.1289273. (Cited on page 20)

[Nag99] H. Nagel, C. Berge, and A. G. Aberle. *Generalized analysis of quasi-steady-state and quasi-transient measurements of carrier lifetimes in semiconductors*. J. Appl. Phys. **86**, 6218 (1999). doi:10.1063/1.371633. (Cited on page 70)

[Nay11] B. Naydenov, F. Dolde, L. T. Hall, C. Shin, H. Fedder, L. C. L. Hollenberg, F. Jelezko, and J. Wrachtrup. *Dynamical decoupling of a single-electron spin at room temperature*. Phys. Rev. B **83**, 081201 (2011). doi:10.1103/PhysRevB.83.081201. (Cited on page 4)

[Neu95] A. Neugroschel, C.-T. Sah, and M. S. Carroll. *Random telegraphic signals in silicon bipolar junction transistors*. Appl. Phys. Lett. **66**, 2879 (1995). doi:10.1063/1.113460. (Cited on page 14)

[New84] D. New and T. G. Castner. *Donor clusters in silicon. Results of ESR measurements*. Phys. Rev. B **29**, 2077 (1984). doi:10.1103/PhysRevB.29.2077. (Cited on page 128)

[Nie00] M. A. Nielsen and I. L. Chuang. *Quantum Computation and Quantum Information*. Cambridge University Press, Cambridge, UK, 2000. (Cited on page 1)

[Nov04] K. S. Novoselov, A. K. Geim, S. V. Morozov, D. Jiang, Y. Zhang, S. V. Dubonos, I. V. Grigorieva, and A. A. Firsov. *Electric field effect in atomically thin carbon films*. Science **306**, 666 (2004). doi:10.1126/science.1102896. (Cited on page 10)

[Nov05a] K. S. Novoselov, A. K. Geim, S. V. Morozov, D. Jiang, M. I. Katsnelson, I. V. Grigorieva, S. V. Dubonos, and A. A. Firsov. *Two-dimensional gas of massless Dirac fermions in graphene*. Nature **438**, 197 (2005). doi:10.1038/nature04233. (Cited on page 10)

[Nov05b] K. S. Novoselov, D. Jiang, F. Schedin, T. J. Booth, V. V. Khotkevich, S. V. Morozov, and A. K. Geim. *Two-dimensional atomic crystals*. Proc. Natl. Acad. Sci. USA **102**, 10451 (2005). doi:10.1073/pnas.0502848102. (Cited on page 10)

[Nyg00] J. Nygård, D. H. Cobden, and P. E. Lindelof. *Kondo physics in carbon nanotubes*. Nature **408**, 342 (2000). doi:10.1038/35042545. (Cited on page 88)

[Nyg01] J. Nygård and D. H. Cobden. *Quantum dots in suspended single-wall carbon nanotubes*. Appl. Phys. Lett. **79**, 4216 (2001). doi:10.1063/1.1428117. (Cited on page 110)

[Nyg08] J. Nygård. *Carbon nanotubes: Old nanotubes, new tricks*. Nature Phys. **4**, 266 (2008). doi:10.1038/nphys924. (Cited on page 88)

[Oka04] M. Okamato, T. Ooya, K. Hosoya, and S. Kawaji. *Spin polarization and metallic behavior in a silicon two-dimensional electron systematic*. Phys. Rev. B **69**, 041202 (2004). doi:10.1103/PhysRevB.69.041202. (Cited on pages 133 and 135)

[Ono02] K. Ono, D. G. Austing, and S. Tarucha. *Current rectification by Pauli exclusion in a weakly coupled double quantum dot system*. Science **297**, 1313 (2002). doi:10.1126/science.1070958. (Cited on page 33)

[Orb61] R. Orbach. *On the theory of spin-lattice relaxation in paramagnetic salts*. Proc. Phys. Soc. **77**, 821 (1961). doi:10.1088/0370-1328/77/4/301. (Cited on page 141)

[Pak73] G. E. Pake and T. L. Estle. *The Physical Principles of Electron Paramagnetic Resonance*. W. A. Benjamin, Massachusetts, USA, 1973. (Cited on page 27)

[Pea49] G. L. Pearson and J. Bardeen. *Electrical properties of pure silicon and silicon alloys containing boron and phosphorus*. Phys. Rev. **75**, 865 (1949). doi:10.1103/PhysRev.75.865. (Cited on page 31)

[Pet05] J. R. Petta, A. C. Jonhson, J. M. Taylor, E. A. Laird, A. Yacoby, M. D. Lukin, C. M. Marcus, M. P. Hanson, and A. C. Gossard. *Coherent manipulation of coupled electron spins in semiconductor quantum dots*. Science **309**, 2180 (2005). doi:10.1126/science.1116955. (Cited on pages 4 and 7)

[Piz86] S. Pizzini, L. Bigoni, M. Beghi, and C. Chemelli. *On the effect of impurities on the photovoltaic behavior of solar grade silicon*. J. Electrochem. Soc. **133**, 2363 (1986). doi:10.1149/1.2108409. (Cited on page 16)

[Pio08] M. Pioro-Ladrière, T. Obata, Y. Tokura, Y.-S. Shin, T. Kubo, K. Yoshida, T. Taniyama, and S. Tarucha. *Electrically driven single-electron spin resonance in a slanting Zeeman field*. Nature Phys. **4**, 776 (2008). doi:10.1038/nphys1053. (Cited on page 7)

[Pla04] G. Platero and R. Aguado. *Photon-assisted transport in semiconductor nanostructures*. Phys. Rep. **395**, 1 (2004). doi:10.1016/j.physrep.2004.01.004. (Cited on page 6)

[Pla11] J. Pla and A. Morello. *International Workshop on Silicon Quantum Electronics, Denver, USA, and private communication*. 2011. (Cited on page 4)

[Poi81] E. H. Poindexter, P. J. Caplan, B. E. Deal, and R. R. Razouk. *Interface states and electron spin resonance centers in thermally oxidized (111) and (100) silicon wafers*. J. Appl. Phys. **52**, 879 (1981). doi:10.1063/1.328771. (Cited on pages 18 and 61)

[Poo83] C. P. Poole. *Electron Paramagnetic Resonance: A Comprehensive Treatise on Experimental Techniques*. Dover Publications Inc., Mineola, New York, USA, 1983. (Cited on pages 6, 38, 107, 120, 136, and 162)

[Pow02] M. J. Powell, S. C. Deane, and R. B. Wehrspohn. *Microscopic mechanisms for creation and removal of metastable dangling bonds in hydrogenated amorphous silicon*. Phys. Rev. B **66**, 155212 (2002). doi:10.1103/PhysRevB.66.155212. (Cited on page 19)

[Pud02] V. M. Pudalov, G. Brunthaler, A. Prinz, and G. Bauer. *Weak anisotropy and disorder dependence of the in-plane magnetoresistance in high-mobility (100) Si-inversion layers*. Phys. Rev. Lett. **88**, 076401 (2002). doi:10.1103/PhysRevLett.88.076401. (Cited on pages 133 and 135)

[Rab37] I. I. Rabi. *Space quantization in a gyrating magnetic field*. Phys. Rev. **51**, 652 (1937). doi:10.1103/PhysRev.51.652. (Cited on page 43)

[Rad52] L. V. Radushkevich and V. M. Lukyanovich. *O strukture ugleroda, obrazujucegosja pri termiceskom razlozenii okisi ugleroda na zeleznom kontakte (about the structure of carbon formed by thermal decomposition of carbon monoxide on iron substrate)*. Zurn. Fisic. Chim. **26**, 88 (1952). http://nanotube.msu.edu/HSS/2006/4/2006-4.pdf. (Cited on page 85)

[Ral84] K. S. Ralls, W. J. Skocpol, L. D. Jackel, R. E. Howard, L. A. Fetter, R. W. Epworth, and D. M. Tennant. *Discrete resistance switching in submicrometer silicon inversion layers: Individual interface traps and low-frequency ($1/f$?) noise*. Phys. Rev. Lett. **52**, 228 (1984). doi:10.1103/PhysRevLett.52.228. (Cited on page 14)

[Ram50] N. F. Ramsey. *A molecular beam resonance method with separated oscillating fields*. Phys. Rev. **78**, 695 (1950). doi:10.1103/PhysRev.78.695. (Cited on page 43)

[Rei08] D. J. Reilly, J. M. Taylor, J. R. Petta, C. M. Marcus, M. P. Hanson, and A. C. Gossard. *Suppressing spin qubit dephasing by nuclear state preparation*. Science **321**, 817 (2008). doi:10.1126/science.1159221. (Cited on page 8)

[Rei05] S. Rein and S. W. Glunz. *Electronic properties of interstitial iron and iron-boron pairs determined by means of advanced lifetime spectroscopy*. J. Appl. Phys. **98**, 113711 (2005). doi:10.1063/1.2106017 (Cited on page 17)

[Rug04] D. Rugar, R. Budakian, H. J. Mamin, and B. W. Chui. *Single spin detection by magnetic resonance force microscopy*. Nature **430**, 329 (2004). doi:10.1038/nature02658. (Cited on page 29)

[Sai09] J. Sailer, V. Lang, G. Abstreiter, G. Tsuchiya, K. M. Itoh, J. W. Ager, E. E. Haller, D. Kupidura, D. Harbusch, S. Ludwig, and D. Bougeard. *A Schottky top-gated two-dimensional electron system in a nuclear spin free Si/SiGe heterostructure*. Phys. Stat. Sol. RRL **3**, 61 (2009). doi:10.1002/pssr.200802275. (Cited on page 8)

[San06] S. Sanvito and A. R. Rocha. *Molecular-Spintronics: The art of driving spin through molecules*. J. Comput. Theor. Nanosci. **3**, 624 (2006). doi:10.1166/jctn.2006.003. (Cited on page 1)

[Sar08] M. Sarovar, K. C. Young, T. Schenkel, and K. B. Whaley. *Quantum nondemolition measurements of single donor spins in semiconductors*. Phys. Rev. B **78**, 245302 (2008). doi:10.1103/PhysRevB.78.245302. (Cited on page 13)

[Sat08] Y. Sato, K. Yanagi, Y. Miyata, K. Suenaga, H. Kataura, and S. Iijima. *Chiral-angle distribution for separated single-walled carbon nanotubes*. Nano Lett. **8**, 3151 (2008). doi:10.1021/nl801364g. (Cited on page 89)

[Saz04] V. Sazonova, Y. Yaish, H. Üstünel, D. Roundy, T. A. Arias, and P. L. McEuen. *A tunable carbon nanotube electromechanical oscillator*. Nature **431**, 284 (2004). doi:10.1038/nature02905. (Cited on page 88)

[Sch66] J. Schmidt and I. Solomon. *Modulation de la photoconductivité dans le silicium á basse température par résonance magnetique électronique des impuretés peu profondes*. Compt. Rend. **263**, 169 (1966). (Cited on pages 29 and 37)

[Sch81] E. A. Schiff. *Spin polarization effects in the photoconductivity of a-Si:H*. AIP Conf. Proc. **73**, 233 (1981). doi:10.1063/1.33036. (Cited on pages 39, 73, and 78)

[Sch95] B. Schumacher. *Quantum coding*. Phys. Rev. A **51**, 2738 (1995). doi:10.1103/PhysRevA.51.2738. (Cited on page 3)

[Sch99] D. Schmalbein, G. G. Maresch, A. Kamlowski, and P. Hoefer. *The Bruker high-frequency-EPR system*. Appl. Magn. Reson. **16**, 185 (1999). doi:10.1007/BF03161933. (Cited on pages 29 and 116)

[Sch01] A. Schweiger and G. Jeschke. *Principles of pulse electron paramagnetic resonance*. Oxford University Press, England, UK, 2001. (Cited on page 41)

[Sch02] T. Schenkel, A. Persaud, S. J. Park, J. Meijer, J. R. Kingsley, J. W. McDonald, J. P. Holder, J. Bokor, and D. H. Schneider. *Single ion implantation for solid state quantum computer development.* J. Vac. Sci. Technol. B **20**, 1071 (2002). doi:10.1116/1.1518016. (Cited on page 13)

[Sch06] T. Schenkel, J. A. Liddle, A. Persaud, A. M. Tyryshkin, S. A. Lyon, R. de Sousa, K. B. Whaley, J. Bokor, J. Shangkuan, and I. Chakarov. *Electrical activation and electron spin coherence of ultralow dose antimony implants in silicon.* Appl. Phys. Lett. **88**, 112101 (2006). doi:10.1063/1.2182068. (Cited on page 136)

[Sch07] R. E. I. Schropp, R. Carius, and G. Beaucarne. *Amorphous silicon, microcrystalline silicon, and thin-film polycrystalline silicon solar cells.* MRS Bull. **32**, 219 (2007). doi:10.1557/mrs2007.25. (Cited on page 19)

[Sel06] H. Sellier, G. P. Lansbergen, J. Caro, S. Rogge, N. Collaert, I. Ferain, M. Jurczak, and S. Biesemans. *Transport spectroscopy of a single dopant in a gated silicon nanowire.* Phys. Rev. Lett. **97**, 206805 (2006). doi:10.1103/PhysRevLett.97.206805. (Cited on page 13)

[Sha04] A. V. Shah, H. Schade, M. Vanecek, J. Meier, E. Vallat-Sauvain, N. Wyrsch, U. Kroll, C. Droz, and J. Bailat. *Thin-film silicon solar cell technology.* Prog. Photovolt.: Res. Appl. **12**, 113 (2004). doi:10.1002/pip.533. (Cited on page 19)

[Sha08a] N. Shaji, C. B. Simmons, M. Thalakulam, L. J. Klein, H. Qin, H. Luo, D. E. Savage, M. G. Lagally, A. J. Rimberg, R. Joynt, M. Friesen, R. H. Blick, S. N. Coppersmith, and M. A. Eriksson. *Spin blockade and lifetime-enhanced transport in a few-electron Si/SiGe double quantum dot.* Nature Phys. **4**, 540 (2008). doi:10.1038/nphys988. (Cited on pages 9 and 33)

[Sha08b] S. Shankar, A. M. Tyryshkin, S. Avasthi, and S. Lyon. *Spin resonance of 2D electrons in a large-area silicon MOSFET.* Physica E **40**, 1659 (2008). doi:10.1016/j.physe.2007.10.030. (Cited on pages 128 and 136)

[Sha10] S. Shankar, A. M. Tyryshkin, J. He, and S. A. Lyon. *Spin relaxation and coherence times for electrons at the Si/SiO_2 interface.* Phys. Rev. B **82**, 195323 (2010). doi:10.1103/PhysRevB.82.195323. (Cited on pages 4 and 136)

[Shi05] T. Shinada, S. Okamato, T. Kobayashi, and I. Ohdomari. *Enhancing semiconductor device performance using ordered dopant arrays.* Nature **437**, 1128 (2005). doi:10.1038/nature04086. (Cited on page 13)

[Shi12] Z. Shi, C. B. Simmons, J. R. Prance, J. K. Gamble, T. S. Koh, Y.-P. Shim, X. Hu, D. E. Savage, M. G. Lagally, M. A. Eriksson, M. Friesen, and S. N. Coppersmith. *Fast hybrid silicon double-quantum-dot qubit.* Phys. Rev. Lett. **108**, 140503 (2012). doi:10.1103/PhysRevLett.108.140503. (Cited on page 3)

[Sho52] W. Shockley and W. T. J. Read. *Statistics of the recombinations of holes and electrons*. Phys. Rev. **87**, 835 (1952). doi:10.1103/PhysRev.87.835. (Cited on page 34)

[Sim07] C. B. Simmons, M. Thalakulam, N. Shaji, L. J. Klein, H. Qin, R. H. Blick, D. E. Savage, M. G. Lagally, S. N. Coppersmith, and M. A. Eriksson. *Single-electron quantum dot in Si/SiGe with integrated charge sensing*. Appl. Phys. Lett. **91**, 213103 (2007). doi:10.1063/1.2816331. (Cited on pages 5 and 9)

[Sim11] C. B. Simmons, J. R. Prance, B. J. van Bael, T. S. Koh, Z. Shi, D. E. Savage, M. G. Lagally, R. Jooynt, M. Friesen, S. N. Coppersmith, and M. A. Eriksson. *Tunable spin loading and T_1 of a silicon spin qubit measured by single-shot readout*. Phys. Rev. Lett. **106**, 156804 (2011). doi:10.1103/PhysRevLett.106.156804. (Cited on page 4)

[Sin96] R. A. Sinton and A. Cuevas. *Contactless determination of current-voltage characteristics and minority-carrier lifetimes in semiconductors from quasi-steady-state photoconductance data*. App. Phys. Lett. **69**, 2510 (1996). doi:10.1063/1.117723. (Cited on pages 20, 46, 50, and 53)

[Slo58] J. C. Slonczewski and P. R. Weiss. *Band structure of graphite*. Phys. Rev. **109**, 272 (1958). doi:10.1103/PhysRev.109.272. (Cited on page 9)

[Smi01] B. W. Smith and D. E. Luzzi. *Electron irradiation effects in single wall carbon nanotubes*. J. Appl. Phys. **90**, 3509 (2001). doi:10.1063/1.1383020. (Cited on page 87)

[Sol77] I. Solomon, D. Biegelsen, and J. C. Knights. *Spin-dependent photoconductivity in n-type and p-type amorphous silicon*. Solid State Commun. **22**, 505 (1977). doi:10.1016/0038-1098(77)91402-8. (Cited on page 73)

[Spe75] W. E. Spear and P. G. Le Comber. *Substitutional doping of amorphous silicon*. Solid State Commun. **17**, 1193 (1975). doi:10.1016/0038-1098(75)90284-7. (Cited on page 19)

[Sta14] J. Stark. *Beobachtungen über den Effekt des elektrischen Feldes auf Spektrallinien. I. Quereffekt*. Ann. Phys. **348**, 965 (1914). doi:10.1002/andp.19143480702. (Cited on page 14)

[Sta77] D. L. Staebler and C. R. Wronski. *Reversible conductivity changes in discharge-produced amorphous Si*. Appl. Phys. Lett. **31**, 292 (1977). doi:10.1063/1.89674. (Cited on pages 19 and 72)

[Sta80] D. L. Staebler and C. R. Wronski. *Optically induced conductivity changes in discharge-produced hydrogenated amorphous silicon*. J. Appl. Phys. **51**, 3262 (1980). doi:10.1063/1.328084. (Cited on page 19)

[Sta08a] C. Stampfer, J. Guettinger, F. Molitor, D. Graf, T. Ihn, and K. Ensslin. *Tunable Coulomb blockade in nanostructured graphene*. Appl. Phys. Lett. **92**, 012102 (2008). doi:10.1063/1.2827188. (Cited on pages 5 and 10)

[Sta08b] C. Stampfer, E. Schurtenberger, F. Molitor, J. Guettinger, T. Ihn, and K. Ensslin. *Tunable graphene single electron transistor*. Nano Lett. **8**, 2378 (2008). doi:10.1021/nl801225h. (Cited on pages 5 and 10)

[Ste83] D. Stein, K. v. Klitzing, and G. Weimann. *Electron spin resonance on GaAs-$Al_xGa_{1-x}As$ heterostructures*. Phys. Rev. Lett. **51**, 130 (1983). doi:10.1103/PhysRevLett.51.130. (Cited on pages 15 and 32)

[Ste98a] A. Stesmans and V. V. Afanes'ev. *Electrical activity of interfacial paramagnetic defects in thermal (100) Si/SiO_2*. Phys. Rev. B **57**, 10030 (1998). doi:10.1103/PhysRevB.57.10030. (Cited on page 69)

[Ste98b] A. Stesmans and V. V. Afanes'ev. *Electron spin resonance features of interface defects in thermal (100)Si/SiO_2*. J. App. Phys. **83**, 2449 (1998). doi:10.1063/1.367005. (Cited on pages 61 and 64)

[Ste06] A. R. Stegner, C. Boehme, H. Huebl, M. Stutzmann, K. Lips, and M. S. Brandt. *Electrical detection of coherent ^{31}P spin quantum states*. Nature Phys. **2**, 835 (2006). doi:10.1038/nphys465. (Cited on pages 29, 36, 44, and 47)

[Ste09a] G. A. Steele, G. Gotz, and L. P. Koewenhoven. *Tunable few-electron double quantum dots and Klein tunneling in ultraclean carbon nanotubes*. Nature Nanotech. **4**, 363 (2009). doi:10.1038/nnano.2009.71. (Cited on pages 11, 87, and 95)

[Ste09b] G. A. Steele, A. K. Hüttel, B. Witkamp, M. Poot, H. B. Meerwaldt, L. P. Kouwenhoven, and H. S. J. van der Zant. *Strong coupling between single-electron tunneling and nanomechanical motion*. Science **325**, 1103 (2009). doi:10.1126/science.1176076. (Cited on page 88)

[Ste11] N. Stemeroff and R. de Sousa. *Quantum readout and fast initialization of nuclear spin qubits with electric currents*. Phys. Rev. Lett. **107**, 197602 (2011). doi:10.1103/PhysRevLett.107.197602. (Cited on page 13)

[Sti95] B. Stich, S. Greulich-Weber, and J.-M. Speath. *Electrical detection of electron paramagnetic resonance: New possibilities for the study of point defects*. J. Appl. Phys. **77**, 1546 (1995). doi:10.1063/1.358906. (Cited on pages 35 and 37)

[Str82] R. A. Street. *Spin-dependent photoconductivity in undoped a-Si:H*. Philos. Mag. B **46**, 273 (1982). doi:10.1080/13642818208246439. (Cited on page 73)

[Stu83] M. Stutzmann and D. K. Biegelsen. *Electron-spin-lattice relaxation in amorphous silicon and germanium*. Phys. Rev. B **28**, 6256 (1983). doi:10.1103/PhysRevB.28.6256. (Cited on page 19)

[Stu85] M. Stutzmann, W. B. Jackson, and C. C. Tsai. *Light-induced metastable defects in hydrogenated amorphous-silicon – A systematic study*. Phys. Rev. B **32**, 23 (1985). doi:10.1103/PhysRevB.32.23. (Cited on pages 19 and 73)

[Stu86] M. Stutzmann, W. B. Jackson, and C. C. Tsai. *Annealing of metastable defects in hydrogenated amorphous silicon*. Phys. Rev. B **34**, 63 (1986). doi:10.1103/PhysRevB.34.63. (Cited on page 19)

[Stu00] M. Stutzmann, M. S. Brandt, and M. W. Bayerl. *Spin-dependent processes in amorphous and microcrystalline silicon: A survey*. J. Non-Cryst. Solids **266-269**, 1 (2000). doi:10.1016/S0022-3093(99)00871-6. (Cited on pages 18, 19, 35, 37, 72, and 74)

[Tab10] M. Tabe, D. Moraru, M. Ligowski, M. Anwar, R. Jablonski, Y. Ono, and T. Mizuno. *Single-electron transport through single dopants in a dopant-rich environment*. Phys. Rev. Lett. **105**, 016803 (2010). doi:10.1103/PhysRevLett.105.016803. (Cited on page 14)

[Tad98] B. M. Tadjikov, A. V. Astashkin, and Y. Sakaguchi. *Quantum beats of the reaction yield induced by a pulsed microwave field*. Chem. Phys. Lett. **283**, 179 (1998). doi:10.1016/S0009-2614(97)01350-X. (Cited on page 44)

[Tan77] T. Y. Tan, E. E. Gardner, and W. K. Tice. *Intrinsic gettering by oxide precipitate induced dislocations in Czochralski Si*. Appl. Phys. Lett. **30**, 175 (1977). doi:10.1063/1.89340. (Cited on page 20)

[Tan98] S. J. Tans, A. R. M. Verschueren, and C. Dekker. *Room-temperature transistor based on a single carbon nanotube*. Nature **393**, 49 (1998). doi:10.1038/29954. (Cited on page 85)

[Tan10] K. Y. Tan, K. W. Chan, M. Möttönen, A. Morello, C. Yang, J. van Donkelaar, A. Alves, J.-M. Pirkkalainen, D. N. Jamieson, R. G. Clark, and A. S. Dzurak. *Transport spectroscopy of single phosphorus donors in a silicon nanoscale transistor*. Nano Lett. **10**, 11 (2010). doi:10.1021/nl901635j. (Cited on page 14)

[Ter03] M. Terrones. *Science and technology of the twenty-first century: Synthesis, properties, and applications of carbon nanotubes*. Annu. Rev. Mater. Res. **33**, 419 (2003). doi:10.1146/annurev.matsci.33.012802.100255. (Cited on page 11)

[The08] C. Thelander, L. E. Fröberg, C. Rehnstedt, L. Samuelson, and L.-E. Wernersson. *Vertical enhancement-mode InAs nanowire field-effect-transistor*

with 50 nm wrap gate. IEEE Electron. Dev. Lett. **29**, 206 (2008). doi:10.1109/LED.2007.915374. (Cited on page 13)

[Tho73] D. D. Thornton and A. Honig. *Shallow-donor negative ions and spin-polarized electron transport in silicon*. Phys. Rev. Lett. **30**, 909 (1973). doi:10.1103/PhysRevLett.30.909. (Cited on pages 15 and 32)

[Tra96] M. M. J. Traecy, T. W. Ebbesen, and J. M. Gibson. *Exceptionally high Young's modulus observed for individual carbon nanotubes*. Nature **381**, 678 (1996). doi:10.1038/381678a0. (Cited on page 88)

[Tri80] A. D. Trifunac and J. P. Smith. *Optically detected time resolved EPR of radical ion pairs in pulse radiolysis of liquids*. Chem. Phys. Lett. **73**, 94 (1980). doi:10.1016/0009-2614(80)85210-9. (Cited on page 34)

[Tyr03] A. M. Tyryshkin, S. A. Lyon, A. V. Astashkin, and A. M. Raitsimring. *Electron spin relaxation times of phosphorus donors in silicon*. Phys. Rev. B **68**, 193207 (2003). doi:10.1103/PhysRevB.68.193207. (Cited on pages 136 and 141)

[Tyr05] A. M. Tyryshkin, S. A. Lyon, W. Jantsch, and F. Schäffler. *Spin manipulation of free two-dimensional electrons in Si/SiGe quantum wells*. Phys. Rev. Lett. **94**, 126802 (2005). doi:10.1103/PhysRevLett.94.126802. (Cited on page 140)

[Tyr11] A. M. Tyryshkin, S. Tojo, J. J. L. Morton, H. Riemann, N. V. Abrosimov, P. Becker, H.-J. Pohl, T. Schenkel, M. L. W. Thewalt, K. M. Itoh, and S. A. Lyon. *Electron spin coherence exceeding seconds in high purity silicon*. Nature Mat., Advanced online publicatiion (2011). doi:10.1038/nmat3182. (Cited on pages 4 and 9)

[Urb53] F. Urbach. *The long-wavelength edge of photographic sensitivity and of the electronic absorption of solids*. Phys. Rev. **92**, 1324 (1953). doi:10.1103/PhysRev.92.1324. (Cited on page 67)

[vHo92] H. van Houten, C. W. J. Beenakker, and A. A. M. Staring. *Coulomb-blockade oscillations in semiconductor nanostructures*. Surf. Sci. **263**, 442 (1992). doi:10.1016/0039-6028(92)90385-J. (Cited on page 7)

[vKl80] K. von Klitzing, G. Dorda, and M. Pepper. *New method for high-accuracy determination of the fine-structure constant based on quantized Hall resistance*. Phys. Rev. Lett. **45**, 494 (1980). doi:10.1103/PhysRevLett.45.494. (Cited on page 127)

[vWe88] B. J. van Wees, H. van Houten, C. W. J. Beenakker, J. G. Williamson, L. P. Kouwenhoven, D. van der Marel, and C. T. Foxon. *Quantized conductance of point contacts in a two-dimensional electron gas*. Phys. Rev. Lett. **60**, 848 (1988). doi:10.1103/PhysRevLett.60.848. (Cited on page 6)

[Van95] J. Vanhellemont, E. Simoen, A. Kaniava, M. Libezny, and C. Claeys. *Impact of oxygen related extended defects on silicon diode characteristics.* J. Appl. Phys. **77**, 5669 (1995). doi:10.1063/1.359209. (Cited on pages 19 and 49)

[Van04] L. M. K. Vandersypen, J. M. Elzerman, R. N. Schouten, L. H. Willems van Beveren, R. Hanson, and L. P. Kouwenhoven. *Real-time detection of single-electron tunneling using a quantum point contact.* Appl. Phys. Lett. **85**, 4394 (2004). doi:10.1063/1.1815041. (Cited on page 6)

[vdP58] L. J. van der Pauw. *A method of measuring specific resistivity and Hall effect of discs of arbitrary shape.* Philips Res. Rep. **13**, 1 (1958). (Cited on page 110)

[Vio03] D. Vion, A. Aassime, A. Cottet, P. Joyez, H. Pothier, C. Urbina, D. Esteve, and M. H. Devoret. *Rabi oscillations, Ramsey fringes and spin echoes in an electrical circuit.* Fortschr. Phys. **51**, 462 (2003). doi:10.1002/prop.200310063. (Cited on page 43)

[Vri00] R. Vrijen, E. Yablonovitch, K. Wang, H. W. Jiang, A. Balandin, V. Roychowdhury, T. Mor, and D. DiVincenzo. *Electron-spin-resonance transistors for quantum computing in silicon-germanium heterostructures.* Phys. Rev. A **62**, 012306 (2000). doi:10.1103/PhysRevA.62.012306. (Cited on page 3)

[War09] J. H. Warner, F. Schäffel, G. Zhong, M. H. Rümmeli, B. Buchner, J. Robertson, and G. A. D. Briggs. *Investigating the diameter-dependent stability of single-walled carbon nanotubes.* ACS Nano **3**, 1557 (2009). doi:10.1021/nn900362a. (Cited on page 89)

[War10] J. H. Warner, M. H. Rümmeli, A. Bachmatiuk, and B. Büchner. *Structural transformations of carbon chains inside nanotubes.* Phys. Rev. B **81**, 155419 (2010). doi:10.1103/PhysRevB.81.155419. (Cited on page 89)

[War11] J. H. Warner, S. R. Plant, N. P. Young, K. Porfyrakis, A. I. Kirkland, and G. A. D. Briggs. *Atomic scale growth dynamics of nanocrystals within carbon nanotubes.* ACS Nano **5**, 1410 (2011). doi:10.1021/nn1031802. (Cited on page 89)

[Wat64] G. D. Watkins and J. W. Corbett. *Defects in irradiated silicon: Electron paramagnetic resonance and electron-nuclear double resonance of the Si-E center.* Phys. Rev. **134**, A1359 (1964). doi:10.1103/PhysRev.134.A1359. (Cited on page 18)

[Web83] E. R. Weber. *Transition metals in silicon.* Appl. Phys. A **30**, 1 (1983). doi:10.1007/BF00617708. (Cited on page 16)

[Weg60] M. Weger. *Passage effects in a paramagnetic resonance experiment*. Bell Syst. Tech. J. **39**, 1013 (1960). http://www.alcatel-lucent.com/bstj/vol39-1960/articles/bstj39-4-1013.pdf. (Cited on pages 26, 39, and 41)

[Wer94] J. H. Werner, U. Spadaccini, and F. Benhart. *Low-temperature ohmic Au/Sb contacts to n-type Si*. J. Appl. Phys. **75**, 994 (1994). doi:10.1063/1.356425. (Cited on page 95)

[Wil04] Z. Wilamowski and W. Jantsch. *Suppression of spin relaxation of conduction electrons by cyclotron motion*. Phys. Rev. B **69**, 035328 (2004). doi:10.1103/PhysRevB.69.035328. (Cited on page 151)

[Wit10] W. M. Witzel, M. S. Carroll, A. Morello, Ł. Cywiński, and S. Das Sarma. *Electron spin decoherence in isotope-enriched silicon*. Phys. Rev. Lett. **105**, 187602 (2010). doi:10.1103/PhysRevLett.105.187602. (Cited on page 9)

[Wol01] S. A. Wolf, D. D. Awschalom, R. A. Buhrman, J. M. Daughton, S. von Molnár, M. L. Roukes, A. Y. Chtchelkanova, and D. M. Treger. *Spintronics: A spin-based electronics vision for the future*. Science **294**, 1488 (2001). doi:10.1126/science.1065389. (Cited on page 1)

[Woo60] H. H. Woodbury and G. W. Ludwig. *Spin resonance of transition metals in silicon*. Phys. Rev. **117**, 102 (1960). doi:10.1103/PhysRev.117.102. (Cited on page 61)

[Wra93] J. Wrachtrup, C. von Borczyskowski, J. Bernard, M. Orritt, and R. Brown. *Optical detection of magnetic resonance in a single molecule*. Nature **363**, 244 (1993). doi:10.1038/363244a0. (Cited on page 29)

[Wu10] M. W. Wu, J. H. Jiang, and M. Q. Weng. *Spin dynamics in semiconductors*. Phys. Rep. **493**, 61 (2010). doi:10.1016/j.physrep.2010.04.002. (Cited on page 140)

[Xia04] M. Xiao, I. Martin, E. Yablonovitch, and H. W. Jiang. *Electrical detection of the spin resonance of a single electron in a silicon field-effect transistor*. Nature **430**, 435 (2004). doi:10.1038/nature02727. (Cited on pages 29, 32, and 33)

[Xia06] J. Xiang, W. Lu, Y. Hu, Y. Wu, H. Yan, and C. M. Lieber. *Ge/Si nanowire heterostructures as high-performance field-effect transistors*. Nature **441**, 489 (2006). doi:10.1038/nature04796. (Cited on page 13)

[Xia10] M. Xiao, M. G. House, and H. W. Jiang. *Measurement of the spin relaxation time of single electrons in a silicon metal-oxide-semiconductor-based quantum dot*. Phys. Rev. Lett. **104**, 096801 (2010). doi:10.1103/PhysRevLett.104.096801. (Cited on page 4)

[Xu09] X. Xu, W. Yao, B. Sun, D. G. Steel, A. S. Bracker, D. Gammon, and L. J. Sham. *Optically controlled locking of the nuclear field via coherent dark-state spectroscopy*. Nature **459**, 1105 (2009). doi:10.1038/nature08120. (Cited on page 8)

[Yab03] E. Yablonovitch, H. W. Jiang, H. Kosaka, H. D. Robinson, D. S. Rao, and T. Szkopek. *Optoelectronic quantum telecommunications based on spins in semiconductors*. Proceedings of the IEEE **91**, 761 (2003). doi:10.1109/JPROC.2003.811799. (Cited on page 4)

[Yaf63] Y. Yafet. *g Factors and spin-lattice relaxation of conduction electrons*. Solid State Phys. **14**, 1 (1963). doi:10.1016/S0081-1947(08)60259-3. (Cited on page 138)

[Zav45] E. Zavoisky. *Paramagnetic relaxation of siquid solutions for perpendicular fields*. J. Phys. USSR **9**, 211 (1945). (Cited on page 24)

[Zav46] E. Zavoisky. *Spin magnetic resonance in the decimeterwave region*. J. Phys. USSR **10**, 197 (1946). (Cited on page 24)

[Zee87] P. Zeeman. *The effect of magnetisation on the nature of light emitted by a substance*. Nature **55**, 347 (1987). doi:10.1038/055347a0. (Cited on pages 6 and 24)

[Zha05] Y. Zhang, Y.-W. Tan, H. L. Stormer, and P. Kim. *Experimental observation of the quantum Hall effect and Berry's phase in graphene*. Nature **438**, 201 (2005). doi:10.1038/nature04235. (Cited on page 10)

[Zhu05] H. Zhu, K. Suenaga, A. Hashimoto, K. Urita, and S. Iijima. *Structural identification of single and double-walled carbon nanotubes by high-resolution transmission electron microscopy*. Chem. Phys. Lett. **412**, 116 (2005). doi:10.1016/j.cplett.2005.06.119. (Cited on page 89)

[Zot90] G. Zoth and W. Bergholz. *A fast, preparation-free method to detect iron in silicon*. J. Appl. Phys. **67**, 6764 (1990). doi:10.1063/1.345063. (Cited on page 59)

[Žut04] J. Žutić, I. Fabian, and S. Das Sarma. *Spintronics: Fundamentals and applications*. Rev. Mod. Phys. **76**, 323 (2004). doi:10.1103/RevModPhys.76.323. (Cited on pages 1 and 138)